Measurement of Charged Triple Gauge Coupling Parameters at e^+e^- Colliders

Dissertation
zur Erlangung des Doktorgrades
des Fachbereichs Physik
der Universität Hamburg

vorgelegt von
Wolfgang Menges
aus Oldenburg (Oldb)

Hamburg
2003

Gutachter der Dissertation	: Prof. Dr. Rolf-Dieter Heuer Prof. Dr. Robert Klanner
Gutachter der Disputation	: Prof. Dr. Rolf-Dieter Heuer Prof. Dr. Peter Schleper
Datum der Disputation	: 01.12.2003
Vorsitzender des Prüfungsausschusses	: Prof. Dr. Götz Heinzelmann
Vorsitzender des Promotionsausschusses	: Prof. Dr. Roland Wiesendanger
Dekan des Fachbereichs Physik	: Prof. Dr. Günther Huber

Abstract

The measurement of triple gauge boson couplings in the reaction $\mathrm{e^+e^-} \to \mathrm{W^+W^-} \to \mathrm{q\overline{q}q\overline{q}}$ is presented. The analysed events are recorded by the OPAL detector at LEP at centre-of-mass energies of 183 – 209 GeV with a total integrated luminosity of 680 pb^{-1}. Only CP-conserving couplings are considered and $\mathsf{SU(2)}_L \times \mathsf{U(1)}_Y$ relations are used, resulting in four independent couplings, $\Delta\kappa_\gamma$, Δg_1^Z, λ and g_5^Z. The method of optimal observables is used to extract the anomalous couplings. One-parameter fits, assuming the other couplings to take their Standard Model values yield

$$\Delta\kappa_\gamma = 0.17^{+0.72}_{-0.28}, \quad \Delta g_1^Z = 0.09^{+0.11}_{-0.10}, \quad \lambda = 0.01^{+0.33}_{-0.14} \text{ and } g_5^Z = -0.37^{+0.24}_{-0.26},$$

where the errors include both statistical and systematic uncertainties. Theses results are combined with the results from the other two W-pair final states measured at OPAL and with the measurements from the other three LEP experiments.

Studies concerning the potential of the measurement of triple gauge boson couplings at a high luminosity linear collider as TESLA are presented. Using the Method of Spin Density Matrix to calculate sensitive observables gives an expected sensitivity of $\sim 3-4\times 10^{-4}$ for the couplings $\Delta\kappa_\gamma$, Δg_1^Z and λ_γ. The unique feature of longitudinally polarised electron and positron beams increases the expected precision on anomalous couplings by a factor of 1.5 – 2 and allows us to disentangle WWγ and WWZ couplings, which is not possible in the unpolarised case.

Zusammenfassung

Die Messung von Drei-Eichboson-Kopplungen im Prozess $\mathrm{e^+e^-} \to \mathrm{W^+W^-} \to \mathrm{q\overline{q}q\overline{q}}$ wird vorgestellt. Die Daten wurden mit dem OPAL Detektor am LEP Speicherring bei Schwerpunktenergien von 183 – 209 GeV aufgezeichnet und entsprechen einer integrierten Luminosität von 680 pb^{-1}. Es werden nur CP erhaltende Kopplungen mit zusätzlichen $\mathsf{SU(2)}_L \times \mathsf{U(1)}_Y$ Relationen betrachtet. Die vier unabhängigen Parameter $\Delta\kappa_\gamma$, Δg_1^Z, λ und g_5^Z genügen diesen Einschränkungen. Die Methode der Optimalen Observablen wird angewendet, um anomale Kopplungsparameter zu extrahieren. Die Messung von jeweils einem Parameter, während die anderen drei Parameter auf ihren Standard Modell Wert fixiert sind, ergibt

$$\Delta\kappa_\gamma = 0.17^{+0.72}_{-0.28}, \quad \Delta g_1^Z = 0.09^{+0.11}_{-0.10}, \quad \lambda = 0.01^{+0.33}_{-0.14} \text{ und } g_5^Z = -0.37^{+0.24}_{-0.26}.$$

Die angegebenen Fehler enthalten sowohl statistische als auch systematische Unsicherheiten. Diese Ergebnisse werden mit den Ergebnissen aus den anderen zwei W-Paar Endzuständen bei OPAL kombiniert. Weiter werden die OPAL Messungen mit den Messungen der anderen drei LEP Experimente kombiniert.

Eine Studie zur Abschätzung des Potenzials der Messung von Drei-Eichboson-Kopplungen an einem Linearcollider mit hoher Luminosität wie TESLA wird vorgestellt. Die Methode der Spin-Dichte-Matrizen wird verwendet, um sensitive Observablen zu berechnen. Die erwartete Sensitivität ist $\sim 3-4\times 10^{-4}$ für die Kopplungen $\Delta\kappa_\gamma$, Δg_1^Z und λ_γ. Die einzigartige Eigenschaft von longitudinal polarisierten Elektron- und Positronstrahlen steigert die erwartete Genauigkeit um einen Faktor 1.5 – 2 und ermöglicht die WWγ und WWZ Kopplungen von einander zu trennen, was im unpolarisierten Fall nicht möglich ist.

There is a theory which states that if ever anyone discovers exactly what the Universe is for and why it is here, it will instantly disappear and be replaced by something even more bizarre and inexplicable.

There is another theory which states that this has already happened.

The Restaurant at the End of the Universe – Douglas Adams

Contents

Chapter 1

Introduction

The investigation of a system for symmetries and transformations, which keep it invariant, is always very fruitful for understanding the physics of this system. Let us consider an example from classical mechanics: If a system is invariant under a coordinate transformation, i. e. the Lagrangian is independent of this coordinate, the corresponding generalised momentum is conserved. For a rotational invariance, the conserved quantity is the angular momentum. Moving from classical mechanics to quantum field theory, the language for the description changes but the symmetry concept is the same. The investigation of symmetries and invariances is very instructive. Here, the transformations are called gauge transformations and must have certain properties. For example, in quantum electrodynamics (QED), a system is invariant under a local gauge transformation, if and only if a vector field is introduced in addition to the particle fields. The gauge transformation can be any scalar functions of the coordinates. The field describes the electromagnetic interactions and manifests itself as the photon. In other words, local gauge invariance is only preserved, if a massless vector field is introduced with which the charged particles interact.

This concept of gauge invariance is used very successfully for the description of the Standard Model of elementary particle physics. The Standard Model describes three of the four fundamental forces, which occur in nature: electromagnetic, weak and strong interactions. Gravity is not included into the Standard Model, because no theoretical concept is yet found, which incorporates general relativity into a quantum field theory, although string theory is considered a good candidate. Besides this theoretical problem, the effect of gravity on elementary particles at energies below a few TeV is negligible.

The matter particles of the Standard Model are classified into leptons and quarks as well as into three families or generations, which differ only by their masses. The particles of the first generations are the electron and its neutrino and the up and down quark. Each of the three interactions can be introduced by considering a certain gauge transformation. Glashow, Salam and Weinberg [1] showed in the 1960s that the gauge group $\mathsf{SU}(2)_L \times \mathsf{U}(1)_Y$ can be used to unify the electromagnetic and weak interactions. Demanding gauge invariance under these two groups introduces four gauge bosons: the photon as the gauge boson of the electromagnetic interaction and the Z and $\mathrm{W}^{\pm}$ gauge bosons of the weak interaction.

Because the groups $\mathsf{U}(1)$ and $\mathsf{SU}(2)$ differ in their algebraic structure, the corresponding gauge bosons have different properties. $\mathsf{U}(1)$ is an Abelian group and hence the photon as the gauge boson of $\mathsf{U}(1)_{em}$ does not couple to itself. On the other hand, $\mathsf{SU}(2)$ is a non-Abelian group and self-couplings of the gauge bosons are explicitly predicted in the Standard Model

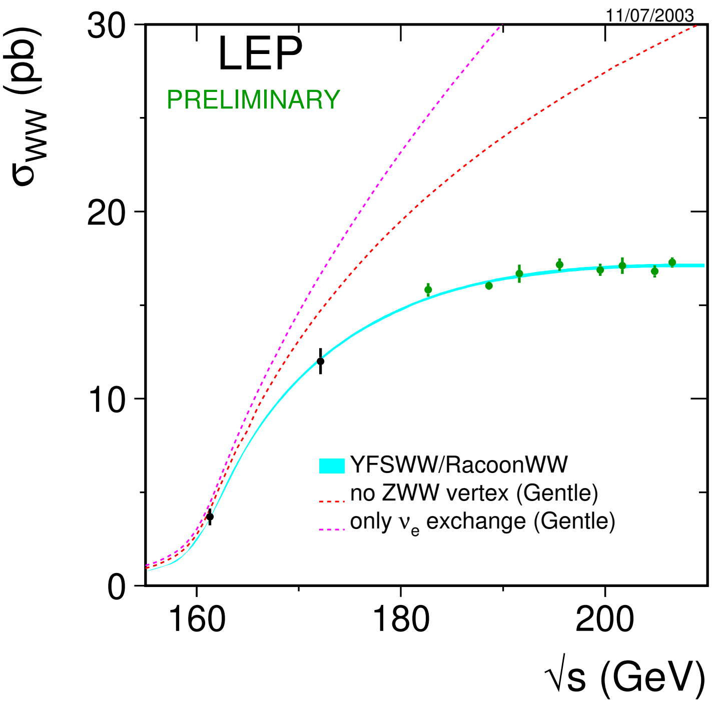

Figure 1.1: Measured cross-section for W-pair production at LEP [2].

as a consequence. The Standard Model predicts two triple gauge boson couplings (WWγ, WWZ) and four quartic gauge boson couplings (WWWW, WW$\gamma\gamma$, WWγZ, WWZZ). These far-reaching predictions have to be tested in order to confirm the electroweak sector of the Standard Model.

In e^+e^- collisions the production of W pairs, single W bosons and single photons is sensitive to triple gauge boson couplings and each reaction has certain advantages for the investigation of these couplings. For example, single-γ production is only sensitive to WWγ couplings. In this thesis the focus is put on W-pair production. This final state involves WWZ and WWγ couplings and is the most sensitive of the three. Already the total W-pair cross-section can be used to search for deviations from the Standard Model predictions, which are introduced by anomalous triple gauge boson couplings. Figure 1.1 shows the combined W-pair cross-section from all four LEP experiments. The data is shown as dots with error bars and the most recent prediction of the Standard Model is plotted as the solid line. Already this inclusive measurement clearly exhibits the presence of both triple gauge boson couplings, WWγ and WWZ. Anomalous couplings do not alter only the production but also the helicity structure of W pairs with respect to the Standard Model. Therefore, the W-production angle and any observable related to the helicity structure of the W bosons can be used to extract further, more precise information about anomalous couplings. In this thesis two methods are used to construct sensitive observables: the Method of Optimal Observables and the Method of Spin Density Matrices. In the first case, the method describes the construction of observables, which have maximal sensitivity, hence the name Optimal Observables. In the second case, a more physical approach is taken and the W polarisation is reconstructed and used as a sensitive observable. The total differential information cannot be reconstructed in all W-pair decay modes. A W boson decays either in a lepton or a quark pair, therefore W pairs can decay either hadronically ($q\bar{q}q\bar{q}$), semileptonically($q\bar{q}\ell\bar{\nu}_\ell$) or leptonically ($\ell\bar{\nu}_\ell\bar{\ell}'\nu_{\ell'}$). The semileptonic final state is the golden channel of all W-pair decays because of the high reconstruction level. The hadronic final state is also interesting because of its high branching ratio, but the reconstruction is quite complex because of four identical jets. The leptonic final state has a low branching ratio, but the decay leptons are normally measured very well.

The thesis is organised as follows. In chapter 2 the theoretical concepts of triple gauge boson couplings in the Standard Model and beyond are introduced. The phenomenology of gauge boson production at e^+e^- colliders is discussed in chapter 3. Some emphasis is put on the description of radiative corrections in W-pair and, as a more general case, in four-fermion production. These corrections are important for the measurement of triple gauge boson couplings in W-pair production. In some details the fragmentation and hadronisation of quarks is presented, as it turned out that its modelling is an important systematic uncertainty for the hadronic decay channel. The experimental apparatus is introduced in chapter 4, namely the LEP collider, which operated up to a centre-of-mass energy of 209 GeV, and the OPAL experiment. The TESLA project is presented as one of the three future e^+e^- linear collider projects. Some details of the accelerator and the proposed detector are given. For both e^+e^- colliders the beam energy measurement is discussed to show that the machine-detector interface is important for the experiments. Without a precise energy measurement the best detector is useless.

In chapter 5 the main analysis of triple gauge boson couplings in the reaction $e^+e^- \to W^+W^- \to q\bar{q}q\bar{q}$ at OPAL is presented. The reconstruction of a W pair out of four jets is not trivial and efficient methods for jet pairing and charge estimation are discussed. For the extraction of the triple gauge boson couplings the Method of Optimal Observables is used. Results for centre-of-mass energies between 183 and 209 GeV including intensive studies of systematic errors are given. The combination of this measurement with other OPAL and LEP measurements is presented in chapter 6. At the end of this chapter these results are compared with the results obtained at the Tevatron in $p\bar{p}$ collisions.

The next linear collider will give an excellent opportunity to study triple gauge boson couplings with very high precision. In chapter 7, a study of triple gauge boson couplings in the framework of the TESLA project is presented. The semileptonic decay channel of W-pair production is analysed to estimate the expected sensitivity and to study some new features of a high luminosity linear collider, e. g. beamstrahlung and longitudinal beam polarisation. In contrast to the OPAL analysis, the Method of Spin Density Matrices is used to extract the triple gauge boson couplings. Here, the W-production angle and the W polarisation are used as sensitive observables.

Finally, the presented results of this work are summarised in chapter 8.

Chapter 2

Theoretical Context

In this chapter the particles of the Standard Model (SM) and their interactions are introduced, with emphasis on the gauge structure of the electroweak sector. The gauge principle is used to derive the charged current triple gauge boson couplings (TGCs) of the SM. The effects of physics beyond the Standard Model can be described by an effective theory, where the new degrees of freedom are integrated out. The most general form of such an effective theory affecting triple gauge boson couplings is shown. As an example the class of theories describing strong electroweak symmetry breaking is presented and their implications on TGCs is discussed.

2.1 Electroweak Theory of the Standard Model

The elementary particles of the Standard Model are classified into leptons and quarks as well as into three families. The first family consists of the electron and its neutrino and the up and down quark. The second family consists of the muon, as the charged lepton, and its neutron and the charm and strange quark. In the last family the tau lepton and its neutrino and the top and bottom quark are combined. The charged leptons have an electric charge of -1, in units of the elementary charge e, while the neutrinos carry no charge. The quarks have fractional charges, $\frac{1}{3}$ for up-type quarks and $-\frac{2}{3}$ for down-type quarks. The corresponding particles in the three families have identical properties in the electromagnetic, weak and strong interactions and differ only in their masses. The neutrinos are assumed to be massless.

The electromagnetic, weak and strong interactions between these particles are introduced by the gauge principle, which is discussed below. Here, the different properties of each interaction are discussed.

The photon is the gauge bosons of the electromagnetic interaction. It couples to the electric charge, therefore to all charged leptons and the quarks. In the Standard Model no photon self-couplings are allowed. The photon-fermion vertex is shown in figure 2.1.

The weak interaction couples only to left-handed particles, which can be incorporated in the Standard Model by defining an adequate charge. All particles are grouped into singlets or doublets of the weak isospin I. Left-handed particles are grouped into doublets with isospin $\frac{1}{2}$, as the electron ($I_3 = -\frac{1}{2}$) and its neutrino ($I_3 = \frac{1}{2}$), and right-handed particles in singlets. Particles in singlets have weak isospin zero and do not interact weakly. The weak interaction is mediated by three massive gauge bosons, the neutral Z boson and the charged

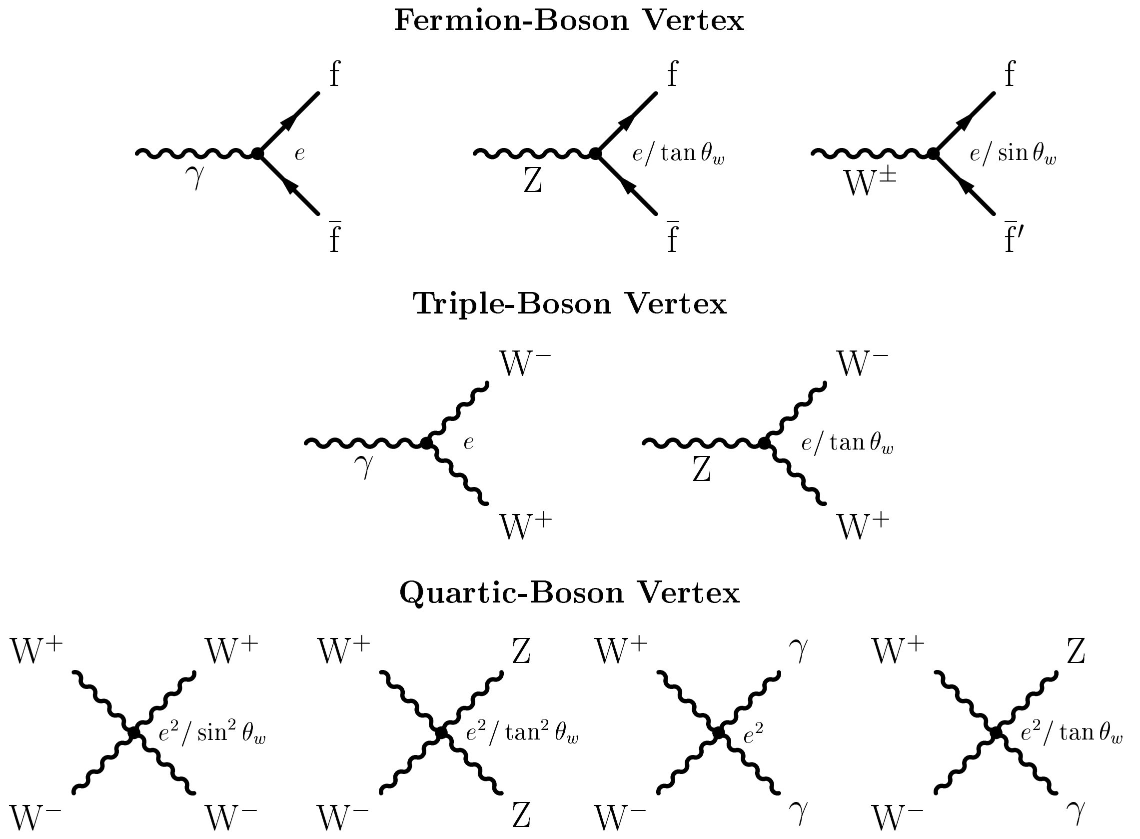

Figure 2.1: All electroweak vertices in the Standard Model. e is the coupling constant of the electromagnetic interaction and θ_w the weak mixing angle.

W$^\pm$ bosons. In figure 2.1 all possible vertices including these gauge bosons are shown. The coupling strength of all electroweak vertices can be expressed in terms of the electric charge e and the weak mixing angle θ_w, as shown in figure 2.1.

The structure of the strong interaction is similar to the weak interaction. A colour charge is introduced as the charge of the strong interaction. Quarks are grouped into triplets, while leptons, which do not interact strongly, are grouped into singlets. The interaction is mediated by eight massless gauge bosons, called gluons. As the quarks, they carry a colour charge. In the Standard Model self-couplings of three and four gluons are predicted, as shown in figure 2.2. The figure also includes the gluon-quark vertex.

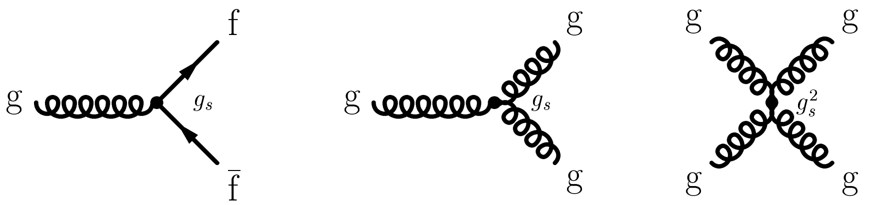

Figure 2.2: The three allowed vertices including at least one gluon. g_s is the coupling constant of the strong interaction.

Gauge Principle

The Standard Model is based on non-Abelian gauge groups, i. e. their generators τ^a do not commute,

$$\left[\tau^a, \tau^b\right] = if^{abc}\tau^c, \tag{2.1}$$

where f^{abc} are the structure constants. The fermion field ψ_i is required to be invariant under local transformations,

$$\psi_i(x) \to \Omega_{ij}\psi_j(x), \tag{2.2}$$

where Ω is a function of spacetime and can be parametrised as

$$\Omega_{ij}(x) = \left(e^{i\theta^a(x)\tau^a}\right)_{ij}. \tag{2.3}$$

The functions $\theta^a(x)$ are arbitrary scalar functions of the spacetime coordinate x^μ, hence the name local transformation. The generators of the group introduce the structure of the gauge group into the corresponding interaction. Now the problem is that the derivatives of the fermion field are not covariant under this transformation. This can be cured by introducing a new field, A_μ, with which we can define the covariant derivative

$$D_\mu \equiv \partial_\mu - igA_\mu \tag{2.4}$$

with $A_\mu = A^a_\mu\tau^a$. A^a_μ has to transform as

$$A^a_\mu(x) \to A^a_\mu(x) - \frac{1}{g}\partial_\mu\theta^a + f^{abc}\theta^b A^c_\mu, \tag{2.5}$$

thus the covariant derivative of the fermion field ψ is gauge covariant. Since D_μ is covariant, the commutator of two covariant derivatives is also covariant. We define the field strength tensor

$$\begin{aligned} F_{\mu\nu} &= \frac{i}{g}\left[D_\mu, D_\nu\right] \\ &= \left(\partial_\mu A^a_\nu - \partial_\nu A^a_\mu + gf^{abc}A^b_\mu A^c_\nu\right)\tau^a \\ &= F^a_{\mu\nu}\tau^a, \end{aligned} \tag{2.6}$$

which includes an additional term compared to QED, where the generators commute. In the case of non-vanishing commutators and hence non-vanishing structure constants f^{abc}, three and four gauge boson vertices are predicted. Canonically, fields are introduced into the Lagrangian as $-\frac{1}{4}F^a_{\mu\nu}F^{a\mu\nu}$, which can be expressed in terms of the field A_μ using equation (2.6). Keeping only interaction terms gives

$$\mathcal{L}_{\text{gauge}} = -\frac{g}{2}\left(\partial_\mu A^a_\nu - \partial_\nu A^a_\mu\right)f^{abc}A^{b\mu}A^{c\nu} + \frac{g^2}{4}f^{abc}f^{ade}A^b_\mu A^c_\nu A^{d\mu}A^{e\nu}. \tag{2.7}$$

Electroweak Sector

In the electroweak sector of the Standard Model the gauge group is $\mathsf{SU(2)}_L \times \mathsf{U(1)}_Y$. $\mathsf{SU(2)}_L$ is the gauge group of the weak interaction with the coupling constant g and the three fields W^1_μ, W^2_μ and W^3_μ. A representation of the group generators are the Pauli matrices, τ^a, and the structure constants f^{abc} are ϵ^{abc}, where ϵ is the total antisymmetric tensor. $\mathsf{U(1)}_Y$ is the gauge group of the hypercharge. The electric charge, Q, is related to the hypercharge, Y, and the third component of the weak isospin, I_3, by $Q = I_3 + Y/2$. The couplings constant is g' and the corresponding field is called B_μ.

The canonical covariant derivative is

$$D_\mu \equiv \partial_\mu - ig\tau^a W_\mu^a - i\frac{g'}{2} Y B_\mu \tag{2.8}$$

and the corresponding field strength tensors are

$$\begin{aligned} W_{\mu\nu}^a &= \partial_\mu W_\nu^a - \partial_\nu W_\mu^a + g\epsilon^{abc} W_\mu^b W_\mu^c \\ B_{\mu\nu} &= \partial_\mu B_\nu - \partial_\nu B_\mu. \end{aligned} \tag{2.9}$$

We are interested in the physical particles which are linear combinations of the B_μ field and the components of the W_μ field. The $W_\mu^\pm$ fields are linear combinations of the first and second component of the W_μ field, while the Z_μ and A_μ fields are a mixture of the B_μ field and the third component of the W_μ field:

$$\begin{aligned} W_\mu^\pm &= \frac{1}{\sqrt{2}} \left(W_\mu^1 \pm i W_\mu^2 \right) \\ A_\mu &= \cos\theta_w B_\mu + \sin\theta_w W_\mu^3 \\ Z_\mu &= -\sin\theta_w B_\mu + \cos\theta_w W_\mu^3, \end{aligned} \tag{2.10}$$

where θ_w is the weak mixing angle, which is defined in terms of the two coupling constants g and g':

$$\tan\theta_w = \frac{g'}{g} \tag{2.11}$$

The electromagnetic coupling constant e is related to g and g' as $e = g\sin\theta_w$ and $e = g'\cos\theta_w$, respectively. After introducing the Higgs field into the theory, in order to give the gauge bosons a finite mass, the Higgs mechanism breaks the $\mathsf{SU(2)}_L \times \mathsf{U(1)}_Y$ symmetry down to $\mathsf{U(1)}_{em}$ and give the following masses

$$\begin{aligned} M_\mathrm{W} &= \frac{gv}{2} \\ M_\mathrm{Z} &= \frac{gv}{2\cos\theta_w} = \frac{M_\mathrm{W}}{\cos\theta_w} \\ M_\gamma &= 0, \end{aligned} \tag{2.12}$$

where v is the vacuum expectation value of the Higgs field. The Z mass is related to the W mass by the weak mixing angle and, by construction, the photon mass is still zero.

The couplings between the physical fields can be read off from the Lagrangian (2.7) after inserting the definition of the field tensors and expressing the fields W_μ and B_μ in terms of the physical fields $W_\mu^\pm$, Z_μ and A_μ using equation (2.10). This is presented for the three gauge boson interaction:

$$\mathcal{L}_{TGC} = -\frac{g}{2}\left(\partial_\mu W_\nu^a - \partial_\nu W_\mu^a\right)\epsilon^{abc} W^{b\mu} W^{c\nu} = -\frac{g}{2}\hat{W}_{\mu\nu}^a \epsilon^{abc} W^{b\mu} W^{c\nu}$$

$$
\begin{aligned}
&= -g\hat{W}^{i}_{\mu\nu}\epsilon^{ij}W^{j\mu}W^{3\nu} - \frac{g}{2}\hat{W}^{3}_{\mu\nu}\epsilon^{ij}W^{i\mu}W^{j\nu} \\
&= -g\left[\hat{W}^{1}_{\mu\nu}W^{2\mu} - \hat{W}^{2}_{\mu\nu}W^{1\mu}\right]W^{3\nu} - \frac{g}{2}\hat{W}^{3}_{\mu\nu}\left[W^{1\mu}W^{2\nu} - W^{2\mu}W^{1\nu}\right] \\
&= ig\left[\hat{W}^{+}_{\mu\nu}W^{-\mu} - \hat{W}^{-}_{\mu\nu}W^{+\mu}\right]W^{3\nu} + \frac{ig}{2}\hat{W}^{3}_{\mu\nu}\left[W^{-\mu}W^{+\nu} - W^{+\mu}W^{-\nu}\right] \\
&= ig\left(\hat{W}^{+}_{\mu\nu}W^{-\mu} - \hat{W}^{-}_{\mu\nu}W^{+\mu}\right)W^{3\nu} + ig\hat{W}^{3}_{\mu\nu}W^{-\mu}W^{+\nu} \\
&= ig\sin\theta_w\left(\hat{W}^{-}_{\mu\nu}W^{+\mu} - \hat{W}^{+}_{\mu\nu}W^{-\mu}\right)A^{\nu} + ig\sin\theta_w\hat{A}_{\mu\nu}W^{-\mu}W^{+\nu} \\
&\quad + ig\cos\theta_w\left(\hat{W}^{-}_{\mu\nu}W^{+\mu} - \hat{W}^{+}_{\mu\nu}W^{-\mu}\right)Z^{\nu} + ig\cos\theta_w\hat{Z}_{\mu\nu}W^{-\mu}W^{+\nu}, \qquad (2.13)
\end{aligned}
$$

where $i, j = 1, 2$ and $\hat{V}_{\mu\nu} = \partial_\mu V_\nu - \partial_\nu V_\mu$, $V_\mu = W_\mu, A_\mu, Z_\mu$. There are two contributions with different structure to each triple gauge vertex, but both have the same coupling strength. In the case of the WWγ vertex this is $g\sin\theta_w = e$, as expected, and in the case of the WWZ vertex this is $g\cos\theta_w = e/\tan\theta_w$.

2.2 Charged Triple Gauge Vertex

New physics beyond the Standard Model introduces new interactions and new particles in addition to the one described by the SM. If the energy scale of the new physics is much higher than the available centre-of-mass energy, its effects can not be observed directly. However, they can contribute to the known interactions via loop effects. Therefore, a low-energy approximation of the new physics can be derived by integrating out the new degrees of freedom. Only the SM fields are kept and effective couplings are introduced into the Standard Model.

This procedure is already known from the description of the β-decay $\mathrm{n} \to \mathrm{pe}^{-}\overline{\nu}_{\mathrm{e}}$ by Fermi. The transition from the neutron to the proton proceeds via the exchange of a W^{+} boson. In the low-energy limit this W^{+} exchange can be approximated by a contact-interaction between the four particles with a couplings of $G_F/\sqrt{2}$, where G_F is the Fermi constant. The W propagator is approximated by a constant factor, which relates the Fermi coupling to the W mass and the weak coupling constant

$$\frac{G_F}{\sqrt{2}} = \frac{g^2}{8M_{\mathrm{W}}^2}. \qquad (2.14)$$

In the case of the description of triple gauge vertex WWV (V=Z or γ) beyond the Standard Model, the most general effective Lagrangian build of all possible triple combinations of electroweak gauge fields is [3, 4]

$$
\begin{aligned}
\frac{\mathcal{L}^{WWV}}{ig_{WWV}} &= g_1^V V^{\mu}\left(\hat{W}^{-}_{\mu\nu}W^{+\nu} - \hat{W}^{+}_{\mu\nu}W^{-\nu}\right) + \kappa_V W^{-}_{\mu}W^{+}_{\nu}\hat{V}^{\mu\nu} + \frac{\lambda_V}{M_{\mathrm{W}}^2}\hat{V}^{\mu\nu}\hat{W}^{+\rho}_{\mu}\hat{W}^{-}_{\rho\nu} \\
&- ig_4^V W^{-}_{\mu}W^{+}_{\nu}(\partial^{\mu}V^{\nu} + \partial^{\nu}V^{\mu}) \\
&+ ig_5^V \varepsilon^{\mu\nu\rho\sigma}\left[(\partial^{\rho}W^{-}_{\mu})W^{+}_{\nu} - W^{-}_{\mu}(\partial^{\rho}W^{+}_{\nu})\right]V_{\sigma} \\
&+ \frac{\tilde{\kappa}_V}{2}W^{-}_{\mu}W^{+}_{\nu}\varepsilon^{\mu\nu\rho\sigma}\hat{V}_{\rho\sigma} + \frac{\tilde{\lambda}_V}{2M_{\mathrm{W}}^2}\hat{W}^{-}_{\rho\mu}\hat{W}^{+\mu}_{\nu}\varepsilon^{\nu\rho\alpha\beta}\hat{V}_{\alpha\beta}, \qquad (2.15)
\end{aligned}
$$

where $\hat{W}_{\mu\nu} = \partial_\mu W_\nu - \partial_\nu W_\mu$ and $\hat{V}_{\mu\nu} = \partial_\mu V_\nu - \partial_\nu V_\mu$. The overall couplings are defined as $g_{\mathrm{WW}\gamma} = e$ and $g_{\mathrm{WWZ}} = e \cot\theta_w$. Each vertex is parametrised by seven couplings. There is no good reason why they can not be complex, but usually they are assumed to be real as is done in this thesis. The behaviour under charge (C) and parity (P) conjugation can be used to divide them into four groups. The three couplings g_1^V, κ_V and λ_V conserve C and P, while g_5^V violates C and P but conserves CP. The couplings g_4^V, $\tilde{\kappa}_V$ and $\tilde{\lambda}_V$ violate CP, but g_4^V conserves P, while $\tilde{\kappa}_V$ and $\tilde{\lambda}_V$ conserve C. Comparing the Lagrangian (2.15) with the Standard Model Lagrangian 2.13, one sees that the couplings are g_1^V=κ_V=1 in the SM, while all other are zero. For convenience we introduce $\Delta g_1^\gamma = g_1^\gamma - 1$, $\Delta g_1^Z = g_1^Z - 1$, $\Delta\kappa_\gamma = \kappa_\gamma - 1$ and $\Delta\kappa_{\mathrm{Z}} = \kappa_Z - 1$ thus we are only considering deviations from the Standard Model values.

The photon couplings can be related to the lowest order terms in a multipole expansion of W-γ interactions [4, 5]: The CP conserving couplings are related to the charge q_{W}, the magnetic dipole moment μ_{W} and the electric quadrupole moment Q_{W}^e of the W boson,

$$\begin{aligned} q_W &= e g_1^\gamma \\ \mu_W &= \frac{e}{2M_{\mathrm{W}}}(g_1^\gamma + \kappa_\gamma + \lambda_\gamma) \\ Q_W^e &= \frac{-e}{M_{\mathrm{W}}^2}(\kappa_\gamma - \lambda_\gamma), \end{aligned} \tag{2.16}$$

while the electric dipole moment d_{W} and the magnetic quadrupole moment Q_{W}^M depend on the CP violating couplings only,

$$\begin{aligned} d_W &= \frac{e}{2M_{\mathrm{W}}}(\tilde{\kappa}_\gamma + \tilde{\lambda}_\gamma) \\ Q_{\mathrm{W}}^M &= \frac{-e}{M_{\mathrm{W}}^2}(\tilde{\kappa}_\gamma - \tilde{\lambda}_\gamma). \end{aligned} \tag{2.17}$$

Imposing the same gauge structure of new physics described by the Lagrangian (2.15) as of the Standard Model the number of free parameters can be reduced. Electromagnetic gauge invariance requires g_1^γ=1 and g_5^γ=0 and reduces the overall number of C and P conserving couplings to five. $\mathsf{SU(2)}_L \times \mathsf{U(1)}_Y$ gauge invariance requires

$$\begin{aligned} \Delta\kappa_{\mathrm{Z}} &= -\Delta\kappa_\gamma \tan^2\theta_w + \Delta g_1^{\mathrm{Z}} \\ \lambda_Z &= \lambda_\gamma = \lambda \end{aligned} \tag{2.18}$$

for the C and P conserving couplings, where θ_W is the Weinberg angle, thus reducing the number of free couplings further.

Considering only C and P conserving couplings there are two different sets which can be studied: the first one includes the three couplings Δg_1^{Z}, $\Delta\kappa_\gamma$ and λ with relation (2.18) and the second set all five couplings Δg_1^{Z}, $\Delta\kappa_\gamma$, $\Delta\kappa_{\mathrm{Z}}$, λ_γ and λ_Z without any relation between them. The first set is the minimal extension of triple gauge boson couplings obeying the same gauge structure as the Standard Model.

The measurement of one coupling at the time is no problem but the simultaneous measurement of more than one coupling depends on the available statistics and the correlation between them. At LEP the number of $\mathrm{W}^+\mathrm{W}^-$ pairs is rather limited and only the simultaneous measurement of up to three couplings is possible. Usually, the three couplings $\Delta\kappa_\gamma$, Δg_1^{Z} and λ are chosen with relation 2.18, representing the minimal extension of the SM. But with the high luminosity of TESLA and the novel option of polarised beam is should be possible to measure all five C and P conserving couplings at the same time which gives the possibility to explore the $\mathsf{SU(2)}_L \times \mathsf{U(1)}_Y$ gauge structure of the Standard Model further.

For C or P violating couplings some relations between WWγ and WWZ couplings can be derived using $\mathsf{SU(2)}_L \times \mathsf{U(1)}_Y$ gauge invariance but usually only WWZ couplings are considered because the photon couplings are rather constrained by experiments measuring electric dipole moments of the electron, neutron and various nuclei [6, 7].

2.3 Strong Electroweak Symmetry Breaking

In this section a more specific class of models for physics beyond the Standard Model is considered, which restricts the operators in the effective Lagrangian (2.15) by exploring the symmetries of the electroweak sector. Some ideas and concepts used for this class of models are taken from the strong interactions.

In the absence of a light Higgs particle or other light resonances, unitarity requires that gauge boson self-interactions becomes strong at high energies. In this case, the physics of electroweak symmetry breaking (EWSB) below the symmetry breaking scale $\Lambda \approx 3\,\mathrm{TeV}$ is described by the most general effective Lagrangian for Goldstone bosons required by $\mathsf{SU(2)}_L \times \mathsf{U(1)}_Y \to \mathsf{U(1)}_{em}$ breaking. The study of the ratio of the W mass to the Z mass gives hints, what kind of symmetries new physics have to obey. Therefore, the ρ-parameter [8] is introduced as

$$\rho = \frac{M_{\mathrm{W}}^2}{M_{\mathrm{Z}}^2 \cos^2\theta_w}. \tag{2.19}$$

At tree level the ρ-parameter is unity in the Standard Model, which is a direct consequence of the $\mathsf{SU(2)}_L \times \mathsf{U(1)}_Y$ gauge structure of the electroweak sector. Small deviations from unity measured by LEP 1/SLC can be accounted for by loop corrections. However, the $\mathsf{SU(2)}_L \times \mathsf{U(1)}_Y$ group of the Standard Model is not the maximal group which constrains the ρ-parameter to unity. The Standard Model group can be enlarged to $\mathsf{SU(2)}_R \times \mathsf{SU(2)}_L$, where $\mathsf{U(1)}_Y \subset \mathsf{SU(2)}_R$. The right-handed fermions are doublets under $\mathsf{SU(2)}_R$ and the left-handed fermion doublets under $\mathsf{SU(2)}_L$. Spontaneous symmetry breaking in this sector then takes the form

$$\mathsf{SU(2)}_R \times \mathsf{SU(2)}_L \to \mathsf{SU(2)}_c, \tag{2.20}$$

where $\mathsf{SU(2)}_c$ is the custodial $\mathsf{SU(2)}$ symmetry of the electroweak interactions. This suggests that the EWSB sector appears to have an approximate global $\mathsf{SU(2)}_c$ custodial symmetry, which constrains the ρ-parameter to unity. This symmetry is only broken by the hypercharge couplings to the Goldstone bosons. Thus it is reasonable to investigate possible $\mathsf{SU(2)}_c$-conserving deviations from the SM as a first approximation.

Assuming only $\mathsf{SU(2)}_L \times \mathsf{U(1)}_Y \to \mathsf{U(1)}_{em}$ symmetry breaking, the most general effective Lagrangian affecting C and P conserving TGCs contains three dimension-four interactions. The corresponding operators of this Lagrangian [9] are

$$\begin{aligned} L_1 &= \tfrac{\alpha_1}{16\pi^2}\tfrac{gg'}{2} B_{\mu\nu}\,\mathrm{tr}\Big(\sigma_3 W^{\mu\nu}\Big) \\ L_2 &= \tfrac{\alpha_2}{16\pi^2} ig' B_{\mu\nu}\,\mathrm{tr}\Big(\sigma_3 V^\mu V^\nu\Big) \\ L_3 &= \tfrac{\alpha_3}{16\pi^2} 2ig\,\mathrm{tr}\Big(W_{\mu\nu} V^\mu V^\nu\Big), \end{aligned} \tag{2.21}$$

where $W_{\mu\nu} = (\partial_\mu W_\nu^a - \partial_\nu W_\mu^a + g\epsilon^{abc}W_\mu^b W_\nu^c)\tau^a$ and V_μ simplifies to $-ig\tau^a W_\mu^a + ig'\tau^3 B_\mu$ in unitarity gauge. L_3 conserves the approximate $\mathsf{SU(2)}_c$, while L_1 and L_2 break it linearly. There are no terms contributing to C and P conserving TGCs, which break it quadratically. The coefficients α_i are related to scales of new physics Λ_i^* by naive dimensional analysis [10]

$$\frac{\alpha_i}{16\pi^2} = \left(\frac{v}{\Lambda_i^*}\right)^2 \tag{2.22}$$

where the Fermi scale $v = 246\,\text{GeV}$ is fixed by low energy weak interactions.

The standard parametrisation of anomalous TGCs is related to the coefficients of the effective Lagrangian (2.21) by

$$\begin{aligned}
g_1^Z &= 1 + \frac{e^2}{\cos^2\theta_w(\cos^2\theta_w - \sin^2\theta_w)}\frac{\alpha_1}{16\pi^2} + \frac{e^2}{\sin^2\theta_w\cos^2\theta_w}\frac{\alpha_3}{16\pi^2} \\
\kappa_Z &= 1 + \frac{2e^2}{\cos^2\theta_w - \sin^2\theta_w}\frac{\alpha_1}{16\pi^2} - \frac{e^2}{\cos^2\theta_w}\frac{\alpha_2}{16\pi^2} + \frac{e^2}{\sin^2\theta_w}\frac{\alpha_3}{16\pi^2} \\
\kappa_\gamma &= 1 - \frac{e^2}{\sin^2\theta_w}\frac{\alpha_1}{16\pi^2} + \frac{e^2}{\sin^2\theta_w}\frac{\alpha_2}{16\pi^2} + \frac{e^2}{\sin^2\theta_w}\frac{\alpha_3}{16\pi^2}\,.
\end{aligned} \tag{2.23}$$

2.4 Triple Gauge Couplings in the SM and Beyond

In the Standard Model the couplings g_1^Z, g_1^γ, κ_γ and κ_Z are one at tree level while all others are zero. Already in the Standard Model one loop contributions lead to a deviation from the tree level values, however, calculations show that they are only of the order 10^{-3} at a centre-of-mass energy of around 200 GeV [11, 12]:

$$\begin{aligned}
|\Delta\kappa_\gamma| &\simeq -4.1 \times 10^{-3} \\
|\Delta\kappa_\mathrm{Z}| &\simeq -3.2 \times 10^{-3} \\
|\lambda_\gamma| &\simeq -0.8 \times 10^{-3} \\
|\lambda_Z| &\simeq -0.8 \times 10^{-3}
\end{aligned}$$

It must be noted that such loop calculations of contributions to individual couplings are controversial. For example, the standard way to calculate one-loop corrections is to select a particular final state and to calculate all possible one-loop Feynman diagrams. This will preserve the gauge invariance of such a calculation. But there is no gauge invariant way to select the diagrams contribution to one particular anomalous coupling. Therefore, such loop calculations should be taken as an estimate of the order of magnitude of the contribution to anomalous couplings.

Many extensions of the Standard Model predicts anomalous triple gauge boson couplings via loop effects. This is also the case, if the accessible centre-of-mass energy is below the mass of the new particles such that they are not directly accessible. There exist calculations for an additional generation of heavy quarks [13] and heavy leptons [14], but their effects are not very big. For example, the contribution to the CP violating parameter $\tilde{\kappa}_\gamma$ is below 5×10^{-3} in the lepton model.

In supersymmetric models the loop contributions to anomalous couplings might be more pronounced, but usually there are many model parameters to tune them in one or the other way. The Minimal Supersymmetric Standard Model (MSSM) is the minimal supersymmetric extension of the Standard Model. An estimate of loop contributions to CP conserving and violating anomalous couplings yields the following limits [12, 15]

$$\begin{array}{rcl} |\Delta\kappa_\gamma| &<& 2\times 10^{-2} \\ |\Delta\kappa_{\mathrm{Z}}| &<& 2\times 10^{-2} \\ |\lambda_\gamma| &<& 6\times 10^{-3} \\ |\lambda_Z| &<& 6\times 10^{-3}. \end{array} \qquad \begin{array}{rcl} |g_4^Z| &<& 2\times 10^{-5} \\ |\tilde{\kappa}_\gamma| &<& 5\times 10^{-4} \\ |\tilde{\kappa}_Z| &<& 5\times 10^{-4} \end{array}$$

They are for a centre-of-mass energy around 200 GeV and a set of model parameters, where the new particles are heavy enough not to be directly accessible at an energy of 500 GeV and below. The contributions to these couplings are almost one order of magnitude small at an energy of 500 GeV.

Chapter 3

W-Pair Production in e^+e^- Collisions

The production and decay of W pairs in e^+e^- collisions is illustrated in figure 3.1 as an example for any reaction in e^+e^- collisions. Such a reaction can be modelled as follows. The first stage is the hard scattering process which describes the production and decay of a W pair. It includes radiative corrections depicted in this case by an initial-state photon. If the W boson decays into leptons, the reaction chain is already complete at this stage. If the W boson decays into quarks, additional stages must be considered: the fragmentation and hadronisation process and finally the decay of the hadrons into quasi stable particles. In the fragmentation process additional gluons and quarks are emitted from the primary quarks. For a small number of partons this process can be calculated explicitly otherwise parton-shower models are used. The hadronisation process, which describes the transition from partons into hadrons, cannot be calculated perturbatively at all. For this stage only phenomenological models are used to describe this transition represented as a simple box in figure 3.1.

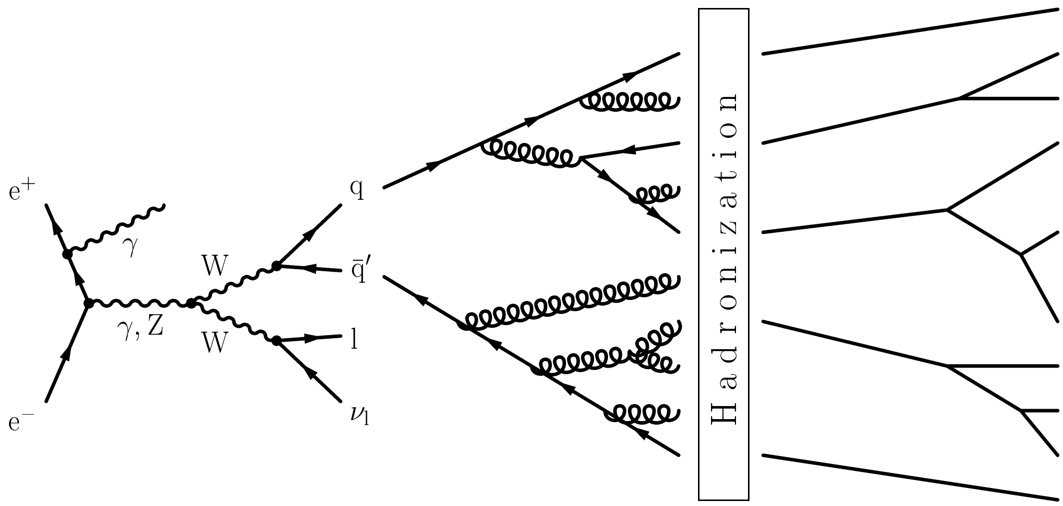

Figure 3.1: The whole process from the incoming beam electrons to the detectable particles can be split into four stages: The hard scattering process with radiative correction and, if quarks are produced, the fragmentation, hadronisation and decay of hadrons.

We present all these stages in some more details in the next sections and close the chapter with their implementation in Monte Carlo generators.

3.1 Hard Processes

The cross-sections for the most important Standard Model processes in e^+e^- collisions are shown in figure 3.3 as a function of the centre-of-mass energy up to 1 TeV. At low energies two-fermion production via the exchange of a Z boson or a photon dominates. At around 200 GeV, twice the mass of Z and W bosons, the production of massive gauge boson pairs is kinematically allowed. At the same time an additional photon can also be produced leading to three boson production like $WW\gamma$ or $ZZ\gamma$. At even higher energies three massive gauge bosons can be produced with cross-sections below the two-fermion production. Only processes with t-channel behaviour like single-W ($We\nu_e$) and single-Z (Zee) production exceed the two-fermion cross-section at 400 GeV and rise continuously.

The classification of processes using intermediate gauge bosons is very instructive to illustrate the underlying physics but has some shortcomings. After the decay on the intermediate particles many processes lead to the same final states and conclusions of the intermediate bosons cannot always be drawn from the final state, in particular if one keeps in mind that intermediate particles can be off-shell. To solve this problem, a clean signal definition must be used based either on a subset of diagrams or phase space cuts. In the following, the important physical reactions in two, four, six and more fermion final states are discussed.

Two-Fermion Final States

The largest cross-section, apart from two-photon processes (see below), at LEP energies (see figure 3.3) is the production of a fermion anti-fermion pair via the exchange of either a virtual photon or a Z boson. The fermions can be either quarks or leptons. The two Feynman diagrams for this process are shown in figure 3.2. In the case of Bhabha scattering ($e^+e^- \to e^+e^-$), the exchange of either a γ or Z in the t-channel has to be included. The cross-section has a strong peak at the Z boson mass of $M_Z = 91$ GeV, and decreases with energy like $\frac{1}{s}$ as all pure s-channel processes, where $\sqrt{s}$ is the centre-of-mass energy. The contributions from an intermediate photon and Z boson interfere and cannot be distinguished. However, the peak at the Z resonance is dominated by Z production, hence the properties of the Z boson can be studied directly. At higher energies the contribution from the Z boson diagram

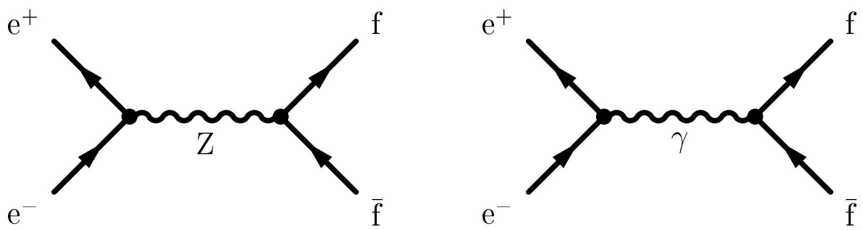

Figure 3.2: Feynman diagrams for the process $e^+e^- \to f\bar{f}$. For Bhabha scattering ($e^+e^- \to e^+e^-$) additional t-channel diagrams contribute.

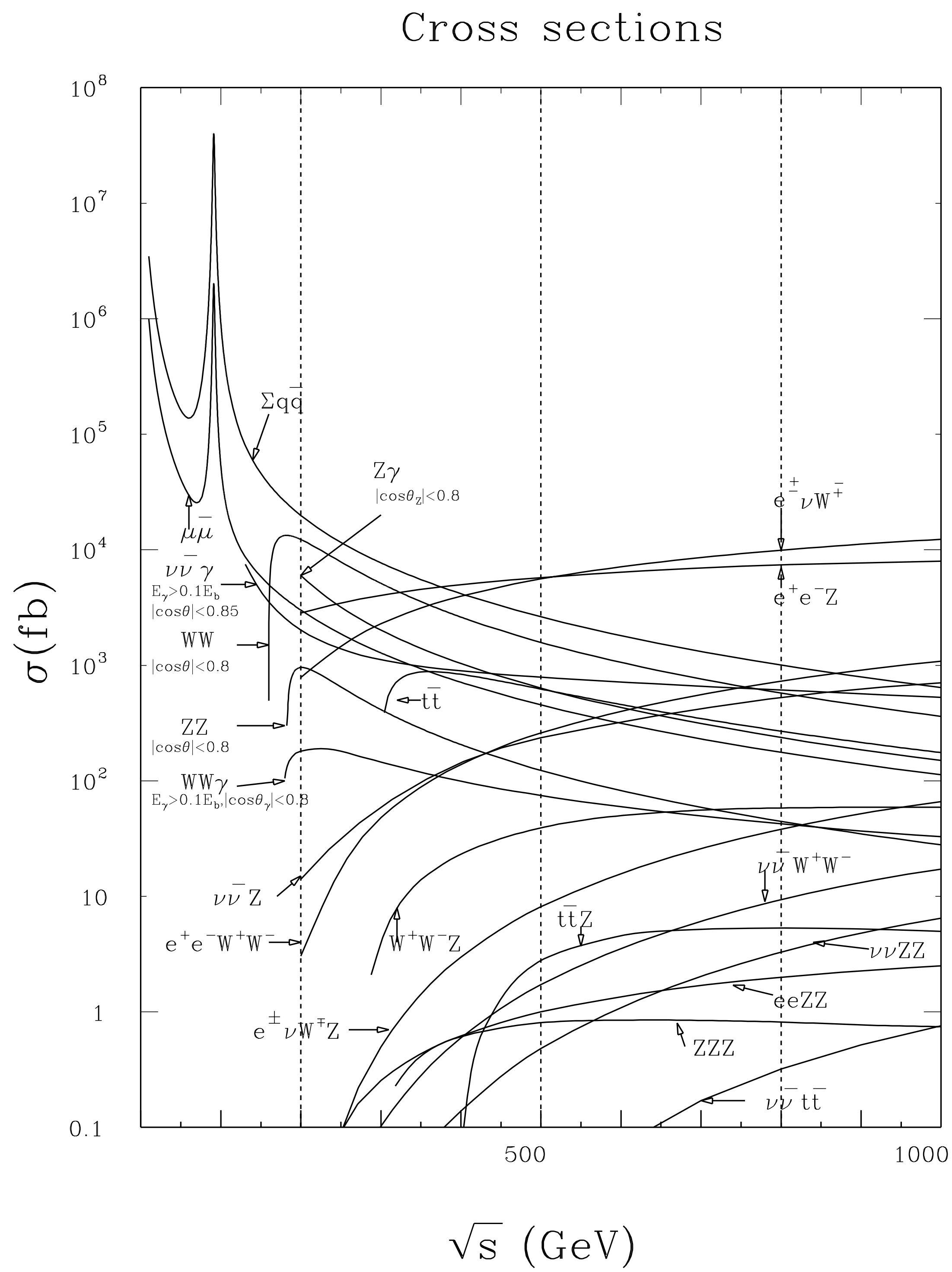

Figure 3.3: Cross-section for a variety of physics processes in e^+e^- collisions up to an centre-of-mass energy of 1 TeV. The plot is taken from reference [16].

is suppressed by its mass and the relative contribution from the massless photon increases. A general feature of e^+e^- collisions at these energies is a radiative return to the Z. If one or more initial-state radiation photons are emitted, which reduce the effective centre-of-mass energy of the subsequent e^+e^- collision, $\sqrt{s'}$, to the region of the Z resonance, the cross-section is greatly enhanced. A separation can be made between radiative events and non-radiative events for which $\sqrt{s'} \simeq \sqrt{s}$. The properties of radiative events are similar of those measured in Z decays at LEP 1, they are only modified by the boost due to recoil against hard initial-state radiation. Non-radiative events have different properties, reflecting the increased relative importance of photon-exchange processes above the Z resonance.

Because of the high cross-section, the two-fermion production is a background to most other processes at LEP energies and above.

Four-Fermion Final States

The classification of four-fermion final states is far more complex than in the two-fermion case. Many different reactions contribute to a certain final state. First, we describe these reactions in terms of gauge boson production and afterwards we introduce the classification based on the fermions in the final-state.

At $\sqrt{s} = 2M_{\mathrm{W}}$, the production of two real W bosons is kinematically allowed and the cross-section starts to rise very steeply. It rises up to $\sim 17\,\mathrm{pb}$ at around 206 GeV and then decreases as $\frac{1}{\sqrt{s}}$ in contrast to $\frac{1}{s}$ for a pure s-channel process. Figure 3.9(a) shows the W-pair production cross-section measured by all four LEP collaborations [2,17–22] including the latest theoretical predictions [23–28]. The three Feynman diagrams for W-pair production are depicted in figure 3.4, which are the exchange of either a photon or a Z boson in the s-channel and an electron neutrino in the t-channel. It must be pointed out that the s-channel diagrams with the self-coupling of three gauge bosons are a direct consequence of the non-Abelian structure of the electroweak sector of the Standard Model. Each W boson decays into two fermions, which are doublets under the weak isospin, e. g. $(e^+\nu_e)$ or $(u\bar{d})$. Since weak and mass eigenstates do not coincide which can be described by the CKM matrix for the quark sector, flavour non-diagonal decays like $(c\bar{d})$ can occur.

The SM predicts also self-coupling diagrams of four gauge bosons leading to quartic gauge boson vertices. The production of an additional photon is not mass suppressed like a Z boson and therefore possible at the same time as W-pair production. The cross-section

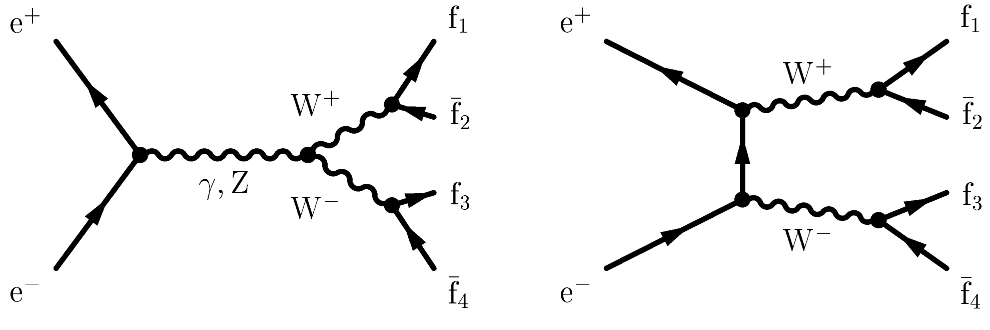

Figure 3.4: Feynman diagrams for the process $e^+e^- \rightarrow W^+W^-$ (CC03).

for WWγ production depends strongly on the signal definition. The interesting diagram is the quartic gauge boson vertex as shown in figure 3.5, where a virtual photon or Z boson couples to two W bosons and a real photon. The cross-section for WWγ production is a factor 50 – 100 smaller than the one for W-pair production, depending on the cuts on the photon energy and angle. Both cuts help to separate the contributions from initial-, final- and intermediate-state radiation and the quartic gauge boson vertex.

The OPAL collaboration was the first LEP collaboration, which measured the WWγ cross-section at LEP 2. The photon must have at least an energy of 2.5 GeV and be well separated from the beam pipe ($|\cos\theta_\gamma| < 0.975$) and any charged lepton ($\cos\theta_{\gamma\mathrm{f}} < 0.9$). The cross-section grows from 277 ± 118 fb at 183 GeV up to 489 ± 76 fb at 206 GeV [29]. Figure 3.9(b) shows the combined cross-section for WWγ production from all LEP measurements [2, 29–31]. The contribution from the quartic gauge boson vertices are very small at LEP 2 energies. With this measurement the description of real photon radiation can be tested to a very high level, including radiation from the intermediate W bosons. This measurement is used to set limit on anomalous quartic gauge couplings.

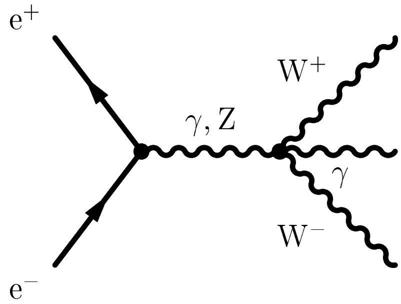

Figure 3.5: Diagram of the quartic gauge boson vertices contributing to WWγ production.

At slightly higher energies, the production of real Z pairs is kinematically allowed. The cross-section is maximal at 210 GeV (~ 1 pb) and decreases with energy. Figure 3.6 depicts the two dominant Feynman diagrams with the exchange of an electron[1] in the t-channel. In contrast to the W-pair production, no s-channel diagrams are contributing because the coupling of two Z bosons to either a photon or a Z boson is not allowed in the Standard Model. Each Z boson decays into a fermion anti-fermion pair as in the case of two-fermion production. The measurement of the Z-pair production cross-section from all LEP experiments [2, 32–35] is shown in figure 3.9(d). Such measurements can be directly interpreted in the context of anomalous neutral current triple gauge couplings leading to ZZZ and ZZγ couplings.

[1]Both electrons and positrons are refered to as electrons.

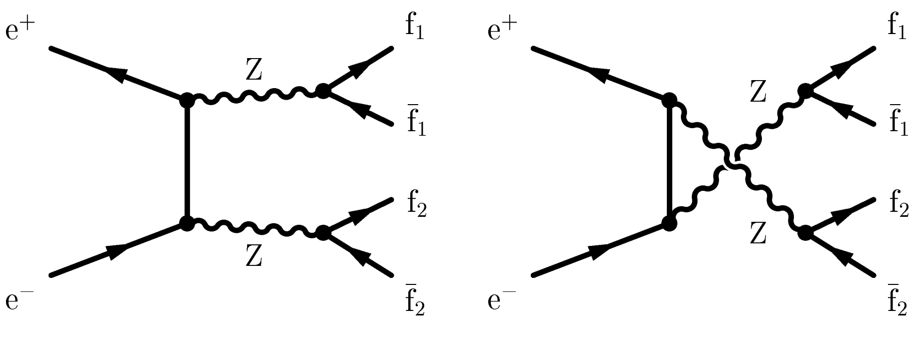

Figure 3.6: Feynman diagrams for the process $e^+e^- \to ZZ$ (NC02).

As for the W-pair case, an additional photon to the Z pair can be produced leading to $ZZ\gamma$ production. As before the cross-section is suppressed by a factor of ~ 100.

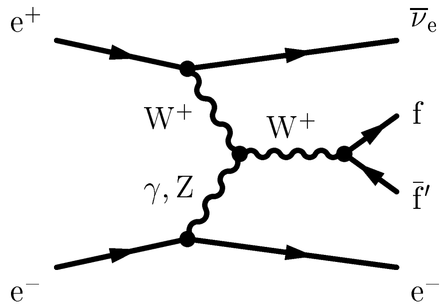

Figure 3.7: Feynman diagram for single-W production involving a triple gauge bosons vertex.

The processes discussed above involve two resonant gauge bosons. The production of single gauge bosons is also possible, where the gauge boson is accompanied by either e^+e^- or $\nu_e\overline{\nu}_e$. Figure 3.7 shows the diagrams for single-W production which involve triple gauge boson vertices. The definition of the cross-section is difficult because the process $e^+e^- \rightarrow W^+W^- \rightarrow We\nu_e$ leads to the same final state and the signal must be defined either by a gauge invariant set of diagrams or by phase space cuts. The cross-section rises with energy because most contributions for single-W production come from diagrams with a t-channel behaviour. The cross-section is between 0.5 – 1 pb at LEP 2 energies (see figure 3.9(c)) and exceeds the W-pair production at approximately 400 GeV.

The LEP experiments measured the single-W cross-section [2, 18, 36–38]. The measurement can be used to set limits on anomalous triple gauge couplings. They are more stringent for $WW\gamma$ couplings than for WWZ couplings because the contribution from the triple gauge vertex involving the Z boson is mass suppressed.

For the production of single Z bosons (figure 3.8) there are two different reactions: $Z\nu\bar{\nu}$ and Zee. A Feynman diagram including a triple gauge boson vertex contributes to the first process. Unfortunately the cross-section is below 20 fb at LEP 2 energies, but it increases with energy like all t-channel processes, and it should be possible to measure the cross-section at LC energies.

The dominant contribution of single-Z production with two electrons comes from diagrams, where a quasi-real photon is exchanged between the incoming electrons and a Z boson is emitted from one electron (figure 3.8(b)). A diagram like figure 3.8(a), where the W bosons are replaced by Z bosons, is not allowed in the SM. The cross-section is around 0.7-0.8 pb

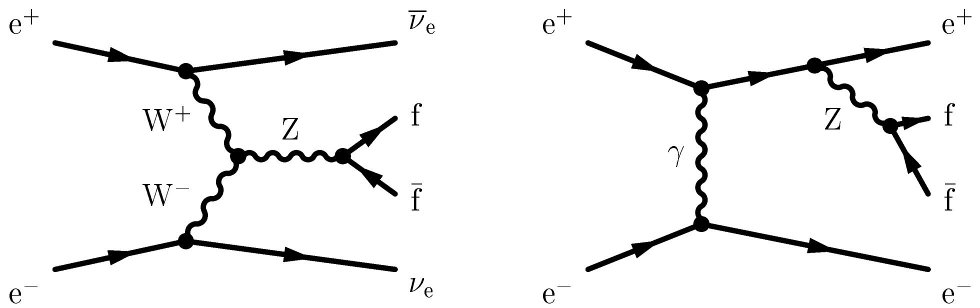

(a) Single-Z production ($Z\nu\bar{\nu}$). (b) Single-Z production (Zee).

Figure 3.8: Diagrams contributing to single-Z production ($Z\nu\bar{\nu}$ and Zee). The $Z\nu\bar{\nu}$ diagram shows a triple gauge bosons vertex which does not exist in the Zee case.

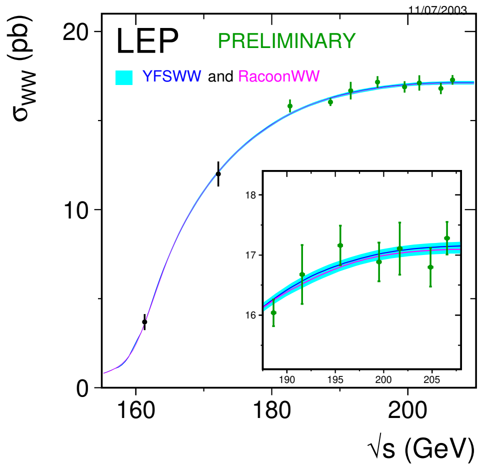

(a) W-pair production.

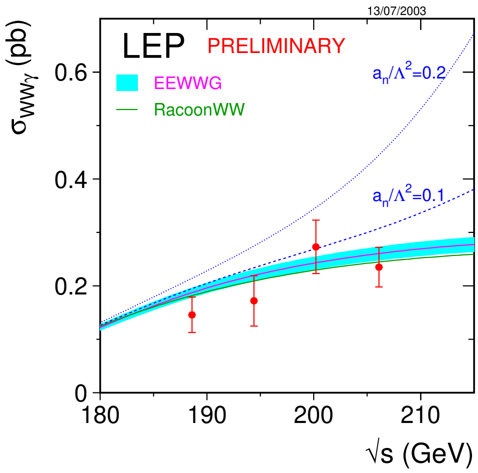

(b) WWγ production.

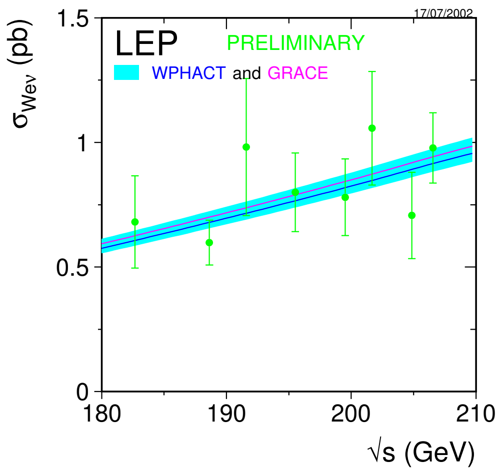

(c) Single W production.

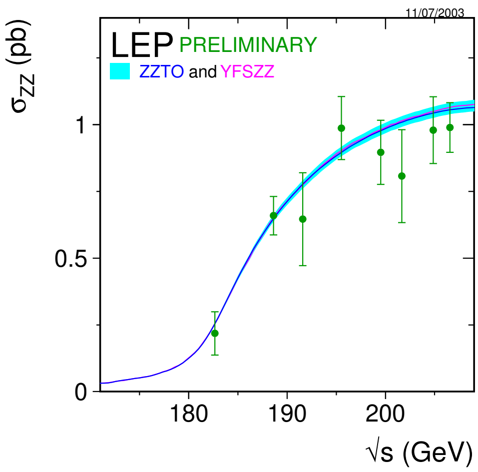

(d) Z-pair production.

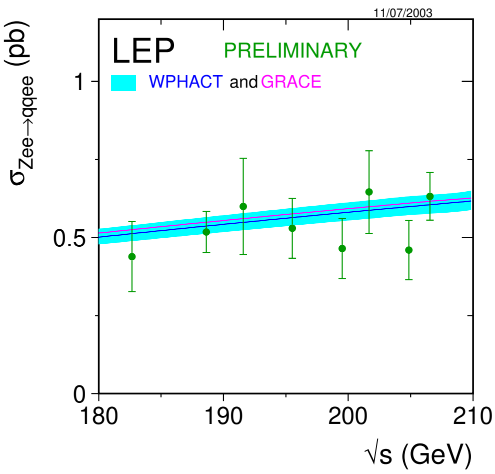

(e) Single Z (Zee) production.

Figure 3.9: LEP combined measurements of cross-sections for W-pair, Z-pair, WWγ, single-W and single-Z (Zee) production from the LEP electroweak working group [2].

at LEP 2 energies [2, 39]. The cross-section for the final state $e^+e^- \to Ze^+e^- \to q\bar{q}e^+e^-$ is shown in figure 3.9(e). As for single-W production, the cross-section increases with energy and exceeds the W-pair cross-section already at $\sim 300\,\mathrm{GeV}$.

As already mentioned, the signal definition is not straight forward. A certain combination of fermions in the final state can have contributions from more than one gauge boson production process. For example, the final state $e^+\nu_e u\bar{d}$ has contributions from single-W and W-pair production and the final state $u\bar{d}\bar{u}d$ has contributions from W-pair and Z-pair production. For this reason all four-fermion final states are divided into two main categories: The first case consists of final states compatible with the production of a W pair and are called charged current (CC) reactions. The second case consists of those compatible with a Z pair and are called neutral current (NC) reactions. Obviously, these two classes overlap and, therefore a third class is introduced for mixed charged and neutral current (MIX) reactions. Further they are classified by using the number of contributing diagrams for this final state [40].

All diagrams contributing to an arbitrary four-fermion final state can be expressed by a set of six generic diagrams (figure 3.10). The Abelian class of the diagrams figure 3.10(a)-3.10(d) include only vertices of the structure $(Bf\bar{f})$, where $B = Z, \gamma$, and $(Wf\bar{f}')$. The conversion diagram 3.10(a) shows the pair production of two gauge bosons with a fermion exchanged in the t-channel, figure 3.10(b) and 3.10(c) show the exchange of a gauge bosons in the s and t-channel normally leading to a two-fermion final state, but here an additional

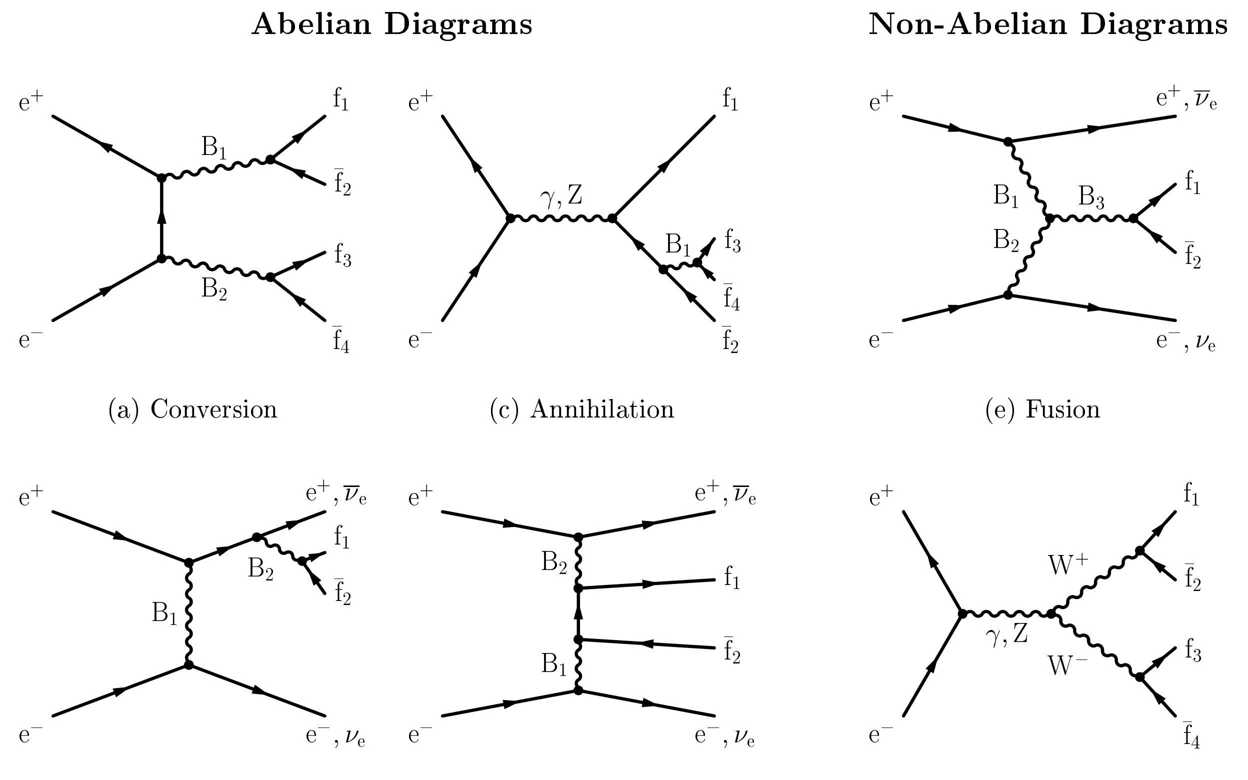

(a) Conversion (c) Annihilation (e) Fusion

(b) Bremsstrahlung (d) Multiperipheral (f) Annihilation

Figure 3.10: Generic diagram classes for four-fermion production ($B_i = Z, \gamma, W^\pm$).

- CC reactions:
  - $e^+e^- \to f\bar{f}'F\bar{F}'$ (CC11 family)
  - $e^+e^- \to \nu_e e^+ f\bar{f}'$ (CC20 family)
  - $e^+e^- \to f\bar{f}' e^- \overline{\nu}_e$ (CC20 family)
- NC reactions:
  - $e^+e^- \to f\bar{f}F\bar{F}$ (NC32 family)
  - $e^+e^- \to f\bar{f}f\bar{f}$ (NC4 · 16 family)
  - $e^+e^- \to e^+e^- f\bar{f}$ (NC48 family)
  - $e^+e^- \to \nu_e\overline{\nu}_e f\bar{f}$ (NC21 family)
  - $e^+e^- \to e^+e^-e^+e^-$ (NC4 · 36 family)
  - $e^+e^- \to \nu_e\overline{\nu}_e\nu_e\overline{\nu}_e$ (NC4 · 9 family)
- Mixed CC/NC reactions:
  - $e^+e^- \to f\bar{f}f'\bar{f}'$ (mix43 family)
  - $e^+e^- \to e^+\nu_e e^- \overline{\nu}_e$ (mix56 family)

Table 3.1: List of charged-current and neutral-current reactions in four-fermion production. f and F denote different fermions ($f \neq F$), that are neither electrons nor electron neutrinos ($f, F \neq e, \nu_e$), and their weak-isospin partners are denoted by f' and F'.

gauge boson is emitted from the outgoing fermions. With the multiperipheral diagram (figure 3.10(d)) the Abelian class is complete. It contributes mainly to the exchange of two virtual photons leading to a low invariant-mass f_1f_2 system with both electrons escaping detection. Two additional non-Abelian diagrams complete the description of the self-coupling of gauge bosons. Figure 3.10(e) shows the fusion of three gauge bosons and figure 3.10(f) the coupling of either a photon or Z boson to two W bosons, named annihilation.

The classification of each four-fermion final state is shown in table 3.1. The three dominant diagrams for W-pair production are named CC03 (figure 3.4) because it is a charged current reaction and involves three diagrams, namely one conversion and two non-Abelian annihilation diagrams. If no identical fermions nor electrons are in the final state, the minimal gauge invariant set of diagrams is the CC11 family, where additionally single-resonant diagrams of type 3.10(c) are included. There are less diagrams if neutrinos are produced (CC09 and CC10 reactions). If one electron is in the final state and no identical fermions, t-channel fusion and bremsstrahlung diagrams have to be included to form the CC20 family. For pure leptonic final states the number of diagrams is reduced to 18.

The minimal set of diagrams for Z-pair production is called NC02 (figure 3.6). As the CC03 set for W-pair production, but it is also not gauge invariant. The minimal gauge invariant set is NC32 including annihilation diagrams, if no electrons and electron-neutrinos nor identical fermions are in the final state. The number of diagrams can be reduced drastically if neutrinos are in the final state, e. g. only 9 diagrams contribute to $\nu_\mu\overline{\nu}_\mu\nu_\tau\overline{\nu}_\tau$. If both fermion pairs are identical but neither e^+e^- nor $\nu_e\overline{\nu}_e$ pairs, the set grows to NC4 · 16 because of diagram permutations. Final states with either one e^+e^- or $\nu_e\overline{\nu}_e$ pair are described by the NC48 family, where additional bremsstrahlung, fusion and multiperipheral diagrams are allowed. In the case of electron-neutrinos the number of diagrams is reduced to at least 21 diagrams. The final state of four electrons and four electron-neutrinos is described by the NC4 · 36 and NC4 · 9 set, respectively.

Two classes have not been discussed so far, namely final states of the type $f\overline{f}f'\overline{f}'$ and $e^+\nu_e e^-\overline{\nu}_e$. For example, the second final state has contributions from charged current single-W and W-pair production but also from neutral current single-Z and Z-pair production. This is the most complex and demanding final state, described by the mix56 set. The first final state is described by the mix43 family and has contributions from W-pair and Z-pair production.

Six and more Fermion Final States

Already at LEP 2 energies the production of W or Z pairs in association with e^+e^- or $\nu_e\overline{\nu}_e$ pairs is kinematically allowed, but the cross-sections are very small. The process $e^+e^- \rightarrow e^+e^-W^+W^-$ has the highest cross-section of these four reactions and grows from ~ 200 fb at a centre-of-mass energy of 500 GeV up to around 1 pb at 1 TeV, which is high enough to be measured. The cross-sections of the other three processes are below 2 fb at $\sqrt{s} = 500$ GeV and might be difficult to observe, depending on the background. Nevertheless, these final states involve quartic gauge bosons couplings and can be used to measure anomalous quartic gauge couplings and to study the scattering of longitudinal W bosons.

At centre-of-mass energies above 240 – 270 GeV the production of three massive gauge bosons is kinematically allowed, leading to WWZ and ZZZ production. The cross-section for ZZZ production rises gently up to 1 fb and might be difficult to measure, but the cross-section for WWZ production is around 50 fb at 500 GeV which is large enough to study this process in detail.

At $\sqrt{s} = 350$ GeV the top quark can be produced in $e^+e^- \rightarrow t\bar{t}$. Because of its high mass, top quarks decay immediately into a bottom quark and a W boson. This leads to a six-fermion final state with two b-quarks as shown in figure 3.11. The cross-section reaches almost 1 pb at threshold and decreases only slightly. With a linear collider at a centre-of-mass energy of 350 or 500 GeV, high precision measurements of the top-quark properties, i. e. mass, width, couplings to gauge bosons, can be done.

All these reactions lead to six-fermion final states. The production of four massive gauge bosons is not excluded in the Standard Model, but the cross-section will be even lower than for three gauge bosons. The associative production of three gauge bosons with a e^+e^- or $\nu_e\overline{\nu}_e$ pair might have a slightly higher cross-section. The cross-section for production of a $t\bar{t}$ pair in association with a Z boson, leading to a eight-fermion final state, is around a few fb at 500 GeV and can be studied at a linear collider.

Two-Photon Processes

The term two-photon process is used for the reaction of type $e^+e^- \rightarrow e^+e^-X$ which proceeds via the exchange of two virtual photons γ^* (see figure 3.12). In the case of $X = f\overline{f}$ this is a four-fermion reaction involving multiperipheral diagrams, which can be calculated

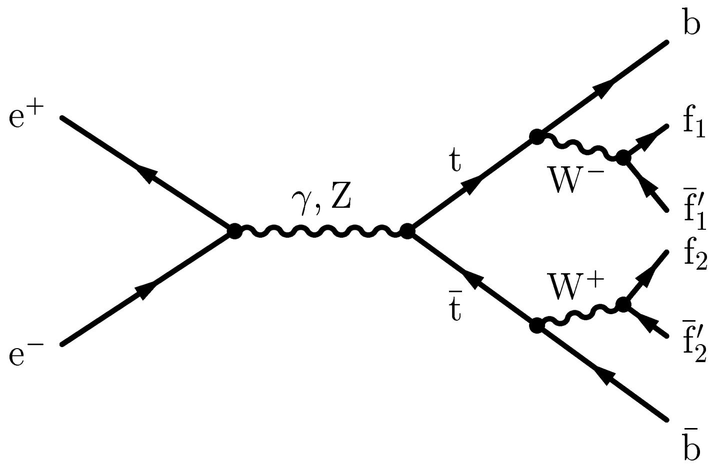

Figure 3.11: Feynman diagram for the production and decay of a $\mathrm{t\bar{t}}$ pair.

in QED. In the more general case of arbitrary X the picture is more complex because the photon can fluctuate into a charged fermion anti-fermion system with the same quantum numbers as the photon. If, during such a fluctuation, one of the fermions interacts via a gauge boson with another object, then the parton content of the photon is resolved and the photon reveals its structure.

A first categorisation is based on the photons' virtuality Q^2, which is defined as the negative squared four-momentum $Q^2 = -q^2 = -(E^2 - \vec{p}^2)$. The photons are called quasi-real, if Q^2 is small. In this case, the corresponding electron transfers only a small transverse momentum to the photon and disappears in the beam pipe. With increasing virtuality the beam electrons carry a larger transverse momentum and eventually will be detected. Depending on the number of visible electrons, two-photon events are classified as un-tagged, single-tagged or double-tagged.

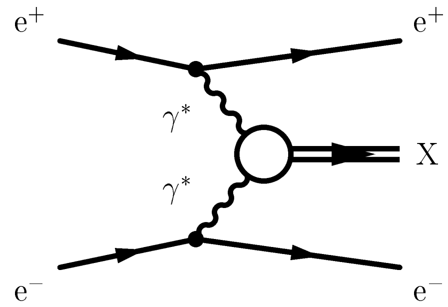

Figure 3.12: Illustration of two-photon processes.

The two-photon cross-section is as large as $\mathcal{O}(10)\,\mathrm{nb}$ at $\sqrt{s} = 200\,\mathrm{GeV}$ in case of un-tagged processes. The cross-section rises logarithmically with the energy and dominates all other processes. Fortunately the invariant mass of the system X peaks strongly at low values and the detection of very forward electron helps further to reject two-photon events. For a detailed review of the photon structure see reference [41].

3.2 Radiative Corrections

The study of the properties of the Z boson at LEP 1 already showed that the tree-level calculation is not sufficient to describe the data completely, because of gauge boson radiation. One very prominent category is gluon radiation of quarks leading to a three jet topology. The four jet topology is dominated by the emission of two gluons or a gluon splitting into two quarks. W and Z bosons can also be radiated of any fermion, but the probability for this process is highly suppressed at LEP 1 energies because of the boson masses. This argument is not true for the photon and hence photon radiation from charged particles has a considerable probability.

Photon radiation, or gauge bosons radiation in general, can be classified into two categories: Photon exchange between two charged particles and emission of a real photon. One example from the first category is the emission and absorption of a photon by the same charged particle, which leads to a modification of the self-energy of this particle. Initial state radiation is the most prominent example of the second category. A beam electron radiates a photon under small angle, which often escapes detection through the beam pipe. The photon energy is lost for the hard process and the effective centre-of-mass energy is reduced. A few examples of photon radiation in W pairs are shown in figure 3.13.

The following discussion is focused mainly on electroweak radiative corrections to four-fermion final states, but the basic concepts can certainly be applied to other multiple fermion final states.

In principle radiative corrections up to all orders can be calculated by considering all possible Feynman diagrams. But the complexity of this problem rises very quickly. Even in the massless-fermion approximation the number of Feynman diagrams grows from 9 – 56 per channel at tree level to an enormous 3579 – 15948 at one-loop level [42]. The full one-loop calculations have not been finished yet, not even for the simpler case of considering only diagrams, where one or two gauge bosons are nearly on-shell [43]. Even if these calculations exist the numerical evaluation in a Monte Carlo generator would be extremely sizeable and very slow. Hence approximations have to be made to get suitable and efficient predictions.

Radiative corrections are split up into universal corrections and non-universal corrections. The former comprise leading process-independent effects like leading-logarithmic (LL) corrections from initial-state radiation, higher-order corrections which can be included by a proper choice of the leading-order (LO) input-parameters, and the so-called Coulomb corrections. The remaining corrections are called non-universal because they depend on the considered process. Further they are split into real and virtual corrections. Real corrections describe the emission of a real photon, which may lead to a visible photon in the detector, while virtual corrections represent the exchange of photons between charged particles involved in the reaction. The different corrections will be described in the following.

Initial and Final State Radiation

Photons can be radiated off any charged particle involved in the scattering process. The radiation from the incoming electrons is called initial-state radiation (ISR) and from outgoing fermions final-state radiation (FSR). In W-pair production also the charged W bosons can radiate photons, which is sometimes called intermediate state radiation (WSR). Examples are shown in figures 3.13(a) to 3.13(c).

ISR is implemented in most Monte Carlo generators at the leading-logarithmic level in the *structure function* (SF) approach [44], which assumes that photon radiation from the incoming electrons and the hard process factorises. The tree-level cross-section is multiplied by the probability that photons are radiated of the incoming electron beams and hence reduce the energy fraction x_i of the beam electrons. The total cross-section including photon radiation is written as an integral over the electron energy fractions

$$\int \mathrm{d}\sigma^{\mathrm{LL}} = \int_0^1 \mathrm{d}x_1 \int_0^1 \mathrm{d}x_2\, S_{ee}^{\mathrm{LL}}(x_1, Q^2) S_{ee}^{\mathrm{LL}}(x_2, Q^2) \int \mathrm{d}\sigma_{\mathrm{Born}}^{\mathrm{e^+e^-}\to 4\mathrm{f}}(x_1 p_+, x_2 p_-), \tag{3.1}$$

where p_+ and p_- are the momenta of the incoming beam electrons. In the structure function $S_{ee}^{\mathrm{LL}}(x, Q^2)$ soft-photon effects are exponentiated and collinear logarithms are included up to order $\mathcal{O}(\alpha^3)$ [45]. The QED splitting scale Q^2 is a free parameter in leading-logarithmic approximation and has to be set to a typical momentum scale of the process, i. e. $Q^2 = s$.

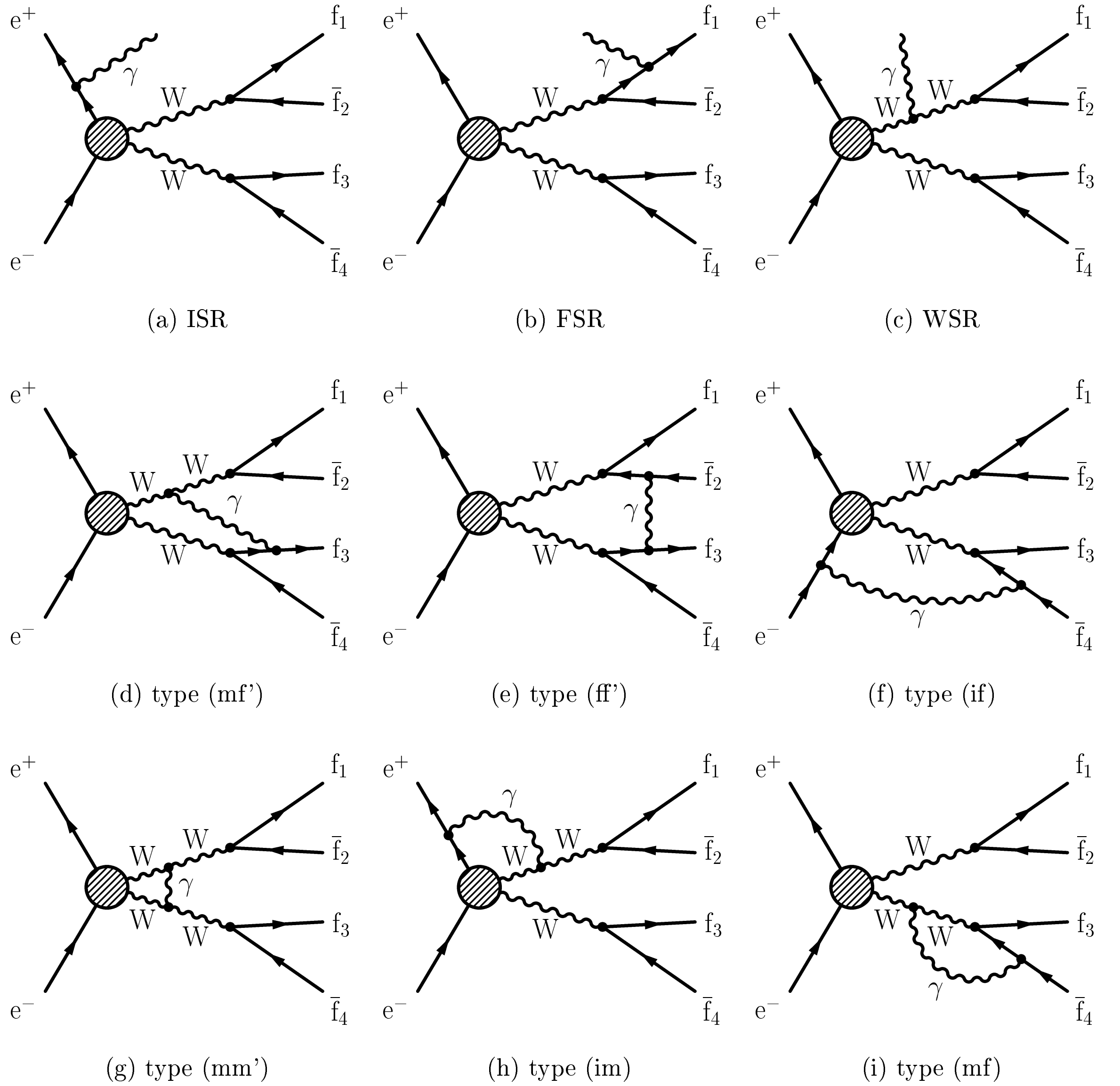

(a) ISR (b) FSR (c) WSR

(d) type (mf') (e) type (ff') (f) type (if)

(g) type (mm') (h) type (im) (i) type (mf)

Figure 3.13: Examples of Feynman diagrams of radiative corrections for the process $\mathrm{e^+e^-} \to \mathrm{W^+W^-} \to 4\mathrm{f}$. The first row shows photon radiation from initial electron, final fermions and intermediate W bosons. The second and third row shows examples of non-factorisable photonic corrections. In the case of the coupling between a photon and a fermion, it is implicitly assumed that the fermions carries charge.

The treatment of infrared singularities in photon radiation is a known problem. The probability for emitting a very soft photon in the limit $k \to \infty$ rises to infinity. Assuming that real photons below a certain energy will escape detection, it is possible to show, that real and virtual infrared divergences cancel each other. One treatment of this problem is described by the *Yennie–Frautschi–Suura (YFS) exclusive exponentiation* [46], which is a technique of summing up all infrared (IR) singularities for a given arbitrary process to infinite order. The YFS technique is not bound to the leading-log summation technique or approximations. It is applicable to arbitrary stable particles in the initial and final state. The matrix element which enters the YFS exponentiation can be split into different parts, e. g. into exact $\mathcal{O}(\alpha)$ corrections and higher order corrections in leading-log approximations. The only requirement is that all parts have the right infrared limit.

For the process $e^+e^- \to W^+W^- \to 4f + n\gamma$ the cross-section has the following form:

$$\mathrm{d}\sigma = e^{2\alpha \mathrm{Re} B + 2\alpha \tilde{B}} \sum_{n=0}^{\infty} \frac{1}{n!} \int \prod_{j=1}^{n} \frac{\mathrm{d}^3 k_j}{k_j^0} \int \frac{\mathrm{d}^4 y}{(2\pi)^4} e^{iy\left(p_1+p_2-Q_1-Q_2-\sum_j k_j\right)+D(y)}$$
$$\bar{\beta}_n(p_1, p_2, Q_1, Q_2, p_{f_1}, \ldots, p_{f_4}, k_1, \ldots, k_n) \frac{\mathrm{d}^3 p_{f_1}}{p_{f_1}^0} \frac{\mathrm{d}^3 p_{f_2}}{p_{f_2}^0} \frac{\mathrm{d}^3 p_{f_3}}{p_{f_3}^0} \frac{\mathrm{d}^3 p_{f_4}}{p_{f_4}^0}, \qquad (3.2)$$

where the IR singularities are exponentiated into the real infrared function $\tilde{B}(p_1, p_2, Q_1, Q_2)$ and the virtual infrared function $B(p_1, p_2, Q_1, Q_2)$. Up to n hard photons with momenta k_i can be emitted, described by the hard photon residual $\bar{\beta}_i$. The function $D(y)$ describes a damping factor for infrared photon emission. The momenta of the initial and final fermions and of the intermediate W bosons are denoted by p_i, p_{f_j}, Q_i $(i = 1, 2, j = 1, 4)$, respectively, with $Q_1 = p_{f_1} + p_{f_2}$ and $Q_2 = p_{f_3} + p_{f_4}$.

The infrared functions $\tilde{B}$ and B are independent of the hard process and can be calculated easily for fermions and bosons by just considering the single Feynman diagram, where a photon is emitted from either a fermion or a boson. The resulting functions are generic for fermions and bosons, except for the different charge and mass. The information of the scattering process and higher order corrections to hard photon radiation enter through the hard photon residuals $\bar{\beta}_i$, e. g. $\bar{\beta}_0$ is proportional to the tree-level cross-section.

An alternative to the structure function approach it the *matrix element* approach. The radiation of real photons is calculated exactly by considering all possible Feynman diagrams including a particular number of real photons. One starts with tree-level diagrams and add the appropriate number of external photon lines. Already adding one real photon results in the replacement of each tree-level diagram by up to 8 diagrams involving photon radiation. The increase in complexity for two photons is even higher. Some calculations exist for the approximation of W-pair production [47], for particular final states [48], and for all four-fermion final states [26, 49, 50]. The authors of reference [26] assume massless fermions, which reduces the complexity of the problem so much that the amplitudes can be expressed analytically by a few generic functions, which ease numerical evaluation.

One important question is the choice of the energy scale Q^2, which should be used in the structure function: either the full centre-of-mass energy $Q^2 = s$ or the minimal momentum transfer in the t-channel exchange $Q^2 = t_{min}$. For W-pair production the first case is more appropriate and for single-W production the second case. But the distinction is not quite so easy to make at the Monte Carlo generator level without further a priori knowledge, e. g. the final state $e\overline{\nu}_e q\overline{q}$ has contributions from both processes. Also the CC03 diagrams for W-pair production consist of two s-channel and one t-channel diagram, where the latter contribution rises very fast with the centre-of-mass energy. Luckily this distinction is not really an issue for W-pair production at LEP 2 energies, but at LC energies this have to be revised and the choice of $Q^2 = t_{min}$ seems more appropriate for higher energies. This problem does not occur in the matrix element approach, because the photon is treated explicitly with the hard process.

Other corrections

The *Coulomb corrections* (CC) [51] are very important near the W-pair production threshold. They arise from Feynman diagrams, where soft photons are exchanged between two nearly on-shell W bosons close to their kinematical production threshold. An example is shown in figure 3.13(g). The correction in $\mathcal{O}(\alpha)$ can be expressed as a multiplicative factor $1 + \delta_{\text{Coul}}$ to the tree-level cross-section σ_{Born}:

$$\delta_{\text{Coul}} = \frac{\alpha\pi}{2\bar{\beta}} \left[1 - g(\bar{\beta}) \frac{2}{\pi} \arctan\left(\frac{|\beta|^2 - \bar{\beta}^2}{2\bar{\beta}\,\text{Re}(\beta)} \right) \right], \tag{3.3}$$

where

$$\begin{aligned} \beta &= \sqrt{\tfrac{M_{\text{W}}}{2} \left(\sqrt{E^2 + \Gamma_{\text{W}}^2} - E \right) - i \tfrac{M_{\text{W}}}{2} \left(\sqrt{E^2 + \Gamma_{\text{W}}^2} - E \right)}, \\ \bar{\beta}^2 &= \tfrac{1}{4s} \left(s^2 - 2s(k_+^2 + k_-^2) + (k_+^2 - k_-^2)^2 \right), \\ E &= \tfrac{s - 4M_{\text{W}}^2}{4M_{\text{W}}}, \quad s = (k_+ + k_-)^2 \end{aligned} \tag{3.4}$$

and the W boson momenta are denoted by k_+ and k_-. It must be noted that these Coulomb corrections depend in addition to the W boson momenta only on their mass and width. The auxiliary function $g(\bar{\beta})$ is equal one for normal Coulomb correction and $g(\bar{\beta}) = 1 - \bar{\beta}$ for the screened Coulomb Corrections [52]. This gives an additional damping factor for high velocity W bosons, which reflect screening effects from the finite W width and the off-shellness of the W bosons.

The effect of $\mathcal{O}(\alpha)$ Coulomb corrections are $\sim 6\%$ at the W-pair production threshold decreasing to around 2% at 200 GeV. Already the $\mathcal{O}(\alpha^2)$ Coulomb corrections are small enough to be of little impact for measurements at LEP 2 energies. At threshold they are around 0.2% decreasing by at least a factor 10 at 200 GeV [53]. The Coulomb corrections are already an efficient approximation of virtual non-factorisable corrections, which are discussed in more detail in the next section.

The choice of the *gauge scheme* is a result of the freedom in the renormalisation procedure of the electroweak sector. One can choose different sets of input parameters to express the cross-section. There is a large number of schemes discussed in the literature using different sets of input parameters and therefore different relations to calculate derived quantities. Possible parameters are the gauge boson masses M_{Z} and M_{W}, the Higgs and top mass, the electromagnetic, weak and strong coupling constants and the Fermi constant G_μ. Not all parameters are equally suitable as input parameters, e. g. the gauge boson masses should be input parameters because of their high precision and direct involvement in the process under investigation. On the other side the electromagnetic coupling constant α depends on the energy scale. At $\mu = M_{\rm W}$, the effective α is $\alpha_W = \frac{\alpha}{1-\Delta r}$, where Δr describes radiative loop corrections. Hence the running of α introduces a large corrections factor. Fortunately, an equation for α_W can be derived from the precise definition of Δr:

$$\alpha_W = \frac{\sqrt{2} G_\mu M_{\rm W}^2 \sin^2\theta_W}{\pi}, \tag{3.5}$$

where θ_W is the electroweak mixing angle. This means that the use of G_μ as an input parameter instead of α still reproduce the running of α, but G_μ itself is almost completely scale independent up to scales of $\mu = M_{\rm W}$.

For these reasons the *G_μ-scheme* is mainly used. The input parameters are the gauge boson masses $M_{\rm Z}$ and $M_{\rm W}$ and the Fermi constant G_μ. The couplings constants α_W and g and $\sin^2\theta_W$ are derived quantities and calculated in the following way:

$$\begin{aligned} \alpha_W &= \frac{\sqrt{2} G_\mu M_{\rm W}^2 \sin^2\theta_W}{\pi} \\ \sin^2\theta_W &= 1 - \frac{M_{\rm W}^2}{M_{\rm Z}^2} \\ g^2 &= \frac{4\pi\alpha_W}{\sin^2\theta_W} \end{aligned} \tag{3.6}$$

The *bare Born scheme* differs only in the definition of α_W from the G_μ scheme, which is set to the low energy value of $\alpha = 1/137$.

QCD corrections enter the process $\rm e^+e^- \to W^+W^- \to 4f$ at two different places. On one hand, the hadronic W width receives QCD corrections, namely a factor $(1+\alpha_s/\pi)$ in $\mathcal{O}(\alpha_s)$. This effects the total W width $\Gamma_{\rm W}$ in the resonant W propagator. On the other hand, each hadronically decaying W boson receives a QCD correction to the W$\rm q\overline{q}$' vertex. Integrating over the full phase space for gluon emission, this correction is reduced to a multiplicative correction factor $(1+\alpha_s/\pi)$ for each hadronic W boson in $\mathcal{O}(\alpha_s)$. The application of this inclusive factor is usually called *naive QCD correction.* In the total cross-section these naive QCD factors cancel against the corresponding factors in the W width in the resonant W propagators.

Full $\mathcal{O}(\alpha)$ Corrections

As already pointed out, the full $\mathcal{O}(\alpha)$ corrections are not yet calculated. Nevertheless the expected experimental sensitivity based on around 10 000 W pairs for each LEP experiment needs a theoretical uncertainty of $\leq 0.5\%$ so that the uncertainty on the theoretical predictions are far below the experimental ones. To reach this goal radiative corrections must be included which go beyond the standard corrections discussed above, and more or all $\mathcal{O}(\alpha)$ corrections must be included. An efficient approach is, instead of calculating the full $\mathcal{O}(\alpha)$ corrections for arbitrary four-fermion final states, just to calculate the corrections for $\rm e^+e^- \to W^+W^- \to 4f$ using the double pole approximation (DPA) [54, 55]. In the DPA, only those terms of the scattering amplitude are kept, which are enhanced by two resonant W propagators since the other contributions are at least suppressed by a factor of order $\mathcal{O}(\frac{\Gamma_{\rm W}}{M_{\rm W}}) \sim 3\%$. The novel idea is to calculate the $\mathcal{O}(\alpha)$ radiative corrections, which are

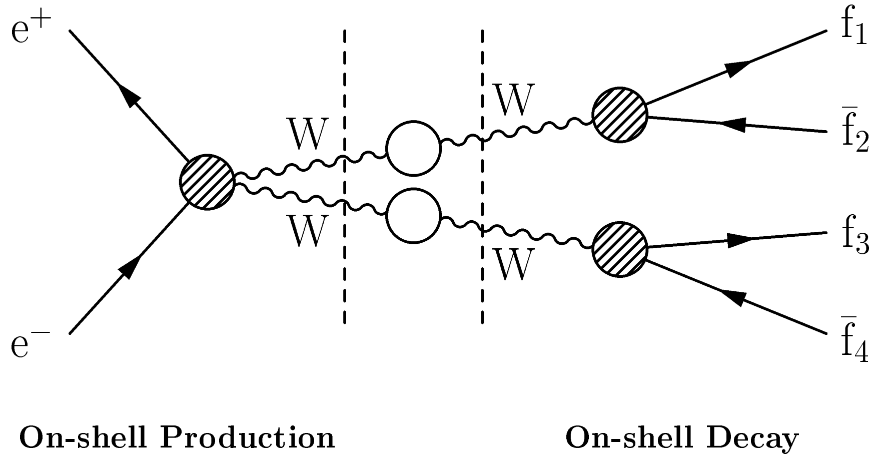

Figure 3.14: Diagrammatic structure of virtual factorisable corrections for $e^+e^- \to W^+W^- \to 4f$.

suppressed by a factor $\frac{\alpha}{\pi}$, only for the doubly resonant part. Hence the non-included $\mathcal{O}(\alpha)$ corrections for the non-doubly resonant part are of $\mathcal{O}(\frac{\alpha}{\pi}\frac{\Gamma_W}{M_W}) \sim 0.1\%$, which is fully sufficient for the set goal of 0.5%.

In such an approximation there are factorisable corrections, which are the ones to on-shell W-pair production and decay, and non-factorisable corrections, which originate from soft-photon exchange between the production and decay stages. Figure 3.14 depicts the factorisable correction. The shaded circles represents the production and decay of W bosons, which will be treated on-shell, and the open circles represent the W boson self-energies. Example Feynman diagrams of manifestly non-factorisable corrections are shown in figures 3.13(d) to 3.13(f). The diagrams of figures 3.13(g) to 3.13(i) are factorisable but contribute also to non-factorisable corrections. This fact results from the definition of non-factorisable corrections in the DPA in order to keep gauge invariance in the calculations. The virtual factorisable corrections can be taken from the calculations for on-shell W-pair production [56] and on-shell W decay [57]. This nice procedure is not applicable for the virtual non-factorisable corrections, which have to be calculated for the case of W-pair mediated four-fermion production [58, 59].

The full $\mathcal{O}(\alpha)$ radiative corrections for the process $e^+e^- \to W^+W^- \to 4f$ in the DPA are incorporated in only two Monte Carlo generators, namely KandY and RacoonWW.

At LC energies of 0.5 TeV and above, one expects at least 100 times more W pairs and hence the sensitivity is expected to increase by a factor of 10. Therefore the precision of the DPA will not be enough and the full $\mathcal{O}(\alpha)$ corrections to $e^+e^- \to 4f(\gamma)$ and more $\mathcal{O}(\alpha^2)$ corrections are necessary. Such calculations must also include the emission of soft and collinear massive gauge bosons, which will become more important at these high centre-of-mass energies. These corrections will give rise to so-called Sudakov logarithms of the type $\alpha \ln^2(s/M_W^2)$, which are partly calculated [60, 61], but only the first order is included in the DPA approach and therefore in some Monte Carlo generators.

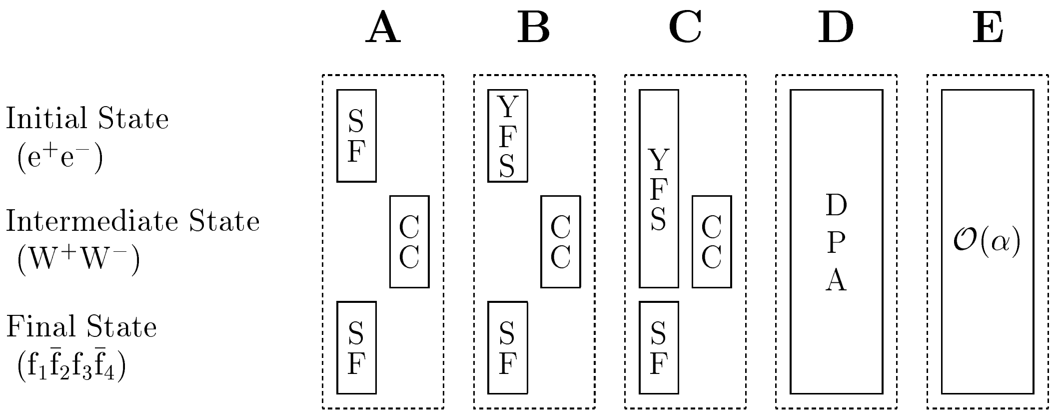

Figure 3.15: Schematic overview of different schemes for the breakup of radiative corrections in the process $e^+e^- \rightarrow W^+W^- \rightarrow f_1\bar{f}_2f_3\bar{f}_4$. The left and right columns in one scheme represents real and virtual corrections, respectively.

Summary of Radiative Corrections

In figure 3.15 five different schemes of combinations of radiative corrections are summarised. Case (A) is the simplest one. Real corrections for ISR and FSR are treated in the structure function approach. Virtual corrections from the intermediate W's are included in the form of the Coulomb corrections. Soft-photon radiation is better treated by using the YFS exponentiation instead of the SF approach leading to scheme (B). Here, soft-photon effects are treated up to all orders. The effect of FSR is subdominant compared to ISR and usually the SF approach is still used for FSR. A major improvement is reached, if photon radiation from the intermediate W's is included in the YFS exponentiation giving scheme (C). This needs $\mathcal{O}(\alpha)$ matrix element calculation of photon radiation from electrons and W bosons in order to treat interference effects correctly. Scheme (D) goes one step further and treats radiative corrections from all three stages at the same time. To reduce the complexity in the calculation, radiative corrections are treated in the DPA approximation, neglecting corrections from subdominant processes. The full $\mathcal{O}(\alpha)$ corrections (scheme (E)) are the correct description but are too complex in order to calculate in full detail. Usually scheme (D) is further improved by including higher order effects, such as from ISR in the SF approach and second order Coulomb corrections. Therefore, scheme (C) and (D) can describe radiative corrections in the process $e^+e^- \rightarrow W^+W^- \rightarrow f_1\bar{f}_2f_3\bar{f}_4$ at the present state of calculations most accurately.

3.3 From Quarks to Hadrons

Phenomenologically, the transition from quarks to hadrons is usually split into two stages. The fragmentation, where additional quarks, gluons and photons are radiated of the partons, and the hadronisation, where colour neutral bound quark states are formed. Because of the energy scale in the fragmentation process, perturbative QCD can be used to calculate at least some fragmentation aspects. For the hadronisation process only phenomenological models are available. The splitting into these two stages is conveniently done around a scale of

1 GeV, where quarks hadronise and perturbative QCD breaks down. See section A.1 and A.2 for more details.

Fragmentation

The radiation of high energy gluons from quarks can in principle be calculated to an arbitrary order using perturbative QCD. The three-parton matrix element for the process $\mathrm{q\overline{q}} \rightarrow \mathrm{q\overline{q}g}$ has been calculated up to two-loop level and first order matrix elements are available for final states up to five partons, but calculations of higher order or with more partons in the final state are very complex. Implementations of these matrix elements in Monte Carlo generators exist, but their ability to describe hadronic $\mathrm{e^+e^-}$ events at high energy is limited because of the limited number of partons and the limited precision due to low order α_s calculations.

A more suitable approach of this issue is the *parton shower method*. A shower is a sequence of consecutive branchings of a mother parton a into two daughter partons b and c. Each daughter is free to branch again, and therefore a tree-like structure is build up. This procedure is repeated until a cutoff is reached, which is usually chosen to be of the order of 1 GeV. In addition to quarks and gluons photons are also treated as partons in this process.

Parton shower models are very successful in modelling the distributions of daughter partons, which are comparably soft and almost collinear to the mother parton, but their results for additional high energy partons with large transverse momentum (leading to three or more distinct jets) is not optimal. To give a better description of these properties an additional weight is included at the first branching, which is derived from matrix element calculations for three partons. Hence the parton shower is matched to the matrix element calculations.

An alternative approach is the *colour dipole model* [62], where the initial $\mathrm{q\overline{q}}$ pair is treated as a colour dipole, which can radiate off gluons. For the second gluon radiation the three partons $\mathrm{qg\bar{q}}$ are split into two dipoles, namely qg and $\mathrm{g\bar{q}}$. For further gluon radiation this procedure is repeated. The process of splitting gluons into a $\mathrm{q\overline{q}}$ pair cannot simply be introduced into the dipole picture. Looking at the diagrams for $\mathrm{e^+e^-} \rightarrow \mathrm{q\overline{q}q'\bar{q}'}$ in the limit of small $p_\perp^2$ and small invariant mass of the $\mathrm{q'\bar{q}'}$ pair, it can be factorised into $\mathrm{e^+e^-} \rightarrow \mathrm{qg\bar{q}} \rightarrow \mathrm{q\overline{q}q'\bar{q}'}$.

Hadronisation

For the hadronisation process there are mainly three different approaches: The independent, the cluster and the string hadronisation. See section A.2 for more details.

The *independent hadronisation* [63] is the simplest and oldest one but has a couple of disadvantages and is not used anymore. Nevertheless the model is quite good to introduce the main ideas of hadronisation. An iterative procedure is applied for each parton from the fragmentation process. In each step a $\mathrm{q\overline{q}}$ pair is created and one of the new (anti-)quarks is combined with the isolated parton to form a hadron. The energy of the isolated parton is shared between the new hadron and the left over parton, which is the start parton for the next iteration. Since this method does not work for gluons, these are usually split into a $\mathrm{q\overline{q}}$ pair before hadronisation.

This approach has some shortcomings: There is no adequate termination of the iteration.

If insufficient energy is left over to form another hadron, the remaining isolated parton is usually discarded. This means that energy, momentum, charge, colour and flavour are not strictly conserved and must be fixed afterwards. Jet correlations, as observed in data, are by construction not implemented in this scheme. There are more properties of independent hadronisation which have been clearly excluded by e^+e^- data.

One goal of the *cluster hadronisation* [64] is to fix some shortcomings of the independent hadronisation. This is done by combining the partons from the fragmentation process into massive, colourless clusters, which then undergo hadronisation. They are treated, in analogy to hadronic resonances with averaged properties, i. e. isotropic decay, predominantly two-body, and other decay properties from first principles.

The *string hadronisation* [65] is the last and very popular class of hadronisation models. The picture of a rubber string is used for the colour flux tube connecting two quarks. While the two quarks move further apart, their movement is slowed down and energy is transfered into the colour field. If enough energy is transfered, the string breaks and the colour flux tube is interrupted by a virtual $q\overline{q}$ pair coming from the vacuum along the string. In the Lund string model [66], the string is broken exactly where it is necessary to form on-shell hadrons. Since all string breaks are causally disconnected, they can be treated in arbitrary order. The Lund scheme starts from the outer ends of the string and moves inside until the invariant mass of the remaining string drops below a cutoff. The remainder is then split into two on-shell hadrons like in a cluster decay.

Monte Carlo Implementation

There are mainly three programs with different implementations of the fragmentation or hadronisation process discussed above, namely Jetset [67], Herwig [68] and Ariadne [69]. The Lund fragmentation model [70] is implemented in Jetset. The parton shower is followed by the Lund string hadronisation. Herwig also uses a parton shower approach with branchings described by splitting kernels like Jetset, but uses different kinematic variables. The cluster model is used for the hadronisation. One important aspect is, that the Jetset implementation of the parton shower is explicitly Lorentz covariant at all stages of the branching in contrast to the Herwig implementation. Ariadne is an implementation of the colour dipole model for the parton shower and the hadronisation is usually done using the Lund string model within the Jetset framework.

These three Monte Carlo programs allow us to compare different fragmentation and hadronisation schemes with each other and study their effect on a measurement. This is explicitly important for analysing four-quark final states. For such a comparison, all implementations have to be tuned to give a good agreement between data and Monte Carlo and fortunately all tunes, using $Z/\gamma \to$ hadrons decays, describe the data reasonable well.

Di-Boson Fragmentation and Hadronisation

The models for fragmentation and hadronisation discussed above are strictly only valid for $Z/\gamma \to q\overline{q}$ decays and it is a priori not clear how to proceed for di-boson decays like $W^+W^- \to q\overline{q}q\overline{q}$ and $ZZ \to q\overline{q}q\overline{q}$. Assuming that spin-related correlations in the angular distributions of the boson decay products are treated correctly, one can assume that the fragmentation and hadronisation of each colourless boson system can be treated independently. Considering full four-fermion event generation, the situation is more complex. For instance, a $\mathrm{u\bar{d}d\bar{u}}$ final state has contributions from diagrams involving $\mathrm{W^+W^-}$ and ZZ pairs. Further single-resonant diagrams are contributing to this final state, where $\mathrm{W^\pm}$ and Z bosons are radiated off an initial quark anti-quark pair. In this case, the interpretation of grouping two quarks into a boson is totally unphysical. The correct treatment is to track down the colour flow in the hard scattering process and then transfer this information to the fragmentation process. Unfortunately, not many Monte Carlo generators are able to handle this. Nevertheless, for the fragmentation process one of the two quark pairing hypotheses ($\mathrm{W^+W^-}$ or ZZ) must be chosen. The easiest way is to fix one for each final state. A more elegant way is to choose it randomly on an event by event basis by considering the ratio of the cross-sections for pure $\mathrm{W^+W^-}$ or ZZ production, ignoring any interference. This issue is even more complex in six-quark final states from triple-boson production or the decay of a $\mathrm{t\bar{t}}$ pair, but can also be handled with the cross-section ratio method.

At LEP 2 energies, the decay length for W/Z bosons is about 0.1 fm, significantly less than the typical hadronisation scale of approximately 1 fm. The hadronisation of the two W bosons in the $\mathrm{W^+W^-} \rightarrow \mathrm{q\bar{q}q\bar{q}}$ channel may have a significant space-time overlap allowing possible final state interactions between the decay products of different W bosons. Two possible sources of final state interactions, both leading to non-independent hadronisation, have been widely considered: Bose-Einstein Correlation (BEC) and Colour Reconnection (CR). These two sources, if realised in nature, can significant distort the reconstruction of W pairs and their properties.

Most of the particles produced in hadronic events are pions and kaons obeying Bose-Einstein statistics. It is therefore expected, that the production of identical particles at small momentum separation is enhanced, relative to what uncorrelated production would have lead to. BEC has been observed in various experiments in hadron-hadron and $\mathrm{e^+e^-}$ collisions. With the possibility of producing W pairs at LEP 2 the question was raised, if BEC can take place between identical bosons coming from different W bosons, but the theoretical discussion is not yet settled. Intra-W BEC is observed using charged pion pairs, but the measurements of full BEC, namely intra-W and inter-W BEC, are not significant enough to hint in any direction. Hopefully, the combination of measurements from all four LEP collaborations with the full integrated luminosity will favour one scenario. See section A.4 for more details about BEC and its implementation in Monte Carlo generators.

Colour Reconnection describes the class of final state interactions where colour is exchanged between the decay products of the two W bosons. This is in principle possible because the separation of both W decays is small compared to the characteristic hadronic distance scales of about 1 fm. With the current understanding of non-perturbative QCD, such interference can be estimated only in the context of specific models, where a colour reconnection can occur if the two colour flux tubes overlap. See section A.5 for a description of the Sjöstrand-Khoze models (SK-I, SK-II and SK-II').

3.4 W-Pair Event Topology

In the previous sections the production and decay of W pairs have been presented. In this section the three W decay modes are discussed and the topological description of W pairs is introduced.

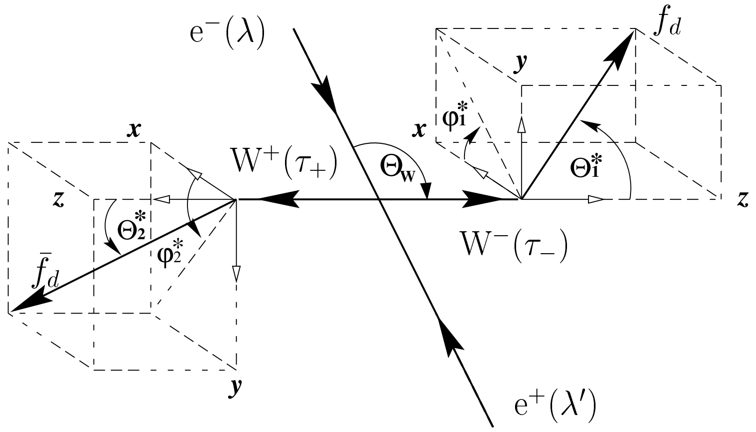

Figure 3.16: Definition of the angles and helicities in a W^+W^- event.

A W boson can decay either into a charged lepton and its neutrino or into a quark and anti-quark. This gives three final states for W^+W^- pairs: the leptonic ($\ell\bar{\nu}_\ell\bar{\ell}'\nu_{\ell'}$, $Br = 0.10$), the semileptonic ($q\bar{q}\ell\bar{\nu}_\ell$, $Br = 0.43$) and the hadronic ($q\bar{q}q\bar{q}$, $Br = 0.47$) final state. The event can be fully described by five angles, ignoring finite width effects and initial state radiation. Figure 3.16 shows the W production angle θ_W, which is the angle between the incoming electron and the outgoing W^- and the four decay angles $\cos\theta^*_{1,2}$ and $\phi^*_{1,2}$, two for each W boson. The two decay angles $\cos\theta^*$ and ϕ^* describe the direction of the down-type fermion f_d in the rest frame of the W where both decay fermions are back-to-back. The axes of the right-handed coordinate system in the W rest-frame are defined such that the z-axis is along the parent W flight direction in the overall centre-of-mass system, and the y-axis is in the direction $\vec{e}^- \times \vec{W}$ where $\vec{e}^-$ is the electron beam direction and $\vec{W}$ is the parent W flight direction.

The tree level distributions of the W production angle $\cos\theta_W$ and the two W^- decay angles $\cos\theta^*_1$ and ϕ^*_1 are shown in figure 3.17 and 3.18, respectively. For the W^+ $\cos\theta^*_2$ is the same as $\cos\theta^*_1$, but ϕ^*_2 is shifted by π compared to ϕ^*_1. This is due to the construction of the coordinate system in the W^+ rest frame. The y-axis is perpendicular to the W^+ flight direction and the electron beam direction and not the positron beam direction.

Not all three decay channels can be fully reconstructed from the measured particles. In the $\ell\bar{\nu}_\ell\bar{\ell}'\nu_{\ell'}$ channel all five angles can only be reconstructed by assuming energy and momentum conservation and forcing both W bosons to the same, fixed mass. These six constrains make it possible to reconstruct the two unmeasured neutrinos up to a twofold ambiguity. This is only true for events with no tau leptons in the final state.

The semileptonic final state is the "golden channel" of all three W^+W^- final states because the reconstruction is very easy. The two jets are assigned to one W and the charged lepton to the other. Its charge resolves directly the charge of the W bosons. Only for events with tau leptons some special care is needed because the τ decays in the detector and only its decay products without the τ-neutrino are measured. But with some assumptions the τ can be reconstructed from its decay products in most of the cases. Without flavour tagging there is a twofold ambiguity in the hadronic decay angles $\cos\theta^*_j$ and ϕ^*_j and not the total distributions can be measured. Because the quark and the anti-quark are back-to-back in the W frame, this ambiguity is $(\cos\theta_j^*, \phi_j^*) \leftrightarrow (-\cos\theta_j^*, \phi_j^* + \pi)$. The folding will be done usually as

$$\begin{aligned} \phi_j^* > 0 \quad &\rightarrow \quad (\cos\theta_j^*,\, \phi_j^*) \\ \phi_j^* < 0 \quad &\rightarrow \quad (-\cos\theta_j^*,\, \phi_j^* + \pi). \end{aligned} \tag{3.7}$$

This folding procedure is illustrated in figure 3.18 for the W^- decay angles. Events with a true ϕ_1^* greater then zero are shown in dark grey and events with the true ϕ_1^* smaller then zero are shown in light grey. The effect of the folding procedure is that the distributions for $\phi_1^* < 0$ are just the mirrored distributions for $\phi_1^* > 0$. The sum of both distributions are symmetric.

The four-quark final state is a very demanding channel: Without flavour tagging the decay angle of both W bosons are folded like for the hadronically decaying W in the semileptonic final state. But there are two additional problems because four identical jets are measured in the detector: These four jets must be combined into two di-jet systems and only one out of three possible combinations is the right one. On top of this problem, the sign of the charge of the W's must be measured which can be done partly using a jet-charge method.

3.5 Monte Carlo Generators

Monte Carlo generators are a main tool for particle physicists. Theoretical calculations, either for the SM or for physics beyond it, are transferred by means of Monte Carlo techniques into simulated events which can be used to study and understand the detector and compared with data.

The issue of precise predictions for W-pair production, or more generally four-fermion production, was always very important at LEP 2 energies and will be even more important at LC energies. Therefore two workshops on LEP 2 physics were held at the beginning and end of LEP 2 to summarise the existing calculations for LEP 2 physics, compare the different implementations of Monte Carlo generators and make to some extend a statement about their precision. For the part about the W^+W^- or four-fermion Monte Carlo generators, see reference [71, 72].

We close the chapter by briefly describing Monte Carlo generators used for analysis of W pairs.

YFSWW3

YFSWW3 [23] is a specialised Monte Carlo generator for W-pair production. Only the CC03 diagrams are considered for calculating the scattering amplitudes and not the full four-fermion set, but the radiative corrections are very sophisticated including Coulomb corrections. ISR is implemented up to order $\mathcal{O}(\alpha^3)$ in the YFS scheme, which allows an arbitrary number of non-zero p_t photons, while FSR for leptonically decaying W bosons is incorporated using the PHOTOS [73] program (see below). In the latest version of YFSWW3, the complete $\mathcal{O}(\alpha)$-corrections to W-pair production have been implemented in the double-pole approximation (DPA).

Effects of anomalous couplings are also incorporated in the program.

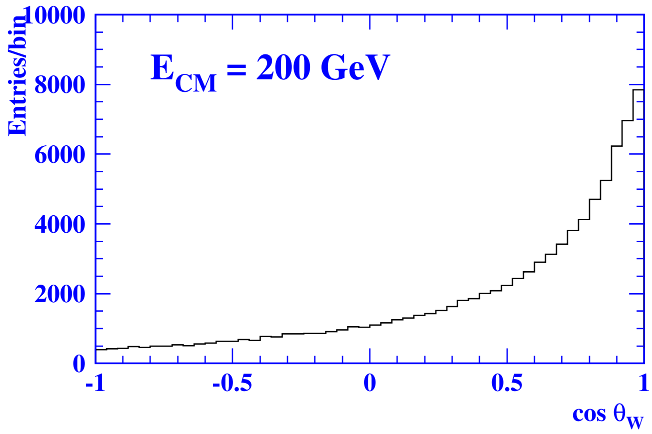

Figure 3.17: True distribution of the W production angles $\cos\theta_{\mathrm{W}}$ in the process $\mathrm{e^+e^-} \rightarrow \mathrm{W^+W^-} \rightarrow \mathrm{q\bar{q}q\bar{q}}$ at $\sqrt{s} = 200\,\mathrm{GeV}$ at generator level.

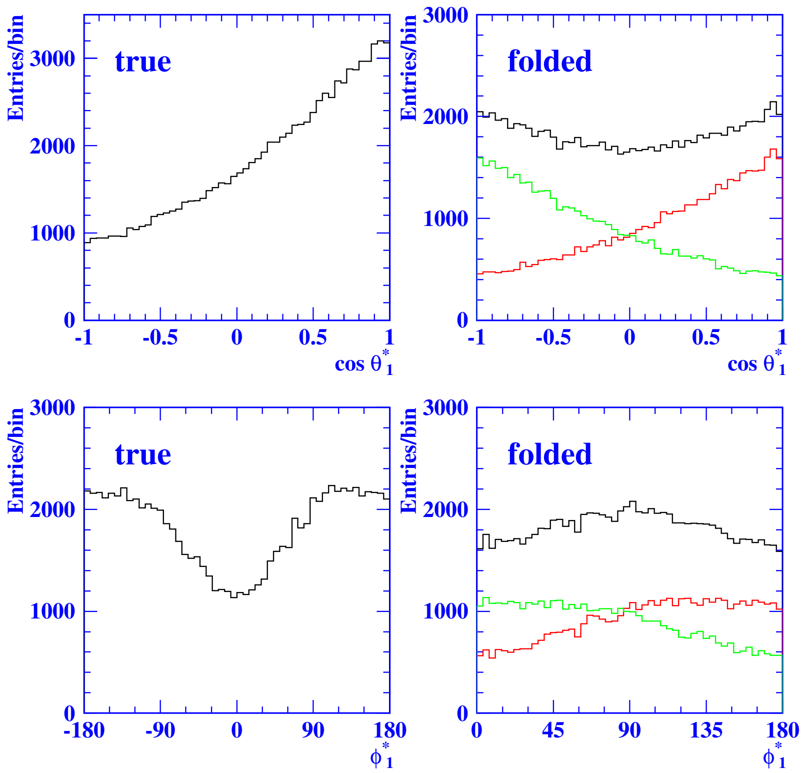

Figure 3.18: True and folded distribution of the W$^-$ decay angles $\cos\theta_1^*$ and ϕ_1^* in the process $\mathrm{e^+e^-} \rightarrow \mathrm{W^+W^-} \rightarrow \mathrm{q\bar{q}q\bar{q}}$ at $\sqrt{s} = 200\,\mathrm{GeV}$ at generator level. The black lines show the true and folded distributions using all events, respectively. In the folded distributions the light and dark lines show the events with the true ϕ_1^* greater or less than zero.

KoralW

KoralW [24] is a full four-fermion Monte Carlo generator using `grc4f` [74] matrix elements for the evaluation of the scattering amplitudes treating all fermions massive. The inclusion of radiative corrections is also quite advanced. ISR and FSR are implemented in the same way as in YFSWW3, as are the Coulomb corrections. Unfortunately, no full $\mathcal{O}(\alpha)$-corrections to W pairs are implemented.

Effects on anomalous triple gauge boson couplings are only implemented in the CC03 part of the scattering amplitudes.

KandY

The main Monte Carlo generator used to simulate the W-pair signal at OPAL is the KandY generator, which is a combination of KoralW and YFSWW3 running concurrently [25]. This approach combines the advantages of full four-fermion calculations with the full $\mathcal{O}(\alpha)$-corrections for W pairs.

Technically KoralW is used for the generation of the event kinematics and the calculation of weights for radiative corrections like ISR and FSR. Meanwhile, the event kinematics are passed to YFSWW3, which calculates the $\mathcal{O}(\alpha)$-corrections for W pairs. A weight is passed back to KoralW and finally all weights are combined and the event generation process is completed by choosing or rejecting the event. The direct implementation of the $\mathcal{O}(\alpha)$-corrections into KoralW would give an easier usage of the generator, but because of the complexity of the calculations this was not possible on a short time scale. This approach was chosen in order to use these more correct calculations in the final publications.

As YFSWW3 and KoralW, anomalous triple gauge boson couplings are implemented in KandY, but again just in the CC03 part of the scattering amplitudes.

RacoonWW

The second Monte Carlo generator for four-fermion final states including $\mathcal{O}(\alpha)$ corrections in the DPA is RacoonWW [26–28]. Analytic matrix element calculations for massless four-fermions and four-fermions with one real photon are used for the hard process to give a very good description of real photon radiation. The full $\mathcal{O}(\alpha)$ radiative corrections are done only to W-pair production in the DPA. Further standard corrections are included like Coulomb corrections, naive QCD corrections and higher order radiative corrections to the initial state up to $\mathcal{O}(\alpha^3)$ via the structure function approach.

This Monte Carlo generator is one of the newest programs designed for an extensive application in four-fermion physics. Anomalous triple and quartic gauge couplings in all four-fermion final states can be switched on and the incoming electron beams can be longitudinally polarised. It is not very suitable for processes with forward-scattered electrons or positrons in the final state (single-W production), because of the assumption of massless fermions in the matrix element calculations. Unfortunately, final state photon radiation can be switched off for neither leptonically nor hadronically decaying bosons. From one point of view this is the correct theoretical treatment, because interference effects do not always factorise. On the other side final state photon radiation compete with gluon radiation of quarks in the fragmentation process and must be addressed there. The complete treatment of the hard process including radiative corrections and the fragmentation process is not possible at the moment, because the fragmentation process is to complex and not very well calculable. For further discussion see section 3.3.

Excalibur

Excalibur [75] is a full four-fermion Monte Carlo generator like Koralw, but the evaluation of the matrix element is done in a different way. The matrix element calculations are done with massless fermions and at the end the event kinematic is transfered into massive fermions. ISR is implemented in the structure function approach up to $\mathcal{O}(\alpha^2)$ generating photons without p_t. Naive QCD corrections are also included.

One great advantage is the implementation of all CP conserving anomalous triple gauge boson couplings in all relevant four-fermion diagrams and not only in the CC03 part. This is important for single-W and single-Z production, in particular for the process $e^+e^- \rightarrow We\nu_e$. Here, diagrams for W-pair and single-W production contribute, which both have contributions from triple gauge vertices.

Excalibur is used at OPAL to generate samples with anomalous triple gauge boson couplings, in order to test analysis methods with couplings different from the SM.

Wopper

Wopper [76] is a specialised W-pair generator for CC03 or CC11 diagrams including ISR and beamstrahlung via Circe [77]. The CC11 diagrams include only single-resonant diagrams and this Monte Carlo generator is not very suitable for all final states. Semileptonic W-pair decays including a muon or a tau are treated completely but already for the $q\overline{q}e\overline{\nu}_e$ decay the single-W fraction is missing. The great advantage is that Wopper implements longitudinal beam polarisation and all triple gauge couplings except the CP violating $WW\gamma$ couplings. This makes it to a good choice to study W-pair production at TESLA.

Pythia

Pythia [78] is a multi purpose Monte Carlo generator with many extensions beyond the SM. At OPAL, Pythia is used mainly for cross checks for SM processes, e. g. $Z/\gamma \rightarrow q\overline{q}$ production. But the radiative corrections are not as advanced as for other generators and the calculations of the hard process are also sometimes rather simplified. W-pairs are generated using only CC03 diagrams. No full four-fermion calculations are implemented. Nevertheless, it comes with many processes and extensions and is widely used for LC physics studies.

Whizard

Whizard [79] is multi-purpose Monte Carlo generator capable of almost every physics process. For the generation of a specific process the initial and final state must be specified and a matrix element calculation must be choose. Whizard automatically generates the scattering amplitude, optimises the phase space for the chosen process and generates events. Processes up to six or eight fermions in the final state are tested, theoretically there is no limit on the number of particles in the final state.

The generator comes with three matrix element calculators: Madgraph [80], CompHep [81] and O'MEGA [82]. O'MEGA is the most flexible and fastest of the three allowing not only SM processes but also anomalous triple and quartic gauge couplings.

Longitudinal and, in the latest version, also transverse polarisation of the incoming electron beams can be chosen. Because of this feature, it will become the first choice for LC physics studies. The radiative corrections are not as complete as specialised four-fermion Monte Carlo generators. Only ISR is implemented to $\mathcal{O}(\alpha)$ using the structure function approach generating photons along the beam axis without p_t.

PHOTOS

The PHOTOS [73] program is no Monte Carlo generator but listed here because it is used by YFSWW3, KORALW and KANDY for the simulation of final-state radiation. The structure function approach is used to generate up to two final-state photons for each gauge boson decay. The $\mathcal{O}(\alpha^2)$ corrections are implemented in the leading logarithmic approximation.

Chapter 4

Accelerators & Detectors

The best theory is useless if its predictions cannot be confirmed. Therefore, a setup is needed to carry out experiments. In high-energy physics such setups have grown to a size, where they fit no longer into a small room. A large accelerator is needed to produce particle beams of a certain energy and a huge detector to study the particles, which are produced in collisions of the beams.

In this chapter, we describe the utilised experimental apparatus: the LEP storage ring, the OPAL detector, the future TESLA linear collider and the future TESLA detector. Some details are given about the instrumentation of the accelerator in order to measure beam parameters essential for the experiment, i. e. beam polarisation and beam energy.

4.1 General Remarks to Accelerators

In general, there are two important aspects which drive the design of accelerators. First, the beam energy should be as high as possible in order to gain deeper insight into the structure of matter due to a better resolution of smaller sizes. Second, the luminosity $\mathcal{L}$ defined as

$$\mathcal{L} = \frac{1}{\sigma}\frac{\mathrm{d}N}{\mathrm{d}t}, \tag{4.1}$$

where $\mathrm{d}N/\mathrm{d}t$ is the event rate of a process and σ the corresponding cross-section, should be large enough to obtain a decent event rate. The luminosity of a collider can be described in terms of its machine parameters:

$$\mathcal{L} = \frac{N_\mathrm{e}^2 f_b}{4\pi\sigma_x\sigma_y}, \tag{4.2}$$

where N_e is the number of particles per bunch, f_b the number of bunch crossings per second and σ_x and σ_y the transverse beam dimensions at the interaction point in x and y, respectively. This formula directly shows one advantage of a storage ring. The intrinsic luminosity is increased by f_b, the number of bunch crossings per second. A second advantage, unrelated to the luminosity, is that the accelerated beams can be used more than once, until the beam quality is not sufficient anymore, and only the energy loss due to synchrotron radiation must be compensated. Both advantages are lost for linear colliders and one solution to increase the luminosity is to decrease the beam size drastically.

4.2 The LEP Collider

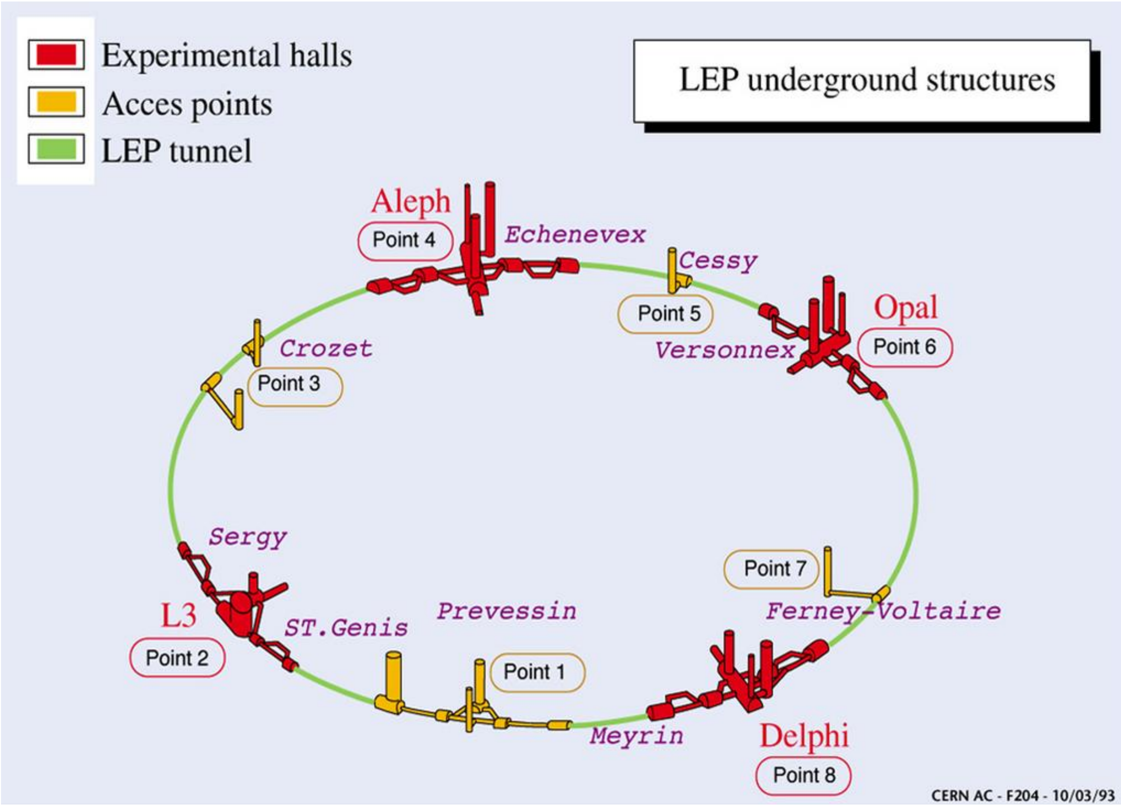

Figure 4.1: Schematic view of the LEP ring with the four experiments.

The Large Electron Positron (LEP) collider was the source of electron and positron beams for the four multi-purpose experiments ALEPH, DELPHI, L3 and OPAL, which were equally distributed over the LEP ring as shown in figure 4.1. The LEP tunnel is situated approximately 100 m below the Swiss and French surface at CERN[1] near Geneva and had a circumference of almost 27 km. Some typical machine parameters are shown in table 4.1 [83].

In the years 1989 to 1995, LEP was operated at a beam energy of about half the Z boson mass. This phase is known as LEP 1. The energy was chosen to take advantage of the Z resonance in the e^+e^- collision cross-section, which enhances the total cross-section by 2 – 3 orders of magnitude with respect to the non-resonant photon exchange, which is dominant at lower energies. In this time about 4.5 million hadronic and 0.65 million leptonic Z decays were recorded per experiment giving the excellent opportunity to study the properties of the Z boson with high accuracy.

In 1996, the second phase of LEP was started and the energy was gradually increased to a maximum of 209 GeV in the year 2000, when LEP was finally shut down and dismantled to make place for the LHC[2]. The highest possible energy was needed for the search of the Standard Model Higgs boson and other new particles emerging from physics beyond the Standard Model in order to increase the sensitivity to new effects as much as possible. Each

[1] European Laboratory for Particle Physics — the abbreviation has been kept from the first name of the laboratory: **C**entre **E**uropéen pour la **R**echerche **N**ucléaire.

[2] **L**arge **H**adron **C**ollider

experiment was able to collect around 10 000 W pairs and 400 Z pairs. This data is used to study the properties of the W boson with high precision and the self-couplings of gauge bosons.

Beam Energy Measurements at LEP

Besides a very precise luminosity measurement, which was done by specialised forward detectors installed at each experiment, a very good energy measurement was needed at both LEP 1 and LEP 2. The uncertainty on the beam energy is directly proportional to the uncertainty in the measurement of particle masses like the Z and W boson.

The best determination of the beam energy is by means of *resonant depolarisation* of the beams [84]. At LEP 1 the beams could build up a non-negligible transverse polarisation through the Sokolov-Ternov mechanism [85]. The degree of polarisation can be measured by the angular distribution of Compton-scattered polarised laser light. By exciting the beam with a transversely oscillating magnetic field, the transverse polarisation can be destroyed when the excitation frequency matches the spin precession frequency. Determining the resonant depolarisation frequency[3] allows a precise determination of the beam energy E_b through

$$E_\mathrm{b} = \frac{\nu_s m_\mathrm{e} c^2}{(g_\mathrm{e} - 2)/2} = \nu_s \cdot 440.6486(1)\,[\mathrm{MeV}], \tag{4.3}$$

where m_e is the electron mass, c the speed of light and $(g_\mathrm{e} - 2)$ the anomalous magnetic-moment of the electron. Here, ν_s is the spin tune, the number of electron-spin precessions per turn of LEP. This is the spin precession frequency divided by the particle revolution frequency. ν_s is around 100 at a beam energy of 45 GeV. A depolarisation takes place over many thousand turns of the beams, given that the frequency sweep lasts at least 12 seconds. The precision achievable is 200 keV. The overall uncertainty of the beam-energy measurement was around 1 MeV, giving an excellent relative uncertainty of 2×10^{-5} at LEP 1 energies.

Before this high precision was reached, the polarisation measurement must have been understood very well and a detailed energy model for LEP was set up. Many parameters were needed to describe the actual beam energy, ranging from the behaviour of the dipoles, the geology of the Geneva area and the LEP civil engineering structures. One of the last discovered effects were the parasitic currents flowing along the beam pipe, produced by the TGV passing from Geneva central station to Paris.

As the beam energy was increased beyond 60 GeV a polarisation level sufficient for the resonant depolarisation method could not be achieved and the beam energy was inferred from the *magnetic extrapolation method*. It relied on 16 nuclear magnetic resonant (NMR) probes which measured the local magnetic field in several of the LEP main bend dipole magnets. The field readings of the probes were calibrated using a fit to the beam energy measured by resonant depolarisation in the region of 41 to 61 GeV. The fit is linear, with two free parameters: $E_\mathrm{pol} = a + bB_\mathrm{NMR}$. From this fit, the beam energy in physics runs can then be determined from the average field measured by the probes.

[3] The resonant condition happens when the excitation frequency divided by the LEP orbit frequency matches the non-integer part of the spin tune ν_s.

The essential assumption for this procedure is that the relationship between beam energy and measured magnetic field is linear between the calibration region and the physics regime. The largest systematic uncertainty on this measurement comes from a comparison of the total bending field measured by the flux loop and the predicted total bending field from the average over the NMR probes: $B_{\mathrm{FL}} = c + dB_{\mathrm{NMR}}$. The preliminary uncertainty on the beam energy for the LEP 2 data is between 20 and 30 MeV [86].

Unfortunately, this is not small enough to be of little influence of the measurement of the W mass. The knowledge of the beam energy is needed to considerably improve the quality of the kinematic fit resolution used in the measurement of the W mass, which exploits energy and momentum conservation, and sets the relative energy scale of the energy measurement to an uncertainty of $\Delta M_{\mathrm{W}}/M_{\mathrm{W}} \sim \Delta E_{\mathrm{b}}/E_{\mathrm{b}}$. To reduce the systematic contribution from the beam energy adding to the 25 MeV expected statistical uncertainty on M_{W}, the target for the beam energy calibration at LEP 2 was $\Delta E_{\mathrm{b}}/E_{\mathrm{b}} \sim 10^{-4}$, i. e. a ~ 10 MeV uncertainty at a beam energy of 100 GeV.

To achieve this goal, the *LEP spectrometer* [87] was installed in 1998. The principle used to measure the energy of a particle beam is to bend the beam with a known magnetic field, and measure the bend angle, as depicted in figure 4.2. For a simple spectrometer, the beam energy in the small angle approximation is given by the ratio of the integral bend field of the bend magnet and the measured bend angle θ

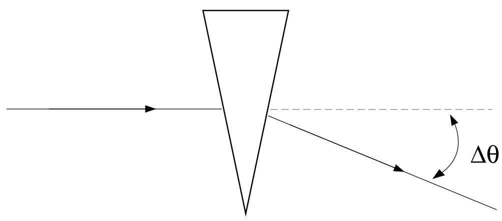

Figure 4.2: The spectrometer principle.

$$E_{\mathrm{b}} = e\,c\,\frac{\int B \cdot \mathrm{d}l}{\theta}, \tag{4.4}$$

where e is the electron charge and c the speed of light. The setup of the spectrometer is shown in figure 4.3 and consisted of a steel bending magnet flanked by a triplet of Beam Position Monitors (BPM) at each side providing a measurement of changes in the bending angle when the beams are accelerated to physics energies. The precise knowledge of the dipole bending strength to a 30 ppm accuracy and the BPM resolution of 1 μm were essential to achieve the goal of a 100 ppm relative precision on the beam energy.

As before in the case of the NMR based method, the spectrometer is calibrated at a polarisable energy, E_{RD}, using the resonant depolarisation method. At physics energies, E_ϕ, the ratio of the two energies is directly obtained from the comparison of the bending angles θ_{RD} and θ_ϕ and the knowledge of the bending strengths at the two energies:

$$\frac{E_\phi}{E_{RD}} = \frac{\int B \cdot \mathrm{d}l|_{E_\phi}}{\int B \cdot \mathrm{d}l|_{E_{RD}}} \left(\frac{\theta_{RD}}{\theta_\phi}\right) \tag{4.5}$$

The preliminary analysis of the beam energy measurements using data from 1999 give an uncertainty of 15 MeV on the beam energy, but it is expected that the final understanding of the spectrometer will reduce this uncertainty further. The final LEP measurements of the W mass are waiting for these numbers.

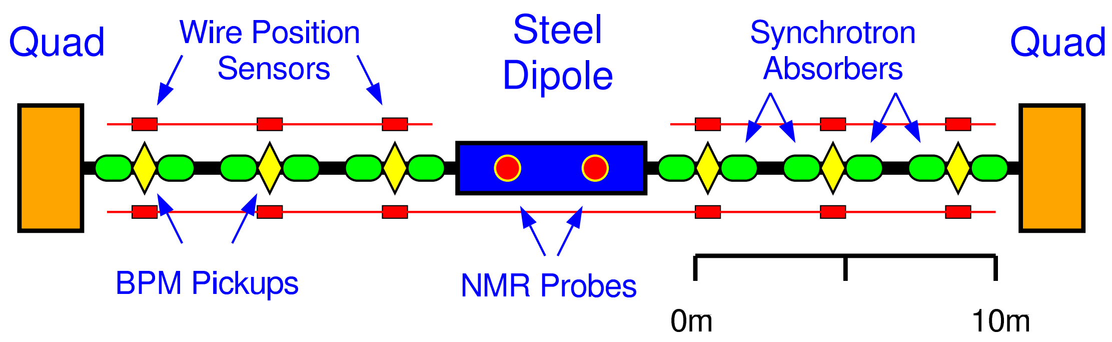

Figure 4.3: Layout of the LEP magnetic spectrometer. A steel dipole magnet is flanked by three-BPM stations at each side provide reconstruction of the bending angle.

Limitations of LEP

During its final year LEP reached its technical limits. A further increase in energy would not have been possible without a major upgrade of the accelerating structures. Because of synchrotron radiation the beams lose energy with each revolution,

$$E_{\mathrm{Rad}} \propto \frac{1}{r}\left(\frac{E_{\mathrm{b}}}{m}\right)^{4}, \tag{4.6}$$

where r is the radius of the collider and m the beam particle mass. The energy loss for electrons is around 2 GeV per turn for a 100 GeV beam at LEP. This amount of energy has to be restored at each revolution and therefore a higher energy was not possible at LEP without additional accelerating structures. Nevertheless, there are two directions to increase the beam energy in order to carry out further experiments in particle physics. The radiation loss is proportional to m^{-4} and already negligible for protons. This way was chosen by CERN, where at the moment the LHC is built. At the LHC protons are accelerated up to a centre-of-mass energy of 14 TeV. The other direction is to decrease the curvature of the collider. In the ideal case of zero curvature no energy is lost due to synchrotron radiation from bending the beams, but still there is some loss from the linear acceleration, which depends on the accelerating gradient and is always negligible. This direction is chosen for the next generation of electron-positron linear colliders.

4.3 The TESLA Linear Collider

The next stage in accelerator-based particle physics will be an electron-positron linear collider for high precision measurements of the particles discovered at the LHCṪhe TESLA[4] project [88] is planed and designed by an international collaboration at DESY in Hamburg, Germany, and aims at centre-of-mass energies up to about 1 TeV. Besides TESLA, there are two further linear collider projects: the American NLC[5] [89, 90] and the Asian JLC[6] [91].

[4]**T**era **E**lectron Volt **E**nergy **S**uperconducting **L**inear **A**ccelerator
[5]**N**ext **L**inear **C**ollider
[6]**J**apan **L**inear **C**ollider

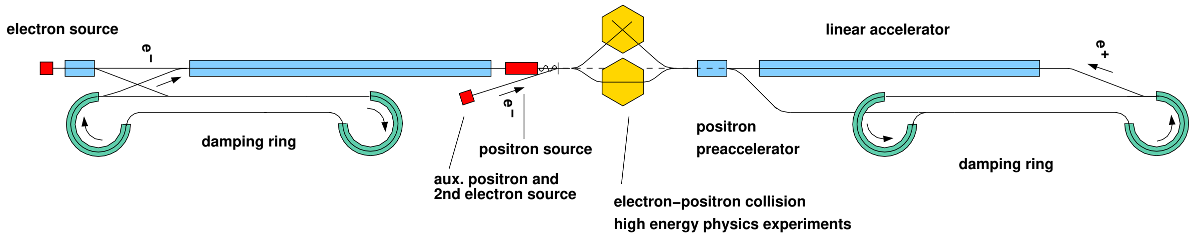

Figure 4.4: Sketch of the overall layout of TESLA.

A sketch of the overall layout of TESLA [92] is shown in figure 4.4. The overall length is 33 km. Unlike a storage ring collider, a linear collider cannot serve several interaction regions simultaneously with the same beams. Nevertheless the design integrates a second interaction region, but it must be kept in mind that the total luminosity must be shared between these two. The second interaction region will have a crossing angle of ~ 34 mrad, and is therefore suitable for eγ and $\gamma\gamma$ collisions. Using the crab-crossing scheme the same luminosity for $\mathrm{e}^+\mathrm{e}^-$ collisions can be reached as at the first interaction region.

TESLA uses 9-cell niobium cavities cooled by superfluid Helium to $T = 2$ K and operated at a frequency of 1.3 GHz instead of 11.4 GHz used by the warm copper technology for NLC and JLC. For the base design of 500 GeV centre-of-mass energy an accelerating gradient of at least 23.4 MeV/m must be reached for the 33 km long design. Recent tests of accelerating structures showed that gradients of 35 MeV/m can be reached in normal operation, which are needed to achieve a centre-of-mass energy of 800 GeV at the same length. The two main linear accelerators are each constructed from roughly 10 000 one-meter long superconducting cavities. Groups of eight cavities are installed in a common, 12 m long cryostat.

In order to realise a high luminosity, equation (4.2) gives two possible solutions: A high repetition rate and a small beam spot size. The superconducting accelerator structures allow for rather long RF pulses of around 1 ms, which can accelerate a train of 2820 bunches. This gives a large bunch spacing of 337 ns. The train repetition rate is 5 Hz. The decrease of the beam spot is non-trivial and the choice of the right size is constraint by beamstrahlung: the particles emit hard synchrotron radiation in the strong electromagnetic spacecharge field of the opposing bunch as depicted in figure 4.5. The average fractional beam energy loss from beamstrahlung is approximately given by [93]

$$\delta_E = 0.86 \frac{r_\mathrm{e}^3 N_e^2 \gamma}{\sigma_z (\sigma_x + \sigma_y)^2}, \tag{4.7}$$

where r_e is the electron radius, N_e the number of beam particles per bunch and γ the relativistic factor. The beam size is described by σ_x, σ_y and σ_z. Besides the reduction of the collision energy, beamstrahlung can lead to severe background in the detector coming from interactions of pair and photon background with detector and accelerator components as depicted in figure 4.5. By choosing a large aspect ratio $R = \sigma_x/\sigma_y \gg 1$, δ_E becomes independent of the vertical beam size and the luminosity can be increased by making σ_y as small as possible. The beam parameters for a centre-of-mass energy of 500 and 800 GeV are shown in table 4.1. Because of the huge beam spot size at LEP the effect of beamstrahlung was negligible.

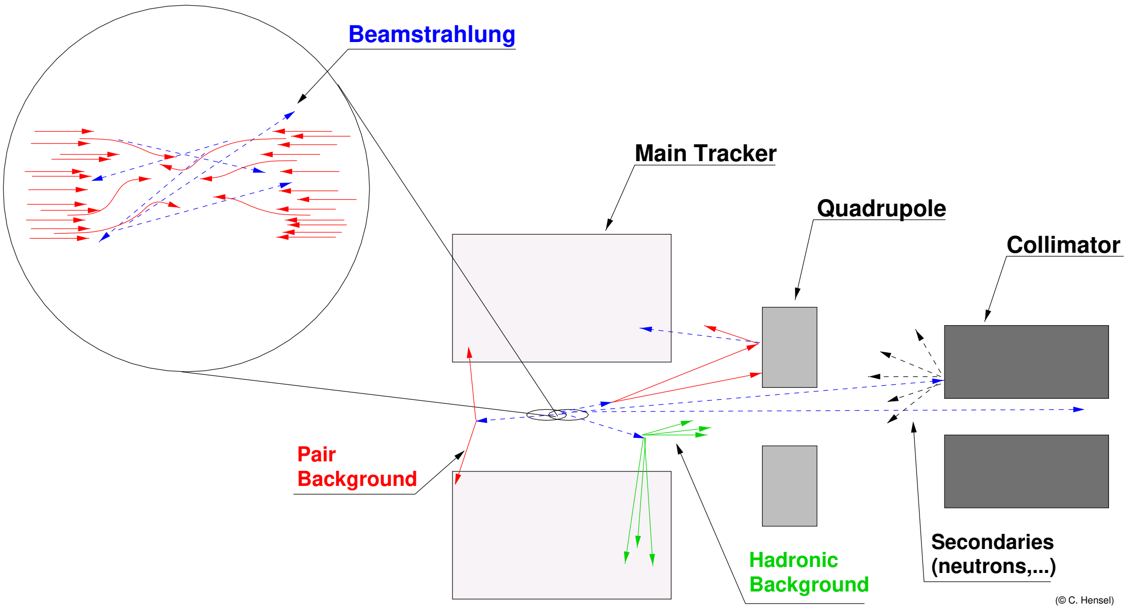

Figure 4.5: Detector sketch showing the origin of beamstrahlung and production of beam induced, neutron, hadronic and pair background.

Beam Polarisation at TESLA

The construction of a high intensity electron source is more or less standard technology [94]. Even the production of polarised electrons with a polarisation of 80% was already achieved for SLC[7] [95]. The design of the TESLA gun is based on this technology. Polarised electrons are produced by illuminating a GaAs cathode with circularly polarised laser light. The quantum efficiency of the cathode at SLC was only 0.1% [96] which determines the required laser power. A too high laser intensity can cause problems with the vacuum and studies of a better technique are underway [97].

The standard way to produce positrons is to shot high energy electrons on a target. Photons from bremsstrahlung can create electron-positron pairs from which the positrons must be captured outside the target. The fundamental intensity limit of such a source is given by the thermal stress in the target due to the energy deposition of the primary

[7] **S**tandford **L**inear **C**ollider

	LEP	TESLA		
$\sqrt{s}$	209	500	800	GeV
$\mathcal{L}$	$1 \cdot 10^{31}$	$3.4 \cdot 10^{34}$	$5.8 \cdot 10^{34}$	cm^{-2}s^{-1}
IP beam size (x,y)	200 000, 2 500	553, 5	391, 2.8	nm, nm
bunch spacing	22 000	337	337	ns
bunch charge	$3 \cdot 10^{11}$	$2 \cdot 10^{10}$	$1.4 \cdot 10^{10}$	e^{-1}
accelerating gradient	7	23.4	35	MV/m

Table 4.1: Comparison of LEP and TESLA machine parameters.

electrons. Rotating the target would help to distribute the heat load over a wider area, but in general this technique must be considerably improved in order to reach the design intensity for TESLA.

The proposed design for TESLA splits the production of photons and electron-positron pairs [98]. High energy photons are produced from the high energy electron beam while passing an undulator, which is located upstream the interaction point. The photons are used to produce electron-positron pairs in a thin conversion target. The conversion of photons leads to a small optimal target thickness of 0.4 radiation length. Using titanium alloy, the rotating target will be 1.4 cm thick. The advantages of titanium alloy are the excellent mechanical properties and a very high heat capacity. A velocity of about 50 m/s at the circumference of the target is necessary to spread out a single bunch train over a distance of 5 cm.

This proposed positron source opens up the possibility to produce polarised positrons, which is non trivial at all: Exchanging the undulator by a helical undulator will produce circularly polarised photons in the beamstrahlungs process. Therefore, the positrons from pair production are longitudinal polarised. The demands on the precision of beam and undulator are very high, because only on-axis photons are completely polarised. Detailed simulations of the whole process indicate a maximum longitudinal positron polarisation of 45 – 60%. The experiment E-166 [99] will use the Final Focus Test Beam at SLAC[8] in order to determine whether the use of a helical undulator can produce a polarised positron beam of sufficient quality. The flux and polarisation of the undulator photons and the spectrum and polarisation of the produced positrons will be measured and compared to simulations in order to validate the simulation tools used for physics of polarised pair production in matter for the first time.

Once longitudinal beam polarisation is achieved, transversely polarised beams can be produced for almost free by using spin rotators to rotate the spin axis. Spin rotators work almost 100% efficient and the same degree of polarisation can be used for transversely polarised beams than for longitudinally polarised beams.

A Polarimeter for TESLA

One very interesting feature of TESLA is the ability to produce electron and positron beams with a high degree of longitudinal polarisation. In order to use this potential in physics analysis, the polarisation must be measured to a high precision, which will be done by a dedicated polarimeter. Polarised electrons were already used at SLC and polarisation was measured up to 0.5% using Compton scattering [100]. Photons from a laser beam are scattered on the beam electrons and the measured spin asymmetry depends on the polarisation degree.

The same principle will be used for the TESLA Compton Polarimeter as described in more detail in reference [101]. It will be situated 630 m upstream from the interaction region. This far place is suitable as long as the beam and spin directions are precisely aligned with the e^+e^- interaction and detector axis. The main challenge of this device is the construction of a high intensity laser source matching the bunch structure and the energy profile of the TESLA accelerator. At least three different photon energies are needed to measure the polarisation

[8] **S**tanford **L**inear **A**ccelerator **C**enter

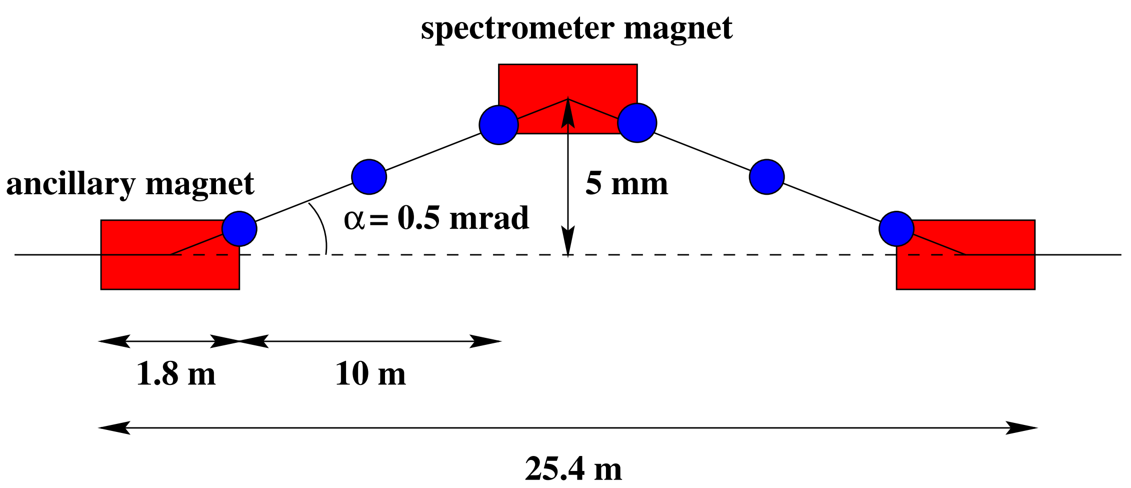

Figure 4.6: Magnetic spectrometer (not to scale). The circles indicate the beam position monitors.

at beam energies of 45, 250 and 400 GeV. The scattered photons will be measured by a segmented gas Cherenkov counter which may be complemented by a photon calorimeter.

The event rate of scattered photons will be around 20 million per second and therefore the expected statistical error will be negligible. On the other hand the systematic error and therefore the total error is estimated to be around 0.5% and will be dominated by beam-beam induced depolarisation.

As a second option a beam polarimeter based on Møller and Bhabha scattering is investigated [102]. With this kind of polarimeter the beam energy can be measured at the same time as the beam polarisation.

A total different approach was already proposed A. Blondel for the case of LEP [103], where the polarisation can be measured from data. For a pure s-channel process, like Z boson production (except Bhabha scattering), the cross-section for given beam polarisation depends only on the unpolarised cross-section and the left-right asymmetry A_{LR} in addition to both polarisations. Measuring the cross-section at all five polarisation combinations (unpolarised, LL, LR, RL, RR) gives five constraints for the simultaneous measurement of cross-section asymmetry and polarisation. In the case of processes with t-chanel contributions, e. g. W-pair production, the formula for the polarised cross-section is not so simple anymore, but the method can still be applied to these kind of reactions.

An Energy Spectrometer for TESLA

As pointed out in section 4.2, the relative energy scale is related to the relative uncertainty in the measurement of particle masses. One important goal of TESLA is the precise study of the Higgs boson, if it exists, and the top quark. For example the aim for the precision on the top mass is 100 MeV which translates into a relative uncertainty of $5 \cdot 10^{-4}$. Therefore the uncertainty on the beam energy measurement should not exceed a few 10^{-4} in order to be not the dominant systematic error source.

Magnetic spectrometers have already been used at LEP [87] and at SLC [104] with a resolution of a few 10^{-4}. The proposed design for TESLA (see figure 4.6) is based on the

LEP spectrometer. The bending of an electron beam in a magnetic field is described by equation (4.4). The main components are the spectrometer magnet and six beam position monitors used for a high precision measurement of the bending angle. Because TESLA is a linear collider two additional ancillary magnets are needed to bend the beam away from the straight section to the spectrometer magnet and back again. The spectrometer has a total length of around 25 m and can be installed somewhere in one of the straight sections of the final focus beam line.

The field of the spectrometer magnet has to be mapped to a resolution of a few 10^{-5}, which was demonstrated for the LEP spectrometer magnet, and the spatial resolution of better than 1 μm is needed for the beam position monitors in order to reach an energy resolution of a few 10^{-4}. Unfortunately the resolution of 1 μm must be achieved over a range of 5 mm, which might be difficult. A possible solution is to mount the beam position monitors on precision translatable stages and move them over the required 5 mm. The position of the beam position monitors can be calibrated using the ballistic path of the beam. To increase the resolution further, better beam position monitors and a better field map is needed.

The bending angle at the spectrometer magnet is around 1.6 mrad for a beam energy of 250 GeV and decreases to 1 mrad at 400 GeV beam energy. A higher magnetic field would give a bigger bending angle and would increase the relative resolution of the beam position monitors but lead also to an increase in synchrotron radiation, which has a negative effect on the beam emittance. At a beam energy of 250 GeV the emittance grow $\Delta\epsilon_x/\epsilon_x$ of such a device is negligible but already at 400 GeV it is 3.5%.

Already at LEP a beam spectrometer using Møller or Bhabha scattering was proposed [105] but was never build. Intensive simulations showed that such a device might reach a relative resolution of 10^{-5}. For TESLA a second energy spectrometer is proposed based on this principle to reach an energy resolution $\Delta E/E$ of a few 10^{-5}, which is needed for example for high precision measurements at the Z resonance.

4.4 General Remarks to Detectors

The design of a detector for high-energy particle physics is driven by the physics which should be investigated. A multi-purpose detector needs a few specialised subdetectors for measuring certain aspects of a particle. The tracker system inside a magnetic field measures the momentum of charged tracks very precisely and allows a charge measurement. The calorimeter system measures the energy of all particles and helps to distinguish between charged and neutral particles. An additional subdetector at the outermost layer of the detector can identify muons because of their minimal ionising character. Further particle identification is important for many physics processes. For example the Higgs boson decays dominantly into a $\mathrm{b\bar{b}}$ pair at LEP 2 energies and a silicon micro-vertex detector can help to find secondary vertices, which are typical of b decays. For searches for physics beyond the Standard Model including invisible particles, the detector should cover as much as possible of the complete solid angle and forward detectors are needed to cover the region close to the beam pipe.

Another important aspect of the detector design is the technology which is available. At the beginning of LEP micro-vertex detectors based on silicon detectors were a novel technology. For example, the ALEPH experiment started with a silicon micro-vertex prototype, which was only used for tests and not for physics. In 1991 a full functioning silicon micro-vertex detector was installed, after the technology was understood better. On the one hand this technology was new and difficult to handle, on the other hand the LEP beam pipe was not small enough to give sufficient space for a detector installation. Now the technology of silicon detectors is very well understood and widely used. The TESLA silicon micro-vertex detector will be five layered and start at a radius of 1.5 cm. With a very ambitious resolution of $\sim 1\,\mu$m it will not only be possible to tag b-quarks but also c-quarks, which was less efficient at LEP.

The following sections describe the past OPAL and the future TESLA detector and how they tackle the mentioned demands.

4.5 The OPAL Detector

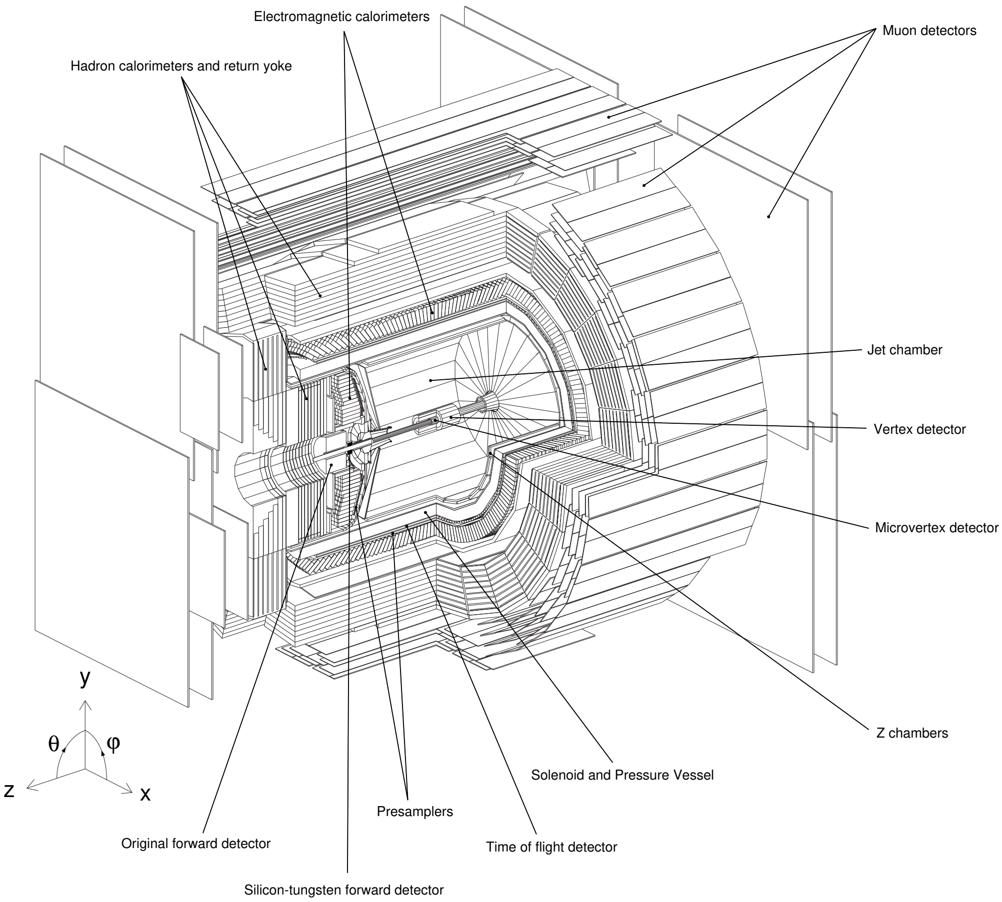

Figure 4.7: General layout of the OPAL detector.

One of the four detectors at LEP was OPAL[9]. It was a multi-purpose detector with a coverage of almost 4π. The general layout of the OPAL detector is shown in figure 4.7, where the right-handed coordinate system is indicated in the lower left corner. It is defined such

[9]**O**mni **P**urpose **A**pparatus at **L**EP

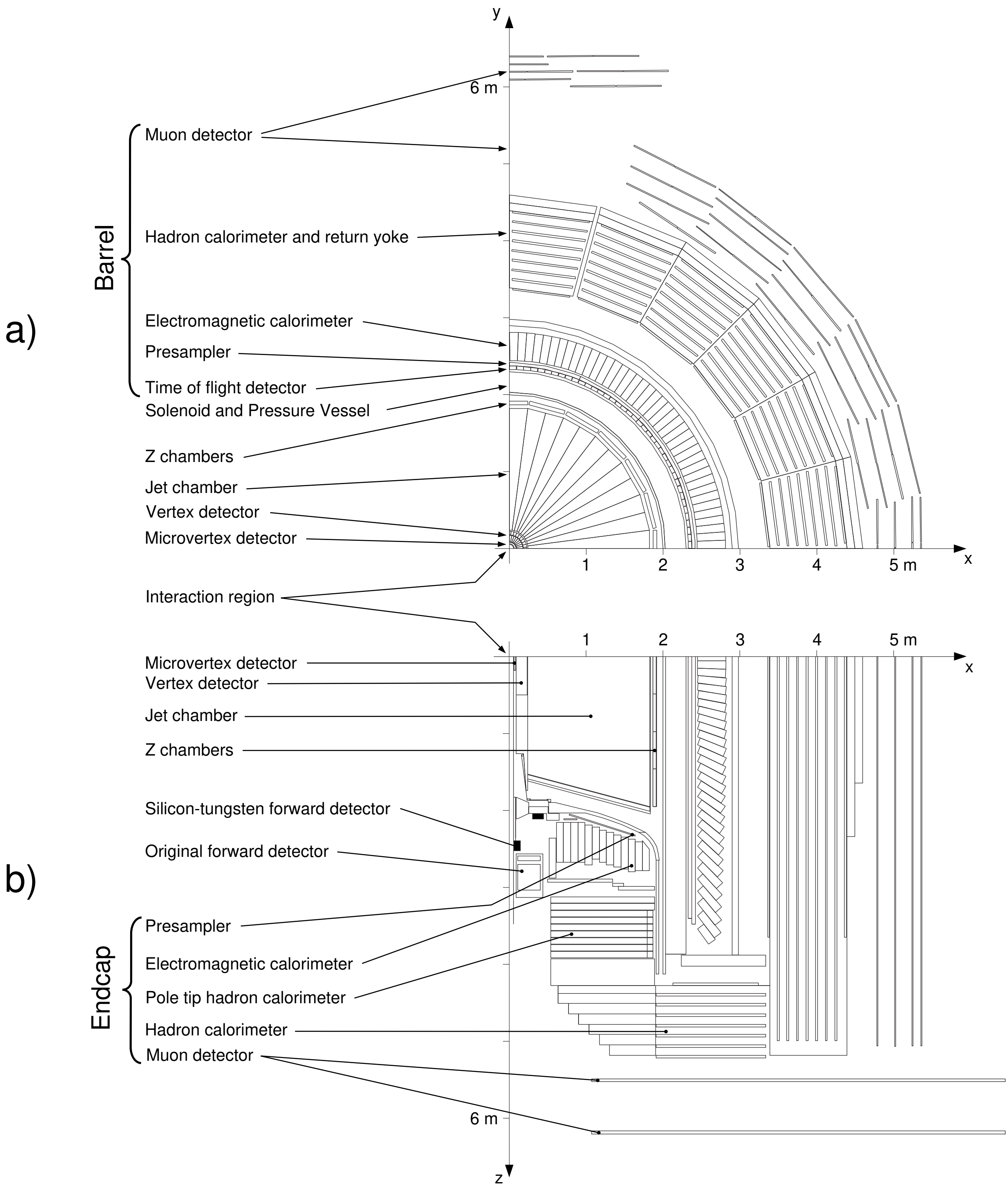

Figure 4.8: Cross section of a quadrant of the detector (a) perpendicular to the LEP beam axis, and (b) parallel to the beam axis.

that the x-axis points towards the centre of the LEP ring, the y-axis upwards and the z-axis in the direction of the electron beam. Because both electron and positron beams have the same energy, the centre-of-mass system is at rest and no preferred direction exists, except the z-axis. Therefore, the detector has a cylindrical symmetry along the z-axis and the polar angle θ and the azimuthal angle ϕ are defined with respect to the z-axis and x-axis, respectively. Figure 4.8 shows cross sections of the detector parallel and perpendicular to the beam axis.

The OPAL detector [106] was build like almost all high-energy detectors at collision experiments. Around the nominal interaction point, a precise tracker system was set up followed by a calorimeter system to measure the particles energies. The detector was completed by a muon system and specialised subdetectors in the forward region. In the case of OPAL the tracking system was enclosed inside a solenoid, which provided a uniform magnetic field of 0.435 T.

For the analysis of the recorded data, it is essential to understand the structure and performance of all detector components. The `Geant3` program package [107] was used to describe and simulate the physical response of the detector in great detail [108].

The Tracking System

The tracking system should allow one to measure the momentum and charge of charged particles with a high accuracy and give the possibility to do particle identification. For this purpose it consisted of five different subdetectors: The silicon micro-vertex detector, the central vertex chamber, the central jet chamber, the z-chambers and the time-of-flight system.

The *silicon micro-vertex detector* [109] was mounted between the beryllium beam pipe and the inner wall of the pressure vessel, which contained the central tracking system. It was installed in 1991, two years after the start of LEP, when it was found out, that the low beam backgrounds permitted the use of a smaller diameter beam pipe. The main purpose was the reconstruction of primary and secondary vertices. In its final assembly stage in 1995 it consisted of two concentric layers of silicon strip detectors with an inner layer at radius of 6.1 cm and an outer layer at radius 7.5 cm, consisting of 12 and 15 ladders. The length of the ladders was 18.3 cm giving an angular coverage of $|\cos\theta| < 0.93$ in the first layer and $|\cos\theta| < 0.89$ in the second one. The spatial resolution was 5 μm in $r\phi$ and 13 μm in z giving an impact parameter resolution of $\sigma(d_0) = 18\mu$m and $\sigma(z_0) = 24\,\mu$m.

Before the installation of the micro-vertex detector, the *vertex chamber* had been the only instrument to measure tracks near the interaction point. Therefore, it was used to improve the momentum resolution and to locate the primary vertex and decay vertices of short-lived particles. The vertex chamber was a cylindrical drift chamber of 1 m length with an inner radius of 8.8 cm and an outer radius of 23.5 cm. The chamber consisted of an inner layer of 36 cells with axial wires and an outer layer of 36 small angle stereo cells. The chamber had a resolution of 55 μm in the $r\phi$ plane and 700 μm in the z direction. The vertex chamber is essential for the extrapolation of tracks out of the central jet chamber to the micro vertex detector.

The *central jet chamber* [110] was designed to combine good space and double hit resolution, essential for the efficient recording of jet-like events, with the possibility of particle identification, within a solid angle of almost 4π. The sensitive volume of the chamber was a cylindrical volume with a length of 4 m at radii of 25 cm to 185 cm. The volume was divided into 24 sectors and separated by cathode planes. The planes are realised by potential wires strung between the endplates. The anode plane in the middle of each sector was build by potential wires and 159 sense wires, which were spaced equidistantly in the radial direction and were staggered by 100 μm up and down out of the plane. The maximum drift distance varies from 3 cm for the innermost sense wire to 25 cm at the outermost wire.

In the range $43° < \theta < 137°$ 159 points were measured along each track, and at least 8 points on a track are obtained over a solid angle of 98% of 4π. For each point, true three-dimensional coordinates (r, ϕ, z) were determined from the wire position, the drift time, and from a charge division measurement. The ratio of these charges determines z, and their sum was used to calculate the energy loss $\mathrm{d}E/\mathrm{d}x$ of the particle. The chamber gas was a mixture of argon (88.2%), methane (9.8%) and isobutane (2.0%) at a pressure of 4 bar.

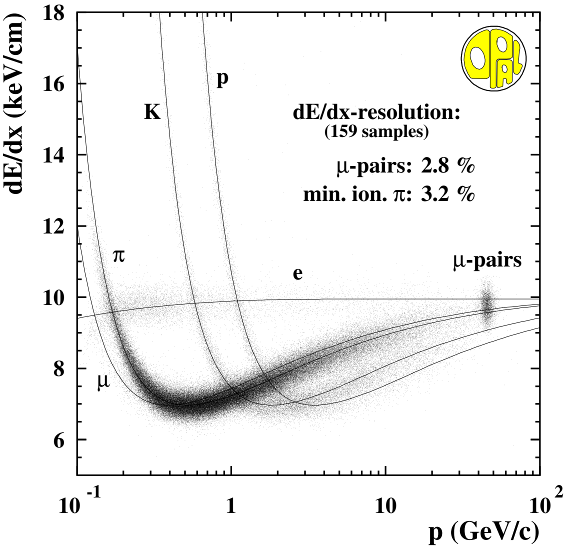

Figure 4.9: Measured energy loss in the jet chamber as a function of momentum for tracks in multihadronic and $e^+e^- \to \mu^+\mu^-$ events.

The average resolution in the $r\phi$ direction was 135 μm at the mean drift distance of 7 cm. The average resolution in z was 6 cm. With 159 points the relative uncertainty on the measurement of the specific energy loss was 3.1% for dimuons and 3.8% for minimum ionising pions in jets [111]. The energy loss is shown in figure 4.9 for tracks in multihadronic and $e^+e^- \to \mu^+\mu^-$ events and was used in conjunction with the measured momentum to identify particles. The average transverse momentum resolution was measured to be:

$$\frac{\sigma_{p_t}}{p_t} = \sqrt{(0.02)^2 + (0.0015 \cdot p_t)^2}, \tag{4.8}$$

where p_t in GeV/c is the momentum component transverse to the beam axis.

The *z-chambers* were designed to make precision measurements of the z coordinates of charged particles as they leave the jet chamber. This improves both the polar angle and invariant mass resolutions. They consisted of 24 planar drift chambers, 4 m long, 50 cm wide and 59 mm thick using the same gas and pressure as the jet chamber. They were located outside the jet chamber. Each chamber was divided into 8 $50 \times 50\,\mathrm{cm}^2$ cells with an intrinsic resolution of 100 – 200 μm. The absolute resolution in the z direction is determined by the precision of the survey, and was around 300 μm. The $r\phi$ resolution was measured to be around 15 mm.

The *time-of-flight system* covers the barrel region $|\cos\theta| < 0.82$ and was installed in front of the calorimeter system at radius 2.36 m. It generated trigger signals and, by measuring the time of flight from the interaction region, allowed charged particle identification in the range of 0.6 – 2.5 GeV. It also aided in the rejection of cosmic muons. It consisted of 160 scintillator counters of length 6.48 m with an intrinsic timing resolution of 280 – 350 ps depending on the z position. The detector resolution was measured using $e^+e^- \rightarrow \mu^+\mu^-$ events and the stand-alone resolution in z was 7.5 cm. The measured flight time for muons compared to their expected flight time had a resolution of 460 ps.

Analogous to the barrel region the endcap region was equipped with a scintillator counter in 1996 providing time-of-flight information for the region $0.82 < |\cos\theta| < 0.95$ [112].

The Calorimeter System

The calorimeter system was located outside the pressure vessel, the solenoid and the time-of-flight counters. The total material in front of the calorimeter adds up to approximately two electromagnetic radiation lengths. Usually the electromagnetic showers were initiated before reaching the calorimeters.

The *presampler* was installed outside the solenoid, between the time-of-flight counter and the electromagnetic calorimeter, in order to measure the size of the shower. This information was used to estimate the amount of energy deposited before entering the calorimeters and to correct for this deficit. The presampler in the barrel consisted of 3 cm thick streamer tubes while drift chambers were used for the endcap. The typical shower size was 4 – 6 mm in the barrel and 2 – 4 mm in the endcap. The energy deposition was derived from the number of particles measured in the shower.

The *electromagnetic calorimeter* detected and measured the energies and position of electrons, positrons and photons ranging from tens of MeV to 100 GeV. In addition, it provided π^0-γ discrimination. It was a total absorption calorimeter and built of 9440 lead glass blocks in the barrel and 1132 blocks in each endcap. In the barrel blocks of size $10 \times 10 \times 37\,\mathrm{cm}^3$ corresponding to 24.6 electromagnetic radiation lengths were located at a radius of 2.46 m giving an angular coverage of $|\cos\theta| < 0.82$. The longitudinal axis of the lead glass blocks point towards the interaction region to minimise the probability of a particle traversing more than one block. However, the blocks were tilted slightly from a perfectly pointing geometry to prevent neutral particles from escaping through gaps between the blocks. They were pointing to different z positions (56 – 158 mm) depending on the position of the block. In addition, each block was tilted by 0.6° such that the gaps pointed away from the beam by 3 cm. For this geometry blocks of 16 different shapes were needed. Because of geometrical constraints the blocks in the endcap were of three different sizes (38, 42 and 52 cm) and arranged over the endcap to give a total depth of at least 20.5 radiation lengths. The blocks were aligned parallel to the beam with an angular coverage of $0.81 < |\cos\theta| < 0.98$.

The achieved energy resolution was

$$\frac{\sigma_E}{E} = 0.2\% + \frac{6.3\%}{\sqrt{E(\mathrm{GeV})}} \tag{4.9}$$

in the barrel region and

$$\frac{\sigma_E}{E} = \frac{5\%}{\sqrt{E(\mathrm{GeV})}} \tag{4.10}$$

in the endcap region for a single particle, combining information from the presampler and the electromagnetic calorimeter. The intrinsic spatial resolution was around 11 mm.

The *hadron calorimeter* measured the energy of hadrons emerging from the electromagnetic calorimeter and assisted in the identification of muons. The iron of the return yoke provided four or more hadronic interaction lengths of absorber over a solid angle of 97% of 4π. The yoke was segmented into layers, with planes of detectors between each layer, and formed a cylindrical sampling calorimeter about 1 m thick. The barrel part consisted of 9 layers of chambers, alternating with 8 iron slabs, and spanned radii from 3.39 m to 4.39 m covering an angle of $|\cos\theta| < 0.81$. This range was extended up to $|\cos\theta| < 0.91$ by the endcap part, consisting of 8 layers of chambers, alternated with the same iron slabs of 100 mm thickness. The gaps of 25 and 35 mm, respectively, were instrumented with streamer tubes. Finally, the pole tip part had an angular coverage of $0.91 < |\cos\theta| < 0.99$ and consisted of 10 layers. The gaps of 10 mm size were instrumented by multiwire chambers, alternated with iron slabs of 80 mm thickness.

The energy resolution is

$$\frac{\sigma_E}{E} = \frac{120\%}{\sqrt{E(\mathrm{GeV})}} \tag{4.11}$$

for all three hadron calorimeter parts and a single particle. Since there was a high probability of hadronic interactions being initiated in the 2.2 interaction lengths of material before the hadron calorimeter, the overall hadronic energy had to be determined by combining signals from the electromagnetic and hadron calorimeters. A good estimate of the energies of a hadron was given by weighted sum, $E_{\mathrm{HCAL}} + RE_{\mathrm{ECAL}}$, where E_{HCAL} is the energy recorded in the hadronic calorimeter, assuming the particle is a hadron, and E_{ECAL} is the energy from the electromagnetic calorimeter, assuming the particle is an electron. R is the e/π ratio, the relative response of the electromagnetic calorimeter to electrons and pions, decreasing from 3 to 2 in an energy range of 6 – 20 GeV.

The Muon System

The last detector layer was formed by the *muon detector*, which was designed to identify muons, in particular in the presence of a background of hadrons. 93% of the full solid angle was covered by this detector. The total amount of material in front of the muon chambers were at least 7 interaction lengths for pions reducing the probability of a pion to not interacting before to less than 0.001. Ignoring the complexity of hadrons in jets, the efficiency for detecting isolated muons above 3 GeV and within the 93% solid angle was essentially 100%. The probability that an isolated pion of 5 GeV was misidentified as a muon was less than 1%.

The barrel part of the muon chambers consisted of drift chambers, 1.2 m wide and 9 cm deep, where the wires were parallel to the z direction and staggered by typically 50 μm in the ϕ direction. Four layers covered $|\cos\theta| < 0.68$ and one or more layers covered $|\cos\theta| < 0.72$. The achieved spatial resolution was better than 1.5 mm in the ϕ and 2mm in the z direction. The endcap part was instrumented with four layers of limited streamer tubes covering the range from 0.67 to 0.98 in $|\cos\theta|$. Here, the spatial resolution of 1 mm in the ϕ and 3 mm in the z direction was only slightly different from the barrel part.

The Forward Detectors

The hermeticity of the OPAL detector was improved by a set of specialised forward detectors close to the beam axis. An important task was the luminosity measurement using small angle Bhabha-scattering.

The *forward detector* was build to measure the luminosity using Bhabha scattering, and also to tag electrons from $\gamma\gamma$ interactions. It consisted of an array of components: drift chambers, scintillators and a lead-scintillator sampling calorimeter with an angular acceptance of $47\,\mathrm{mrad} < \theta < 120\,\mathrm{mrad}$, which were installed between 2 and 3 m from the interaction point. At a distance of 7.85 m a further lead-scintillator sampling calorimeter was installed with an angular coverage of $5\,\mathrm{mrad} < \theta < 10\,\mathrm{mrad}$.

The *silicon tungsten calorimeter* [113] was a sampling calorimeter designed to detect low angle Bhabha scattering events in order to improve the luminosity measurement. Two calorimeters were installed in 1993 each at ± 2.4 m in the z direction from the interaction point with an angular acceptance of 25 mrad to 59 mrad. In 1996, additional shields were installed to protect the central detector against an increase in beam background reducing the acceptance to $33\,\mathrm{mrad} < \theta < 59\,\mathrm{mrad}$. Each calorimeter consisted of 19 layers of silicon detectors and 18 layers of tungsten. The high granularity and the lower angular acceptance compared to the forward detector improved the accuracy of the luminosity measurement to a relative error of 0.15%.

The *MIP plug* [112] was installed in 1996 to supplement the poletip calorimeter. It extended the instrumented region from 200 mrad down to 43 mrad. The main purpose of this device was to improve background rejection and supply timing information in order to simplify the unambiguous determination of the collision time. This required a time resolution better than 5 ns. The detector consisted of 4 layers of 1 cm thick plastic scintillators. The time resolution of 3 ns was reached and the efficiency exceeded 99%.

The *gamma catcher* filled the hole between the forward detector and the electromagnetic calorimeter. It was a ring of lead-scintillator sandwich modules, 7 radiation lengths thick. It was sensitive to electrons and photons above 2 GeV, giving a veto on background events, e. g. to the neutrino counting channel $\mathrm{e^+e^-} \to \mathrm{Z}\gamma$, with $\mathrm{Z} \to \nu\bar{\nu}$.

4.6 A Detector for TESLA

The reactions which are accessible at a centre-of-mass energy of 500 GeV and above guide the design of the TESLA detector. First, we discus how design goals of a detector can be derived from precision requirements on future measurements and then the future TESLA detector is presented in some more detail.

The study of the Higgs boson can be used to formulate requirements for a detector. The main production process for a light Higgs boson is the reaction $\mathrm{e^+e^-} \to \mathrm{ZH}$, where the Higgs boson is radiated off a virtual Z boson. From the recoil of the Z boson the Higgs mass can be deduced, independent of the Higgs decay. To maximise the sensitivity to the Higgs mass the Z bosons have to be reconstructed as precisely as possible. A momentum resolution of $\delta(1/p_t) < 5 \times 10^{-5}\,(\mathrm{GeV}/c)^{-1}$ is needed to be limited by the natural width of the Z boson. Another example is the measurement of the branching ratios of the Higgs boson into quarks.

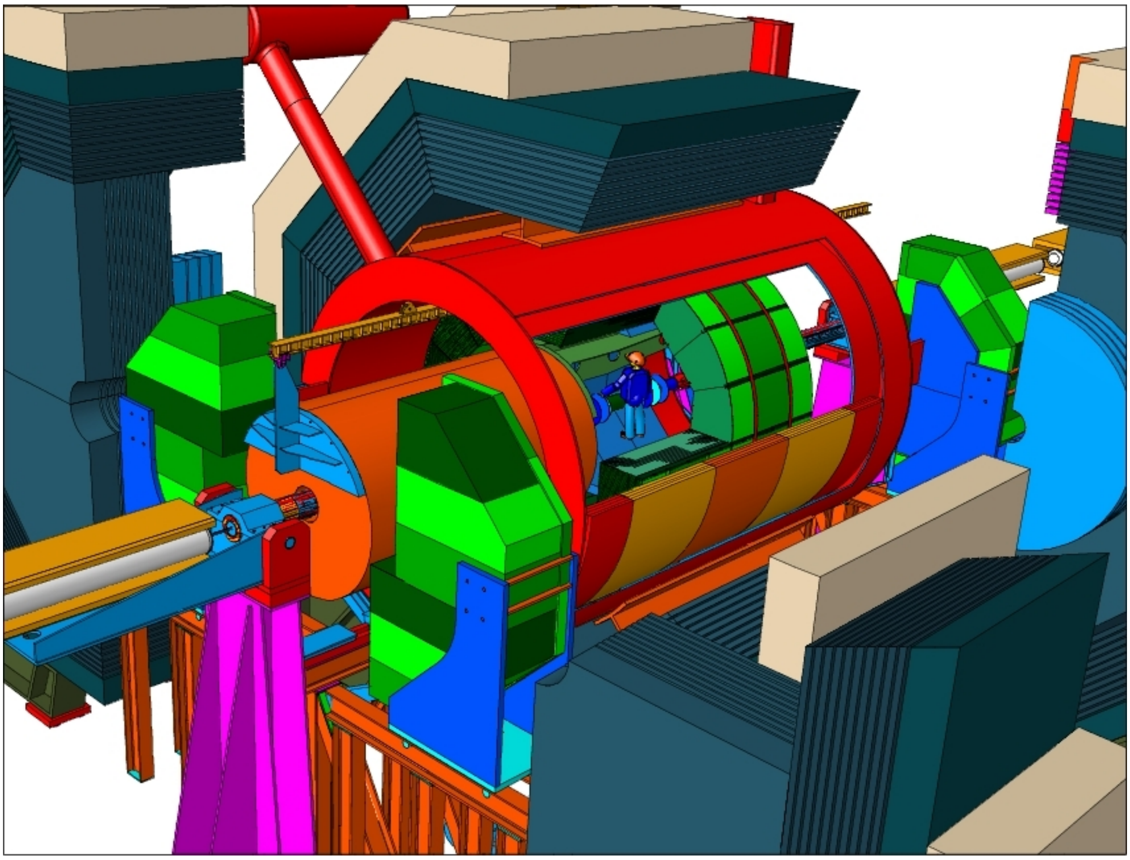

Figure 4.10: A three-dimensional view of the proposed TESLA detector.

A precise measurement for charm and bottom quarks can help to distinguish the Standard Model from supersymmetric models and other new physics. This requires a good separation of charm and bottom quarks, which can be achieved with an excellent vertex detector. The ultimate measurement to pin down the Higgs mechanism is the investigation of the Higgs self-coupling. The dominant final state consists of one Z boson and two Higgs bosons, decaying dominantly into b quarks giving a six-parton final state. The same occupancy can be observed in top-pair production and a very good jet energy resolution is needed in order to reconstruct the top quarks efficiently. Also searches for particles from physics beyond the Standard Model are very demanding. Many theories predict particles which are hard to detect or even worse escape detection at all, like neutralinos in supersymmetric models. This demands that the detector covers as much as possible of the solid angle in order to allow for an accurate missing energy measurement. The high luminosity of a future linear collider makes many precision measurements possible. For many reactions the number of expected events will be high enough to give a significant small statistical error. All the more a precise understanding of the detector is essential in order to limit systematic uncertainties from it.

The requirements from these physical questions can be combined into the following list:

- An excellent momentum resolution is required.
- The vertex detector should be capable to separate charm and bottom quarks.

- The track finding should work very efficiently even for events with high track densities.
- The tracking and calorimeter system should provide an optimum hermeticity.
- An excellent jet energy resolution is mandatory for multi-parton final states.

A three-dimensional cut-away of the proposed TESLA detector is shown in figure 4.10. The design goals and a detailed description of the TESLA detector can be found in reference [114]. The proposal for a detector is not final yet and for various detector components a number of alternative implementations based on different technologies exist. In the next sections we outline the baseline detector design without describing all proposed alternatives.

The Tracking System

The TESLA system consists of a series of single tracking devices as shown in figure 4.11. Close to the beam pipe a silicon micro-vertex (VTX) detector is located. The silicon intermediate tracker (SIT) closes the gap between the vertex detector and the large volume time projection chamber (TPC). The forward region is covered with the forward tracking disks (FTD) as an extension of the vertex detector and with the forward chambers (FCH), located behind the TPC endcap.

A very precise tracking device near the interaction region is mandatory for measuring secondary vertices, which is needed to tag b and c-quarks. In the baseline layout, the *vertex detector* will have 5 layers, starting at a radius of 1.5 cm and reaching out to 6 cm. The general performance goal is to reach a point-measurement resolution of $\sim 1\,\mu$m. Four different pixel technologies are under discussion: CCD [115], CMOS [116], DEPFET [117] and a hybrid option [118].

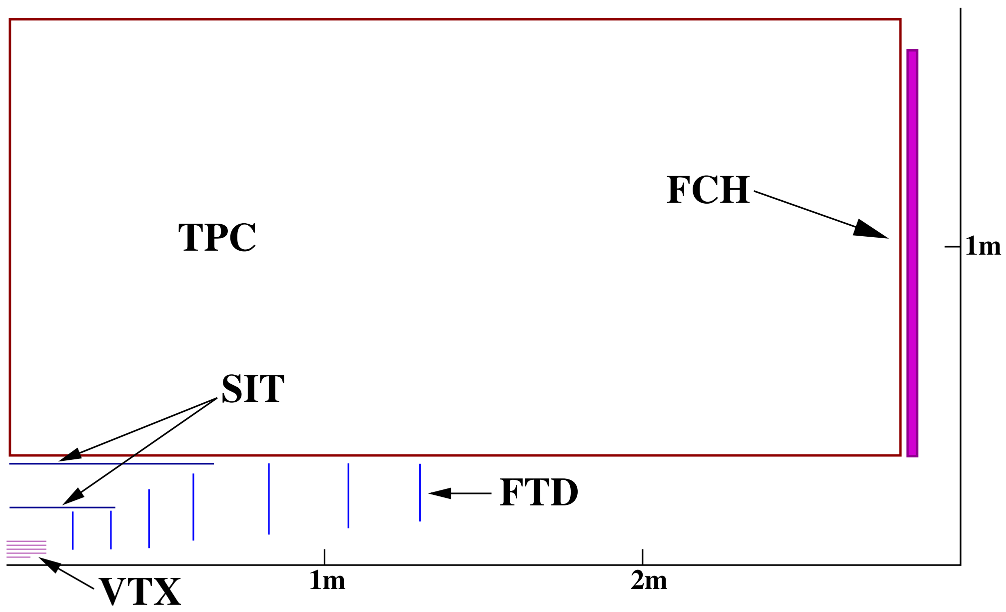

Figure 4.11: General layout of the TESLA tracking system. See the text for an explanation of the tracking devices.

In order to improve the overall momentum resolution and to connect the vertex detector with the TPC, it is foreseen to install a two-layered *silicon intermediate detector* in the gap between the vertex detector and the TPC. The first cylinder is located at a radius of 16 cm and the second at 30 cm. For the goal of improving the momentum resolution, a spatial resolution of 10 μm in $r\phi$ and of 50 μm in z is sufficient [119].

In terms of momentum resolution the seven *forward tracking disks* will play the same role as the SIT. The first three disks, starting from the interaction region, will be pixel detectors, while the other four will be implemented as silicon strip detectors. The required resolution is 25 μm.

For the central tracking device a *time projection chamber* is proposed. A TPC combines many advantages. A minimum amount of material, many three-dimensional space points and particle identification via the measurement of the specific energy loss $\mathrm{d}E/\mathrm{d}x$. The mandatory performance goals are $\delta(1/p_t) < 2 \times 10^{-4}\,(\mathrm{GeV}/c)^{-1}$ (TPC only) and $\sigma(\mathrm{d}E/\mathrm{d}x) \leq 5\%$. The sensitive volume will have a length of twice 2.5 m, with an inner radius of 36.2 cm and an outer radius of 161.8 cm. The TPC is designed for a continuous operation during one train (1 ms) and will hold up to 150 events in its volume. Extensive simulations showed that the proposed TPC alone already reaches a momentum resolution of $\delta(1/p_t) = 1.5 \times 10^{-4}\,(\mathrm{GeV}/c)^{-1}$ [120].

To improve the momentum resolution in the region in $|\cos\theta|$ between 0.87 and 0.99, straw tubes will be installed behind the TPC endplate as *forward chambers*. They will give another precise track measurement and therefore allow for a compensation of the degrading track reconstruction performance in the forward region, due to multiple scattering in the endplates.

For a high efficient track finding and a very good momentum resolution all tracking devices must be used. The interplay of them, their performance and efficiency was extensively studied and the overall efficiency was found to be above 98% [121].

The Calorimeter System

The tracking system is surrounded by a calorimeter system, consisting of an electro-magnetic and a hadronic calorimeter, as show in figure 4.12. The fact that both the tracking and the calorimeter system are located inside the magnetic field is a great advantage over older detector concepts. The calorimeter performance will not be distorted by dead material in front of it. On the other hand this increases the demands on the hardware used.

For the *electro-magnetic calorimeter* (ECAL) two different options are proposed. One scenario is based on tungsten absorbers and silicon diode pads [122]. The high granularity of 32 million cells would provide an excellent energy and spatial resolution. It would be possible to do tracking with such a device in the sense that the direction of a shower can be measured and the path of minimum ionising particles can be reconstructed. The alternative option is a shashlik calorimeter [123]. The scintillation light from plastic scintillators is read out via wavelength shifting fibres. This kind of calorimeter has the advantages of lower cost and easier assembly and operation. Both options should be capable to meet the energy resolution requirement of

$$\frac{\sigma_E}{E} \leq 1\% + \frac{10\%}{\sqrt{E(\mathrm{GeV})}}. \tag{4.12}$$

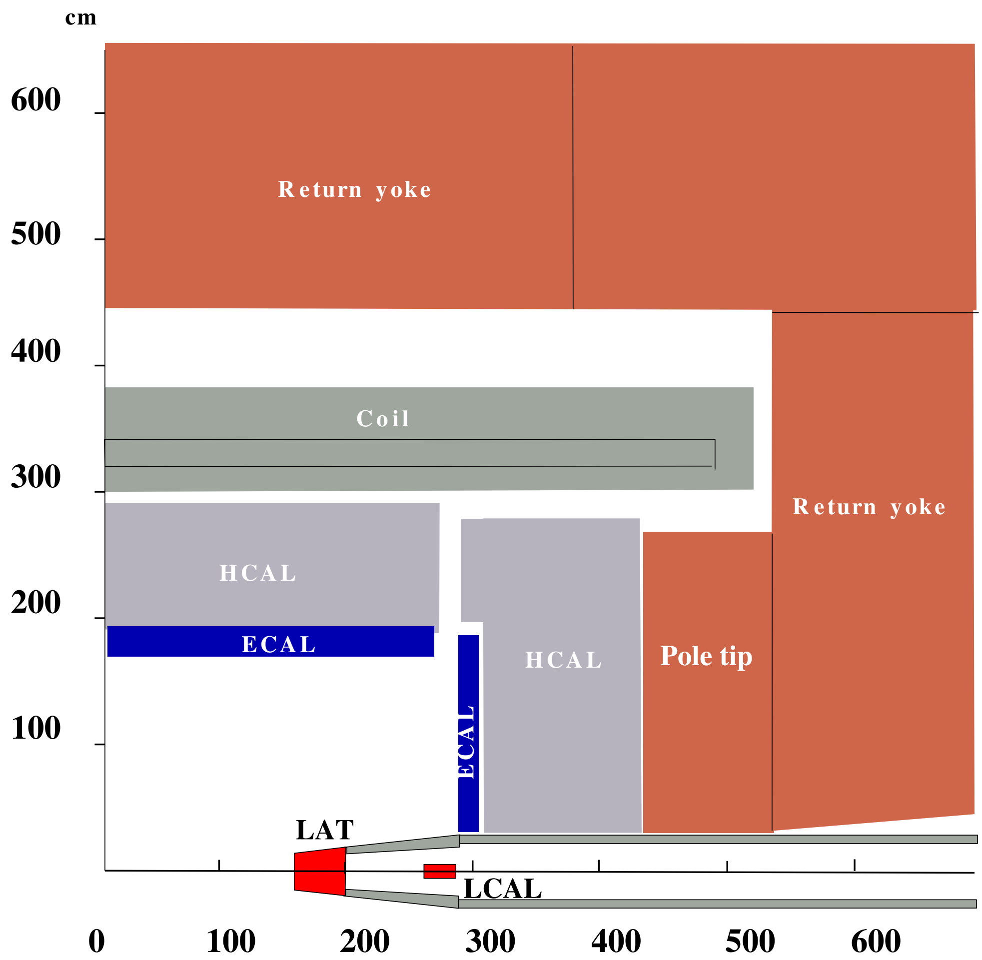

Figure 4.12: General layout of the TESLA calorimeter system. See the text for an explanation of the calorimeter devices.

Also for the *hadronic calorimeter* two options are discussed. The *tile hadron calorimeter* option [124] is constructed as a sampling calorimeter consisting of alternating layers of stainless steel and scintillator as active material. For the *digital calorimeter* simply counting the fired cells would be sufficient enough to reconstruct the hadronic shower energy, if the readout cells in the active layers are small enough. It will have a slightly worse energy resolution but has the advantage of lower cost compared to a sampling calorimeter. A cell size of $1\,\mathrm{cm}^2$ is proposed. As in the sampling calorimeter case, stainless steel would be the preferred absorber material. A wide range of technologies can be used for the active layers: resistive plate chambers, wire chambers operated in limited Geiger mode or thin wire chambers. Independent of the final technology choice a large granularity is needed for the compensation by software weighting, for the identification and separation of neutral hadrons in jets. The energy resolution for single hadrons was found in simulations to be

$$\frac{\sigma_E}{E} = 3\% + \frac{35\%}{\sqrt{E(\mathrm{GeV})}}. \tag{4.13}$$

The Muon Detector and Magnet

In order to reach the excellent momentum resolution of $\delta(1/p_t) < 5 \times 10^{-5}\,\mathrm{GeV}^{-1}$ the magnetic field must be high. The TESLA *magnet* has to provide a magnetic field of at least 3 T and its current design, based on the CMS magnet [125], allows 4 T. Both the tracking and the calorimeter system will be located inside the magnet while the iron joke is used to house the *muon detector*. This outermost detector layer is used to identify muons and to catch tails of hadronic showers leaking out of the HCAL. It is proposed to implement the muon detector using resistive plate chambers (RPC) [126].

The Forward Detectors

As pointed out before, the hermeticity of the detector is vitally important for event topologies with missing energy as in searches for new particles. The detector described so far has already an excellent coverage of $|\cos\theta| > 120\,\mathrm{mrad}$. In order to narrow the remaining gap a set of specialised forward detectors are installed in the mask region. Up to here, radiation hardness of the detector components is not an issue. The background rate is low in all components except for those in the forward region. In the collision of two highly focused beams strong electromagnetic fields are produced which lead to the production of beamstrahlung. While the photons themselves disappear in the beam pipe they are source of background from secondary effects (see figure 4.5). The main effect is e^+e^- pairs, which traverse the forward region, while hadronic background and neutrons are not so important.

The *low angle tagger* (LAT) is foreseen to be build as a sampling calorimeter with tungsten as absorber and silicon as active material and will extend the electro-magnetic calorimeter down to a polar angle of 27.5 mrad. It will be used mainly for electron detection in order to tag low-angle Bhabha and $\gamma\gamma$ events.

At even smaller polar angles of 28 down to 4.6 mrad the *luminosity calorimeter* (LCAL) is located. It will mainly serve as a fast luminosity monitor and will measure the amount of beam-induced background. The measured signal is very sensitive to luminosity variations within one train and will be used to tune the beam on a very short timescale of a few bunches. To accomplish this task, a statistical error on the energy measurement of less than 1% and a response time of 30-50 ns will be needed [127]. The LCAL will be build as a sampling calorimeter using either silicon or diamond sensors for the active layers. Because of the high rate of e^+e^--pair background, radiation hard technology has to be chosen. In the region of the LCAL close to the beam, electromagnetic doses of the order of 1 MGy per year are expected and LCAL should be able to sustain a dose of $\mathcal{O}(\infty\prime)$ MGy to operate several years.

Simulation Tools

The simulation of the accelerator and detector is essential for testing and improving the design of these two parts. For the proposed TESLA detector two detector simulations exist. The `Brahms` program [128] is based on the `Geant` toolkit and implements a realistic detector simulation and event reconstruction. The `Simdet` program [129] is a fast detector simulation with an idealised event reconstruction. The fast detector simulation is tuned on the `Brahms` output and smears the resolution for each subdetector separately. The output of the fast event simulation is usually sufficient for physics studies unless very detailed detector information is needed.

Chapter 5

Measurement of Triple Gauge Couplings at LEP

In the following sections the measurement of triple gauge boson couplings (TGCs) using the process $e^+e^- \to W^+W^- \to q\bar{q}'q''\bar{q}'''$ with data collected with the OPAL detector is described in full detail. After discussing the analysed data set and the used Monte Carlo samples the selection and reconstruction of hadronic W-pairs is described. As an example of observables sensitive to anomalous couplings, the five W angles are shown but the method of optimal observables is used for the extraction of the triple gauge boson couplings. From the total 14 anomalous couplings introduced in section 2.2 we consider only the C and P conserving couplings $\Delta\kappa_\gamma$, Δg_1^Z, λ and g_5^Z with the relations (2.18) motivated by $\mathsf{SU(2)}_L \times \mathsf{U(1)}_Y$ invariance. A χ^2-fit is performed including the effects of many systematic errors and the results are shown for one and more free parameters.

In chapter 6 this measurement is combined with the other two W-pair final states and the measurement of the total cross-section. The combination of results from all four LEP experiments is done using not only W-pairs but also single-W and single-γ production. These results are then compared to the measurements carried out by experiments at the Tevatron.

5.1 Data and Monte Carlo samples

The analysed data were collected with the OPAL detector during 1997-2000 around eight different centre-of-mass energies ranging from 183 GeV up to 209 GeV. The integrated luminosity at each energy is evaluated using small angle Bhabha scattering events observed in the silicon tungsten forward calorimeter. The energy range and the luminosity weighted average values of the centre-of-mass energies and the corresponding luminosities for each energy point are given in table 5.1. In total, an integrated luminosity of 678.5 pb^{-1} is analysed.

The KandY Monte Carlo generator is used to simulate the W-pair signal. All four-fermion final states which involve diagrams with triple gauge vertices are defined as signal and are sometimes referred to as TGC-depended four-fermion final states. Using four-fermion final states, which involve W-boson propagators, give the same signal definition. For each centre-of-mass energy, samples of 500 000 events are generated with SM couplings and are used as reference samples in the TGC analysis. The Excalibur Monte Carlo generator is used to generate samples of 50 000 or 100 000 events with anomalous TGCs which are used

Energy	Range	$<\sqrt{s}>$	$\mathcal{L}$
183	180.0 - 188.0 GeV	182.7 GeV	57.4 pb^{-1}
189	188.0 - 190.0 GeV	188.6 GeV	183.0 pb^{-1}
192	190.0 - 194.0 GeV	191.6 GeV	29.3 pb^{-1}
196	194.0 - 198.0 GeV	195.5 GeV	76.4 pb^{-1}
200	198.0 - 201.0 GeV	199.5 GeV	76.6 pb^{-1}
202	201.0 - 202.5 GeV	201.6 GeV	37.7 pb^{-1}
205	202.5 - 205.5 GeV	204.9 GeV	81.6 pb^{-1}
207	205.5 - 209.0 GeV	206.6 GeV	136.5 pb^{-1}
all	180.0 - 209.0 GeV		678.5 pb^{-1}

Table 5.1: The energy binning used by the W^+W^- selection. The energy range, the mean luminosity weighted centre-of-mass energy $\sqrt{s}$ and the integrated luminosity $\mathcal{L}$ are listed for the single energies and all combined.

to cross-check the TGC extraction method. Although EXCALIBUR includes less complete $\mathcal{O}(\alpha)$ radiative effects, the difference compared to the KANDY samples is expected to be small but not negligible. For further studies of pure W-pair properties samples of 200 000 events were generated with SM couplings with KORALW using CC03 diagrams only.

Background sources to the W-pair signal are four-fermion final states, such as $q\overline{q}\ell^+\ell^-$, which are produced only by diagrams that do not involve the triple gauge vertex, two-fermion final states and two-photon processes. The four-fermion background is generated using KORALW1.42 and `grc4f`. As an alternative for systematic studies KORALW is replaced by EXCALIBUR. Two-fermion final states are generated using KK2F [130,131]. For systematic studies KORALZ [132] is used for $e^+e^- \rightarrow \mu^+\mu^-$, $e^+e^- \rightarrow \tau^+\tau^-$ and $e^+e^- \rightarrow \nu\bar{\nu}$ and BHWIDE [133] for $e^+e^- \rightarrow e^+e^-$. Backgrounds from two-photon interactions are evaluated using HERWIG [68], the Vermaseren [134] and BDK [135] generators. These backgrounds can be neglected in multi-hadronic final states, as $W^+W^- \rightarrow q\overline{q}q\overline{q}$.

The explicit run numbers of all used Monte Carlo samples are given in table B.1 for the Standard Model processes and in table B.4 for anomalous couplings. All Monte Carlo samples mentioned above are processed by the full OPAL detector simulation program and then reconstructed in the same way as the data.

5.2 $W^+W^- \rightarrow q\overline{q}q\overline{q}$ Cross-Section Selection

The selection of hadronic W^+W^- candidates for the measurement of triple gauge boson couplings starts from the selected $W^+W^- \rightarrow q\overline{q}q\overline{q}$ candidates used in the measurement of the W^+W^- cross-section which can be called preselection for the triple gauge boson coupling measurement.

All events which are classified as hadronic [136] and which have not been selected by either the $W^+W^- \rightarrow \ell^+\nu_\ell\ell'^-\bar{\nu}_{\ell'}$ or $W^+W^- \rightarrow q\overline{q}\ell\bar{\nu}_\ell$ selections are considered as candidates for the $W^+W^- \rightarrow q\overline{q}q\overline{q}$ cross-section selection. In addition, any event which is rejected as four-fermion background in the $W^+W^- \to q\overline{q}\ell\overline{\nu}_\ell$ selection is also rejected.

Tracks and calorimeter clusters are combined into four jets using the Durham $k_\perp$ algorithm [137] and the total momentum and energy of each track and calorimeter cluster is corrected for double-counting of energy [138]. To remove events which are clearly inconsistent with a hadronic W^+W^- decay, candidate events are required to satisfy a set of preselection cuts. The dominant background comes from hadronic two-fermion reactions. Therefore, a high visible energy and invariant mass are required for the the signal. A cut on the most energetic cluster in the electromagnetic calorimeter is applied to reject events with a high-energy photon, which are common in radiative return events. In order to enhance the signal to background separation a likelihood selection is used. The actual set of cuts and likelihood input variables vary slightly for a centre-of-mass energy of 183 GeV [21] and 189 GeV [22, 139] and higher. Both selections are included in the OPAL `WW` package [140][1].

At a centre-of-mass energy of 183 GeV the following preselection cuts are applied, where $\sqrt{s}$ denotes the centre-of-mass energy:

- The ratio, R_{vis}, of the visible energy of the event, E_{vis}, to the centre-of-mass energy, $\sqrt{s}$, must be greater than 0.7.
- The fitted invariant mass of the event, $\sqrt{s'}$, must be greater than $0.75\sqrt{s}$.
- The ratio, R_{max}, of the energy of the most energetic electromagnetic cluster, $E^{max}_{cluster}$, to the centre-of-mass energy, $\sqrt{s}$, must be less than 0.3.
- Each jet is required to contain at least one charged track, but only one jet is allowed to contain exactly one charged track. In radiative return events with at least on high-energy photon, the photon alone often forms a jet.
- The quantity j_{ang} must be greater than $0.05\sqrt{s}$. With the four jets ordered by energy $j_{ang} = E_{low}(1 - c_{12}c_{13}c_{23})$, where $c_{ij} = \cos\theta_{ij}$ is the cosine of the angle between jet i and jet j. E_{low} is the energy of the forth jet with the lowest energy. This quantity is strongly peak towards zero for two-fermion events.
- The logarithm of the QCD matrix element W_{420} [141], calculated using the jet momenta as estimates of the parton momenta, is required to be less than zero. W_{420} is an event weight formed from the tree level $\mathcal{O}(\alpha_s^2)$ matrix element [142] for the QCD process $Z/\gamma \to q\overline{q}q\overline{q}, q\overline{q}gg$. It is assigned the largest value of any of the 24 permutations of associated jets to partons. In a sizeable fraction of two-fermions events additional gluons and quarks are emitted via the QCD process $Z/\gamma \to q\overline{q}q\overline{q}, q\overline{q}gg$ leading to a distinct four jet topology. This event weight is a good discriminator between four-jet events from QCD and W pairs.

In order to increase further the signal to background ratio a likelihood selection with four input variables is used. After the preselection cuts, the main background is $Z/\gamma \to q\overline{q}$, with a distinct four-jet topology. The input variables are:

- The logarithm of the QCD matrix element, $\log_{10}(W_{420})$.

[1] At 183 GeV the `PC` selection is used. At 189 GeV and above the `PA` selection is used.

- The modulus of the cosine of the modified Nachtmann-Reiter angle [143], $|\cos(\theta_{N-R})|$. With the four jets ordered by energy θ_{N-R} is defined as the angle between $\vec{p}_1 - \vec{p}_2$ and $\vec{p}_3 - \vec{p}_4$. This variable tends to be flat for the two-fermion background and peaked for the $W^+W^- \to q\overline{q}q\overline{q}$ signal.

- The logarithm of the Durham jet resolution parameter at which an event is reclassified from four to five jets, $\log_{10}(y_{45})$.

- The event sphericity, which is around zero for a two-jet event and one for an isotropic event.

Only two classes are used for the calculation of the likelihood variable. The signal class includes all TGC-dependent four-fermion final states, while the background class includes the remaining four-fermion final states and the two-fermion final states. Rather than using the product of the individual probability density functions to construct a classic likelihood discriminator, a multi-dimensional likelihood technique is used to account for the correlations between the four likelihood input variables [144]. Events which exceeds a likelihood output of 0.18 are selected.

For the selection of candidates at an energy of 189 GeV and above the cut on j_{ang} is dropped and the Nachtmann-Reiter angle is replaced by the logarithm of the Excalibur matrix element for the process $W^+W^- \to q\overline{q}q\overline{q}$ using only CC03 diagrams. Both variables are kind of an angle and angles measured in the lab frame are not invariant with changes in the centre-of-mass energy. For example the opening angle between two jets coming from a W boson in the lab frame depends strongly on the boost of the W boson, which increases with the centre-of-mass energy. Such variables change with the centre-of-mass energy and the selection has to be tuned a lot when applied to a different energy. Replacing j_{ang} and the Nachtmann-Reiter angle for higher energies solves this issue and only the cut on the likelihood output must be tuned for a different energy to achieve the same performance. The exclusive effect of each preselection cut is shown in figure 5.1 for a centre-of-mass energy of 189 GeV. The reference distributions for the likelihood selection are tuned with Monte Carlo samples at 189, 200 and 206 GeV. The corresponding cuts on the likelihood output for the cross-section selection are 0.24, 0.22 and 0.22. For energies without a set of reference distributions these and the cut value on the likelihood output are taken from the nearest available energy. For example at 205 GeV the reference distributions from 206 GeV and a cut value of 0.22 is used. The reference distributions of the four input variables after the preselection cuts and the likelihood output are shown in figure 5.2 for $\sqrt{s} = 189$ GeV.

In table 5.2 the details of the two slightly different versions of the selection are summarised.

5.3 TGC Event Selection and Reconstruction

We take all $W^+W^- \to q\overline{q}q\overline{q}$ candidates from cross-section selection and perform kinematic fits on the reconstructed jets to improve the resolution of the measured jets and therefore on the reconstructed W mass, which is one of the main ingredients for the pairing of jets into W candidates. In order for the fitting procedure to be reliable, it is necessary that the Monte Carlo simulation gives a as faithfully representation of the data as possible.

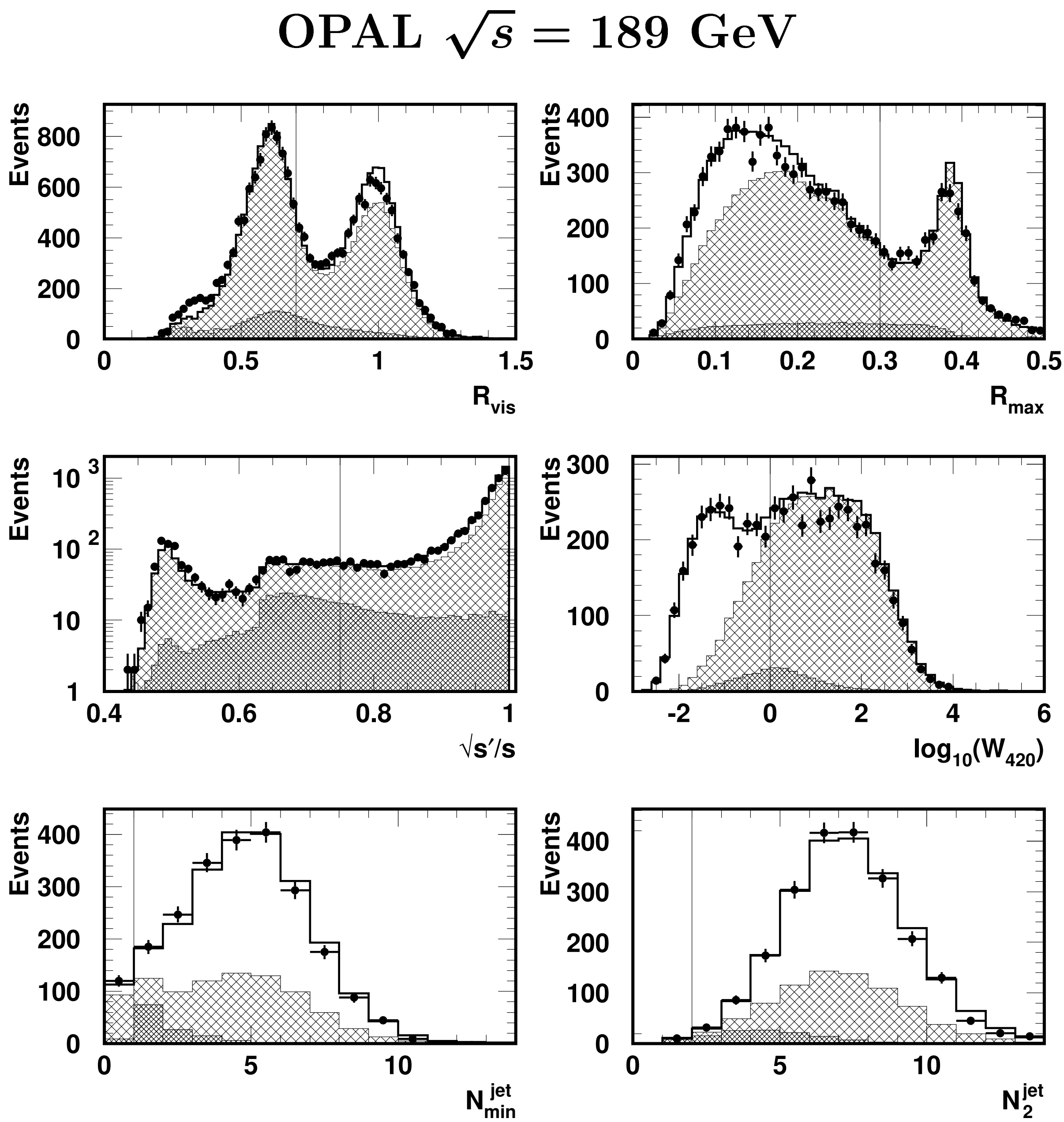

Figure 5.1: Exclusive preselection cuts. The observed data at $\sqrt{s} = 189\,\text{GeV}$ is compared to Monte Carlo expectations for each preselection cut. In each plot, all other preselection cuts have been applied, thereby showing the events removed exclusively by each cut. The position of each cut is indicated by the vertical line. The data is indicated by the points, the four-quark Monte Carlo is shown by the open histograms and the background by the hatched histograms. The two-fermion final states are light and the remaining four-fermion final states are dark hatched.

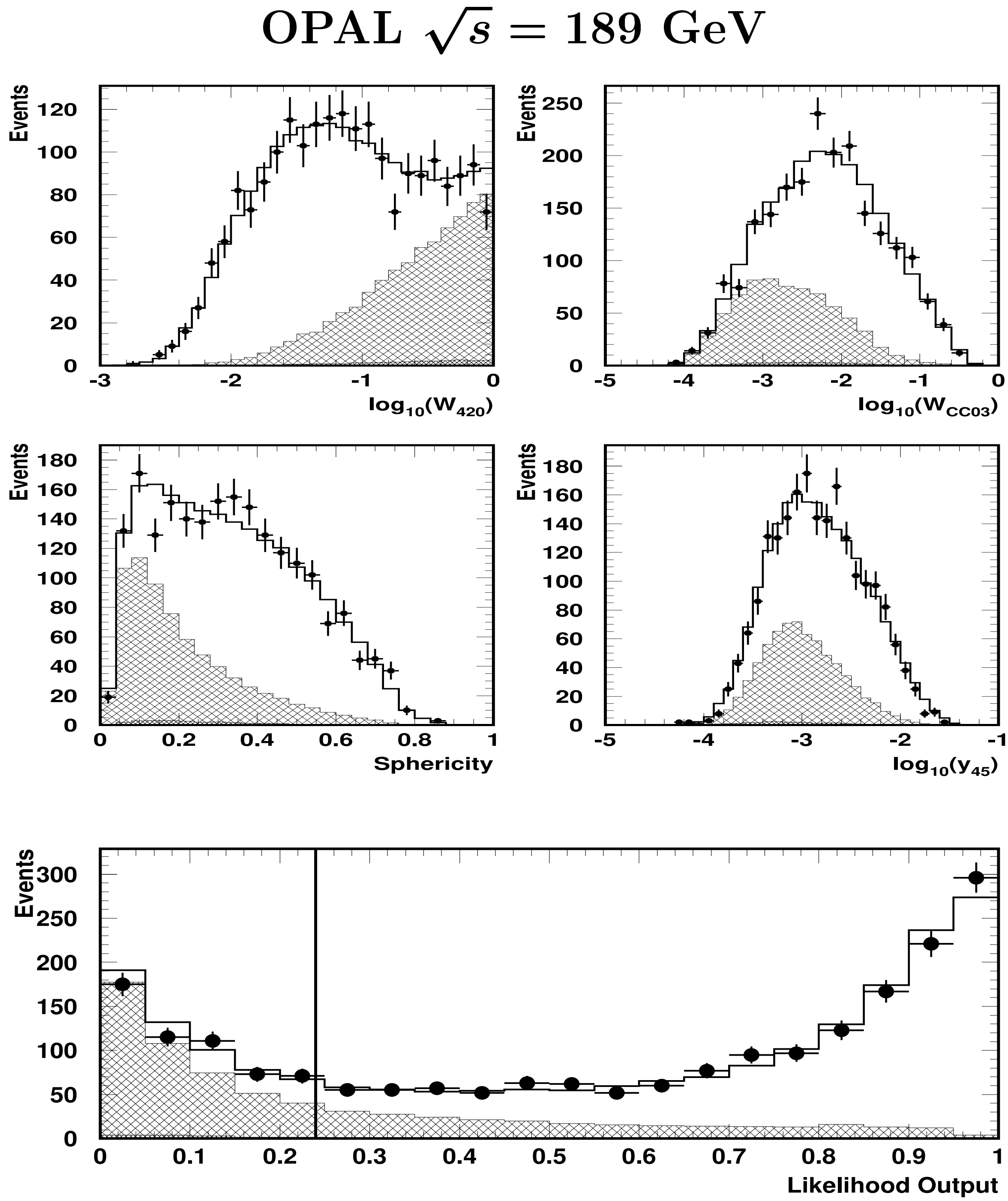

Figure 5.2: Distributions of the cross-section $W^+W^- \rightarrow q\overline{q}q\overline{q}$ likelihood selection variables at a centre-of-mass energy of 189 GeV. The four likelihood input variables and resulting likelihood discriminant are shown for all events passing the cross-section $W^+W^- \rightarrow q\overline{q}q\overline{q}$ preselection. The data is indicated by the points, the four-quark Monte Carlo is shown by the open histograms and the background by the hatched histograms. The two-fermion final states are light and the remaining four-fermion final states are dark hatched.

183 GeV		**189 - 209 GeV**	
Selection Cuts	Likelihood Variables	Selection Cuts	Likelihood Variables
• $R_{vis} > 0.7$	• $\log_{10}(W_{420})$	• $R_{vis} > 0.7$	• $\log_{10}(W_{420})$
• $\sqrt{s'}/\sqrt{s} > 0.75$	• $\lvert\cos\theta_{N-R}\rvert$	• $\sqrt{s'}/\sqrt{s} > 0.75$	• $\log_{10}(W_{\mathrm{CC03}})$
• $R_{max} < 0.3$	• $\log_{10}(y_{45})$	• $R_{max} < 0.3$	• $\log_{10}(y_{45})$
• $N^{jet}_{min} > 0$	• event sphericity	• $N^{jet}_{min} > 0$	• event sphericity
• $j_{ang} < 0.05$		• $\log_{10}(W_{420}) < 0$	
• $\log_{10}(W_{420}) < 0$			

Table 5.2: Selection cuts and likelihood input variables for the $\mathrm{W^+W^-} \rightarrow \mathrm{q\overline{q}q\overline{q}}$ cross-section selection.

The OPAL detector is calibrated using Z decays collected during calibration runs at the Z resonance which were taken regularly every year before and sometimes at intervals during the high energy running of LEP 2.

Normally the Monte Carlo generation and detector simulation take place before the corresponding data taking and the actual detector performance is not known. The correct detector calibration is then used to correct the Monte Carlo events at the time of the analysis using the `ODFIX` routine from the OPAL `OD` package in order to get good agreement between data and Monte Carlo. Unfortunately still some small discrepancies between data and Monte Carlo are left over after processing the Monte Carlo events with `ODFIX`. These discrepancies lead to systematic errors in the W mass and TGC measurements and additional effort was undertaken to understand and correct for these remaining discrepancies as well as possible.

Hence further studies with Z calibration data have been performed and the results are implemented in the `WWFIX` routine [145] from the OPAL `WW` package. The studies concentrate mainly on two jet events and the jet angle $\cos\theta$ is calculated as $\frac{1}{2}(|\cos\theta_1| + |\cos\theta_2|)$. For hadronic events the following five quantities are of interest:

Jet energy scale: The distribution of the two jet energies E_1+E_2 was studied as a function of $\cos\theta$ and of year. The ratio of the mean energy sum normalised by the centre-of-mass energy between data and Monte Carlo is within 1% of unity for $\cos\theta < 0.85$. The data in the different years are consistent with each other except for some small up- or downward shifts of the scale. Therefore the corrections have been split up into a $\cos\theta$ dependent part ranging from 0.9906 to 1.0365 and a year dependent part ranging from 0.9933 to 1.0044.

Jet energy linearity: In the above study only jets with energies around 45 GeVwere used. To investigate the jet energy in data and Monte Carlo at different jet energies three jet events from Z decays and two jet events from high energy Z decays are used. These additional events suggest a linear behaviour of the jet energy. The slope of the data/MC ratio in each year is compatible with an overall slope of $(-2.0 \pm 0.3)\, 10^{-4}\,\mathrm{GeV}^{-1}$.

Jet energy resolution: The r.m.s. of $E_1 + E_2$ has been studied in data and Monte Carlo as a function of $\cos\theta$ and it was found that the data show a poorer resolution than the Monte Carlo. The ratio of data to Monte Carlo is almost constant around 1.036 for $\cos\theta < 0.85$. For far forward jets the ratio can increase up to 1.23. No dependence on the year could be found.

Jet angular resolution: The resolution of the measured jet angle $\cos\theta$ is investigated by looking at $\cos\theta_1 + \cos\theta_2$, which is peaked around zero for two jet events. The width of this distribution corresponds to the resolution of $\cos\theta$. The ratio in data and Monte Carlo is 1.040 ± 0.004, independent of $\cos\theta$ and of year. The resolution on the measured ϕ of the jets was investigated in the same way by looking at the distribution of $\phi_1 - \phi_2 - \pi$. The ratio of the width in data to that in Monte Carlo is 1.012 ± 0.003, independent of $\cos\theta$ and of year.

Jet angular bias: The possibility of having a bias in $\cos\theta$ has been studied by calculating the difference in the measurement of $\cos\theta$ using only the central tracker or the electromagnetic calorimeter. No significant bias was found to correct for.

After applying the detector corrections to the Monte Carlo samples the measured jets can be paired into W-bosons in three possible ways. To improve the resolution of the jet four-momentum we can perform for each possible jet pairing kinematic fits with different constraints. In the simplest case we use energy and momentum conservation and perform a kinematic fit with four constrains (4C). Further we constrain the invariant mass of both di-jet systems to be the same. This results in a kinematic fit with five constrains (5C) and depends on the chosen jet pairing in contrast to the 4C fit. We require a successful 4C fit and consider only good jet pairings, namely those pairings with a successful 5C fit yielding a W-mass between 70 and 90 GeV/c^2. We accept only events with at least one good jet pairing. In addition to the improved four momentum resolution further background is rejected.

After all cuts the overall efficiency is around 80%, varying slightly with the centre-of-mass energy as shown in table 5.3. The contamination from other $\mathrm{W}^+\mathrm{W}^-$ decays is around 0.2% and constant over energy. The major background contribution of around 13.5% comes from $\mathrm{Z}/\gamma \to \mathrm{q\overline{q}}$ production where additional quarks and gluons are radiated of the primary quarks. The contribution from TGC-independent four-fermion final states is 4.5%, except at 183 GeV where it drops to 3%. In table 5.3 the exact number of observed and expected events, split up into signal and the different background sources, is shown.

Jet Pairing and Charge Assignment

The four reconstructed jets can be paired into W-bosons in three possible ways. For each pairing there are two possible ways to assign the charge to the W-boson candidates. Fortunately we are only interested in the sign of the charge and not in the absolute value, which should be one.

For the estimate of the charge of a di-jet systems we use the jet charge technique which was already used very successfully in LEP 1 analyses [146, 147]. The jet charge is a momentum weighted sum of all charged tracks in a jet normalised to the momentum sum. The jet charge

Energy	Observed	Expected	ϵ_s[%]	N$_s$	N$_b$	N$_b^{\mathrm{WW}}$	N$_b^{\mathrm{4f}}$	N$_b^{\mathrm{q\overline{q}}}$
183 GeV	408	418.9	81.6	335.8	83.0	0.6	12.3	70.1
189 GeV	1437	1388.3	81.4	1127.8	260.6	2.3	59.3	199.0
192 GeV	223	222.8	80.5	182.4	40.4	0.4	10.1	30.0
196 GeV	637	594.3	80.4	482.5	111.8	1.2	27.6	83.0
200 GeV	557	585.0	79.2	481.9	103.1	1.3	27.3	74.6
202 GeV	296	286.1	78.7	235.8	50.3	0.6	13.1	36.6
205 GeV	578	606.5	77.6	503.9	102.5	1.3	27.7	73.6
207 GeV	1051	1012.3	77.0	839.2	173.1	2.5	45.6	125.0
all	5187	5114.2	79.5	4189.3	924.8	10.1	222.9	691.8

Table 5.3: Observed and expected number of events after all cuts and for all different centre-of-mass energies. ϵ_s is the signal efficiency, N$_s$ and N$_b$ are the number of signal and background events, respectively. The number of expected background events is broken up into the different background sources. These are other W$^+$W$^-$ decays, N$_b^{\mathrm{WW}}$, TGC-independent four-fermion final states, N$_b^{\mathrm{4f}}$, and two-quark final states, N$_b^{\mathrm{q\overline{q}}}$.

for a di-jet system is calculated in the following way:

$$Q_{di-jet} = \frac{\sum\limits_{i=1}^{N_{di-jet}} q_i |p_{||,i}|^{0.5}}{\sum\limits_{i=1}^{N_{tot}} |p_{||,i}|^{0.5}}, \tag{5.1}$$

where N_{di-jet} and N_{tot} are the numbers of charged tracks in the di-jet system and in the total event, respectively, q_i is the charge of the i^{th} track and $p_{||,i}$ the momentum component parallel to the jet axis. Equation (5.1) represents a special choice to calculate a jet charge for a di-jet system. For example, the total momentum p_i can be used instead of its projection along the jet axis or the momentum weighting factor of 0.5 can be changed. Several variations have been studied [148] and this particular choice gives the highest probability for correct charge assignment for W-pairs.

The di-jet system with the more positive jet charge is taken as the W$^+$ and the other as the W$^-$ candidate. This rule is general enough to handle also the case where the W$^-$ candidate has a positive jet charge and vice versa.

The probability for correct charge assignment of the W pairs is around 77% and varies only slightly with the centre-of-mass energy. In table 5.4 the probabilities are listed for all energies separately. These numbers assume a 100% jet pairing efficiency because a probability for correct charge assignment for wrong jet pairings is not defined at all.

Around 38% of the events have more than one good jet pairing, but the fraction of events where all three possible jet pairings are good is below 5%. The correct di-jet pairing is selected using a likelihood algorithm [144], which takes into account correlations between the input variables. The algorithm is implemented in the OPAL `PC` package [149]. We use as input variables to our likelihood function the mass as obtained from the 5C kinematic

Energy [GeV]	183	189	192	196	200	202	207
p_p [%]	78.8	79.0	79.6	79.8	80.2	79.9	80.3
p_c [%]	77.9	77.5	77.3	77.0	77.0	76.9	77.6
p [%]	61.4	61.2	61.5	61.4	61.8	61.4	62.3

Table 5.4: Probability for correct jet pairing, p_p, and correct charge assignment, p_c, and the overall probability for correct jet pairing and correct charge assignment, p, for all centre-of-mass energies.

fit, the absolute value of the difference between the W candidate masses as obtained from the 4C kinematic fit, and the absolute value of the jet charge difference between the two W candidates. The data distributions of the input variables are shown separately for the highest, second highest and third highest likelihood output in figure 5.3 for all centre-of-mass energies. The data is described well by the Standard Model Monte Carlo predictions for all three likelihood outputs.

The following three classes are used for signal and background:

- correct jet pairing and correct charge assignment (signal)
- correct jet pairing and wrong charge assignment (background)
- wrong jet pairing (background)

The reference distributions for signal and background are taken from W^+W^- Monte Carlo samples generated with the KoralW Monte Carlo generator program using only CC03 diagrams. Unfortunately there is no W^+W^- Monte Carlo sample available at 205 GeV. For this energy the reference distributions from 206 GeV are used. In the case of jet pairing we are not interested in the exact four-fermion calculations. These calculations involve single and non-resonant diagrams and the meaning of W bosons is not clearly defined.

The first row of figure 5.4 shows the reference distributions at a centre-of-mass energy of 200 GeV for the three input variables and the three different classes. Both mass variables distinguish only between the correct and wrong jet pairing. The sensitivity to the correct charge is coming only from the jet charge variable, where both background classes peak at zero and the signal around 0.15 with a much broader distribution.

There is no extra class for $Z/\gamma \to q\overline{q}$ background because the shape of the $Z/\gamma \to q\overline{q}$ distributions looks like the case of wrong pairing. This has been explicitly tested by looking at the probability of correct charge assignment and at the expected statistical error of the anomalous coupling measurements. Both tests gave no improvement to the case of three classes and hence the jet pairing was kept as simple as possible.

The input variables vary only slightly with the centre-of-mass energy. This can be seen from the second to forth row of figure 5.4, where the input variables at the different energies normalised to the distributions at 200 GeV are shown for the signal and the two background classes. In the regions where enough statistics is available, we see that the variation with energy is small. See, for example, the distribution of the 5C mass of the signal class around 80 GeV/c^2. From all three input variables the difference in the 4C masses has the highest energy dependence.

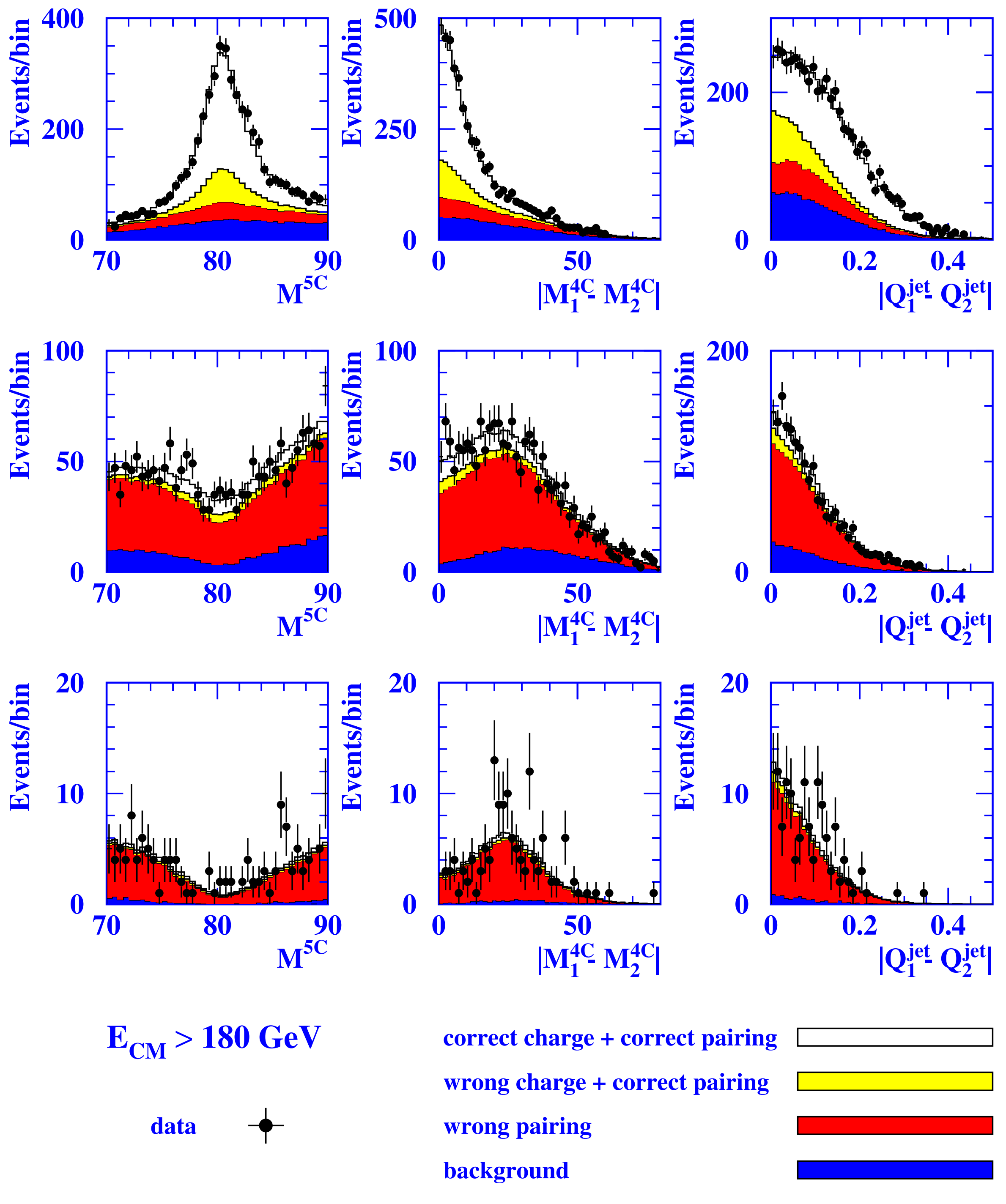

Figure 5.3: Input variables for the jet pairing likelihood function for all centre-of-mass energies. The first row shows the distributions of the three input variables for the jet pairing with the highest likelihood output. The second and third row show the distributions for the second and third highest likelihood output.

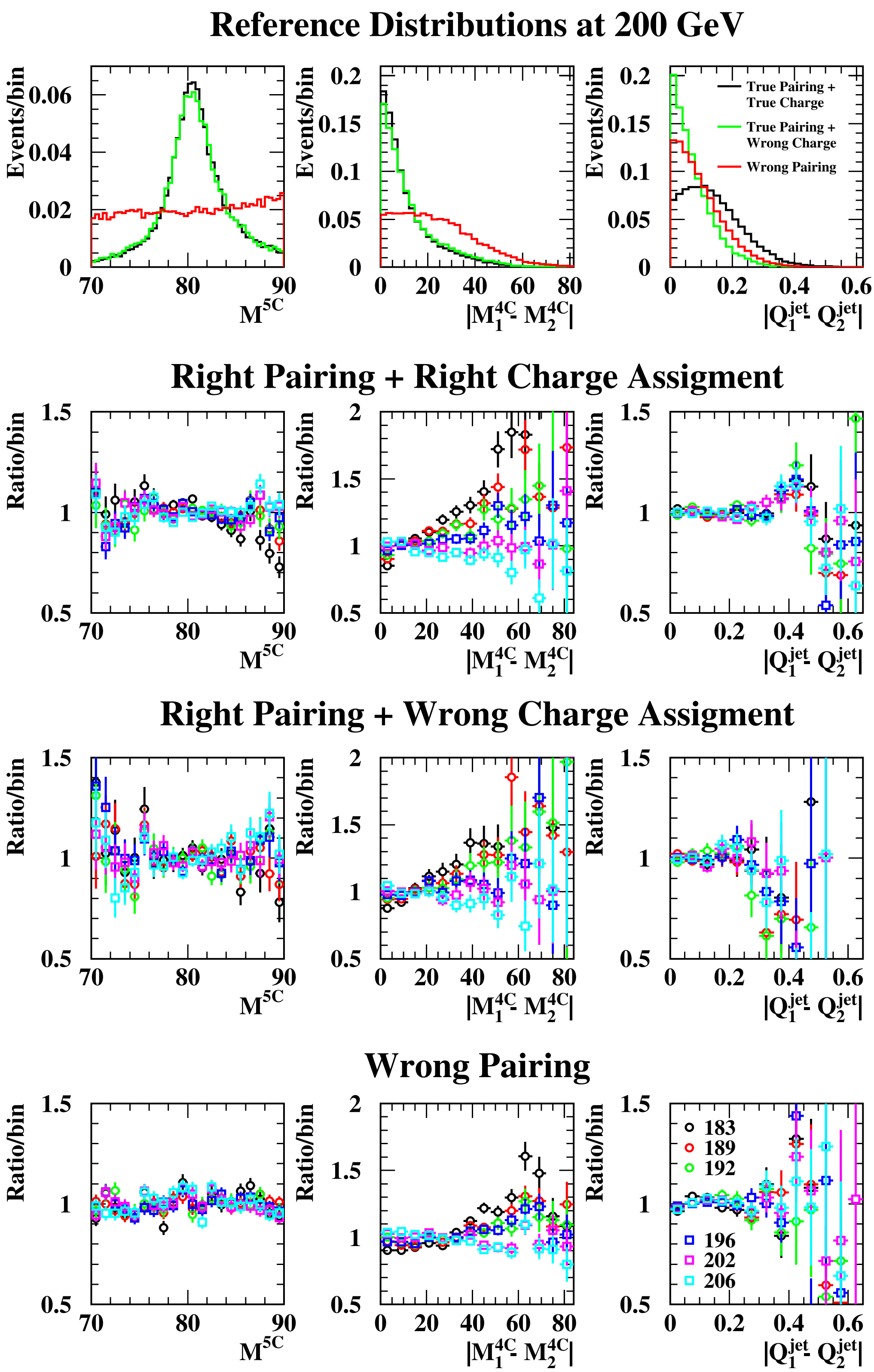

Figure 5.4: The three input variables for the jet pairing likelihood are shown in the first row for a centre-of-mass energy of 200 GeV. The other rows show the ratio of the distributions at a certain $\sqrt{s}$ to that at $\sqrt{s} = 200\,\mathrm{GeV}$.

Nevertheless, we use for each analysed centre-of-mass energy a set of tuned reference distributions from Monte Carlo samples generated at this energy instead of using one set of reference distributions for all energies. For a centre-of-mass energy of 205 GeV we deviate from this scheme and use the reference distributions from 206 GeV because no suitable W^+W^- Monte Carlo samples are available at 205 GeV. The remaining difference in the centre-of-mass energy between the used Monte Carlo and the data samples is small and the effect on the reference distributions is negligible.

The di-jet pairing with the highest likelihood is taken as the correct pairing. The distribution of the likelihood output of the jet pairing with the highest likelihood output is shown in figure 5.5(a) for all energies. The background from two- and four-fermion final states and from wrong pairing is almost flat over the whole range and decreases for higher likelihood output. The correct pairing increases from 0 to 0.5 and stays then constant. The distribution of the W charge separation for the jet pairing with the highest likelihood output is shown in figure 5.5(b). The distributions are shown in figures C.1 to C.8 in the appendix for each analysed energies separately.

According to the W^+W^- KORALW Monte Carlo, the probability of selecting the correct di-jet combination is about 80%, and the probability of correct assignment of the W charge, once the correct pairing has been chosen, is about 77%. Both probabilities vary slightly with the centre-of-mass energy but depend strongly on the jet pairing likelihood output and the jet charge separation.

Figure 5.6(a) shows the probability of choosing the correct jet pairing as a function of the likelihood output. The probability starts rising from around 33% and increases linearly to almost 100% at the maximal likelihood output of one. The probability of correct jet charge assignment is shown as a function of the likelihood output in figure 5.6(b). It starts around 65% and stays almost constant up to a likelihood output of 0.5. At this point the power of the jet charge separation kicks in and the probability raises steeply to almost 100% at a likelihood output of one.

In order to reflect this strong dependency on the likelihood output in the correct jet pairing and correct charge assignment probability, we divide our events into four quality classes using the likelihood output as a quality variable. We have performed studies with one to four classes and different class boundaries. The use of two classes separated at 0.5 is already sufficient to give a visible increase in the sensitivity of the measurement of anomalous couplings. Using four classes whose likelihood ranges listed in table 5.5 yields a slightly better expected sensitivity on the later measurements as the discussed case of two classes. Compared to the case of no classes we expect an increase in sensitivity on the measurement of anomalous couplings of around 6%. The probabilities for correct jet pairing and correct charge assignment for the different classes are given along with the average fraction of events in each class in table 5.5. Each class contains around a quarter of all events and the probabilities in the best class (a) are 91.8% and 89.4% for correct pairing and correct charge assignment, respectively.

Angular Distributions

The selection efficiency is quite high in the $q\bar{q}q\bar{q}$ channel but the reconstruction is more involved. As described in the last section, the combined efficiency of correct jet pairing and charge assignment is around 61%. This reflects directly how well we can reconstruct the

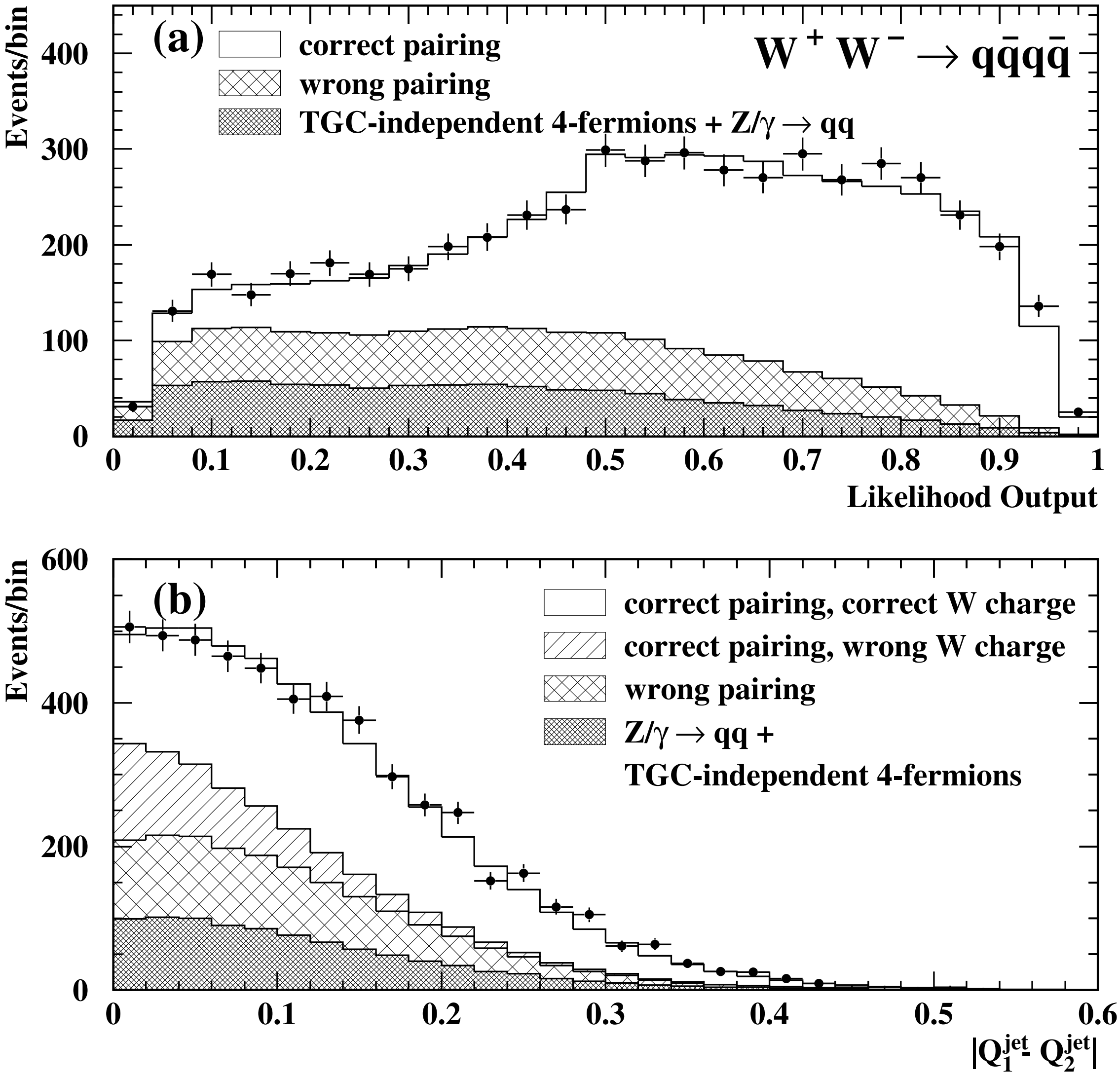

Figure 5.5: Distributions for $q\overline{q}q\overline{q}$ data events (points) for all centre-of-mass energies and for the KANDY four-fermion Monte Carlo (histogram) of (a) jet-pairing likelihood corresponding to the combination with the largest likelihood where the double hatched area represents the contribution of wrong pairing (assuming all four quark final states compatible with W pair production are coming from such events), and the dark area represents the contribution of the TGC-independent four-fermion and of the $Z/\gamma \to q\overline{q}$ background; (b) charge separation between the two W candidates where the hatched area shows the contribution of correct pairing and incorrect W charge, the double hatched area shows the contribution of wrong pairing and the dark area represents the contribution of the $Z/\gamma \to q\overline{q}$ and TGC-independent four-fermion background.

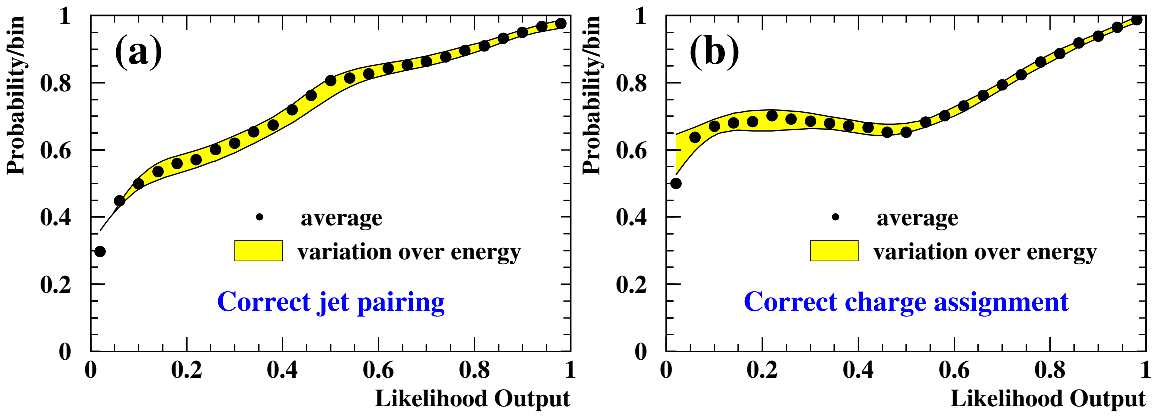

Figure 5.6: The probability of choosing the (a) correct jet pairing or the (b) correct charge assignment as a function of the likelihood output. The points show the average probability of all energies and the band shows the variation over the analysed energy range.

W-pair production angle. In figure 5.7 the $\cos\theta_{\rm W}$ distribution is shown for all centre-of-mass energies. The dots represent the data and the open histogram the Standard Model predictions. The solid histograms show the contributions from wrong charge assignment, wrong pairing and background. The contribution from wrong pairing is flat, while the contribution from wrong charge assignment is peak in the backward region. Still, the $\cos\theta_{\rm W}$ distribution is nicely peak in the forward direction. With 100% reconstruction efficiency a very sharp forward peaked distribution is expected.

We do not try to distinguish the quark from the anti-quark in W decays. This can be done for example using the jet charge technique, however the separation power is expected to be very low because the absolute charge difference is only one third. Hence we take the jet with $0 < \phi^*_{jet} < 180°$ as the quark jet from the decay of the $\rm W^-$ or the anti-quark jet from the decay of $\rm W^+$. The theoretical expectation will be adjusted accordingly. The distribution of $\cos\theta^*_{jet}$ and ϕ^*_{jet} from $\rm W^-$ and $\rm W^+$ are expected to be the same for CP conserving couplings and are therefore not distinguished.

The distribution of the variables $\cos\theta_{\rm W}$, $\cos\theta^*_{jet}$ and ϕ^*_{jet} are shown in figure 5.7 for all centre-of-mass energies, along with the expected distributions for the Standard Model

Class	Jet pairing likelihood output	% of events	Correct jet pairing probability	Correct charge assignment probability
(a)	0.72 - 1.00	27.2	91.8%	89.4%
(b)	0.54 - 0.72	24.9	84.4%	74.1%
(c)	0.35 - 0.54	22.4	75.3%	66.2%
(d)	0.00 - 0.35	25.5	56.4%	67.9%

Table 5.5: Definition of the four quality classes. The correct charge assignment probability is calculated only for those events with correct jet pairing.

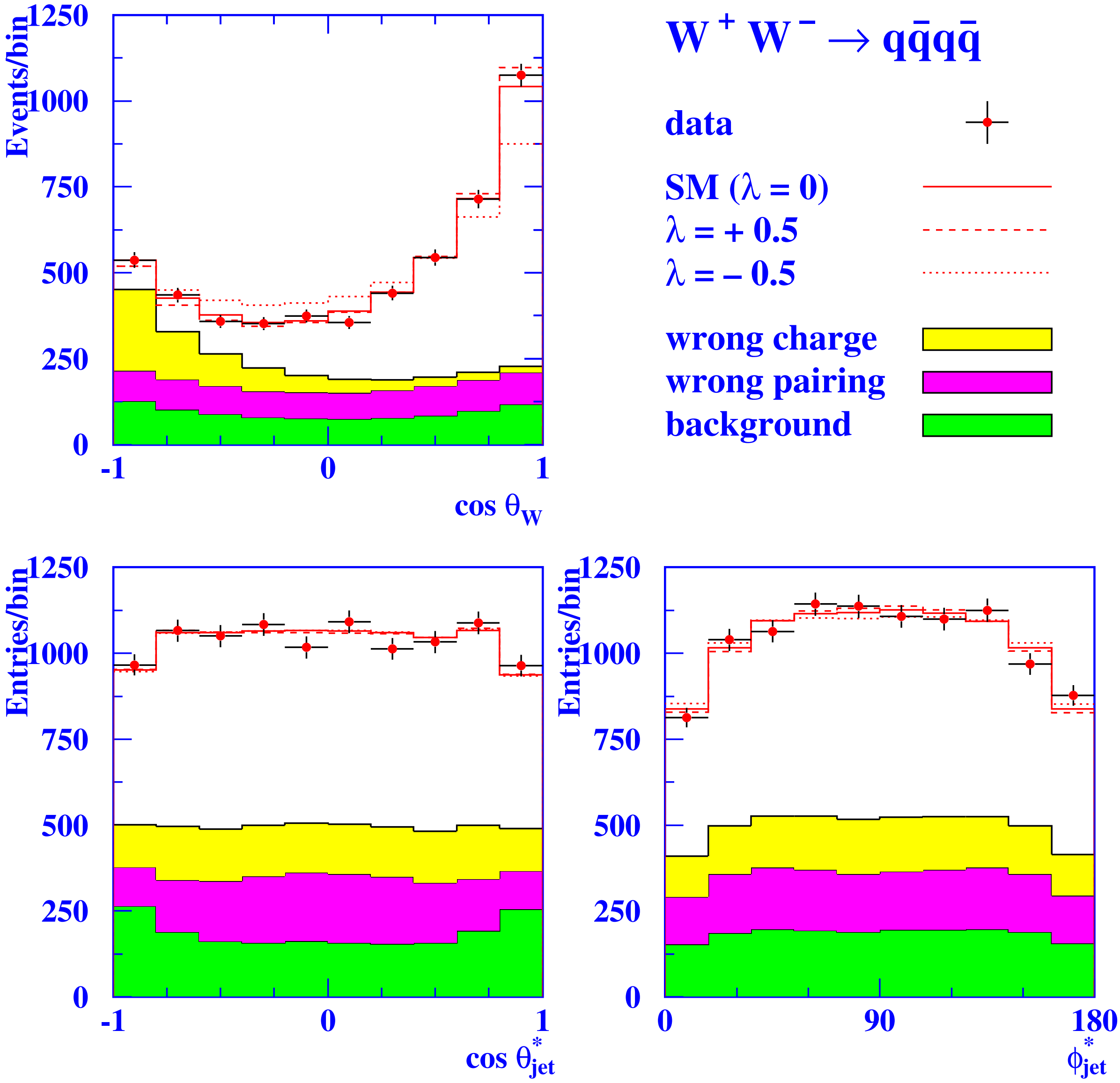

Figure 5.7: Distribution of the kinematic variables $\cos\theta_{\mathrm{W}}$, $\cos\theta^*_{jet}$, and ϕ^*_{jet} for all centre-of-mass energies. In the $\cos\theta^*_{jet}$ and ϕ^*_{jet} distributions there are two entries per event, one per reconstructed W. The solid points represent the data. The histograms show the Monte Carlo expectation of the Standard Model (solid line) and the cases of $\lambda = +0.5$ and $\lambda = -0.5$ (dashed and dotted lines, respectively). The Monte Carlo histograms are normalised to the number of data events. The open histograms show the contribution from correct pairing and correct charge assignment. The other histograms show the contribution from correct pairing but wrong charge assignment, wrong pairing and background.

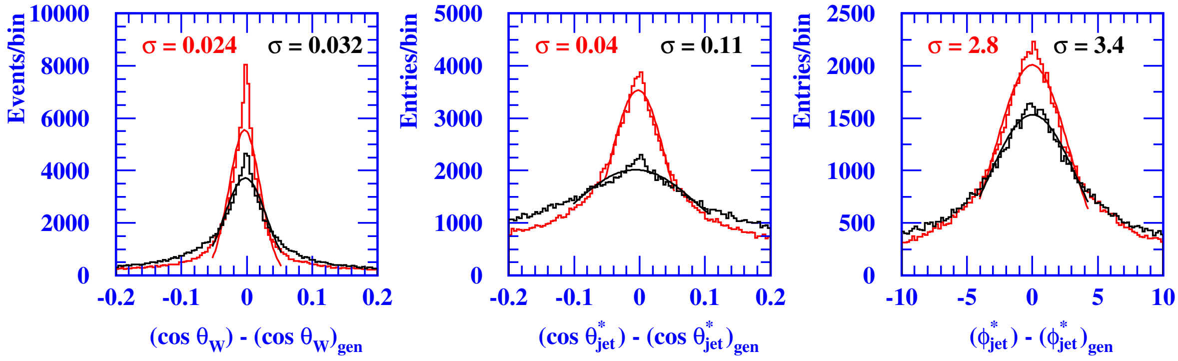

Figure 5.8: Expected resolution for the angles $\cos\theta_{\mathrm{W}}$, $\cos\theta^*_{jet}$ and ϕ^*_{jet} at $\sqrt{s} = 200\,\mathrm{GeV}$ before any kinematic fit (black) and after a kinematic fit with 5 constraints (red). The histograms show the difference between detector and generator level and the curves show a Gaussian fit to the histograms for a rough estimation of the resolution, only. The width of the fit is listed as σ.

($\lambda = 0$) and for two anomalous couplings $\lambda = \pm 0.5$. The Monte Carlo histograms are normalised to the number of data events. In addition the shaded histograms represent the separate contributions from background, wrong pairing and correct pairings but wrong charge assignment. The five angles are shown in figures C.9 – C.16 in the appendix for each analysed centre-of-mass energy separately.

For a good measurement of the triple gauge boson couplings, a good resolution of the production and decay angles is crucial. A very good tool to improve the resolution is the use of a kinematic fit assuming at least energy and momentum conservation. Figure 5.8 show the expected resolution for $\cos\theta_{\mathrm{W}}$, $\cos\theta^*_{jet}$ and ϕ^*_{jet} from Monte Carlo studies using just the measured four-momenta in the calculation of the angles or the fitted four momenta. The use of an additional constraint, assuming that both di-jet systems have the same invariant mass, increases only slightly the resolution. We fit a Gaussian function to the histogram and use its width as an estimate for the angle resolution. For $\cos\theta_{\mathrm{W}}$ a resolution of 0.024 is obtained and is most precise. We gain around 20% in resolution by using a kinematic fit for $\cos\theta$ and ϕ^*_{jet} while the gain in $\cos\theta^*_{jet}$ is around 60%.

5.4 Method of Optimal Observables

For a quantitative study of anomalous couplings we use the method of optimal observables [150,151], where the five-fold differential cross-section is condensed to one-dimensional distributions while most of the sensitivity to triple gauge boson couplings is kept. This method relies on the linear dependence of the triple gauge boson vertex (2.15) on the triple gauge boson couplings, corresponding to a second-order polynomial dependence of the differential cross-section,

$$\frac{d\sigma(\Omega,\vec{\alpha})}{d\Omega} = S^{(0)}(\Omega) + \sum_i \alpha_i \cdot S^{(1)}_i(\Omega) + \sum_{i,j} \alpha_i\alpha_j \cdot S^{(2)}_{ij}(\Omega), \tag{5.2}$$

with $\alpha_i = \Delta\kappa_\gamma$, Δg_1^Z, λ_γ and g_5^Z. The coefficients $S^{(0)}$, $S_i^{(1)}$ and $S_{ij}^{(2)}$ are functions of the five phase-space variables, $\Omega = (\cos\theta_{\mathrm{W}}, \cos\theta_1^*, \phi_1^*, \cos\theta_2^*, \phi_2^*)$. The first and second order optimal observables are defined as

$$\begin{aligned} \mathcal{O}_i^{(1)}(\Omega) &= \frac{S_i^{(1)}(\Omega)}{S^{(0)}(\Omega)} \\ \mathcal{O}_{ij}^{(2)}(\Omega) &= \frac{S_{ij}^{(2)}(\Omega)}{S^{(0)}(\Omega)} \end{aligned} \tag{5.3}$$

and depend only on the phase-space point Ω. For the general case of n independent couplings there are $\frac{1}{2}(n(n+3))$ optimal observables. For each considered parameter, these are split into one first order observable, $\mathcal{O}_i^{(1)}$, and one second order observable, $\mathcal{O}_{ii}^{(2)}$. The rest are second order observables, $\mathcal{O}_{ij}^{(2)}$, involving all mutual correlations between two different parameters. In the case of only one coupling, there are two optimal observables, in the case of two couplings already five and in the case of four couplings 14.

These observables are called optimal because one can show, using the generalised Rao-Cramér-Frét bound [152], that an estimator for the parameter α using the first order optimal observable is joint efficient. The property of joint efficiency for an estimator means that the expected error is the smallest possible, and one may consider the estimation to be optimal. A more hand waving argument uses the maximum likelihood function, which is conventionally considered as the most sensitive estimator. Using the quadratic form (5.2) of the differential cross-section, the maximum likelihood function for one coupling α using N events with the phase-space variables Ω_k is written as

$$L(\alpha) = \prod_{k=1}^{N} \left(S^{(0)}(\Omega_k) + \alpha S^{(1)}(\Omega_k) + \alpha^2 S^{(2)}(\Omega_k) \right). \tag{5.4}$$

The measurement of α, which maximises the likelihood function, is called α_0 and must fulfil

$$\left.\frac{\mathrm{d}(\log L)}{\mathrm{d}\alpha}\right|_{\alpha=\alpha_0} = \sum_{k=1}^{N} \frac{S^{(1)} + 2\alpha_0 S^{(2)}}{S^{(0)} + \alpha_0 S^{(1)} + (\alpha_0)^2 S^{(2)}} = \sum_{k=1}^{N} \frac{\mathcal{O}^{(1)} + 2\alpha_0 \mathcal{O}^{(2)}}{1 + \alpha_0 \mathcal{O}^{(1)} + (\alpha_0)^2 \mathcal{O}^{(2)}} \stackrel{!}{=} 0. \tag{5.5}$$

From this equation we see, that for each event only two quantities enter the likelihood function, which are calculated out of the five phase-space variables. Only the optimal observables $\mathcal{O}^{(1)}$and $\mathcal{O}^{(2)}$enter into the maximisation procedure of the likelihood function and therefore a binned maximum likelihood fit to these two optimal observables has the same sensitivity. Assuming that the coupling α is small the second order optimal observable can be neglected and the first order optimal observable contains the whole sensitivity.

Many authors have studied the use of optimal observables for the measurement of triple gauge boson couplings. The first proposal was to use only the mean value of the first order optimal observable [151], which give the optimal sensitivity under the assumption that the parameters under investigation are small deviations from the Standard Model predictions.

So fare, only the true phase-space variables Ω are used in the definition of the the optimal observables and the study of their properties. Any effects from the measurement, as detector resolution and selection efficiencies, are not taken into account. A priori it is not known if the observables are still optimal. It has been shown that the observables are optimal, if the

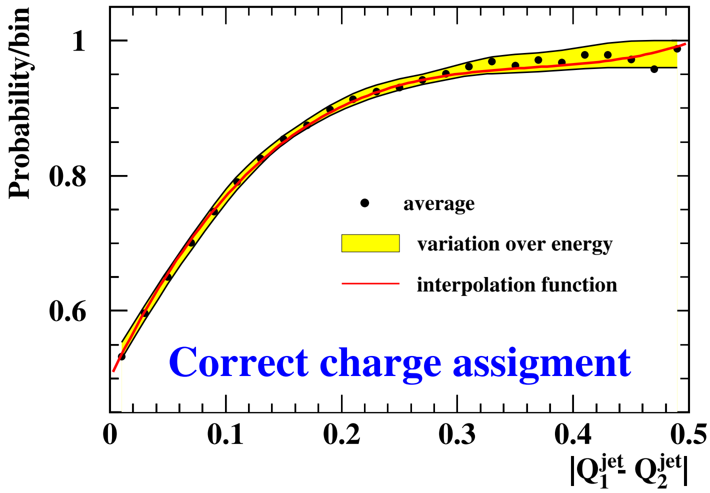

Figure 5.9: The probability of choosing the correct charge assignment as a function of the jet charge difference $|Q_{W_1} - Q_{W_2}|$. The points show the average probability of all energies, the band shows the variation over the analysed energy range and the line the used parametrisation.

detector response is sufficiently modelled. Further, all information contained in the phase-space variables Ω, which is relevant to the considered couplings, is retained in the whole set of first and second order observables [153]. In this analysis we use the mean values of the first order observables $\overline{\mathcal{O}}_i^{(1)}$ and the second order observables $\overline{\mathcal{O}}_{ii}^{(2)}$ and $\overline{\mathcal{O}}_{ij}^{(2)}$. The decrease in sensitivity by using only mean values and not the whole distribution is expected to be small [154].

The calculation of the mean optimal observables and their expected values is done separately for each centre-of-mass energy. The optimal observables are constructed for each event k with the set of phase-space variables Ω_k using the analytic expression for the CC03 Born differential cross-sections [155] to calculate the values of $S^{(0)}(\Omega_k)$, $S_i^{(1)}(\Omega_k)$, $S_{ii}^{(2)}(\Omega_k)$ and $S_{ij}^{(2)}(\Omega_k)$. This calculation takes into account the reconstruction ambiguities of this final state: No flavour identification of the W decays is attempted and the two possible solutions in the decay angles of each W enter with the same weight into the calculation. The ambiguity in the W-charge determination is taken into account by weighting the $S^{(0)}$, $S_i^{(1)}$, $S_{ii}^{(2)}$ and $S_{ij}^{(2)}$ functions for each charge hypothesis with the corresponding probability. This probability is determined from Monte Carlo as a function of the estimated jet-charge difference $|Q_{W_1} - Q_{W_2}|$ between the two W candidates in the event and is shown in figure 5.9. The nine possible observables for the couplings $\Delta\kappa_\gamma$, Δg_1^Z and λ are shown in figure 5.10. The dots show the combined data for all energies and the solid line the Standard Model predictions. The background contribution has a similar shape as the signal and is indicated by the solid histogram. For an estimate of the sensitivity of these observables the expectations from two anomalous couplings ($\lambda = \pm 0.5$) are also shown. The same distributions are shown in figure C.17 – C.24 in the appendix for each energy separately. The first and second order observable for g_5^Z are shown in figure 5.11. Here the expectations for an anomalous coupling of $g_5^Z = \pm 1$ are shown in addition to the SM predictions. The same distributions are shown in figure C.25 – C.32 in the appendix for each energy separately.

Fit Method

We perform a χ^2-fit to extract the anomalous coupling parameters. The χ^2-function is

$$\chi^2 = \left(\vec{\overline{\mathcal{O}}} - \vec{E}[\vec{\mathcal{O}}](\vec{\alpha})\right)^t V^{-1} \left(\vec{\overline{\mathcal{O}}} - \vec{E}[\vec{\mathcal{O}}](\vec{\alpha})\right), \tag{5.6}$$

where $\vec{E}[\vec{\mathcal{O}}]$ is the expectation value of $\vec{\overline{\mathcal{O}}}$ as a function of the anomalous couplings $\vec{\alpha}$ and V the covariance matrix. In the one-parameter fit of α_i we only use the corresponding first order, $\mathcal{O}_i^{(1)}$, and second order, $\mathcal{O}_i^{(2)}$, observables. In this way, the other couplings are not used in the fit. Similarly, in two-parameter fits where two couplings are allowed to vary simultaneously, we use only the five observables corresponding to these couplings and their mutual correlations. When three couplings are allowed to vary, nine observables are used. We minimise the χ^2 to find the best fitting parameters and estimate the errors on the parameter by finding the positions where $\Delta\chi^2 = \chi^2 - \chi^2_{\min}$ exceeds a certain critical value. For a one-parameter fit $\Delta\chi^2 = 1$ corresponds to the 68% confidence level (C.L.) interval.

The covariance matrix is calculated from Standard Model Monte Carlo samples and then scaled to the observed number of data events. In principle the covariance matrix can also be measured from data to reduce any model dependence. But at some centre-of-mass energies the luminosity is not high enough to give a precise enough covariance matrix. We estimate the covariance matrix for the Standard Model and keep it fixed throughout the whole fitting procedure. With this procedure we may mis-estimate the errors on the measured parameters, if the true covariance matrix for the measured couplings is quite different from the SM predictions, but a TGC dependent covariance matrix introduces a bias into the fit for low statistic data samples.

We use the fact that the differential cross-section is quadratic in the couplings to speed up the evaluation of the expectation values $E[\mathcal{O}](\vec{\alpha})$ as a continuous function of the couplings $\vec{\alpha}$. Using equation (5.2), we easily see that the expectation values can be expressed as the ratio of two parabolic functions

$$\begin{aligned}
E[\mathcal{O}_k^{(1)}] &= \frac{1}{\sigma_{tot}} \int \mathcal{O}_k^{(1)}(\Omega) \frac{\mathrm{d}\sigma(\Omega)}{\mathrm{d}\Omega} \mathrm{d}\Omega \\
&= \frac{1}{\sigma_{tot}} \int \frac{S_k^{(1)}(\Omega)}{S^{(0)}(\Omega)} \left(S^{(0)}(\Omega) + \sum_i \alpha_i \cdot S_i^{(1)}(\Omega) + \sum_{i,j} \alpha_i\alpha_j \cdot S_{ij}^{(2)}(\Omega), \right) \mathrm{d}\Omega \\
&= \frac{1}{\sigma_{tot}} \left(\int S_k^{(1)}(\Omega)\mathrm{d}\Omega + \sum_i \alpha_i \int \frac{S_k^{(1)}(\Omega) S_i^{(1)}(\Omega)}{S^{(0)}(\Omega)} \mathrm{d}\Omega + \sum_{i,j} \alpha_i\alpha_j \int \frac{S_k^{(1)}(\Omega) S_{ij}^{(2)}(\Omega)}{S^{(0)}(\Omega)} \mathrm{d}\Omega \right) \\
&= \frac{p^{(2)}(\vec{\alpha})}{\sigma_{tot}},
\end{aligned} \tag{5.7}$$

where $p^{(2)}(\vec{\alpha})$ is a second-order polynomial function in $\vec{\alpha}$. In order to include effects beyond the scope of analytical calculations, as fragmentation, detector effects and selection and reconstruction efficiencies, the reference functions are calculated using large SM Monte Carlo samples. For the numerator and denominator of the expectation values as a function of n

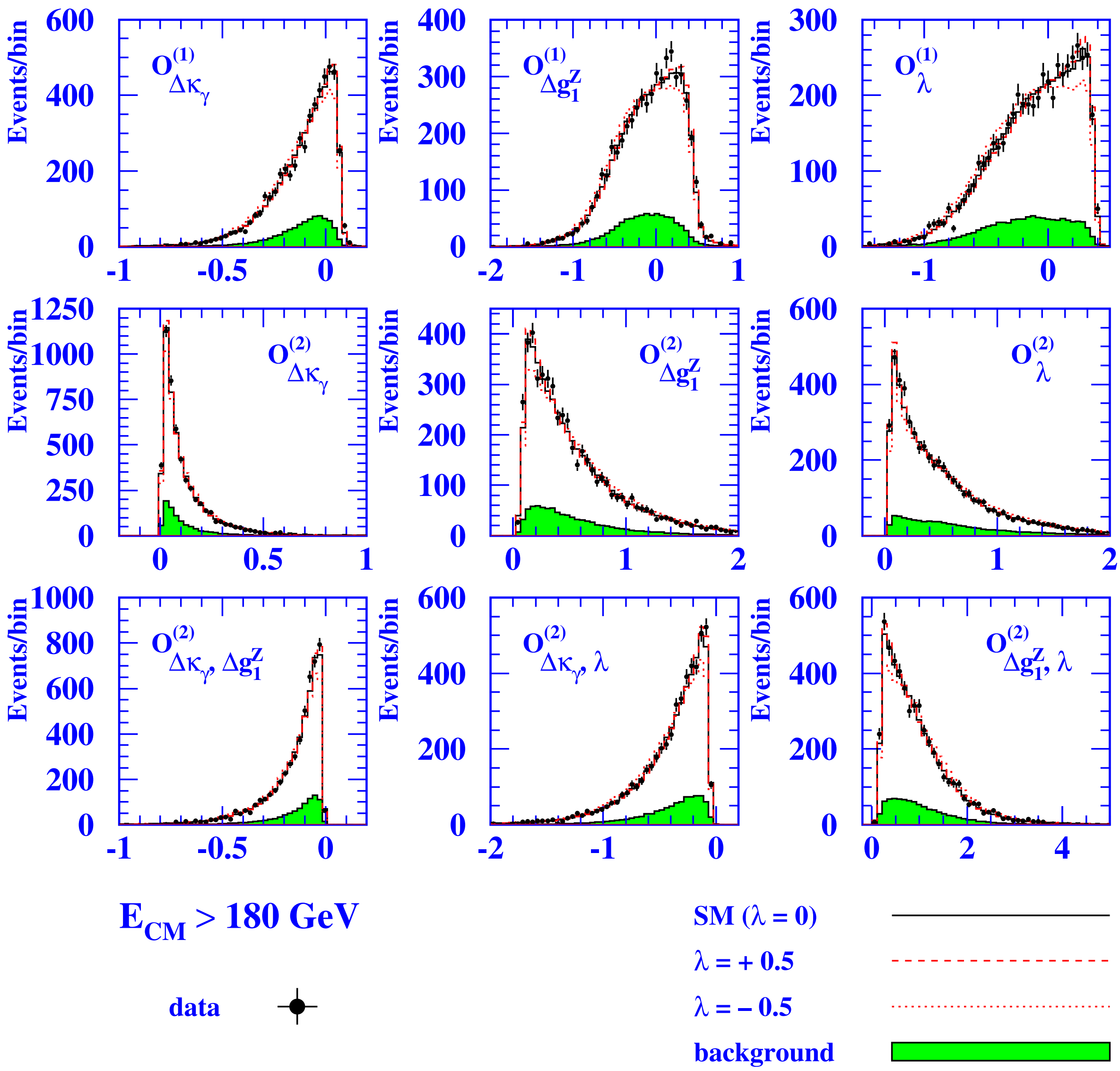

Figure 5.10: All nine optimal observables for the three C and P conserving couplings $\Delta\kappa_\gamma$, Δg_1^Z and λ. The dots show the combined data for all centre-of-mass energies and the solid line the Standard Model expectations. The background is indicated as the solid histogram. Two expectations from anomalous couplings are shown as the dashed ($\lambda = +0.5$) and dotted ($\lambda = -0.5$) lines.

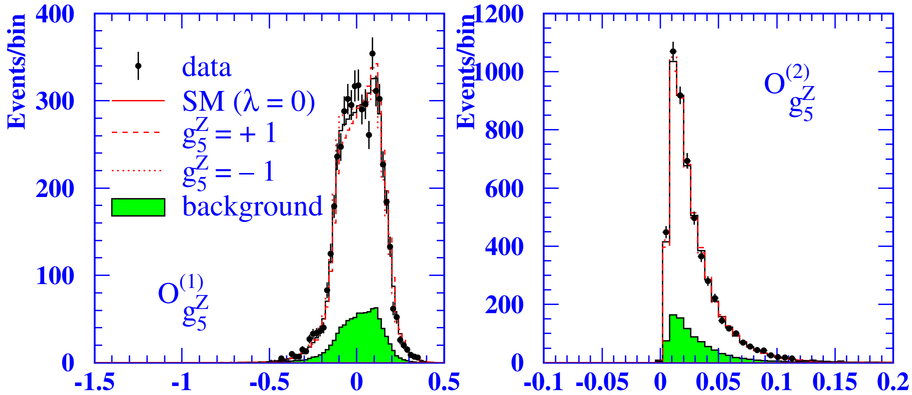

Figure 5.11: The two optimal observables for the CP conserving coupling g_5^Z. The dots show the combined data for all centre-of-mass energies and the solid line the Standard Model expectations. The background is indicated as the solid histogram. Two expectations from anomalous couplings are shown as the dashed ($g_5^Z = +1$) and dotted ($g_5^Z = -1$) lines.

couplings, $\frac{n}{2}(n+3)+1$ Monte Carlo samples with different anomalous couplings are needed. The first sample is always the Standard Model. For an expectation function depending only on one parameter, two Monte Carlo samples with anomalous couplings are needed besides the Standard Model sample in order to have enough interpolation points to calculate the coefficients for the quadratic function. In the case of three couplings, 10 MC samples are needed in total. Besides the Standard Model, samples with parameters of ± 1 are used and three samples with two parameters different from the Standard Model values: (1,1,0), (1,0,1) and (0,1,1).

To avoid the generation and full detector simulation of large MC samples for a set of anomalous couplings the events from the Standard Model sample are reweighted to an anomalous coupling $\vec{\alpha}$ by multiplying each event by a weight

$$w(\vec{\alpha}) = \frac{\mathrm{d}\sigma(\Omega,\vec{\alpha})}{\mathrm{d}\sigma(\Omega,\mathrm{SM})}. \tag{5.8}$$

The differential cross-section $\mathrm{d}\sigma$ is calculated using the matrix elements from EXCALIBUR. The expectation function can thus be written as

$$E[\mathcal{O}](\vec{\alpha}) = \frac{\sum_{n=1}^{N} w_n(\vec{\alpha})\mathcal{O}(\Omega_n)}{\sum_{n=1}^{N} w_n(\vec{\alpha})}. \tag{5.9}$$

As discussed earlier the efficiency of correct jet pairing and charge assignment depends strongly on the jet-pairing likelihood output. In order to reflect this strong dependence we split up the whole event set into n quality classes and assign each classes a different weight, reflecting the quality of the reconstruction. For each class the mean values of the optimal observables are calculated and then a weighted sum is performed

$$\overline{\mathcal{O}} = \frac{\sum_{c=1}^{n} w_c N_c \overline{\mathcal{O}}_c}{\sum_{c=1}^{n} w_c N_c}, \tag{5.10}$$

where N_c is the number of events, $\overline{\mathcal{O}}_c$ the mean optimal observable and w_c the weight for class c. For technical reasons, we would like to keep the parabolic behaviour of the numerator and denominator of the weighted mean observable. Already two classes would spoil this behaviour for a standard weighted sum

$$\begin{aligned}\overline{\mathcal{O}} &= w_1\overline{\mathcal{O}}_1 + w_2\overline{\mathcal{O}}_2 \\ &= \frac{w_1\sum_{i=1}^{N_1}\overline{\mathcal{O}}_i^1}{N_1} + \frac{w_2\sum_{i=1}^{N_2}\overline{\mathcal{O}}_i^2}{N_2} \\ &= \frac{w_1 N_2\sum_{i=1}^{N_1}\overline{\mathcal{O}}_i^1 + w_2 N_1\sum_{i=1}^{N_2}\overline{\mathcal{O}}_i^2}{N_1 N_2}. \end{aligned} \tag{5.11}$$

The weights w_c are calculated using the variances of the optimal observable *resolution* distributions, as obtained from Monte Carlo. In this way, events where the quality of the reconstruction is poor obtain a lower weight.
We vary the number of classes between 1 and 4 and used different ranges in the jet pairing likelihood output to find out which choice is the optimal one. For one class we use all events exceeding a likelihood cut of around 0.5, which varies slightly with the energy and was used in a previous analysis. For two classes, we have two choices: First, we use the complete likelihood range and divide it into two equal ranges (2.1) or into two equal event sizes (2.2). Second, we reject all events below the cut of 0.5 from the one class case and divide the remaining events into two equal likelihood ranges (2.3) or two equal event sizes (2.4). For three classes, we put all events with a likelihood below 0.5 into one class and split the rest of the events at a likelihood of 0.75. In addition to this class we defined two more: All events are used and divided into three samples of either equal likelihood range (3.2) or equal event size (3.3). For four classes, as before, we use all events and divide them into four samples of either equal likelihood range (4.1) or equal event size (4.2).
The expected errors for these different class definitions are shown in figure 5.12 for the four couplings. The general behaviour is for all four classes similar. The main improvement comes from using two classes and including the whole data set with a likelihood output from zero to one. The splitting into more than two classes improves the expected error only slightly.

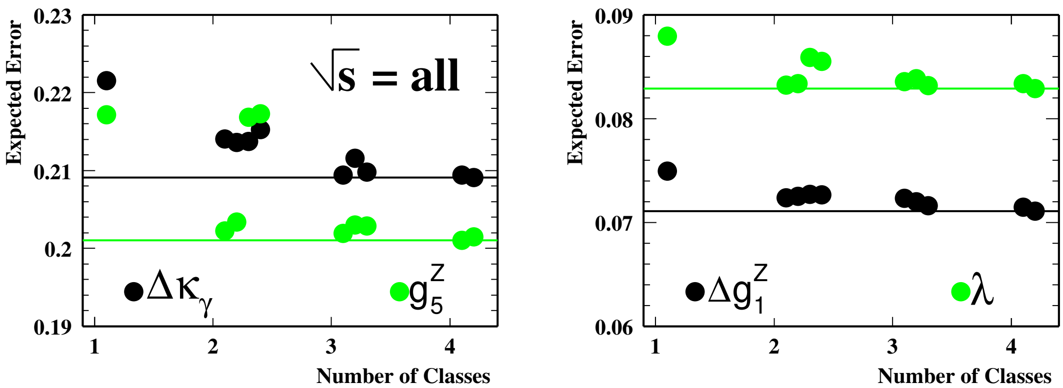

Figure 5.12: Expected sensitivity for different class definitions ranging from one to four classes with different likelihood ranges. For the exact definition of the classes see text. The lines show the highest precision for each coupling.

For the final analysis, we use four quality classes with the ranges listed in table 5.5, which enhances our sensitivity, as expected, by 5% to 10% compared to the case of no classes.

Test of the Fit Method

The fit method is tested with two different simulated data sample sizes: First, high statistics Monte Carlo samples for various different anomalous couplings are fitted to proof that the method performs well and to study any intrinsic bias. Second, ensembles of low statistics Monte Carlo subsamples of the size of the expected number of events are used to check if the modelling of the fit errors is correct.

High Statistics Tests

At each centre-of-mass energy, except 205 GeV, Monte Carlo samples with triple gauge boson couplings different from the Standard Model are used as fake data to test the fit method for any biases. Unfortunately, the MC samples are generated with EXCALIBUR, which does not include the full $\mathcal{O}(\alpha)$ corrections, while KANDY does. However, triple gauge boson couplings are treated more accurate in EXCALIBUR. In order to account for the difference in the implementation of the $\mathcal{O}(\alpha)$ corrections in EXCALIBUR and KANDY, for this tests the reference distributions are calculated by reweighting EXCALIBUR Monte Carlo samples. At each energy samples with anomalous couplings of ± 1 are available for all four couplings. Samples with a value of $\pm\frac{1}{2}$ are only available for some energies and some couplings. See table B.4 for a list of Monte Carlo sample with couplings different from the SM.

In figure 5.13 the fit results for the bias test are shown. The difference between the measured and generated couplings is plotted as a function of the generated couplings for each energy separately and for all energies combined. The generated couplings are displaced around their nominal values for clearness. All the values are scattered nicely around zero. For the Standard Model couplings the results from two different samples are shown: EXCALIBUR and KANDY. The results from the EXCALIBUR SM samples lie directly at zero, as expected, because the same samples are used as fake data and for calculating the reference distributions. These samples test for any inconsistencies in the treating of data and theory predictions. The results from the KANDY SM samples give an estimate of the size of the $\mathcal{O}(\alpha)$ corrections at the Standard Model. In general, no big bias, considering the errors, is seen. However, the shown results indicate that the sensitivity to positive $\Delta\kappa_\gamma$ is worse compared to the sensitivity to positive $\Delta\kappa_\gamma$.

Low Statistics Tests

In some of our fits the χ^2-function has a double minimum and therefore it is necessary to validate the errors obtained from the χ^2-fits. This is performed with a large number of Monte Carlo experiments. In each of these experiments, we use for each centre-of-mass energy a subsample of Standard Model Monte Carlo events. The size of each subsample is Poisson distributed around the number of expected events corresponding to the luminosity at this particular energy. Background events are also included in these subsamples in the appropriate proportions. For each experiment, the subsamples at the eight energies are analysed in the same way as the real data events. The distributions of the 1d-fit results for $\Delta\kappa_\gamma$, Δg_1^Z, λ and g_5^Z using 8991 experiments, where only one parameter is varied at the

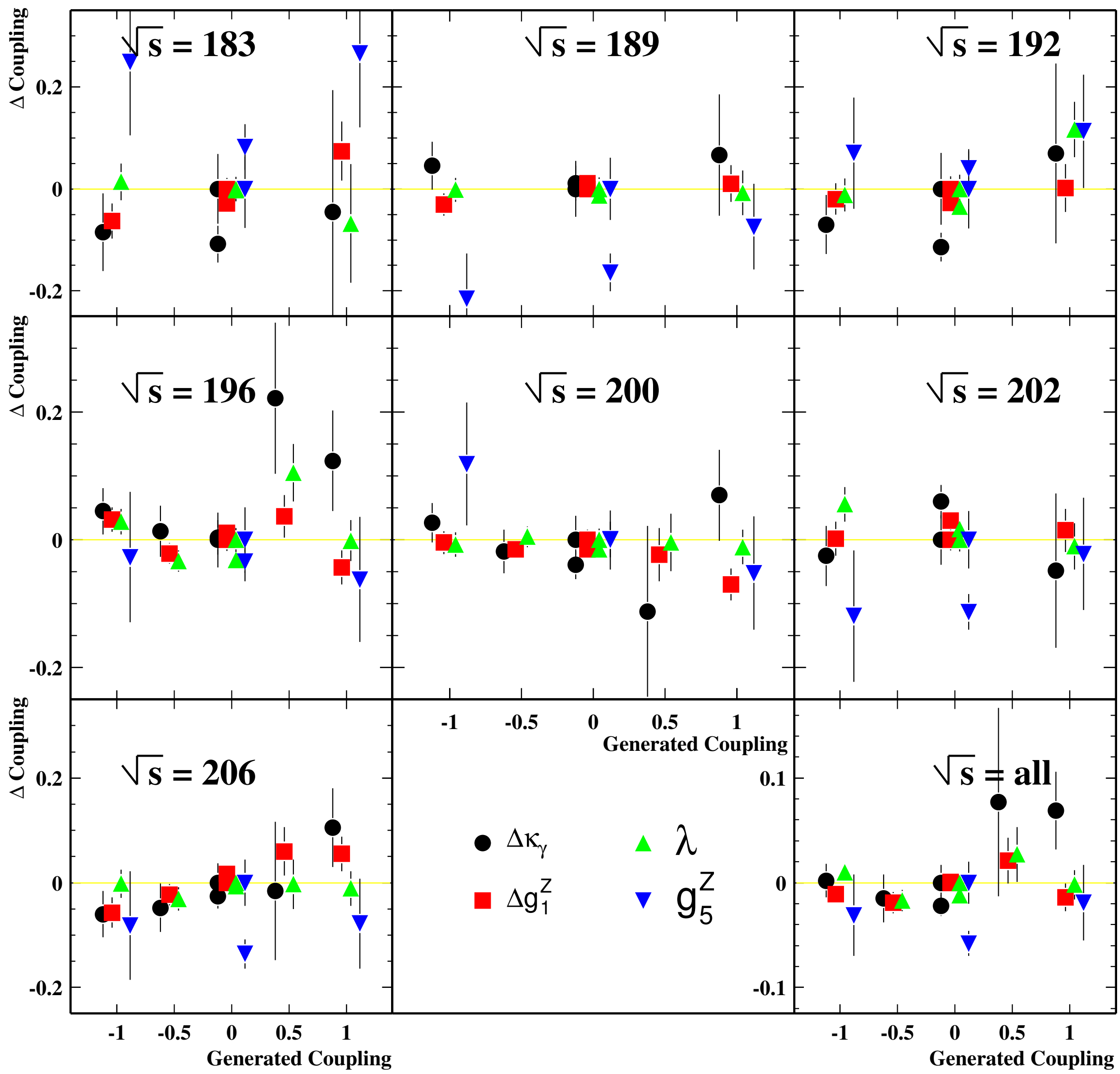

Figure 5.13: Results of high statistics bias tests for one-parameter fits to each of the four couplings. On the y-axis the difference between the measured and generated coupling is plotted (Δ coupling). The test is done at each centre-of-mass energy separately and with all energies combined. The generated couplings are displaced around their nominal values for clearness.

time, are shown in figure 5.14. They are centred around the expected values of zero, but there are some non-Gaussian tails. These tails are more pronounced if only the first or the second order optimal observable is used in the fit, but using both together resolves many of these second minima. Still, the distribution of $\Delta\kappa_\gamma$ shows a small second minimum at 1. Figure 5.15 shows the two-dimensional projections of the 3d-fit results of these experiments. The projection in the Δg_1^Z-λ plane shows the ideal behaviour: no second minima are visible and the error ellipses are clearly visible and centred around the Standard Model expectation. The correlation between these two couplings is around -0.7. For the two other projections, involving $\Delta\kappa_\gamma$, the topology is much more complex. The second minimum at $\Delta\kappa_\gamma = 1$

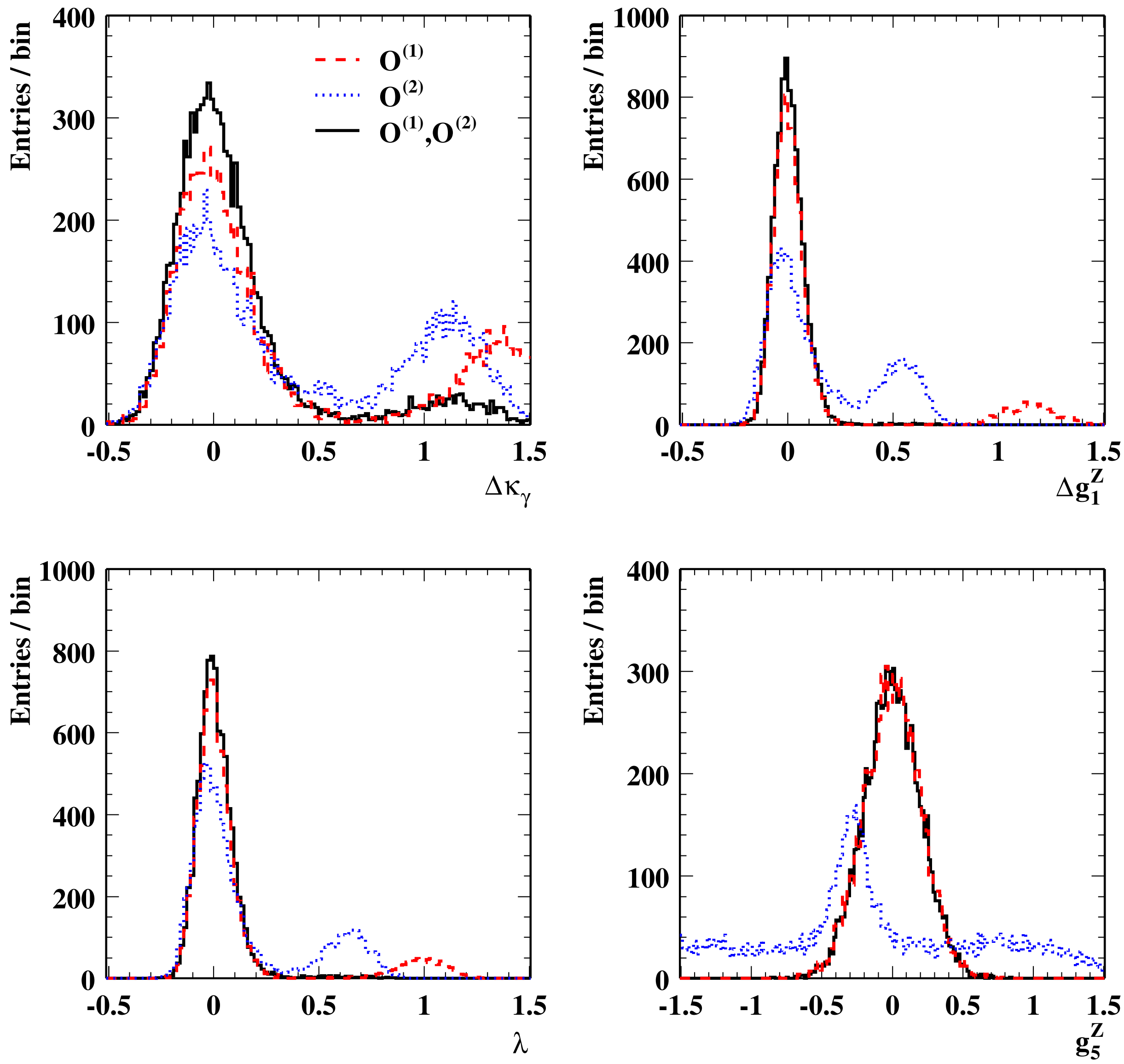

Figure 5.14: Distribution of fitted couplings from a one-parameter fit using an ensemble of 8991 simulated subsamples of the size of the expected number of events. The black histogram shows the results for using the first and second order optimal observable $\overline{\mathcal{O}}^{(1)}$ and $\overline{\mathcal{O}}^{(2)}$, while for the two other histograms only one observable is used.

from the 1d experiments is only slightly visible, but another second minimum is much more pronounced. For the $(\Delta\kappa_\gamma,\Delta g_1^Z)$ plane the largest number of experiments is centred around (0.2, -0.05) but a sizeable fraction is centred around (-0.1, 0.05). The largest number of experiments is centred around (0.2, 0.0) in the $(\Delta\kappa_\gamma,\lambda)$ plane while the second minimum is at (-0.1, 0.0).

The 1d-fit results of our MC experiments show the expected behaviour and we therefore test the reliability of the error interval, as given by the region where χ^2 is no more than 1 above its minimum value, by counting the fraction of "experiments" where the correct

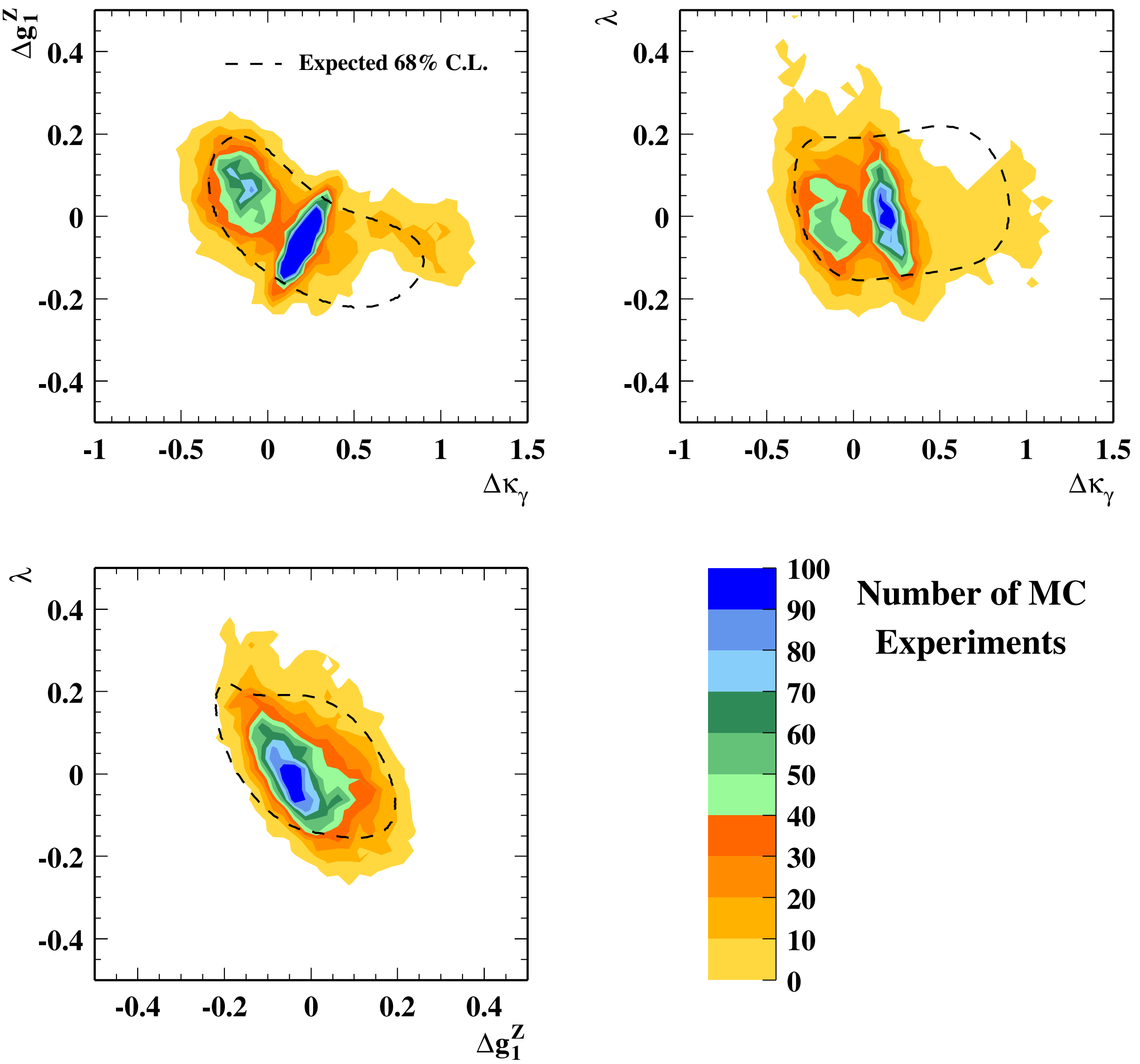

Figure 5.15: Two-dimensional projection of the fitted couplings from a three-parameter fit using an ensemble of 8991 subsamples the size of the expected data. The optimal observables of all energies are included in the fit.

value falls within this region. The error estimate is considered to be reliable if the calculated fraction is consistent with 68%; otherwise the corresponding elements of the covariance matrix for the $\overline{\mathcal{O}}$ values are scaled by the necessary factor to obtain 68% of the subsamples within the error interval. The resulting scaled covariance matrix is also used to analyse the real data. This is done separately for each fit. The resulting scale factors vary between 1.034 and 1.226 for the one-parameter fits as shown in table 5.6. The same procedure can be used to test the error estimate for the three-parameter fit of $\Delta\kappa_\gamma$, Δg_1^Z and λ. Here, $\Delta\chi^2 = 3.526$ corresponds to the 68% C.L. interval. However, in this test a scale factor of 0.945 is obtained. Also in this case, where the scale factor is smaller than one, we apply the factor to the covariance matrix.

	$\Delta\kappa_\gamma$	Δg_1^Z	λ	$\Delta\kappa_\gamma, \Delta g_1^Z, \lambda$	g_5^Z
$\mathrm{q\overline{q}q\overline{q}}$	$1.226^{+0.039}_{-0.041}$	$1.071^{+0.037}_{-0.032}$	$1.107^{+0.031}_{-0.029}$	$0.945^{+0.018}_{-0.015}$	$1.034^{+0.031}_{-0.029}$

Table 5.6: Scale factors for 68% C.L. of the $\mathrm{q\overline{q}q\overline{q}}$ channel for one- and three-parameter fits.

5.5 Systematic Errors

Systematic uncertainties are included in the measurement of the anomalous couplings at the level of the mean optimal observables. From the difference in the mean optimal observables of a systematic variation and the standard predictions, $\Delta\overline{\mathcal{O}}^d = \overline{\mathcal{O}}^{sys} - \overline{\mathcal{O}}$, a systematic covariance matrix is build. The element c_{ij} of the matrix is the product $\Delta\overline{\mathcal{O}}_i^d \times \Delta\overline{\mathcal{O}}_j^d$. The correlation between the different mean optimal observables is 100% and the sign of the product determines if the contribution from different mean optimal observables are correlated or anti-correlated. The systematic covariance matrix is added to the statistical covariance matrix and then used in the fit procedure. This procedure enlarges not only the error of the fit but can also shift the position of the best fit.

This procedure is not very useful to estimate the contribution of a single systematic uncertainty because the statistical and systematic errors are mixed together. One way to obtain this information is to add the shift in the mean optimal observables to the Standard Model predictions and fit then the anomalous couplings. The difference from the Standard Model predictions is an estimate for the size of a systematic error. Another way is to smear the Standard Model mean optimal observables using a Gaussian function, where the function is centred around the mean optimal observable and the difference $\Delta\overline{\mathcal{O}}^d$ is used as the width of the Gaussian, fit a large number of those smeared observables and use the width of the fitted distribution as an estimator for the size of this systematic uncertainty. Both estimators give almost the same results and we use the second one with 10 000 smeared samples further on. It must be remembered that this is only an estimator and the inclusion of the systematic error in the fit procedure is done using the full covariance matrix.

The following sources of systematic uncertainties are considered and their effect on the four measured couplings is shown in table 5.7. The second to last column is the quadratic sum of all uncertainties. For comparison, the expected statistical error is shown in the last column. In table B.5 to B.8 the systematic uncertainties for each centre-of-mass energy are shown. In general the behaviour of the four couplings $\Delta\kappa_\gamma$, Δg_1^Z, λ and g_5^Z is similar for each systematic uncertainty, although the effects on λ are larger compared to the other couplings for the background and final state interactions. In order to give an estimate of the importance of each systematic uncertainty, the mean value of the ratio of the systematic error to the expected statistical error, $r = \frac{\sigma_{\rm sys}}{\sigma_{\rm stat}}$, is given along with the ratios for each coupling.

$\mathcal{O}(\alpha)$ Calculations

There is a theoretical uncertainty in the $\mathcal{O}(\alpha)$ correction due to missing higher orders in the YFSWW3 Monte Carlo generator program which is used, together with KORALW1.51, to simulate the signal events. As a conservative estimate of this uncertainty, this $\mathcal{O}(\alpha)$ correction is removed using a reweighting technique, degrading the events to KORALW1.42

Source	$\Delta\kappa_\gamma$	Δg_1^Z	λ	g_5^Z
$\mathcal{O}(\alpha)$ correction	0.035	0.013	0.013	0.048
ISR	0.026	0.011	0.016	0.010
TGC matrix element	0.014	0.005	0.004	0.013
Detector simulation	0.014	0.007	0.013	0.010
Background	0.049	0.025	0.058	0.026
$\sqrt{s}$	0.002	0.001	0.001	0.003
M_W	0.019	0.008	0.013	0.034
Fragmentation	0.128	0.046	0.081	0.150
Bose-Einstein correlations	0.001	0.004	0.030	0.009
Colour reconnection	0.015	0.012	0.031	0.001
Total systematic error	0.148	0.057	0.112	0.165
Expected statistical error	0.214	0.070	0.083	0.200

Table 5.7: Contributions to the systematic uncertainties in the determination of the TGC parameters. The total systematic error is the quadratic sum of all systematic errors.

level. The effect of this change is taken as a systematic error. The mean effect of this systematic error is around 19% of the expected statistical error σ_stat ($r_{\Delta\kappa_\gamma} = 16\%$, $r_{\Delta g_1^Z} = 19\%$, $r_\lambda = 16\%$, $r_{g_5^Z} = 24\%$).

ISR modelling

KORALW includes ISR up to $\mathcal{O}(\alpha^3)$. As a conservative estimate of missing higher orders, we replace it with ISR up to $\mathcal{O}(\alpha)$ only using a reweighting technique. The mean effect of this change is around 13% of σ_stat ($r_{\Delta\kappa_\gamma} = 12\%$, $r_{\Delta g_1^Z} = 16\%$, $r_\lambda = 19\%$, $r_{g_5^Z} = 5\%$).

TGC Matrix Element Calculation

To assess the uncertainty in the TGC matrix element calculation which is used to weight our Monte Carlo events, we replace the calculation from the EXCALIBUR Monte Carlo generator program with the one from `grc4f`. Both programs use full four-fermion calculations but the implementation is based on different approaches of evaluating the matrix elements.

The mean optimal observables are calculated using the Standard Model Monte Carlo samples using the two matrix element calculations. The difference in the mean optimal observables is used as the systematic uncertainty. Unfortunately, the effect vanishes for the SM couplings because no TGC reweighting must be applied. In order to access this systematic uncertainty we evaluate the mean optimal observables with the TGC values of $\Delta\kappa_\gamma = 0.668$, $\Delta g_1^Z = -0.084$, $\lambda = -0.076$ and $g_5^Z = 0$. These numbers are the fitted values, where the three C and P conserving couplings $\Delta\kappa_\gamma$, Δg_1^Z and λ are varied at the same time and g_5^Z is set to its Standard Model value. In addition to the $\mathrm{q\overline{q}q\overline{q}}$ final state the $\mathrm{q\overline{q}}\ell\bar{\nu}_\ell$ and $\ell\bar{\nu}_\ell\bar{\ell}'\nu_{\ell'}$ final states are included in the fit procedure and therefore these numbers represent our best description of the data. These values affect not only the optimal observables for

$\Delta\kappa_\gamma$, Δg_1^Z and λ but also for g_5^Z. The estimate of this uncertainty is around 6% of the expected statistical error ($r_{\Delta\kappa_\gamma} = 7\%$, $r_{\Delta g_1^Z} = 7\%$, $r_\lambda = 5\%$, $r_{g_5^Z} = 6\%$).

Detector Uncertainties

The Monte Carlo simulation of the OPAL detector has been studied using back-to-back jets and leptons in Z events collected during calibration runs. All Monte Carlo samples used in this analysis are smeared using the `WWFIX` routine from the OPAL `WW` package in order to achieve the best agreement with data.

The uncertainties on the used scaling and smearing factors can be accessed using the `WWFIX` routine. For hadronic events the following five uncertainties have been considered:

Jet energy scale uncertainty: The jet energy scale corrections are smeared by their estimated uncertainties. This is 0.4% over the full jet angle range $\cos\theta$, except for the last bin of $\cos\theta$ where the uncertainty is 0.5%.

Jet energy resolution uncertainty: The corrections of the jet energy errors for Monte Carlo are smeared by their statistical error. In the central region of the jet angle $\cos\theta$ the error is 0.006 but increases to 0.02 for forward jets ($|\cos\theta| > 0.85$).

Jet angular resolution uncertainty: The corrections to the jet angle errors for Monte Carlo are smeared by their statistical errors of 0.004 for $\cos\theta$ and 0.003 for ϕ.

Jet angular bias: The $\cos\theta$ distribution is shifted by $\frac{1}{2}\delta(\cos\theta)$, where $\delta(\cos\theta)$ is the parametrisation of a small bias seen in the comparison between data and Monte Carlo as a function of $\cos\theta$.

Jet energy linearity: The jet energy in `WWFIX` is multiplied by an additional factor $1 + \beta(E - 45)$ with $\beta = -2.0 \times 10^{-4}\,\mathrm{GeV}^{-1}$. β is smeared by its uncertainty of $\beta = 0.3 \times 10^{-4}\,\mathrm{GeV}^{-1}$.

The uncertainties in these corrections correspond to variations in our results which are taken as systematic errors. These corrections are usually applied *after* the event selection. To estimate their effect on the selection of our sample, they were applied as a systematic check *before* the event selection. The overall effect in the detector simulation is around 10% of the expected statistical error ($r_{\Delta\kappa_\gamma} = 7\%$, $r_{\Delta g_1^Z} = 10\%$, $r_\lambda = 16\%$, $r_{g_5^Z} = 5\%$).

Background

Uncertainties in the background estimation are determined by varying both its shape and normalisation. For the TGC-independent four-fermion background we use EXCALIBUR and `grc4f` instead of KORALW. For the $Z/\gamma \to q\overline{q}$ background we use KK2F with HERWIG or ARIADNE rather than PYTHIA fragmentation and use the largest observed difference. In addition, the normalisations of these two background sources are scaled, each one at a time, by the factors 1.1 and 1.15 respectively for centre-of-mass energies of 183 and 189 GeV [22]. At higher energies we apply a safety factor of 2 which gives scale factors of 1.2 and 1.3 because not all systematic studies have been done in full detail yet. We take all single variations as an estimate of the systematic error. The overall effect of the background simulation is with around 35% of σ_{stat} the second largest systematic uncertainty ($r_{\Delta\kappa_\gamma} = 22\%$, $r_{\Delta g_1^Z} = 35\%$, $r_\lambda = 70\%$, $r_{g_5^Z} = 13\%$).

Centre-of-mass Energy

The effect of the centre-of-mass energy uncertainty of 50 MeV at 183 GeV and 40 MeV for higher energies is estimated by using Monte Carlo samples at different centre-of-mass energies as pseudo-data. The difference in the mean optimal observables is rescaled from the energy difference in the Monte Carlo samples to the appropriate energy uncertainty. The shift in the optimal observables is rather small giving a systematic error of 1 – 2% of the statistical error.

W Mass

For the W mass, we assume $M_{\mathrm{W}} = 80.456 \pm 0.059\,\mathrm{GeV}/c^2$ [156–158], which is the W mass measured at the Tevatron. The LEP 2 results for the mass are not used for the TGC measurement, since they have been obtained under the assumption that W pairs are produced according to the Standard Model, whereas the by far dominant W-production channel at the Tevatron ($\mathrm{q\overline{q}'} \to \mathrm{W}^{\pm}$) does not involve any triple gauge boson vertex. This mass is $0.126\,\mathrm{GeV}/c^2$ higher than the one used in our Monte Carlo generators. We do not correct our TGC fit results for this shift in M_{W}, but it is accounted for in our systematic error, along with the M_{W} measurement error. The effect of this shift in M_{W} is assessed using Monte Carlo samples generated with six different W masses centred around our nominal W mass of $80.3\,\mathrm{GeV}/c^2$. Our systematic error is calculated taking into account this shift and its uncertainty. The mean effect of this uncertainties is around 13% of σ_{stat} ($r_{\Delta\kappa_\gamma} = 9\%$, $r_{\Delta g_1^{\mathrm{z}}} = 11\%$, $r_\lambda = 16\%$, $r_{g_5^{\mathrm{z}}} = 17\%$).

Fragmentation and Hadronisation

Another uncertainty in the Monte Carlo generators is related to the Jetset fragmentation and hadronisation model which is used for all standard OPAL Monte Carlo samples. To study the effect of this uncertainty we compare results of the analysis when applied to pure $\mathrm{W^+W^-}$ Monte Carlo samples generated with Koralw1.42 using either Jetset7.408, Herwig6.201 or Ariadne4.08 for the fragmentation and hadronisation phase. The adjustment of the Jetset parameters for the standard OPAL Jetset tune [159] is done by performing a global fit to various OPAL and LEP measurements. The fit uses OPAL measurements of event shape distributions such as thrust, the mean charged particle multiplicity in c and b events, the single particle inclusive momentum spectra for $\pi^\pm$, $\mathrm{K}^\pm$, $\mathrm{p(\bar{p})}$ and Λ, and to the LEP measurements of the single particle inclusive production rates of 26 identified hadrons in hadronic Z decays. Additionally, we use an older OPAL Jetset tune [160], which concentrates more on event shape properties in the tuning process. The tuning of the Herwig fragmentation parameters [161] is done in the same way as for the standard OPAL Jetset tune. In contrast, Ariadne is used with the default settings. Only the Jetset parameters for the hadronisation process, which is interfaced to Ariadne, are taken from the ALEPH collaboration [162]. All tunings describe the OPAL data reasonable well.

In order to study the effect of these four different fragmentation and hadronisation tunes, samples of 1 million pure $\mathrm{W^+W^-}$ events are generated with Koralw at 188.6, 199.5 and 206 GeV, and subsequently fragmented using each of the four tunes. The use of the same four-vectors to produce the Monte Carlo sample for the four fragmentation tunes reduces the statistical fluctuation from independent event samples and the effects from the different tunes can be studied with higher precision.

In table 5.8 the expected systematic errors for the three non-standard tunes compared to the standard JETSET tune are shown for the three energies and for all eight energies combined. For the energies with no dedicated Monte Carlo samples the $\Delta\overline{\mathcal{O}}^d_{f/h}$ from the nearest energy is used instead. The energy dependence of the effect is not very pronounced and Ariadne shows the strongest variation with the centre-of-mass energy. The effect of HERWIG is the largest and is used to estimate the uncertainty.

HERWIG predicts a higher probability of correct jet pairing and correct W charge assignment than JETSET. This effect is partially due to the average charged multiplicity for light quarks being lower in our tuned version of HERWIG than in JETSET. Since the data are in agreement with JETSET, we weight the HERWIG Monte Carlo events so as to reproduce the same charged multiplicity distribution as JETSET. The effect of this weighting is a reduction of the systematic error by about 15 – 30% for the couplings $\Delta\kappa_\gamma$, Δg_1^Z and λ. In order to describe this systematic effect as good as possible at the centre-of-mass energies, where no dedicated Monte Carlo samples are available, we perform a linear fit to the difference in the mean optimal observables $\Delta\overline{\mathcal{O}}^d_{f/h}$ and calculate $\Delta\overline{\mathcal{O}}^d_{f/h}$ at the other energies. This interpolation decreases only very slightly the effect on the triple gauge boson couplings of this uncertainty.

After this detailed estimation of fragmentation and hadronisation uncertainties, the overall systematic error is with around 75% the dominant systematic error for all four couplings ($r_{\Delta\kappa_\gamma} = 60\%$, $r_{\Delta g_1^Z} = 65\%$, $r_\lambda = 98\%$, $r_{g_5^Z} = 75\%$). For λ this systematic uncertainty is almost equal to the expected statistical error.

Bose-Einstein Correlations

Bose-Einstein correlations (BEC) in $\mathrm{q\overline{q}q\overline{q}}$ events might affect the reconstruction of W bosons and measured W charge distribution. We investigate this effect with a set of Monte Carlo samples simulating BEC via re-shuffling of final state momenta as discussed in section A.4 in the appendix. The standard OPAL Monte Carlo samples are generated without any BEC, hence we investigate the effect of intra-W BEC and full BEC on our analysis. Samples of 150 000 $\mathrm{W^+W^-}$ events at an energy of 188.6 GeV and 100 000 $\mathrm{W^+W^-}$ events at 199.5 and 206 GeV where generated using the PYTHIA Monte Carlo generator using the PYBOEI model (see section A.4 in the appendix) and are listed in table B.2. For the samples with intra-W BEC and full BEC, the option BE_{32} is used with `PARJ(92)` $(\equiv \lambda) = 2.15$ and `PARJ(93)` $= 0.26\,\mathrm{GeV}$, which leads to $r = 0.73\,\mathrm{fm}$. The JETSET fragmentation and hadronisation parameters have been retuned to give good agreement between data and Monte Carlo predictions.

The expected systematic errors are listed in table 5.9 for the three energies and all eight energies combined. For the energies without dedicated Monte Carlo samples the $\Delta\overline{\mathcal{O}}^d_{\mathrm{BEC}}$ nearest in energy is used. In contrast to the bias from fragmentation and hadronisation, BEC leads to a systematic effect, which depends strongly on the centre-of-mass energy. Hence, the overall uncertainty on the combined measurement is reduced in comparison to the contributions from the single energies. When both inter W and intra W correlations are taken into account, the bias is found to be larger than the case where only intra W boson correlations are present. The mean uncertainty is around 12% of the expected statistical error ($r_{\Delta\kappa_\gamma} < 1\%$, $r_{\Delta g_1^Z} = 6\%$, $r_\lambda = 36\%$, $r_{g_5^Z} = 5\%$), whereas the effect on λ is very strong compared to the other three couplings.

Colour Reconnection

Colour reconnection can disturb the distribution of W decay products in $q\bar{q}q\bar{q}$ events and hence affect the jet reconstruction and the measured W charge distribution. See section A.5 in the appendix for more details.

To study this effect the Sjöstrand-Khoze (SK) models SK-I, SK-II and SK-II' are considered. In the SK-I model the reconnection probability is a free parameter, while it is fixed in both type II models. Several Monte Carlo samples with and without colour reconnection where generated at three centre-of-mass energies (188.6, 199.5 and 206 GeV). Samples of 500 000 $W^+W^- \to q\bar{q}q\bar{q}$ events without colour reconnection where generated using the KORALW Monte Carlo generator, with fragmentation carried out using the JETSET7.408 model at all three energies. The same four-vectors where used to produce Monte Carlo samples for the scenarios SK-I ($k_I = 100$), SK-II and SK-II'. The fragmentation was carried out again using the appropriate colour reconnection model. With this procedure statistical fluctuations from independent event samples are reduced and the effects from colour reconnection can be studied with higher precision. SK-I scenarios with a k_I different from 100 can be studied by mixing events from the SK-I sample with $k_I = 100$ and the Monte Carlo sample without colour reconnection.

For systematic studies we consider the scenarios SK-I with $k_I = 100$ and $k_I = 0.9$, SK-II and SK-II'. In table B.3 in the appendix the used Monte Carlo run numbers and the reconnection probabilities, P^r, are listed for the three considered energies. The probability is between 35% and 40% for SK-I with $k_I = 0.9$ and between 13% and 20% for SK-II and SK-II'.

In table 5.10 the systematic shift on the measurement of anomalous couplings is shown for the three considered energies and the combined energies. The effect of colour reconnection depends, as BEC, strongly on the centre-of-mass energy. Scenario SK-I with $\rho = 100$ produces the largest effect and we take this scenario as a conservative estimate for the effect of colour reconnection. The mean uncertainty is around 15% of σ_{stat} ($r_{\Delta\kappa_\gamma} = 7\%$, $r_{\Delta g_1^Z} = 17\%$, $r_\lambda = 37\%$, $r_{g_5^Z} < 1\%$), whereas the effect on λ is very strong compared to the other three couplings, as in the case of BEC.

5.6 Results

The results for various one-parameter fits are listed in table 5.11. We give for each centre-of-mass energy the fit results for the four CP conserving couplings $\Delta\kappa_\gamma$, Δg_1^Z, λ and g_5^Z using the corresponding first and second order optimal observable $\overline{\mathcal{O}}_i^{(1)}$ and $\overline{\mathcal{O}}_i^{(2)}$. For comparison, the expected statistical error is listed, reflecting both the sensitivity and the integrated luminosity at the considered energy. The systematic uncertainties are included via a systematic covariance matrix and each fit is repeated. The corresponding $\log L$ curves[2]

[2]Following the convention in LEP, we display our results by the logarithm of the likelihood function, $\log L$, related to the χ^2-function by, $-\log L = \chi^2/2$. The plotted function is $-\Delta\log L$, which is obtained by subtracting from $-\log L$ its minimum value.

	κ_γ				g_1^Z				λ				g_5^Z			
Had model	189	200	206	all	189	200	206	all	189	200	206	all	189	200	206	all
Old JETSET	7.8	8.4	7.4	8.3	2.2	3.2	3.1	2.9	4.1	4.0	4.2	4.2	-2.5	-0.4	-0.8	-1.0
HERWIG	-18.1	-18.0	-15.5	-17.8	-6.6	-6.9	-6.3	-6.9	-9.7	-9.8	-8.6	-9.6	-5.8	-3.0	-3.8	-4.0
Ariadne	0.7	0.2	-1.4	-0.2	-0.3	0.0	-1.1	-0.4	0.5	0.8	-0.2	0.4	-4.9	1.9	-3.1	-1.6
HERWIG[a]	-15.5	-13.1	-10.8	-12.9	-5.2	-4.6	-3.8	-4.9	-8.6	-8.2	-7.2	-8.2	-17.1	-14.9	-14.2	-15.5
HERWIG[b]				-12.8				-4.6				-8.1				-15.0

[a]Weighted to reproduce charged multiplicity distribution as JETSET.

[b]Linear interpolation of $\Delta\overline{\mathcal{O}}^{d}_{f/h}$ at energies without dedicated Monte Carlo samples.

Table 5.8: Bias (in $\times 10^{-2}$) from different fragmentation and hadronisation tunes to the measurement of anomalous couplings.

	κ_γ				g_1^Z				λ				g_5^Z			
BE model	189	200	206	all	189	200	206	all	189	200	206	all	189	200	206	all
intra BEC	3.5	0.5	-5.0	-2.3	1.4	-0.4	-3.9	-0.9	4.4	5.3	-0.5	2.7	-6.3	0.3	8.2	1.4
full BEC	11.9	0.1	-7.2	0.1	4.3	0.2	-3.5	-0.4	5.5	3.5	-0.8	3.0	-3.0	-0.3	5.0	0.9

Table 5.9: Bias (in $\times 10^{-2}$) from different Bose Einstein models to the measurement of anomalous couplings.

	κ_γ				g_1^Z				λ				g_5^Z			
CR model	189	200	206	all	189	200	206	all	189	200	206	all	189	200	206	all
SK-I ($k_I = 100$)	1.9	-0.6	1.0	0.6	0.4	-0.1	0.5	0.2	1.1	0.2	1.0	0.7	0.4	0.1	-0.1	0.1
SK-I ($k_I = 0.9$)	2.9	-0.2	2.5	1.5	1.5	0.7	1.6	1.2	3.7	2.9	2.5	3.1	2.7	0.0	-1.8	0.1
SK-II	0.8	-0.3	1.6	0.7	-0.2	0.1	0.5	0.1	1.0	-0.6	0.2	0.1	3.2	0.2	-0.2	0.8
SK-II'	0.1	-2.3	2.8	0.1	-0.1	-0.6	1.2	0.8	-0.3	-0.8	-0.1	-0.4	-0.1	0.4	-0.3	0.0

Table 5.10: Bias (in $\times 10^{-2}$) from different colour reconnection models to the measurement of anomalous couplings.

for the different energies are shown in figure 5.16.

The combination of all eight energies is summarised in the last row of table 5.11. The following results are obtained from one-parameter fits including only the statistical error:

$$\begin{aligned} \Delta\kappa_\gamma &= 0.18^{+0.44}_{-0.22} \\ \Delta g_1^{\mathrm{Z}} &= 0.08^{+0.09}_{-0.08} \\ \lambda &= 0.00^{+0.09}_{-0.07} \end{aligned} \tag{5.12}$$

for the three C and P conserving couplings and

$$g_5^Z = -0.41^{+0.21}_{-0.21} \tag{5.13}$$

for the C and P violating but CP conserving coupling g_5^Z. Including the systematic uncertainties the results for the one-parameter fits are

$$\begin{aligned} \Delta\kappa_\gamma &= 0.17^{+0.72}_{-0.28} \\ \Delta g_1^{\mathrm{Z}} &= 0.09^{+0.11}_{-0.10} \\ \lambda &= 0.01^{+0.33}_{-0.14} \end{aligned} \tag{5.14}$$

for the three C and P conserving couplings and

$$g_5^Z = -0.37^{+0.24}_{-0.26} \tag{5.15}$$

for the C and P violating but CP conserving coupling g_5^Z.

The measured couplings are consistent with the Standard Model predictions. At some energies a second minimum is pronounced which is not totally excluded and therefore these measurements have asymmetric errors. This behaviour is very pronounced for $\Delta\kappa_\gamma$, but the combination of all energies resolves these second minima as can be seen from the $\log L$ functions (figure 5.16).

To study correlations between the three C and P conserving couplings $\Delta\kappa_\gamma$, Δg_1^{Z} and λ, we perform two- and three-parameter fits with either two or three free parameters at the time, while g_5^Z is always fixed at its Standard Model value. The results for the three-parameter fit including only statistical errors are

$$\begin{aligned} \Delta\kappa_\gamma &= +0.14^{+0.56}_{-0.23} \\ \Delta g_1^{\mathrm{Z}} &= +0.13^{+0.12}_{-0.16} \\ \lambda &= -0.14^{+0.10}_{-0.09} \end{aligned} \tag{5.16}$$

where the correlation coefficients are -0.64, -0.23 and -0.43 between ($\Delta\kappa_\gamma$, Δg_1^{Z}), ($\Delta\kappa_\gamma$, λ) and (Δg_1^{Z}, λ), respectively. Including systematic uncertainties the results are

$$\begin{aligned} \Delta\kappa_\gamma &= +0.02^{+0.72}_{-0.24} \\ \Delta g_1^{\mathrm{Z}} &= +0.14^{+0.12}_{-0.20} \\ \lambda &= -0.09^{+0.17}_{-0.12} \end{aligned} \tag{5.17}$$

with correlation coefficients of -0.58, -0.60 and -0.08 between ($\Delta\kappa_\gamma$, Δg_1^{Z}), ($\Delta\kappa_\gamma$, λ) and (Δg_1^{Z}, λ), respectively. The inclusion of the systematic uncertainties changes the correlation between the three couplings, which leads to slightly shifted central values. The listed errors corresponds to $\Delta\chi^2 = 1$ in order to compare them with the measurements from the various one-parameter fit.

The two-dimensional projection of the 68% and 95% C.L. contours are shown in figure 5.17 for the three parameter combinations. For comparison, the corresponding likelihood contours are plotted for a two-parameter fit where the third parameter is fixed at its Standard Model value. In both cases, the 68% and 95% contours correspond to $\Delta\chi^2 = 2.296$ ($\Delta\log L = 1.148$) and $\Delta\chi^2 = 5.99$ ($\Delta\log L = 2.995$), respectively. These are the $\log L$ definitions for the 2 dimensional case. As expected, the contours are not very symmetric which is an indication that not all second minima are resolved. For example the contours in the ($\Delta\kappa_\gamma$, λ) and (Δg_1^Z, λ) plane from the three-parameter fit look like they consist of two error ellipsis. But the sensitivity of this final state alone is not high enough to make a second minimum visible.

Energy		$\Delta\kappa_\gamma$	Δg_1^Z	λ	g_5^Z
183 GeV	Without systematic	$1.49^{+0.89}_{-1.51}$	$0.37^{+0.57}_{-0.37}$	$0.28^{+1.05}_{-0.39}$	$0.27^{+1.00}_{-1.01}$
	Expected errors	±0.97	±0.33	±0.44	±1.09
	Including systematics	$1.49^{+0.91}_{-1.58}$	$0.37^{+0.57}_{-0.38}$	$0.28^{+1.21}_{-0.42}$	$0.26^{+1.03}_{-1.03}$
189 GeV	Without systematic	$0.21^{+1.47}_{-0.47}$	$0.11^{+0.22}_{-0.15}$	$0.04^{+0.23}_{-0.17}$	$-0.04^{+0.46}_{-0.47}$
	Expected errors	±0.53	±0.16	±0.20	±0.48
	Including systematics	$0.21^{+1.49}_{-0.53}$	$0.12^{+0.27}_{-0.18}$	$0.08^{+0.38}_{-0.25}$	$-0.07^{+0.49}_{-0.51}$
192 GeV	Without systematic	$-0.51^{+2.94}_{-0.65}$	$-0.15^{+0.44}_{-0.27}$	$0.05^{+0.58}_{-0.33}$	$0.81^{+1.16}_{-1.15}$
	Expected errors	±0.92	±0.35	±0.44	±1.13
	Including systematics	$-0.51^{+2.94}_{-0.67}$	$-0.15^{+0.46}_{-0.28}$	$0.05^{+0.62}_{-0.34}$	$0.82^{+1.17}_{-1.16}$
196 GeV	Without systematic	$-0.27^{+0.51}_{-0.37}$	$-0.15^{+0.16}_{-0.14}$	$-0.15^{+0.19}_{-0.16}$	$-0.35^{+0.62}_{-0.65}$
	Expected errors	±0.60	±0.22	±0.26	±0.61
	Including systematics	$-0.27^{+0.55}_{-0.39}$	$-0.16^{+0.17}_{-0.15}$	$-0.15^{+0.24}_{-0.19}$	$-0.29^{+0.63}_{-0.67}$
200 GeV	Without systematic	$0.80^{+0.67}_{-1.00}$	$0.17^{+0.40}_{-0.23}$	$0.05^{+0.27}_{-0.19}$	$-0.27^{+0.59}_{-0.61}$
	Expected errors	±0.58	±0.22	±0.27	±0.59
	Including systematics	$0.79^{+0.69}_{-1.01}$	$0.17^{+0.40}_{-0.23}$	$0.06^{+0.32}_{-0.21}$	$-0.27^{+0.61}_{-0.64}$
202 GeV	Without systematic	$1.58^{+0.48}_{-0.77}$	$-0.12^{+0.35}_{-0.20}$	$-0.30^{+0.21}_{-0.18}$	$-0.17^{+0.79}_{-0.86}$
	Expected errors	±0.67	±0.27	±0.31	±0.78
	Including systematics	$1.58^{+0.50}_{-0.84}$	$-0.12^{+0.38}_{-0.21}$	$-0.29^{+0.22}_{-0.19}$	$-0.13^{+0.80}_{-0.88}$
205 GeV	Without systematic	$1.14^{+0.34}_{-0.47}$	$0.51^{+0.18}_{-0.22}$	$0.69^{+0.18}_{-0.23}$	$-0.30^{+0.49}_{-0.51}$
	Expected errors	±0.47	±0.18	±0.21	±0.51
	Including systematics	$1.17^{+0.35}_{-0.48}$	$0.52^{+0.19}_{-0.23}$	$0.69^{+0.20}_{-0.25}$	$-0.34^{+0.52}_{-0.56}$
207 GeV	Without systematic	$0.15^{+0.47}_{-0.30}$	$0.04^{+0.16}_{-0.12}$	$0.05^{+0.65}_{-0.16}$	$-1.15^{+0.43}_{-0.46}$
	Expected errors	±0.39	±0.15	±0.17	±0.38
	Including systematics	$0.15^{+0.52}_{-0.32}$	$0.03^{+0.17}_{-0.13}$	$0.05^{+0.66}_{-0.19}$	$-1.11^{+0.48}_{-0.55}$
all	Without systematic	$0.18^{+0.44}_{-0.22}$	$0.08^{+0.09}_{-0.08}$	$0.00^{+0.09}_{-0.07}$	$-0.41^{+0.21}_{-0.21}$
	Expected errors	±0.21	±0.07	±0.08	±0.20
	Including systematics	$0.17^{+0.72}_{-0.28}$	$0.09^{+0.11}_{-0.10}$	$0.01^{+0.33}_{-0.14}$	$-0.37^{+0.24}_{-0.26}$
	95% C.L. limits	$[-0.31, 1.28]$	$[-0.08, 0.34]$	$[-0.24, 0.67]$	$[-0.89, 0.10]$

Table 5.11: Measured values of TGC parameters from the $\mathrm{q\bar{q}q\bar{q}}$ final state for each centre-of-mass energy and all energies combined. Only one parameter is varied at the time and for the other parameters the Standard Model values are assumed.

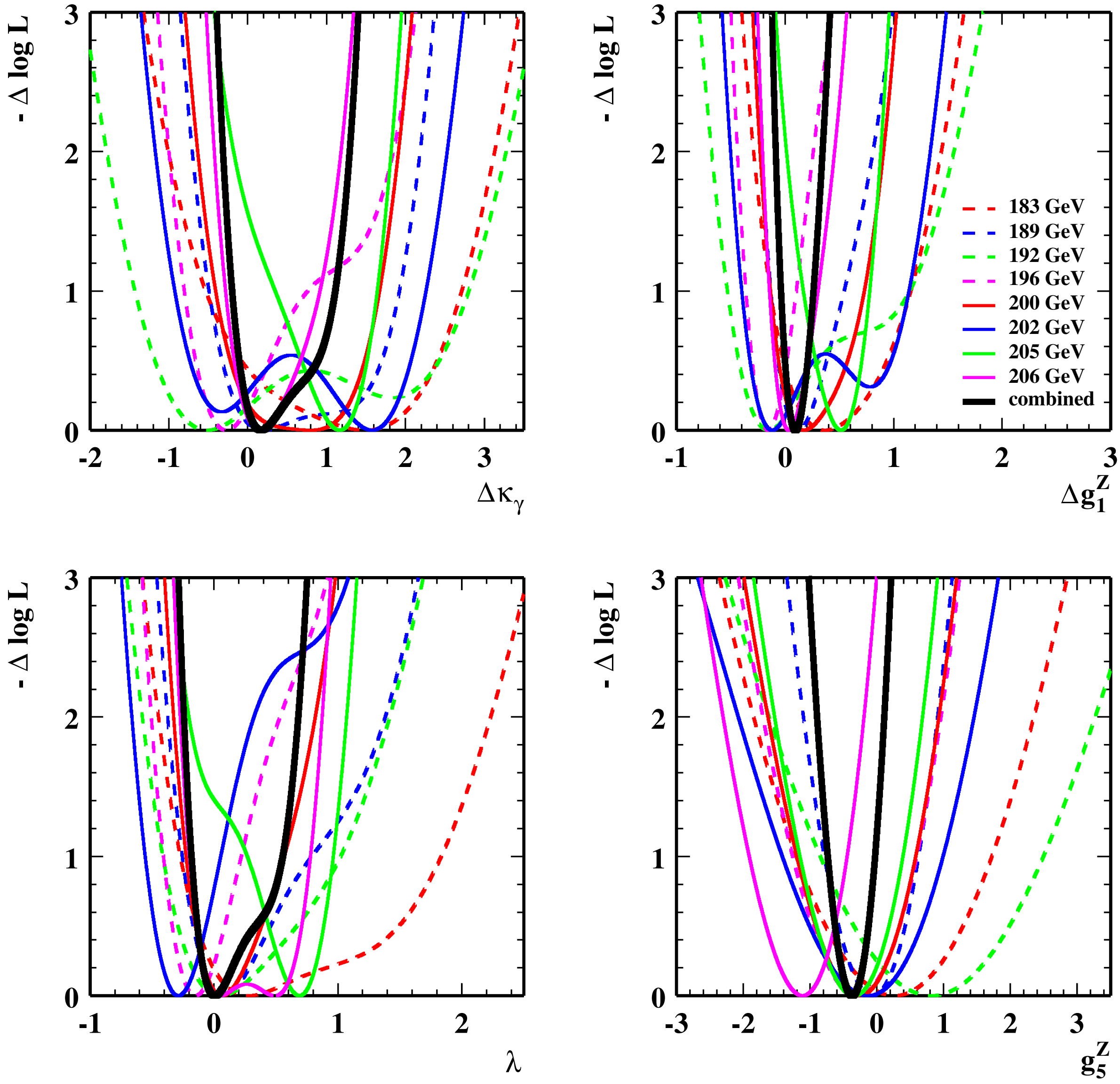

Figure 5.16: Negative log-likelihood curves for the four CP conserving couplings $\Delta\kappa_\gamma$, Δg_1^Z, λ and g_5^Z for each centre-of-mass energy separately (solid and dashed lines) and all energies combined (thick black line). The systematic errors are included. The curves for each TGC parameter are obtained by setting the other three parameters to their Standard Model values.

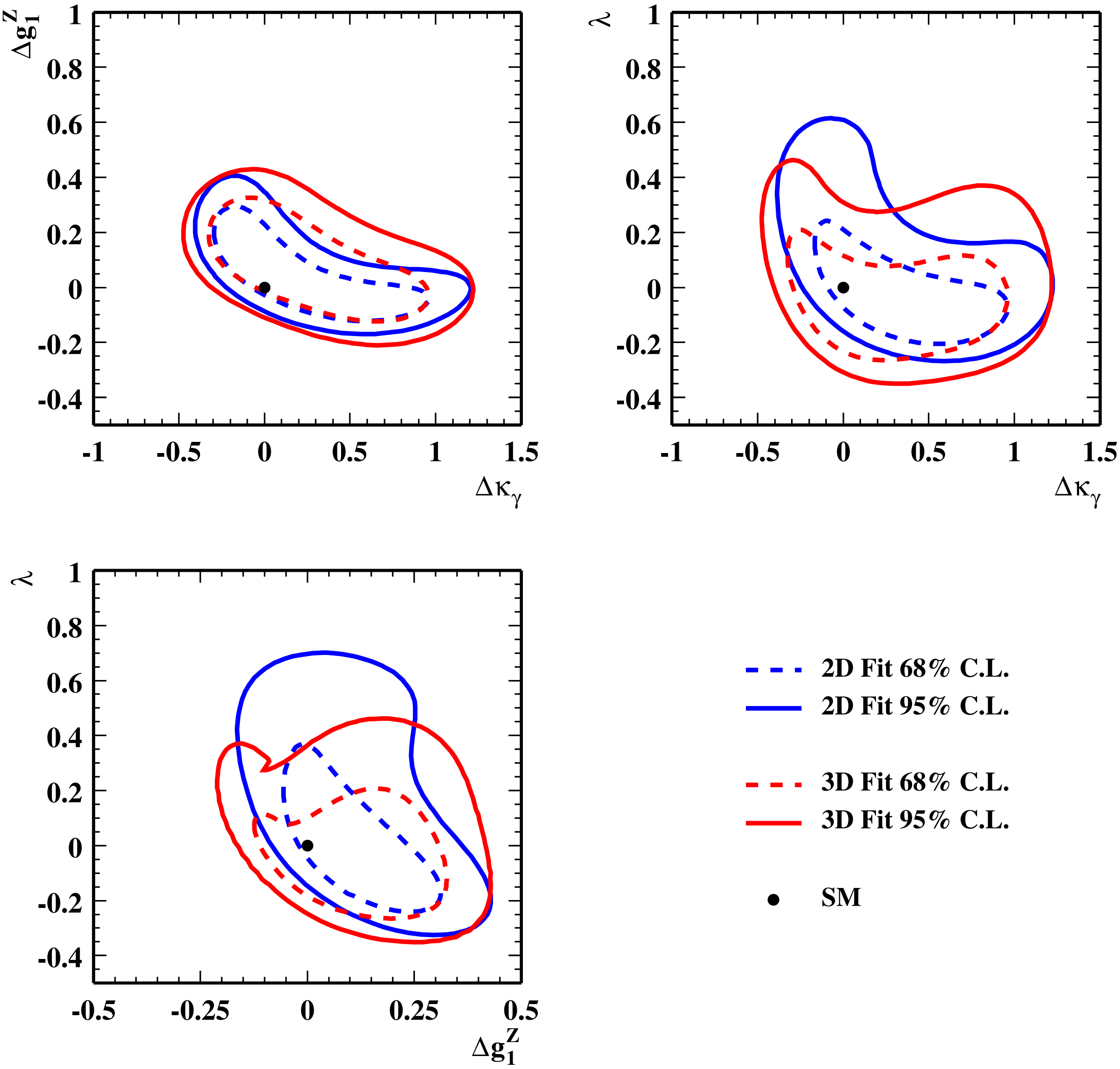

Figure 5.17: The 68% ($\Delta\log L = 1.148$) and 95% ($\Delta\log L = 2.995$) likelihood contour plots for two- and three parameter fits. In the case of a two-parameter fit the third parameter is fixed at its Standard Model value. In the case of the three-parameter fit, the curve is a projection onto the two-dimensional plane of the envelope of the three-dimensional $\Delta\log L$ surface. The dots indicate the Standard Model expectations.

Chapter 6

Combination with Other TGC Measurements

In the previous chapter we discussed the measurement of triple gauge boson couplings in the hadronic final state of W pairs in great detail. Here, some details are given for the other two W-pair final states, i. e. leptonic and semileptonic. Furthermore, the combination of these three analyses with the analysis of the total cross-section is explained.

W-pair production is only one of three reactions in e^+e^- collisions which are sensitive to charged current triple gauge boson couplings. OPAL and the other three LEP experiments analysed not only the W pair but also the single-W and single-γ production to measure triple gauge boson couplings. We give some details about the analysis methods used and show the combined results of all four LEP experiments.

At the end of this chapter we give a short introduction to di-boson production at hadron colliders, especially at the Tevatron. It is sensitive to charged current triple gauge boson couplings. The measurements at Run 1 from the CDF and D0 experiments are summarised and compared to the LEP measurements.

6.1 W-Pair Production at OPAL

At OPAL the analysis of W pairs is split into two parts. In the event rate analysis only the total cross-section is used to measure triple gauge boson couplings, while in the event shape analysis only normalised distributions are used. The three different final states, $\ell^+\nu_\ell\ell'^-\bar{\nu}_{\ell'}$, $\mathrm{q}\overline{\mathrm{q}}'\ell\bar{\nu}_\ell$ and $\mathrm{q}\overline{\mathrm{q}}'\mathrm{q}''\overline{\mathrm{q}}'''$, are treated separately at the selection and reconstruction stage, because of their different properties. As explained in section 3.4 not all final states can be fully reconstructed. In the semileptonic final state only the decay angles of the hadronically decaying W have one ambiguity while in the hadronic final state all decay angles have this ambiguity. The leptonic final state cannot be reconstructed at all without imposing energy and momentum conservation and two further constraints.

After giving some details common to all three event shape analyses, we briefly discuss the $\mathrm{q}\overline{\mathrm{q}}\ell\bar{\nu}_\ell$ and $\ell\bar{\nu}_\ell\bar{\ell}'\nu_{\ell'}$ selection and reconstruction [163]. The $\mathrm{q}\overline{\mathrm{q}}\mathrm{q}\overline{\mathrm{q}}$ channel was already discussed in chapter 5. The analysis method is outlined and the final results from the OPAL experiment of triple gauge boson couplings using W pairs are given.

W-Pair Event Selection and Reconstruction

W-pair events are selected with the same procedure used in the W-pair cross-section measurement as described in references [21, 22]. There are three independent selections corresponding to the three final states. Each candidate is then reconstructed in order to obtain the maximum possible information on the W production and decay angles, which are needed to extract the couplings. Events which cannot be well reconstructed are rejected from the sample, as will be described below. The numbers of candidates left at the different centre-of-mass energies for the three final states are listed, along with the expected values, in table 6.1.

Three kinematic fits with different sets of requirements are used in the event reconstruction:

A. Require conservation of energy and momentum, neglecting ISR.

B. Additionally constrain the reconstructed masses of the two W-bosons to be equal.

C. Additionally constrain each reconstructed W mass to the average measured value from the Tevatron $M_{\mathrm{W}} = 80.456\,\mathrm{GeV}/c^2$ [156–158].

For $\mathrm{q\bar{q}q\bar{q}}$ events, where all four final state fermions are measurable, fits A, B and C have 4, 5 and 6 constraints respectively. For $\mathrm{q\bar{q}e\bar{\nu}_e}$ and $\mathrm{q\bar{q}}\mu\bar{\nu}_\mu$ events the number of constraints is reduced by 3 due to the invisible neutrino. For $\mathrm{q\bar{q}}\tau\bar{\nu}_\tau$ events there is at least one additional unobserved neutrino from the τ decay, resulting in a loss of one constraint. The momentum sum of the track(s) assigned to the τ can still be used as an approximation of the τ flight direction, relying on its high boost, but the τ energy is left unknown. Finally for $\ell\bar{\nu}_\ell\bar{\ell}'\nu_{\ell'}$ events, where none of the leptons is a τ, there are two invisible neutrinos. Hence, six constraints are lost and only requirement C is applied.

$\sqrt{s}$	$\int \mathcal{L}dt$	$\mathrm{q\bar{q}}\ell\bar{\nu}_\ell$ events		$\mathrm{q\bar{q}q\bar{q}}$ events		$\ell\bar{\nu}_\ell\bar{\ell}'\nu_{\ell'}$ events	
[GeV]	[pb^{-1}]	Observed	Expected	Observed	Expected	Observed	Expected
182.7	57.4	328	331.1	408	418.9	32	37.4
188.6	183.0	1090	1123.5	1437	1388.3	130	124.3
191.6	29.3	168	182.8	223	222.8	19	19.9
195.5	76.4	513	478.9	637	594.3	55	52.5
199.5	76.6	451	479.7	557	585.0	52	52.1
201.6	37.7	230	236.3	296	286.1	32	25.3
204.9	81.6	475	512.4	578	606.5	47	53.2
206.6	136.5	899	854.0	1051	1012.3	92	90.0
all	678.5	4154	4198.7	5187	5114.2	459	454.7

Table 6.1: Observed and expected numbers of data candidates selected for the angular distribution analysis after all cuts in the different final states and for different centre-of-mass energies.

The $q\bar{q}\ell\bar{\nu}_\ell$ Selection and Reconstruction

Starting from the sample used for the W-pair cross-sections measurement, we select candidate $q\bar{q}e\bar{\nu}_e$ and $q\bar{q}\mu\bar{\nu}_\mu$ events with a reconstructed lepton track. The track charge is needed to reconstruct the W^- polar angle. For the $q\bar{q}\tau\bar{\nu}_\tau$ events, either one track or a narrow jet consisting of three tracks is assigned as the τ decay product. The OPAL tracking detectors are used to reconstruct the muon momentum and the electron direction, whereas the electromagnetic calorimeters are used to give a more accurate measurement of the electron energy. As explained above, the direction of τ candidates is given directly by the τ decay products, whilst the energy of the τ is estimated using a kinematic fit. The remaining tracks and calorimeter clusters in the event are grouped into two jets using the Durham $k_\perp$ algorithm [137]. The total energy and momentum of each of the jets are calculated using the charged track momenta and calorimeter energies and correcting for double counting employing the method described in [138].

The different kinematic fits described above are used to improve the resolution in the five kinematic variables used for the TGC analysis. This resolution is correlated with the kinematic fit probabilities which indicate the event reconstruction quality. Therefore we use the results of the kinematic fits to classify the events into nine quality classes which are used later in the TGC analysis. The exact definitions of these classes and the fraction of accepted events in each class are listed in table 6.2. The event population in each class is well modelled by the Monte Carlo. To optimise the resolution in the kinematic variables used in the TGC analysis they are taken, according to the quality class, either from the directly measured values or from one of the three kinematic fits, as detailed in table 6.2. The $q\bar{q}\tau\bar{\nu}_\tau$ events which fail kinematic fit B or pass it with fit probability below 0.025 are rejected. This cut suppresses those $q\bar{q}\tau\bar{\nu}_\tau$ events which are correctly identified as belonging to this decay channel, but where the τ decay products are not identified correctly, leading to an incorrect estimate of the τ flight direction or its charge. The fraction of such events in the $q\bar{q}\tau\bar{\nu}_\tau$ sample is thus reduced from 18% to 12%.

Class	Final state	% of events	Requirements on fits A, B, C	Kinem. variables taken from
a)	$q\bar{q}e\bar{\nu}_e$, $q\bar{q}\mu\bar{\nu}_\mu$	30.4	$P_C \geq 0.20$	fit C
b)	$q\bar{q}e\bar{\nu}_e$, $q\bar{q}\mu\bar{\nu}_\mu$	10.1	$0.05 \leq P_C < 0.20$	fit C
c)	$q\bar{q}e\bar{\nu}_e$, $q\bar{q}\mu\bar{\nu}_\mu$	6.9	$0.01 \leq P_C < 0.05$	fit C
d)	$q\bar{q}e\bar{\nu}_e$, $q\bar{q}\mu\bar{\nu}_\mu$	4.7	$0.001 \leq P_C < 0.01$	fit A
e)	$q\bar{q}e\bar{\nu}_e$, $q\bar{q}\mu\bar{\nu}_\mu$	10.0	$P_C < 0.001$	fit A
f)	$q\bar{q}e\bar{\nu}_e$, $q\bar{q}\mu\bar{\nu}_\mu$	8.3	C failed, $P_A \geq 0.001$	fit A
g)	$q\bar{q}e\bar{\nu}_e$,$q\bar{q}\mu\bar{\nu}_\mu$	1.2	C failed, A failed or $P_A < 0.001$	directly measured
h)	$q\bar{q}\tau\bar{\nu}_\tau$	21.7	$P_B \geq 0.20$	fit B
i)	$q\bar{q}\tau\bar{\nu}_\tau$	6.8	$0.025 \leq P_B < 0.20$	fit A

Table 6.2: Definition of the nine quality classes of $q\bar{q}\ell\bar{\nu}_\ell$ events. P_A, P_B and P_C are the probabilities of kinematic fits A, B and C.

Finally, the kinematic variables are used to calculate the optimal observables (see section 5.4) which are used to extract the TGCs. Those events (typically 1% of the sample) with optimal observable values in the far tails of their distributions are interpreted as being badly measured and discarded.

Performing the complete analysis on Monte Carlo samples generated with different anomalous couplings shows that our event selection does not introduce any bias on the TGC results.

The purities of the final samples are about 96%, 98% and 91% for the $\mathrm{q\overline{q}e\overline{\nu}_e}$, $\mathrm{q\overline{q}}\mu\overline{\nu}_\mu$ and $\mathrm{q\overline{q}}\tau\overline{\nu}_\tau$ final states respectively. The background consists mainly of TGC-independent four-fermion final states and $\mathrm{Z}/\gamma \rightarrow \mathrm{q\overline{q}}$ events. Cross migration between the $\mathrm{q\overline{q}}\tau\overline{\nu}_\tau$ and each of the $\mathrm{q\overline{q}e\overline{\nu}_e}$ and $\mathrm{q\overline{q}}\mu\overline{\nu}_\mu$ decay channels is at the level of 4 – 5% and is considered as signal.

In the reconstruction of the $\mathrm{q\overline{q}}\ell\overline{\nu}_\ell$ events we obtain $\cos\theta_{\mathrm{W}}$ as the polar angle of the sum of the two jet-momenta from the measured four-momenta, respectively (see table 6.2). The decay angles of the leptonically decaying W are obtained from the charged lepton four-momentum, after boosting back to the parent W rest frame. For the hadronically decaying W it is not possible to distinguish between the jets of the quark and anti-quark. This ambiguity is taken into account in the analysis.

The $\ell\overline{\nu}_\ell\overline{\ell}'\nu_{\ell'}$ Selection and Reconstruction

The reconstruction of $\ell\overline{\nu}_\ell\overline{\ell}'\nu_{\ell'}$ final states is possible, using kinematic fit C, only if there is no τ-lepton in the final state. To reject events with τ-leptons we use the lepton identification algorithm designed for the W branching ratio measurement [22]. The event rate analysis selection sometimes selects events with only one high momentum charged lepton reconstructed in the detector: such events were removed from the angular distribution analysis as the momenta of both charged leptons must be measured. As a result of these two cuts, the efficiency for $\ell\overline{\nu}_\ell\overline{\ell}'\nu_{\ell'}$ events with $\ell, \ell' = \mathrm{e}, \mu$ drops from ~88% to ~73%, varying slightly with centre-of-mass energy. The contamination left in the sample from $\ell\overline{\nu}_\ell\overline{\ell}'\nu_{\ell'}$ final states with a τ-lepton mainly from $\tau \rightarrow \mathrm{e}, \mu$ is 14% and the background from other final states is 2%.

Kinematic fit C has zero constraints and reduces to solving a quadratic equation. In the ideal case of no measurement errors and satisfying the conditions where fit C is valid, namely no ISR and narrow W width, one expects to obtain two real solutions corresponding to a twofold ambiguity in the angle set $\cos\theta_W$, ϕ_1^* and ϕ_2^*. There is no ambiguity in the angles θ_1^* and θ_2^* which have a one-to-one correspondence with the lepton momenta. In realistic conditions, however, including ISR, finite W width and measurement errors, one may obtain no real solution, but a pair of complex conjugate solutions. The fraction of events with complex solutions falls with increasing centre-of-mass energy from 30% to 24%, in agreement with Monte Carlo prediction. In these events, the imaginary parts of the complex solutions are set to zero, yielding a single real set of angles. The total event weight is one for all events, independent of whether one or two solutions are employed. In the latter case, the two solutions each are assigned a weight of one half.

Combination of the Final States

As in the case of the $\mathrm{q\overline{q}q\overline{q}}$ channel, the angular distributions from the $\mathrm{q\overline{q}}\ell\overline{\nu}_\ell$ and $\ell\overline{\nu}_\ell\overline{\ell}'\nu_{\ell'}$ final states are consistent with the Standard Model expectation and no evidence is seen for any significant contributions from anomalous couplings. For a quantitative study the method of optimal observables is used in the same way as described in section 5.4.

The calculation of the mean optimal observables and their expected values is done separately for each centre-of-mass energy and for each of the $\mathrm{q\overline{q}}\ell\bar{\nu}_\ell$ and $\ell\bar{\nu}_\ell\overline{\ell}'\nu_{\ell'}$ final states taking into account the reconstruction ambiguities for each particular final state. For $\mathrm{q\overline{q}}\ell\bar{\nu}_\ell$ events, similar to $\mathrm{q\overline{q}q\overline{q}}$ events, the mean optimal observables are calculated using weights assigned to the event according to its quality class (see table 6.2). In contrast to $\mathrm{q\overline{q}q\overline{q}}$ events, the weight for a particular $\mathrm{q\overline{q}}\ell\bar{\nu}_\ell$ class is inversely proportional to the variance of the optimal observable distribution of the events in that class. In this way, events where the quality of the reconstruction is poor obtain a lower weight. Using this weighted mean has been found, as expected, to enhance the sensitivity.

The expected mean values of each observable as a function of the TGCs are calculated from four-fermion reference Monte Carlo samples generated according to the Standard Model. The EXCALIBUR matrix element calculation is used to reweight the Monte Carlo events to any TGC value required. The contribution of background events is also taken into account in the calculation of the expected mean values using corresponding Monte Carlo samples.

A χ^2-fit of the measured mean values $\overline{\mathcal{O}}$ to the corresponding expectations $E[\mathcal{O}](\alpha)$ is performed to extract the couplings from the data. The covariance matrix for the mean values is calculated from the Monte Carlo events and scaled to the number of data events.

If we combine the information from all three final states, still in some of our fits the χ^2-function has a double minimum and therefore it is necessary to validate the errors obtained from the χ^2-fits. As for the $\mathrm{q\overline{q}q\overline{q}}$ final state (see section 5.4), we performed a test with a large number of Monte Carlo experiments. In each of these experiments, we now use for each centre-of-mass energy and each final state a subsample of Standard Model Monte Carlo events. The size of each subsample corresponds to the luminosity for that final state at the particular centre-of-mass energy. Background events are also included in these subsamples in the appropriate proportions. For each experiment, the various subsamples are analysed in the same way as the real data events. The distributions of the fit results are centred around the expected values, but there are some non-Gaussian tails. We therefore test the reliability of the error interval, as given by the region where χ^2 is no more than 1 above its minimum value, by counting the fraction of experiments where the correct value falls within this region. The error estimate is considered to be reliable if the calculated fraction is consistent with 68%; otherwise the corresponding elements of the covariance matrix for the $\overline{\mathcal{O}}$ values are scaled by the necessary factor to obtain 68% of the subsamples within the error interval. The resulting scaled covariance matrix is also used to analyse the real data. This is done separately for each fit. The resulting scale factors are listed in table 6.3 and vary between 0.986 and 1.076 for the one-parameter fits. However, in the three-parameter fit of

	$\Delta\kappa_\gamma$	Δg_1^{Z}	λ	$\Delta\kappa_\gamma, \Delta g_1^{\mathrm{Z}}, \lambda$	g_5^Z
$\mathrm{q\overline{q}q\overline{q}}$	$1.226^{+0.039}_{-0.041}$	$1.071^{+0.037}_{-0.032}$	$1.107^{+0.031}_{-0.029}$	$0.945^{+0.018}_{-0.015}$	$1.034^{+0.031}_{-0.029}$
$\mathrm{W^+W^-}$	$1.076^{+0.020}_{-0.029}$	$0.986^{+0.029}_{-0.022}$	$1.048^{+0.019}_{-0.016}$	$1.128^{+0.013}_{-0.018}$	$0.986^{+0.020}_{-0.023}$

Table 6.3: Scale factors for 68% C.L. of the $\mathrm{q\overline{q}q\overline{q}}$ channel and all $\mathrm{W^+W^-}$ channels.

$\Delta\kappa_\gamma$, Δg_1^Z and λ_γ, where double minima occur more frequently, a larger scale factor of 1.28 is obtained. These scale factors have been found to be appropriate also for the 95% C.L. intervals. The scale factors for Δg_1^Z and g_5^Z are consistent with 1 and are not considered. For comparison the scale factors for the $q\overline{q}q\overline{q}$ channel are also shown in table 6.3. They are always larger than the corresponding factors using all final states. The inclusion of two more channels helps to resolve some double minima in the χ^2-function, giving scale factors nearer to 1 and thus a more realistic error estimate in the first place.

Systematic Errors

The same systematic errors as for the $q\overline{q}q\overline{q}$ final state are considered for the other two final states (see section 5.5). The method to incorporate the systematic errors into the fit is also the same as in the $q\overline{q}q\overline{q}$ case: The effect of each of these sources on the mean values of the optimal observables is estimated separately for each centre-of-mass energy and for each final state. The deviations obtained in the mean observables are used to construct a systematic error covariance matrix, where the systematic deviations from each source are assumed to be fully correlated between all centre-of-mass energies. For the combination of all final states, the covariance matrix is extended to incorporate the three final states. All uncertainties, except for those associated with the background, are assumed to be fully correlated between the relevant final states. This matrix is added to the statistical covariance matrix, as in the case of the $q\overline{q}q\overline{q}$ final state, and the fit is redone to obtain the TGC parameters with their total (statistical and systematic) errors.

For demonstration, we also calculate the separate contribution from each source of systematic error to the error on the TGC parameters, after combining the different centre-of-mass energies and final states. These are listed in table 6.4.

Source	$\Delta\kappa_\gamma$	Δg_1^Z	λ_γ	g_5^Z
$\mathcal{O}(\alpha)$ correction	0.029	0.011	0.010	0.031
ISR	0.006	0.002	0.003	0.003
TGC matrix element	0.011	0.005	0.004	0.005
Detector simulation	0.006	0.003	0.005	0.013
Background	0.015	0.004	0.011	0.012
$\sqrt{s}$, M_W	0.008	0.004	0.005	0.017
Fragmentation	0.038	0.013	0.018	0.047
Bose-Einstein correlations	0.001	0.000	0.004	0.005
Colour reconnection	0.004	0.003	0.005	0.000
Total systematic error	0.053	0.019	0.026	0.061

Table 6.4: Contributions to the systematic uncertainties in the determination of the TGC parameters. The total systematic errors are obtained by combining all contributions at the optimal observable level and then calculating the effect on the TGC parameters.

$\sqrt{s}$ [GeV]	Luminosity [pb^{-1}]	Final state	Observed events	Expected events		
				Total	Signal	Background
182.7	57.21 ± 0.25	$\ell\bar{\nu}_\ell\bar{\ell}'\nu_{\ell'}$	78	77.5 ± 3.1	76.1 ± 2.2	1.4 ± 2.2
		$q\bar{q}\ell\bar{\nu}_\ell$	361	364 ± 6	337 ± 6	27 ± 3
		$q\bar{q}q\bar{q}$	438	436 ± 10	344 ± 5	92 ± 9
188.6	183.05 ± 0.40	$\ell\bar{\nu}_\ell\bar{\ell}'\nu_{\ell'}$	276	287.2 ± 5.0	272.6 ± 4.1	14.6 ± 2.9
		$q\bar{q}\ell\bar{\nu}_\ell$	1246	1248 ± 16	1171 ± 13	76 ± 10
		$q\bar{q}q\bar{q}$	1546	1497 ± 26	1189 ± 14	309 ± 21

Table 6.5: Observed and expected numbers of events in each W^+W^- final state for the centre-of-mass energies of 182.7 GeV and 188.6 GeV. The separation between signal and background is explained in the text. All the quoted errors are systematic.

Event Rate TGC Analysis

The event rate study, unlike the angular distribution analysis, requires a detailed investigation of the systematic uncertainties associated with the overall selection efficiency. This investigation is part of the W-pair cross-sections analysis and has to be done separately for each centre-of-mass energy and for each final state. So far, it has been completed for centre-of-mass energies of 183 GeV [21] and 189 GeV [22]. The TGC event rate analysis is therefore also restricted to these two centre-of-mass energies. In the case where the angular distribution analysis has two TGC solutions, one being far away from the Standard Model value, the results from this restricted event rate analysis would still be sufficient to reject that solution. The data from higher centre-of-mass energies would make a negligible additional contribution to our results. Compared with the angular distributions, the sensitivity of the event rates to TGCs around the Standard Model values is much smaller and its dependence on the overall luminosity is weaker.

The event rate analysis has been described already in previous publications [21, 164], where not at every centre-of-mass energy the more complete $\mathcal{O}(\alpha)$ corrections were used. The numbers of expected events are re-evaluated for this analysis using the KandY Monte Carlo samples to obtain the Standard Model expected number of events.

The same selection, efficiency and background estimates as in the total cross-sections analysis are used here. The numbers of selected events in each final state and for each of the two centre-of-mass energies are quoted in table 6.5 along with the Monte Carlo expectations. The systematic errors on the expected values are due to Monte Carlo statistics, 0.5% uncertainty in the total cross-section, 0.2% uncertainty in the luminosity, uncertainties due to data/MC differences, tracking losses, detector occupancy and fragmentation. A detailed description of all these sources can be found in [22]. The expected numbers of signal events include contributions from all four-fermion final states which can be produced by diagrams involving the WWγ and WWZ triple gauge boson vertices. The other four-fermion final states are considered as background along with the two-fermion final states and two-photon processes.

The total numbers of expected events are consistent within the statistical and systematic errors with the observed numbers. Therefore, there is no evidence for any significant contribution from anomalous couplings. A quantitative study of TGCs from these results is performed by comparing the numbers of observed events in each of the three event selection channels at each of the two centre-of-mass energies with the expected numbers of signal and background events, where the number of signal events is parametrised as a second-order polynomial in the TGCs. This parametrisation is based on the second-order polynomial dependence of the cross-sections, as was used also in the optimal observable analysis (see section 5.4). The polynomial coefficients in terms of event rate for each final state are calculated by weighting our Monte Carlo events to correspond to various TGC values using a four-fermion matrix element calculation procedure taken from the EXCALIBUR Monte Carlo generator program.

The probability to observe the measured number of candidates, given the expected value, is calculated using a Poisson distribution. The product of the six probability distributions corresponding to the three event selection channels at the two energies is taken as the event rate likelihood function. The systematic uncertainties are incorporated into the TGC fit by allowing the expected numbers of signal and background events to vary in the fit and constraining them to have a Gaussian distribution around their expected values with their systematic errors taken as the width of the distributions. We assume full correlation between the systematic uncertainties for the three final states except for efficiency and background which are taken to be uncorrelated. All systematic uncertainties are assumed to be fully correlated between the two different centre-of-mass energies.

Combined Results

The results of the various fits are listed in table 6.6. We present first the results of the angular distribution analysis without systematic errors obtained by performing one-parameter fits for each final state simultaneously for the eight centre-of-mass energies. For comparison, the average fit errors of the Monte Carlo experiments are also quoted in table 6.6, demonstrating the different sensitivities for the various final states and TGC parameters. In most cases, the fit errors are rather close to the expected ones, except for $\Delta\kappa_\gamma$, where the fit errors for some final states are also very asymmetric due to the proximity of a second minimum in the χ^2 function. The errors for the $q\overline{q}q\overline{q}$ channel are slightly smaller compared to the ones given in chapter 5 because different error scaling factors are applied. Table 5.11 list the $q\overline{q}q\overline{q}$ results with scale factors calculated using only the $q\overline{q}q\overline{q}$ channel while here the information from all three channels are used in the scale factor calculation.

Next we present the results of the angular distribution analysis with the systematic errors included. This modifies the relative contributions to the fit of the different optimal observables and different centre-of-mass energies, as well as the correlations between them. Therefore, not only the fit errors are affected, but also the fit results themselves. The corresponding $\log L$ curvesfor the different channels are shown in figure 6.1. The results from the three final states are combined, taking into account the common systematic errors, and the combined results are listed in table 6.6.

From the expected errors, a ranking of the three event shape analysis can clearly be drawn. The golden channel is the $q\overline{q}\ell\bar{\nu}_\ell$ final state due to its high branching ratio and the excellent event reconstruction. The $q\overline{q}q\overline{q}$ final state is the second best. Its sensitivity, compared to the $q\overline{q}\ell\bar{\nu}_\ell$ final state, decreases by a factor of 1.3 – 2.4, depending on the coupling. Although the branching ratio is as large as in the $q\overline{q}\ell\bar{\nu}_\ell$ final state, the reconstruction is much more

	$\Delta\kappa_\gamma$	Δg_1^Z	λ_γ	g_5^Z
$\underline{q\bar{q}\ell\bar{\nu}_\ell}$				
Without systematics	$-0.23^{+0.09}_{-0.08}$	$-0.031^{+0.035}_{-0.034}$	$-0.075^{+0.036}_{-0.035}$	$0.15^{+0.16}_{-0.16}$
Expected errors	±0.12	±0.032	±0.033	±0.15
Including systematics	$-0.23^{+0.09}_{-0.08}$	$-0.023^{+0.038}_{-0.037}$	$-0.062^{+0.038}_{-0.037}$	$0.10^{+0.17}_{-0.16}$
Fit χ^2/d.o.f.	10.3/15	13.6/15	13.3/15	14.7/15
$\underline{q\bar{q}q\bar{q}}$				
Without systematics	$0.18^{+0.38}_{-0.20}$	$0.08^{+0.09}_{-0.07}$	$0.00^{+0.09}_{-0.07}$	$-0.41^{+0.20}_{-0.21}$
Expected errors	±0.20	±0.07	±0.08	±0.20
Including systematics	$0.17^{+0.65}_{-0.26}$	$0.09^{+0.11}_{-0.09}$	$0.01^{+0.28}_{-0.14}$	$-0.37^{+0.24}_{-0.25}$
Fit χ^2/d.o.f.	11.3/15	9.2/15	11.0/15	8.8/15
$\underline{\ell\bar{\nu}_\ell\bar{\ell}'\nu_{\ell'}}$				
Without systematics	$0.31^{+0.34}_{-0.27}$	$-0.05^{+0.11}_{-0.11}$	$-0.09^{+0.09}_{-0.08}$	$0.12^{+0.48}_{-0.44}$
Expected errors	±0.29	±0.13	±0.09	±0.34
Including systematics	$0.30^{+0.35}_{-0.28}$	$-0.06^{+0.11}_{-0.11}$	$-0.09^{+0.09}_{-0.08}$	$0.10^{+0.49}_{-0.45}$
Fit χ^2/d.o.f.	14.6/15	12.9/15	9.8/15	14.9/15
<u>All WW final states</u>				
Including systematics	$-0.12^{+0.09}_{-0.08}$	$-0.013^{+0.034}_{-0.033}$	$-0.061^{+0.035}_{-0.034}$	$-0.04^{+0.13}_{-0.12}$
Including event rate	$-0.12^{+0.09}_{-0.08}$	$-0.013^{+0.034}_{-0.033}$	$-0.060^{+0.034}_{-0.033}$	$-0.04^{+0.13}_{-0.12}$
Fit χ^2/d.o.f.	43.4/53	39.4/53	36.2/53	42.0/53
SM χ^2/d.o.f.	45.1/54	39.5/54	39.2/54	42.1/54
95% C.L. limits	[−0.27, 0.07]	[−0.077, 0.054]	[−0.13, 0.01]	[−0.28, 0.21]

Table 6.6: Measured values of the TGC parameters from the angular distributions of each WW final state, using centre-of-mass energies of 183 – 209 GeV and the results after combining all final states. For the individual final states we also list the results before including the systematic errors and the expected statistical errors. We also list the results after combining with the W-pair event rate information from centre-of-mass energies of 183 and 189 GeV. The quality of the fits is demonstrated by their respective χ^2 values and numbers of degrees of freedom. The compatibility with the Standard Model is shown by the χ^2 values obtained when the TGCs assume their Standard Model values.

difficult and much information is lost. The sensitivity of the $\ell\bar{\nu}_\ell\bar{\ell}'\nu_{\ell'}$ final state compared to the $q\bar{q}\ell\bar{\nu}_\ell$ one is worse by a factor of 2 – 4. The very low effective branching ratio is partly compensated by the very good resolution of the two charged leptons.

The results of the event rate analyses are presented by $\log L$ curves shown by the thin black lines in figure 6.1. They are combined with the results of the angular distribution analysis and the combined $\log L$ plots are shown by the thick black lines. The correlation between the results of the two analyses, which is due to uncertainties in the background normalisation, centre-of-mass energy and W mass, is below 7%. Therefore, this correlation is neglected in the combination. The numerical results of the combination are listed in

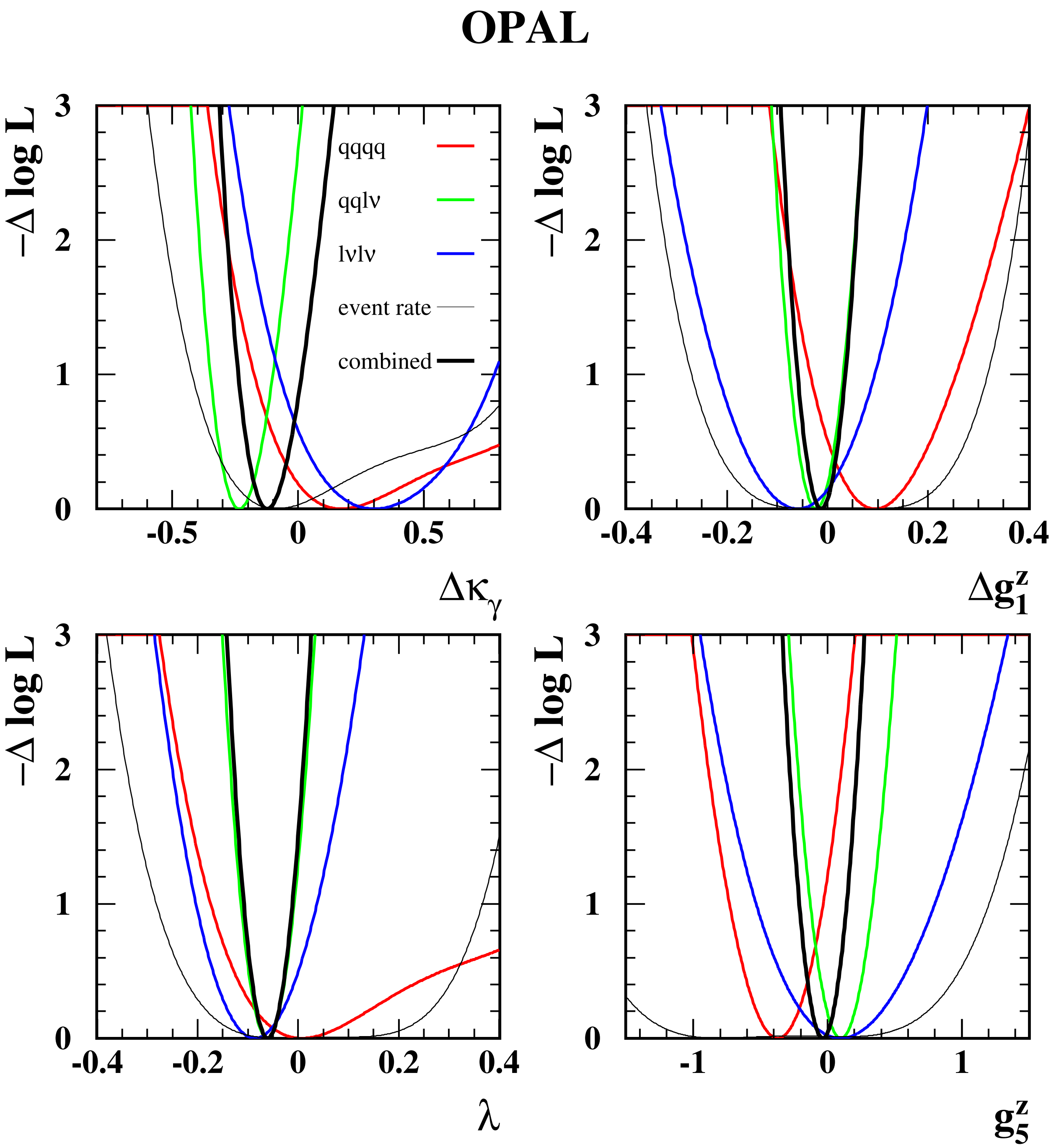

Figure 6.1: Negative log-likelihood curves obtained from the angular distribution information of W-pair events taken at the centre-of-mass energies of 183 – 209 GeV, separately for the three different final states: $q\bar{q}\ell\bar{\nu}_\ell$ (light grey lines), $q\bar{q}q\bar{q}$ (grey lines) and $\ell\bar{\nu}_\ell\bar{\ell}'\nu_{\ell'}$ (dark grey lines). The thin black lines describe the contribution of the event rate information from all final states corresponding to centre-of-mass energies of 183 and 189 GeV. The systematic errors are included. The thick black lines are obtained by combining all sources of information. The curves for each TGC parameter are obtained by setting the other three parameters to their Standard Model values.

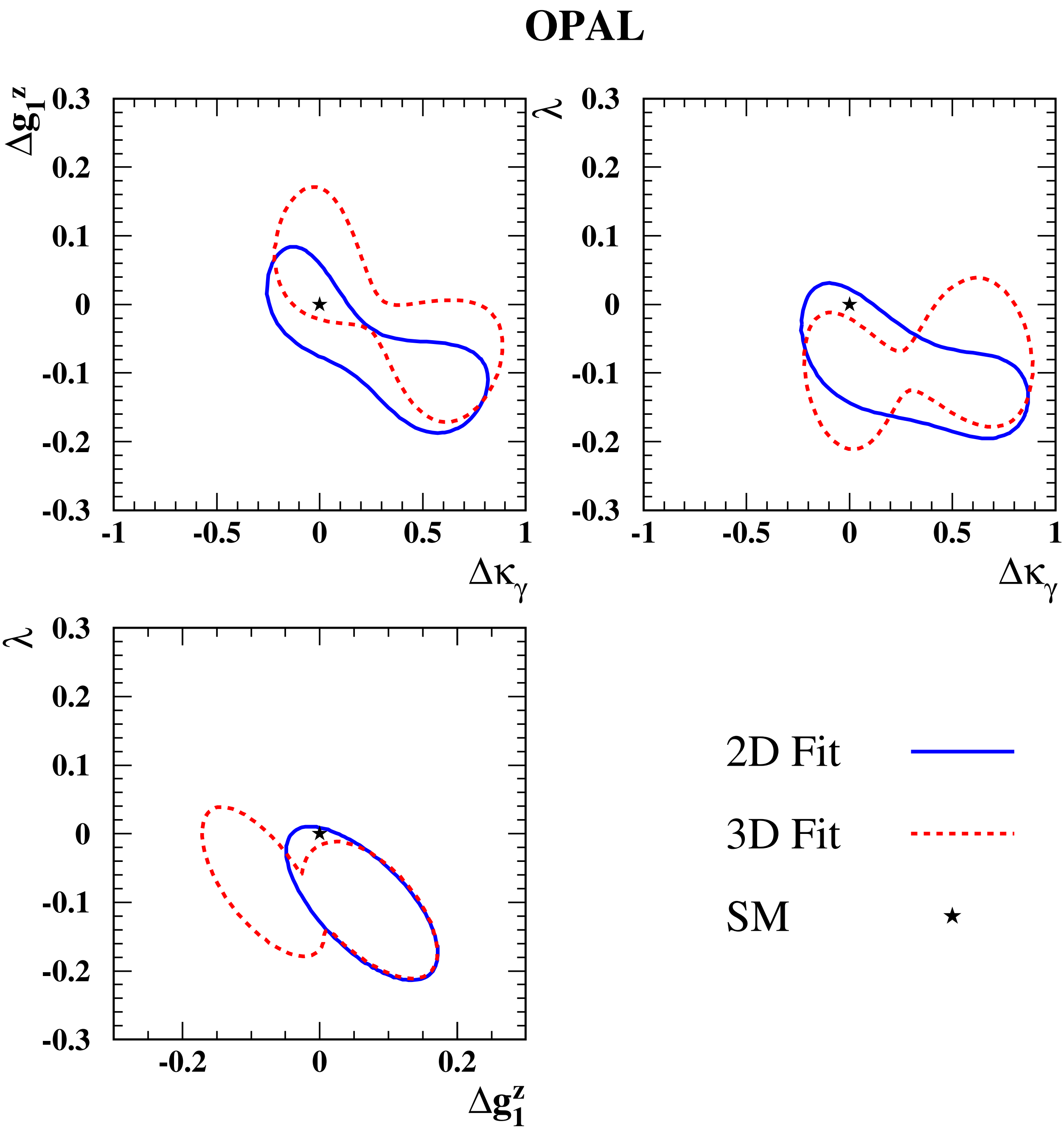

Figure 6.2: The two-dimensional correlation contours corresponding to $-\Delta \log L = 2.995$ for different pairs of TGC parameters, as obtained from two-parameter (solid curves) and three-parameter (dashed curves) fits. The value 2.995 corresponds to a 95% C.L. region in two dimensions. In the case of the three-parameter fit, the curve is a projection onto the two-dimensional plane of the envelope of the three-dimensional $-\Delta \log L = 2.995$ surface. The stars indicate the Standard Model expectations.

table 6.6 along with the corresponding χ^2/d.o.f. As expected, the event rate information has relatively little impact on the final results. The 95% confidence level intervals are also listed in table 6.6. To show the compatibility with the Standard Model we also list in the table the χ^2/d.o.f. for Standard Model TGC values.

To study correlations between the C and P conserving TGC parameters, $\Delta\kappa_\gamma$, Δg_1^Z and λ_γ, we perform fits, where two parameters are allowed to vary while the third parameter and g_5^Z assume their Standard Model values and are not used in the fit, as explained in section 5.4. Similarly, we also perform a three-parameter fit where all three parameters are allowed to vary, leaving out only g_5^Z. Figure 6.2 shows the 95% C.L. contour plots obtained from the two-parameter fits and the corresponding two-dimensional projections of the three-parameter fit. The contour plots show a double minimum structure. Adding information from the single-W channel, where the $\log L$ function tends to have a steep rise with increasing $\Delta\kappa_\gamma$ [18, 36–38], is expected to resolve this ambiguity.

A χ^2-test can be used to study the compatibility of our data with the Standard Model, in the same way as was done for the one parameter fits. Inserting the Standard Model values for the TGC parameters we obtain $\chi^2 = 211.6$ for 222 degrees of freedom.

6.2 LEP Combination

The LEP Electroweak Working Group combines electroweak measurements from all four LEP experiments. The Gauge Coupling subgroup performs the combination of gauge coupling related measurements including the measurements of charged current triple gauge boson couplings. The latest combination for the summer conferences 2003 includes published and preliminary data from all four LEP experiments [2]. After a brief discussion of the three sensitive reactions at LEP, the combination procedure is introduced and the results are shown.

Sensitive Reactions

The main sensitivity to triple gauge boson couplings at e^+e^- colliders comes from W-pair production. All four LEP experiments have analysed the three final states upto 209 GeV. ALEPH [37, 165] and OPAL use the method of optimal observables to calculate sensitive variables used in the extraction of the couplings, while DELPHI [18] and L3 [19, 166] use a plain binned maximum likelihood fit. In this likelihood fit the $\cos\theta_W$ distribution from all three final states is used. For the golden channel ($q\bar{q}\ell\bar{\nu}_\ell$) the decay angles $\cos\theta_\ell^*$ and ϕ_ℓ^* are used additionally to $\cos\theta_W$ in order to increase the sensitivity.

Single-W production (see figure 6.3(a) for the Feynman diagrams) is mainly sensitive to WWγ couplings and particular to $\Delta\kappa_\gamma$. It is very useful to resolve the double minima structure in the likelihood function which is common in the measurement of $\Delta\kappa_\gamma$ in W pairs. Usually, the electron is assumed to escape detection through the beam pipe, leading to missing energy and either a single charged lepton or two jets. All four experiments [18, 36–38] perform a binned maximum likelihood fit to the number of observed events. Some experiments increase the expected sensitivity by adding some differential information, e. g. angle or energy distributions, to the likelihood function.

The last reaction sensitive to triple gauge boson couplings is single-γ production (see figure 6.3(a)). It has a very clear topology, only one photon and missing energy, and a

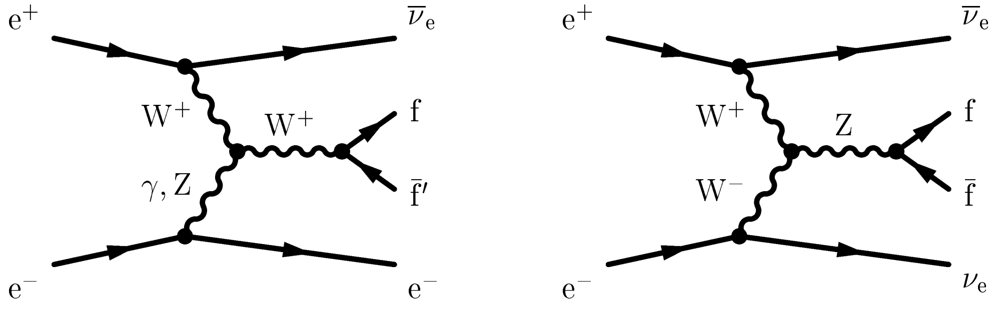

(a) Single-W production (b) Single-Z production

Figure 6.3: Feynman diagram for single-W ($\mathrm{W e}\nu_\mathrm{e}$) and single-Z ($\mathrm{Z}\nu\bar{\nu}$) production.

high cross-section but the sensitivity to triple gauge boson couplings is not very high. All experiments [18, 166, 167] performed a binned maximum likelihood fit to the number of observed events. The inclusion of the energy and angle distribution of the photon increases the sensitivity with respect to the total cross-section.

Combination Procedure

The combination of the measurements discussed above is based on the individual likelihood functions from the four LEP experiments. Each experiment provides the negative log likelihood, $\log L$, as a function of the coupling parameters to be combined. The $\log L$ functions include statistical as well as those systematic errors, which are considered as uncorrelated between experiments. For both single- and multi-parameter combinations, the individual $\log L$ functions are combined. It is necessary to use the $\log L$ functions directly in the combination, since in some cases they are not parabolic, and thus it is not possible to properly combine the results by simply taking weighted averages of the measurements.

The main contributions to the systematic errors that are uncorrelated between experiments arise from detector effects, background in the selected signal samples, limited Monte Carlo statistics and the fitting method where their importance varies for each experiment.

The systematic uncertainties considered correlated between experiments are the theoretical cross-section predictions (0.5% for W-pair production and 5% for single-W production), fragmentation and hadronisation effects, the final state interactions, i. e. Bose-Einstein correlations and colour reconnection, and the uncertainty in the radiative $\mathcal{O}(\alpha)$ corrections. The latter was the dominant systematic error in previous combinations, where the difference between Monte Carlo samples with and without the $\mathcal{O}(\alpha)$ corrections was taken as a conservative estimate. New preliminary analysis on the subject are now available from several LEP experiments, based on fully simulated events. This improved estimation, whilst still being conservative, reduces the systematic uncertainties from $\mathcal{O}(\alpha)$ corrections by about a third for Δg_1^Z and λ and roughly halves it for $\Delta\kappa_\gamma$, compared to the $\mathcal{O}(\alpha)$ correction applied previously.

The systematic errors considered correlated between the experiments amount to roughly 70% of the combined statistical and uncorrelated uncertainties for λ and g_1^Z, whilst for κ_γ their contribution is equal. Hence an improved combination procedure [168] is used. This procedure allows the combination of statistical and uncorrelated and correlated systematic errors, independently of the analysis method used.

The combination uses the likelihood curves (including the statistical and uncorrelated systematic errors) and correlated systematic errors submitted by each of the four experiments. The procedure is based on the introduction of an additional free parameter to take into account the systematic uncertainties, which are treated as shifts on the fitted TGC value, and are assumed to have Gaussian distribution. A simultaneous minimisation of both parameters (TGC and systematic error) is performed to the $\log L$ function. The resulting error on the coupling α will take into account all sources of uncertainties, yielding a measurement of the coupling with the error representing statistical and systematic sources. The projection of the minima of the $\log L$ as a function of α gives the combined $\log L$ curve. The advantage of this procedure is that it treats systematic errors that are uncorrelated between the experiments correctly, whilst not forcing the averaging of these systematic errors into one global LEP systematic scaling factor. In other words, the precision of each experiment is reduced by its own correlated systematic errors, instead of an averaged LEP systematic error.

Results

Before we come to the combined LEP results, the combination procedure is cross-checked four each individual experiment and the results from one-parameter fits using the three sensitive reactions are shown in table 6.7 for the C and P conserving coupling $\Delta\kappa_\gamma$, Δg_1^Z and λ. The listed errors include the statistical and all systematic errors. The splitting of the systematic errors into uncorrelated and correlated ones is only done for the combination procedure. The measurements of the coupling g_5^Z are not combined. All measurements are consistent with the Standard Model predictions and the errors for a single coupling vary only $\sim 30\%$ over the range of experiments. From this fact we cannot draw the conclusion that one detector or analysis method is superior over the others because not all experiments have included yet the full data set for all three reactions.

The combined results of one-parameter fits are listed in table 6.9. The errors include statistical and systematic effects and are compatible with the Standard Model predictions. The gain in sensitivity is a factor of 1.5 – 2 for the combination of the four experiments. The list of systematic errors, which are treated as fully correlated between the LEP experiments,

Experiments	$\Delta\kappa_\gamma$	Δg_1^Z	λ
ALEPH	$0.022^{+0.073}_{-0.072}$	$0.026^{+0.034}_{-0.033}$	$0.012^{+0.033}_{-0.032}$
DELPHI	$-0.045^{+0.090}_{-0.086}$	$0.002^{+0.038}_{-0.040}$	$0.014^{+0.044}_{-0.042}$
L3	$-0.078^{+0.071}_{-0.069}$	$-0.072^{+0.042}_{-0.041}$	$-0.058^{+0.047}_{-0.044}$
OPAL	$-0.071^{+0.085}_{-0.081}$	$-0.015^{+0.035}_{-0.034}$	$-0.063^{+0.036}_{-0.036}$

Table 6.7: The measured central values and one standard deviation errors obtained by the four LEP experiments. In each case only the listed parameters is varied and the other are set to their Standard Model predictions. Both statistical and systematic errors are included.

Parameter	$\Delta\kappa_\gamma$	Δg_1^{Z}	λ
$\mathcal{O}(\alpha)$ corrections	0.020	0.010	0.010
σ_{WW} predictions	0.014	0.003	0.005
Fragmentation & Hadronisation	0.004	0.004	0.002
Bose-Einstein Correlation	0.009	0.005	0.004
Colour Reconnection	0.010	0.005	0.004
$\sigma_{\mathrm{We}\overline{\nu}_{\mathrm{e}}}$ predictions	0.011	-	-
quadratic sum	0.030	0.013	0.013

Table 6.8: The effect of the systematic errors, which are considered correlated between the four LEP experiments, on the TGC measurement.

is given in table 6.8 including their shift on the combined fit results. The uncertainty on the $\mathcal{O}(\alpha)$ correction is by fare the most dominant systematic error. All other correlated systematic uncertainties are small compared to the $\mathcal{O}(\alpha)$ corrections, except the cross-section predictions for κ_γ. Their total contribution to the combined statistical and systematical error is 58% in the case of Δg_1^{Z} and λ and 68% in the case of $\Delta\kappa_\gamma$. Therefore, the combined measurements are still dominated by statistics. The individual $\log L$ curves and their sum are shown in figure 6.4.

The combined results of two-parameter fits from all four LEP experiments are shown in table 6.10, where the errors include both statistical and systematic effects. Since the shape of the $\log L$ functions is not always parabolic, there is some ambiguity in the definition of the correlation coefficients and the values quoted in the table are approximate values.

The three two-patameter contours at 68% and 95% confidence level for the combined fit are shown in figure 6.5. The combination of all reactions from the four experiments clearly resolves the double minima structure in the likelihood function, which is present in the OPAL W-pair measurement.

6.3 TGC Measurements at the Tevatron

Triple gauge couplings can also be studied in hadron collisions, either in $\mathrm{p\bar{p}}$ collisions at the Tevatron or in pp collisions at the LHC. The main production mechanism involving triple gauge couplings is similar to the reaction $\mathrm{e^+e^-} \to \mathrm{W^+W^-}$. Here the beam electrons are replaced by quarks from the colliding beams, which couple to the photon or the Z boson. However, both quarks can couple also to a W boson, leading to three distinct di-boson final states which are depicted in figure 6.6:

WW: The W pair production follows the same rules as in $\mathrm{e^+e^-}$ collisions. In a quark-antiquark annihilation a virtual photon or Z boson is produced which couples to a W pair thus involving both WWZ and WWγ couplings. Observing only the decay products of the two gauge bosons, it is not always possible to identify the di-boson system unambiguously. For example, the $\ell\bar{\nu}_\ell\bar{\ell}'\nu_{\ell'}$ decay can only come from a W pair while the $\mathrm{q\overline{q}}\ell\bar{\nu}_\ell$ decay can also come from a WZ pair.

Parameter	68% C.L.	95% C.L.
$\Delta\kappa_\gamma$	$-0.016^{+0.042}_{-0.047}$	[-0.105, +0.069]
Δg_1^{Z}	$-0.009^{+0.022}_{-0.021}$	[-0.051, +0.034]
λ	$-0.016^{+0.021}_{-0.023}$	[-0.059, +0.026]

Table 6.9: Results for one-parameter fits combining the measurements from the four LEP experiments. In each case only the listed parameter is varied, while the other two are set to their Standard Model predictions. The combined 68% C.L. errors and 95% intervals obtained are shown, including both statistical and systematic errors.

Parameter	68% C.L.	95% C.L.	Correlations	
$\Delta\kappa_\gamma$	$-0.016^{+0.049}_{-0.049}$	[-0.106, +0.084]	1.00	+0.11
Δg_1^{Z}	$+0.004^{+0.024}_{-0.025}$	[-0.046, +0.050]		1.00
$\Delta\kappa_\gamma$	$+0.026^{+0.048}_{-0.051}$	[-0.072, +0.127]	1.00	+0.21
λ	$-0.024^{+0.025}_{-0.021}$	[-0.068, +0.023]		1.00
Δg_1^{Z}	$+0.024^{+0.029}_{-0.029}$	[-0.034, +0.081]	1.00	-0.40
λ	$-0.036^{+0.029}_{-0.029}$	[-0.093, +0.022]		1.00

Table 6.10: Results for two-parameter fits combining the measurements from the four LEP experiments. In each case only the two listed parameters are varied, while the third is set to its Standard Model value. The combined 68% C.L. errors and 95% intervals are listed, including both statistical and systematic errors. Since the shape of the $\log L$ function is not always parabolic, the correlation coefficients are only approximate values.

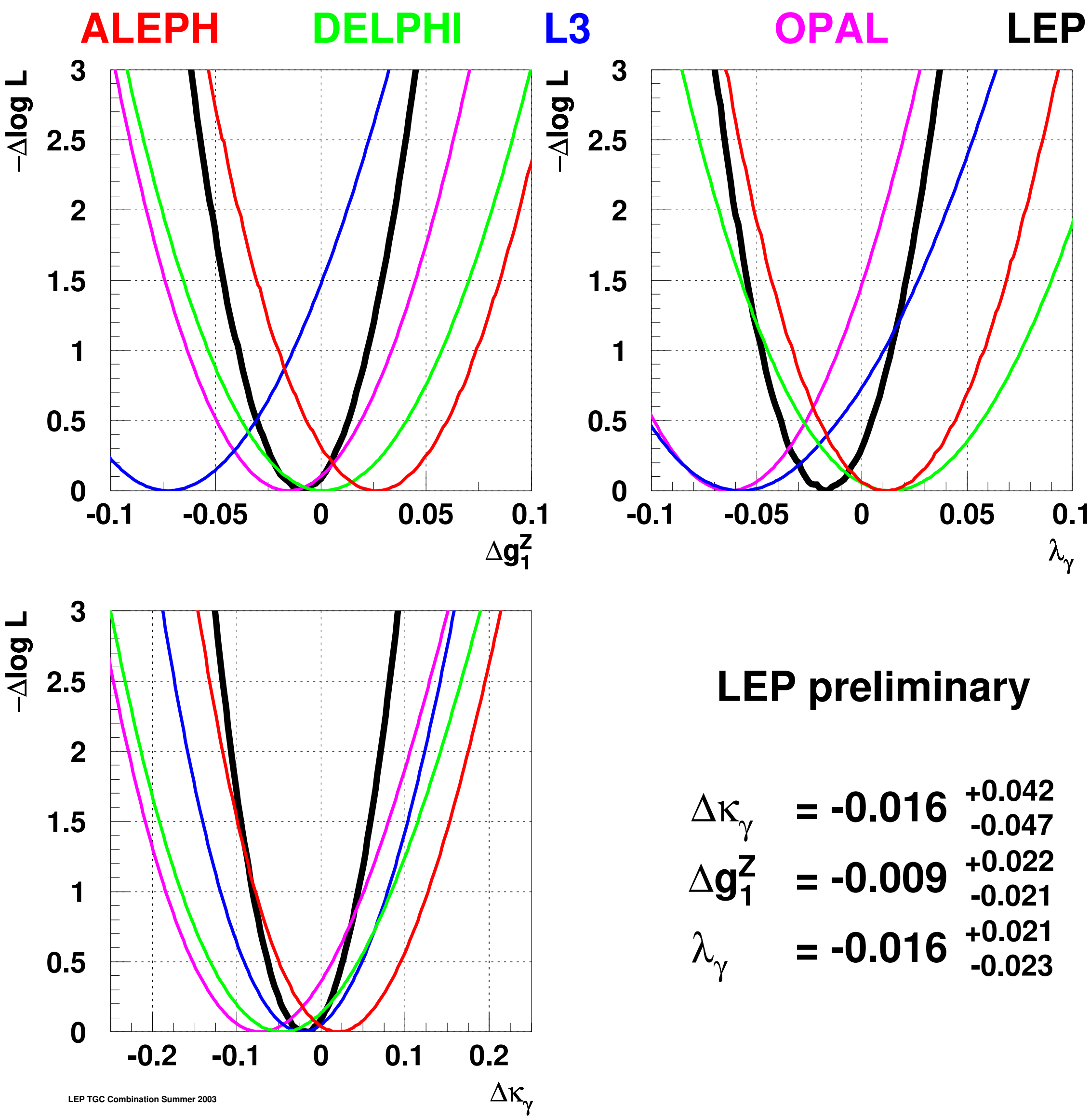

Figure 6.4: The $-\Delta \log L$ curves of the four experiments (thin line) and the LEP combined curve (thick line) for the three parameters $\Delta\kappa_\gamma$, Δg_1^Z and λ. Only one parameter is free to vary at the time and all other are set to their Standard Model predictions.

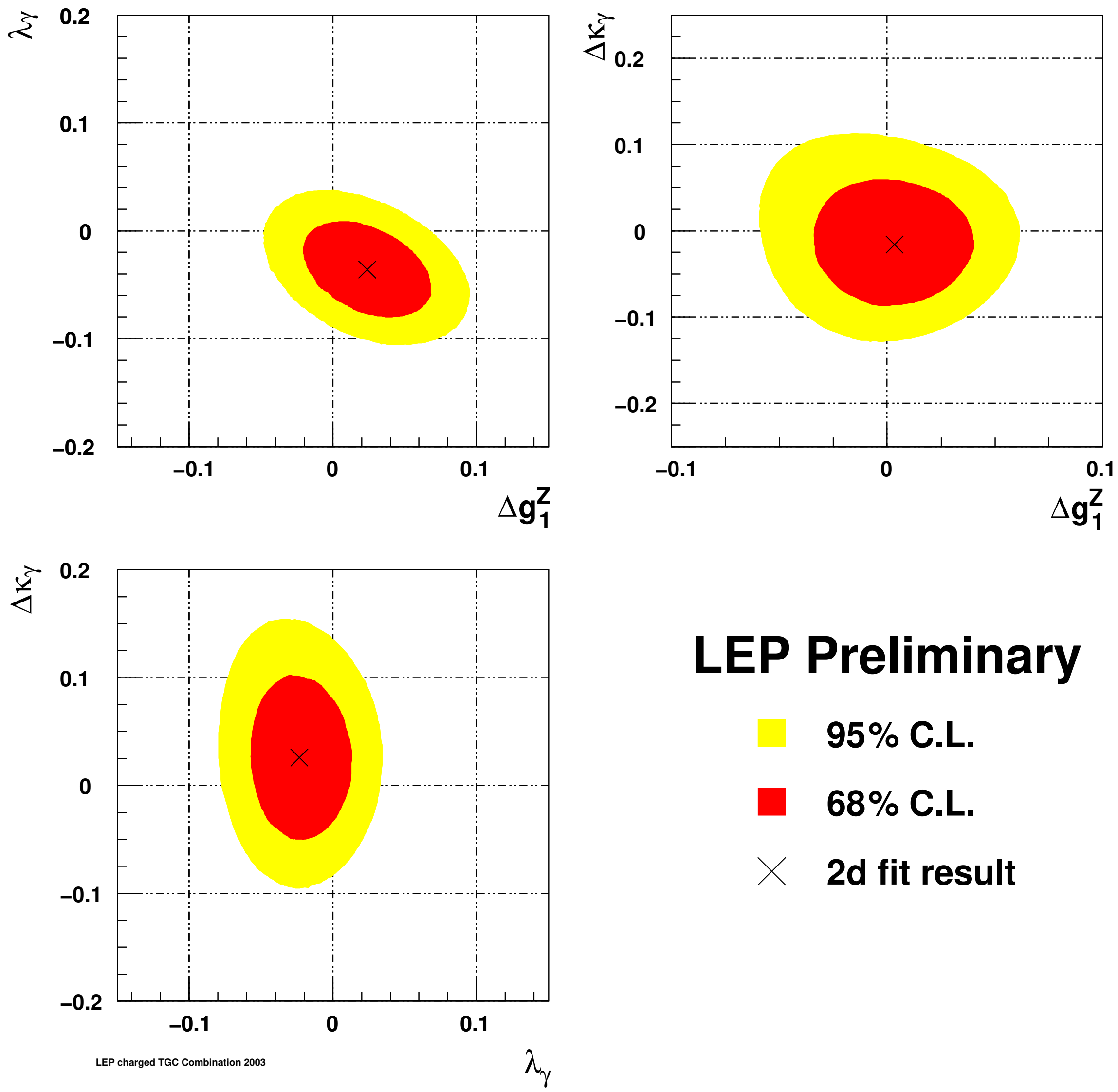

Figure 6.5: The result of two-parameter fits, where two couplings vary at the same time and the third is fixed to its Standard Model value. In each plane, the 68% and 95% confidence level contours are shown. The fitted couplings are indicated by a cross. The contours include the contribution from statistical and systematic effects.

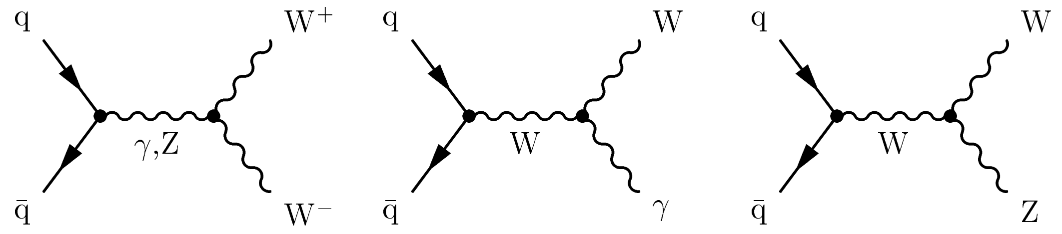

Figure 6.6: Feynman diagrams for di-boson production (W^+W^-, Wγ and WZ) in p$\bar{p}$ and pp collisions via a triple gauge vertex.

Wγ: In contrast to e^+e^- collisions quarks can annihilate into a virtual W boson which can radiate a photon via a WWγ vertex. Usually only the $\ell\bar{\nu}_\ell\gamma$ final state is analysed, where $\ell = e, \mu$. The photon gives this final state a clear signature in the detector and the p_t^γ distribution is very sensitive to anomalous couplings.

WZ: The WZ final state is produced similar to the Wγ. Instead of the photon a Z boson is radiated off the W boson. Hence it is only sensitive to WWZ couplings but only the leptonic Z decays can be experimentally distinguished from other di-boson production. For example, the $q\bar{q}\ell\bar{\nu}_\ell$ decay cannot be distinguished from the corresponding W pair decay.

WW/WZ: Both di-boson pairs have some common decays which cannot easily be disentangled experimentally. Therefore the $q\bar{q}\ell\bar{\nu}_\ell$ decay of WW and WZ pairs are combined at the analysis stage to measure WWZ and WWγ couplings. The hadronic decay mode into four quarks is usually not considered because of high backgrounds.

As at lepton colliders, the di-boson production via triple gauge vertices (figure 6.6) is not the only possibility. The independent production of two gauge bosons via the exchange of a quark in the t-channel, as depicted in figure 6.7, reduces the sensitivity.

Recent measurements come from data taken in Run 1a and 1b by the CDF and D0 experiments at the Tevatron near Chicago, USA. Both experiments have analysed all three di-boson production channels but only D0 has finalised their whole Run 1a and 1b measurements. The results are shown in table 6.11. Combining all di-boson channels analysed by D0 give the following 95% confidence limits on the anomalous couplings $\Delta\kappa = \Delta\kappa_\gamma = \Delta\kappa_Z$ and $\lambda = \lambda_\gamma = \lambda_Z$:

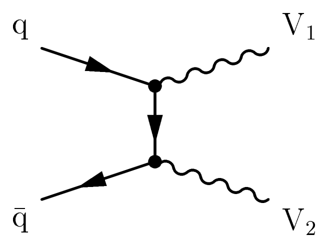

Figure 6.7: Background Feynman diagram for di-boson production ($V_{1,2} = W, Z, \gamma$) in p$\bar{p}$ and pp collisions.

$$-0.27 < \Delta\kappa < 0.42 \;\text{ and }\; -0.20 < \lambda < 0.20 \quad \text{at 95\% C.L.} \tag{6.1}$$

Before comparing these results with the corresponding ones from the LEP experiments two facts have to be taken into account. First, constant anomalous couplings violate unitarity at high energies, and therefore the coupling constants are modified at hadron colliders to

	D0	CDF
$W\gamma \to \ell\bar{\nu}_\ell\gamma$	$-0.93 < \Delta\kappa_\gamma < 0.94$ [169] $-0.31 < \lambda_\gamma < 0.29$	$-2.3 < \Delta\kappa_\gamma < 2.2$ [170] $-0.7 < \lambda_\gamma < 0.7$
$WW \to \ell\bar{\nu}_\ell\bar{\ell}'\nu_{\ell'}$	$-0.62 < \Delta\kappa < 0.77$ [171] $-0.53 < \lambda < 0.56$	$-1.0 < \Delta\kappa < 1.3$ [172] $-0.9 < \lambda < 0.9$
$WZ \to \ell\bar{\nu}_\ell e^+e^-$	$-1.63 < \Delta g_1^Z < 1.63$ [173] $-1.42 < \lambda_Z < 1.42$	
$WZ/WW \to q\bar{q}e\bar{\nu}_e$ $WZ/WW \to q\bar{q}\mu\bar{\nu}_\mu$	$-0.47 < \Delta\kappa < 0.63$ [174] $-0.36 < \lambda < 0.39$ $-0.62 < \Delta\kappa < 0.78$ [173] $-0.45 < \lambda < 0.46$	
WZ/WW → leptons+jets		$-1.11 < \Delta\kappa < 1.27$ [175] $-0.81 < \lambda < 0.84$
Combined	$-0.27 < \Delta\kappa < 0.42$ [173] $-0.20 < \lambda < 0.20$	

Table 6.11: 95% confidence limits on anomalous WWγ and WWZ couplings from the D0 and CDF experiment. The energy scale Λ for new physics is 1.5 TeV and $l = e, \mu$. If a final state involves WWγ and WWZ couplings, the following convention is used: $\Delta\kappa$=$\Delta\kappa_\gamma$=$\Delta\kappa_Z$ and λ=λ_γ=λ_Z.

include a dipole form factor $(1 + \frac{\hat{s}}{\Lambda^2})^2$, where $\hat{s}$ is the square of the invariant mass of the di-boson system and Λ the form factor scale. The scale should be around the centre-of-mass energy and is often chosen to be 1.5 TeV. Including a dipole form factor of 1.5 TeV in the LEP measurements would increase the error by 3.5%, which is not very much. Second, the WWZ and WWγ couplings are related to each other in a different way than at LEP. At the Tevatron experiments usually three different sets of limits are given if WWZ and WWγ couplings are involved: First, the photon couplings are free and the Z couplings are fixed to the Standard Model predictions and vice versa. Second, the photon and Z couplings are the same, e. g. $\Delta\kappa_\gamma = \Delta\kappa_Z$ and $\lambda_\gamma = \lambda_Z$. The combined measurements of the D0 experiment for the three schemes are listed in table 6.12. In general, the assumption of equal WWZ and WWγ couplings strengthen the limits on the couplings. At LEP relations (2.18) are used, motivated by $\mathsf{SU(2)}_L \times \mathsf{U(1)}_Y$ invariance of the Standard Model. Both conventions are identical for λ_γ and λ_Z ($\lambda = \lambda_\gamma = \lambda_Z$) but differ for $\Delta\kappa_\gamma$ and $\Delta\kappa_Z$. The nearest scheme used at D0 is the so-called HISZ scenario, where $\Delta g_1^Z = \frac{\Delta\kappa_\gamma}{2\cos^2\theta_w}$ is used in addition to the relations (2.18). The limits on $\Delta\kappa_\gamma$ in the HISZ scenario are not as stringent as in the case of equal WWZ and WWγ couplings. Therefore one can conclude, that the use of equal WWZ and WWγ couplings at the Tevatron experiments give better limits for $\Delta\kappa_\gamma$ compared to the LEP convention.

Parameter	$\Delta\kappa$	λ
α_γ, $\alpha_Z = 0$	-0.57< $\Delta\kappa_\gamma$ <0.74	-0.27< λ_γ <0.25
$\alpha_\gamma = 0$, α_Z	-0.37< $\Delta\kappa_Z$ <0.55	-0.26< λ_Z <0.29
HISZ	-0.31< $\Delta\kappa$ <0.56	-0.20< λ <0.20
$\alpha_\gamma = \alpha_Z = 0$	-0.27< $\Delta\kappa$ <0.42	-0.20< λ <0.20

Table 6.12: 95% confidence limits on anomalous WWγ and WWZ couplings from the D0 experiment combining all their measurements [173]. The energy scale Λ for new physics is 1.5 TeV. Results for different schemes for the combination of WWγ and WWZ couplings are shown. $\alpha = \Delta\kappa, \lambda$.

After these two remarks, we can compare the combined results from D0 with those obtained from OPAL (see table 6.6). The errors on both couplings are at least a factor 2 better at OPAL than at D0. This gap is even more broadened by the combination of all experiments at each collider, because LEP has twice more experiments than Tevatron. Studies showed that the limits can be decreased by a factor of 2 with 2 fb^{-1} of Run 2 at the Tevatron [176], which is then competitive with one single LEP experiment.

Chapter 7

A Study of Triple Gauge Couplings at TESLA

When proposing a new accelerator and experiment it is essential to show that new scientific knowledge can be gained. Either the experimental setup is unique to allow a measurement for the first time or, if a measurement has already been carried out at previous experiments, such a new measurement must give new insight into the topic. Both is true for TESLA and the achievable results for many different physic topics are described in much detail in the physics part of the TESLA Technical Design Report [177]. In this chapter we describe a study of the measurement of charged current triple gauge couplings in the semileptonic decay mode of W pairs at TESLA [178].

7.1 Goals of the Study

From the results at LEP the statistical sensitivity to anomalous couplings can be easily estimated. The cross-section decreases from $\sim 20\,\mathrm{pb}$ at $200\,\mathrm{GeV}$ to $\sim 8\,\mathrm{pb}$ at $500\,\mathrm{GeV}$. This decrease is compensated by the fact, that the effect of anomalous couplings increases with the centre-of-mass energy, as usual in effective theories. The main gain is achieved by the dramatic increase in luminosity from 500 pb^{-1} at LEP to 500 fb^{-1} at $\sqrt{s} = 500\,\mathrm{GeV}$. Altogether we expect an increase of roughly a factor of 50 in the expected sensitivity. Such a high precision measurement can then be used to constrain extensions of the Standard Model seriously. However, a simple extrapolation from LEP is not possible for the following reasons:

- Can the same W pair selection efficiency be reached as at LEP?
- Are the systematic errors under control?
- Sizeable Beamstrahlung will be present for the first time at TESLA. Which effect has it on a TGC measurement?
- How many couplings can be measured simultaneously? Is the expected event rate high enough to extract all 5 C and P conserving couplings simultaneously, therefore dropping the $\mathsf{SU(2)}_L \times \mathsf{U(1)}_Y$ relations and disentangling the WWZ and WWγ couplings?

- Can longitudinal beam polarisation help to improve the sensitivity of such a measurement?

In the following sections we will give some answers to the raised questions, but beforehand we introduce the general setup of a physics study for TESLA.

7.2 Simulation Setup

For this study we consider three different sets of anomalous couplings. The C and P conserving couplings are studied in two sets: first the three Standard Model like couplings Δg_1^{Z}, $\Delta\kappa_\gamma$ and λ_γ with relation (2.18) and second all five couplings Δg_1^{Z}, $\Delta\kappa_\gamma$, $\Delta\kappa_{\mathrm{Z}}$, λ_γ and λ_Z without any relation between them. This gives us the possibility to explore further the $\mathsf{SU(2)}_L \times \mathsf{U(1)}_Y$ gauge structure of the Standard Model. In addition we consider the set of C or P violating WWZ couplings. We do not consider any C or P violating WWγ couplings. There are other processes like single-W or single-γ [179] production where these couplings are considered. In addition they are rather constrained by experiments measuring electric dipole moments of the electron, neutron and various nuclei [6, 7].

A luminosity of 500 fb^{-1} at a centre-of-mass energy of 500 GeV is assumed, which is the expected amount of data after one or two years of running. Since the luminosity grows with energy, for 800 GeV a luminosity of 1000 fb^{-1} may be expected. At both energies roughly 4 millions W-pair events are expected. This huge amount of events gives us the possibility to do high precision measurements of TGCs.

Only the semileptonic decay channel ($\mathrm{W^+W^-} \to \mathrm{q\overline{q}}\ell\bar{\nu}_\ell$) is used because of the high branching ratio of 43% and the good event reconstruction. There is only one ambiguity in the hadronic decay angles. From LEP analyses [163] we know that the background is small.

All signal Monte Carlo samples are generated by Wopper as described in section 3.5. Wopper includes an interface to Circe for simulating beamstrahlung and the option of longitudinal beam polarisation. Its matrix-element calculations are used to obtain weights for the reweighting of angular distributions as functions of CP conserving and violating couplings. The background samples for two-fermion production ($\mathrm{Z}/\gamma \to \mathrm{q\overline{q}}$) and four-fermion reactions as Z-pair (ZZ), single Z (Zee) and single W (Weν_{e}) production are generated by Pythia including ISR and beamstrahlung.

For the simulation of the proposed detector we use the fast detector simulation `Simdet`3.2 [129], which is based on the proposed detector design, described in the TESLA TDR [114]. It includes a tracking and calorimeter simulation and a reconstruction of energy-flow objects, where tracks and calorimeter clusters are combined using an idealised reconstruction algorithm.

7.3 Event Selection at 500 GeV

The selection of the semileptonic channel $\mathrm{W^+W^-} \to \mathrm{q\overline{q}}\ell\bar{\nu}_\ell$ with $\ell = \mathrm{e}, \mu, \tau$ is a simple cut based selection. It requires one charged lepton and two jets, whose invariant mass should be conform with a W. Missing energy and momentum is required due to the unmeasured neutrino. Further cuts are applied to reject the background, which is dominated by the two-fermion process $\mathrm{Z}/\gamma \to \mathrm{q\overline{q}}$ and four-fermion processes like single-W and single-Z production.

The preselection rejects events with less than five charged tracks. Further the transverse momentum must be greater than 5 GeV to account for the missing momentum due to the neutrino and the visible mass, M_{vis}, must be greater than 100 GeV in order to reject radiative returns from the process $\mathrm{Z}/\gamma \to \mathrm{f\overline{f}}$.

The main selection is split up into two parts. One for the selection of events with an electron or muon, which also include the decay of tau leptons into electrons or muons, and one for the selection of events where the tau lepton decays into hadrons.

Electron and Muon Selection

Each event is searched for an electron or muon with an energy of more than 10 GeV and a separation of more than 5° to the next energy-flow object. The rest of the event is then clustered into two jets using the Durham $k_\perp$ algorithm [137]. The hadronic W candidate is reconstructed from the two jets and the leptonic W candidate from the lepton and the missing energy vector, assuming momentum conservation. The charge of the Ws is assigned from the lepton charge. The invariant masses M_{W_l} and M_{W_j} of the leptonic and hadronic W candidate are good variables for background suppression. For example a misidentified event from the process $\mathrm{W^+W^-} \to \mathrm{q\overline{q}q\overline{q}}$ has a large hadronic invariant mass, because all tracks except the lepton candidate are assigned to the hadronic W. The leptonic mass M_{W_l} must be less than 150 GeV to reject single-W and single-Z production and the hadronic mass M_{W_j} must be less than 150 GeV to suppress misidentified events from $\mathrm{W^+W^-} \to \mathrm{q\overline{q}q\overline{q}}$. For further rejection of four-fermion background, $\cos\theta_{\mathrm{W}}$ should be greater than -0.95.

The prompt decays $\mathrm{W^+W^-} \to \mathrm{q\overline{q}e\overline{\nu}_e}$ or $\mathrm{W^+W^-} \to \mathrm{q\overline{q}}\mu\overline{\nu}_\mu$ are distinguished from the decay of tau leptons into electrons or muons by considering a discriminating variable. This variable is the sum of the squared ratios of the visible energy to the centre-of-mass energy, the lepton energy to the beam energy and the mass of the leptonic decaying W to the nominal W mass. Candidates with a sum smaller than 1 are classified as leptonic τ decays.

For τ candidates the direction of the visible decay products is almost the direction of the τ because of the high boost. Hence the direction of the visible decay products is taken as the τ direction and the energy is calculated from considering momentum and energy conservation. The missing energy vector for the neutrino is recalculated afterwards. This approach is used for example by the OPAL collaboration in their TGC analysis [163].

Hadronic Selection

Each event is clustered into three jets. It must require at least one low multiplicity jet ($N_{track} < 10$) with no high-energy electron or muon ($E > 10\,\mathrm{GeV}$). If only one low-multiplicity jet is found, it is taken as the τ candidate and the other two jets are assigned to the hadronic W candidate. Otherwise the three jets are arranged in turns into a τ candidate and two jets form the hadronic W candidate. The combination with the hadronic mass M_{W_j} nearest to the nominal W mass is chosen. The τ candidate is reconstructed as described above. Further the τ energy must be greater than 10 GeV. The charge of the W bosons is assigned from the sum of the charged tracks of the τ candidate. Events with zero charge are rejected. For background suppression both W masses must be less than 150 GeV and $\cos\theta_{\mathrm{W}}$ greater than -0.95.

Process	σ[pb]	ϵ[%]	N	N[%]
$W^+W^- \to q\bar{q}\ell\bar{\nu}_\ell$	3.51	61.8	1085166	94.66
$W^+W^- \to q\bar{q}q\bar{q}$	3.71	0.07	1299	0.11
$W^+W^- \to \ell^+\nu_\ell\ell'^-\bar{\nu}_{\ell'}$	0.81	0.05	203	0.02
$Z/\gamma \to q\bar{q}$	21.02	0.18	18918	1.65
ZZ	0.67	1.50	5025	0.44
Zee	14.68	0.34	24956	2.18
$We\nu_e$	6.34	0.34	10778	0.94

Table 7.1: Selection efficiencies for signal and background at 500 GeV.

Selection Efficiency

At 500 GeV the overall signal efficiency is 61.8% and the purity is 94.7%. The electron efficiency of 62.9% is lower than the reconstruction efficiency for muons (70.3%) while the τ efficiency is 55.9%. The main background comes from the process $e^+e^- \to Ze^+e^-$. In table 7.1 a detailed account on the selection efficiencies for signal and background is given.

For comparison the efficiency for a LEP analysis of this kind is around 80% with a background contribution of around 5% [163]. In this cut based selection the efficiency can easily be enhanced by loosening some cuts, but on the other side the background contribution grows. A higher efficiency can probably be achieved by using a more sophisticated method, e. g. a likelihood selection.

Angular Distributions

In figure 7.1 the measured distributions of the W production angle $\cos\theta_W$ and the four W decay angles $\cos\theta^*_l$, ϕ^*_l, $\cos\theta^*_k$ and ϕ^*_j are shown. The hadronic decay angles $\cos\theta^*_j$ and ϕ^*_j can only be measured up to a sign ambiguity and are therefore folded using the prescription (3.7). The achieved detector resolution of these five angles is shown in figure 7.2. The $\cos\theta_W$ resolution is more than one order of magnitude better than what is achieved at LEP [180]. The resolution of the four decay angles $\cos\theta^*$ and ϕ^* is still by a factor of two to three better. This is due to the excellent performance of the proposed TESLA detector.

These five angles are not directly used to extract the triple gauge boson couplings. In the case of the OPAL analysis (see chapter 5) the method of optimal observables has been applied in order to transform the five-fold differential cross-section into a simpler form while keeping most of the information about the TGCs. In this study an alternative approach is explored. The spin density matrices, describing the polarisation of the W bosons, are used in addition to the W production angle $\cos\theta_W$ for the measurement of the couplings. With this method the two-fold differential cross-section $\frac{d\sigma}{d\cos\theta^* d\phi^*}(\cos\theta_W)$, describing the W decay, is condensed to nine numbers. Three for the fraction of the three W polarisation states and six numbers for the three complex correlation coefficients between the polarisation states. The spin density matrices are introduced in the following section.

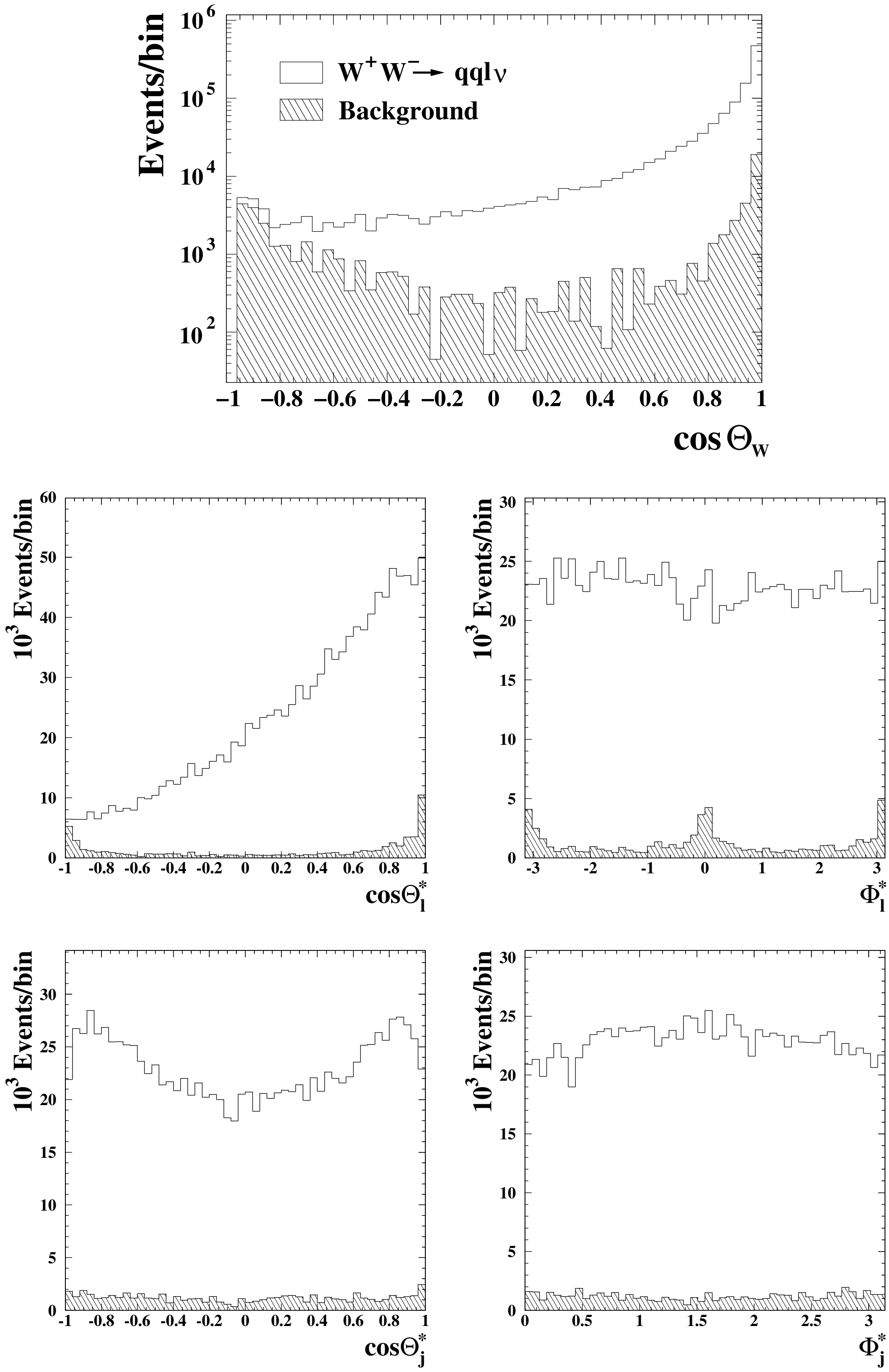

Figure 7.1: The $\cos\theta_W$ distribution and the four decay angles are shown after the detector simulation for a centre-of-mass energy of 500 GeV and a luminosity of 500 fb^{-1}. The hatched curve shows the expected background and the open curve the signal, which is plotted on top of the background.

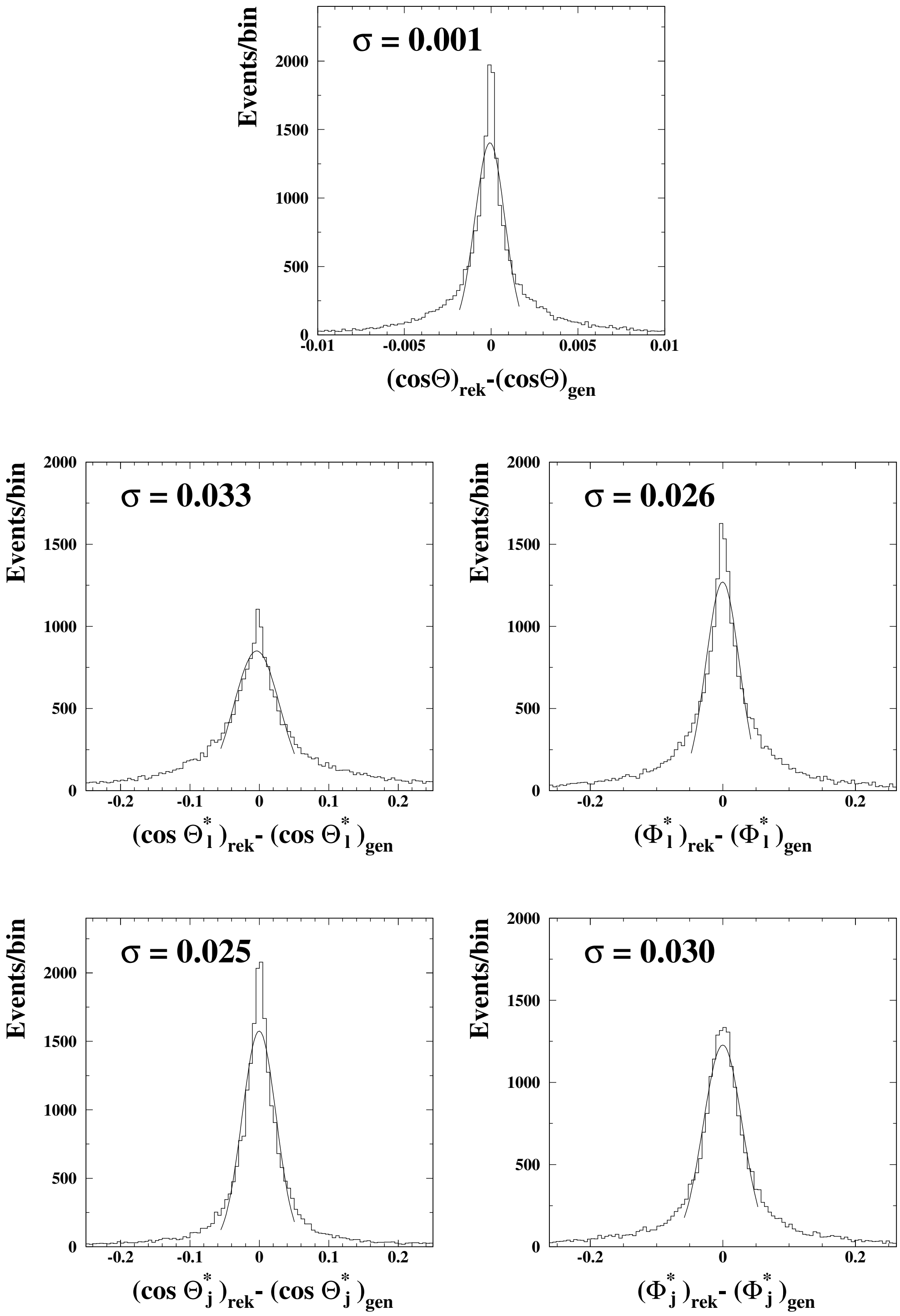

Figure 7.2: The expected resolution of $\cos\theta_{\mathrm{W}}$ and the four decay angles are shown for a centre-of-mass energy of 500 GeV. The histograms show the difference between detector and generator level and the curves show a Gaussian fit to the histograms for a rough estimation of the resolution, only. The width of the fit is listed as σ.

7.4 Spin Density Matrices

Helicity amplitudes are a special representation of matrix elements, where the helicity states of the ingoing and outgoing particles are explicitly given. In the process $\mathrm{e^+e^-} \to \mathrm{W^+W^-}$ the electron helicity is $\lambda = \pm\frac{1}{2}$ (the positron helicity is $\lambda' = -\lambda$ in the limit of massless leptons) and the $\mathrm{W^+}$ and $\mathrm{W^-}$ helicities are $\tau_+ = \pm 1, 0$ and $\tau_- = \pm 1, 0$, respectively. The so-called D-functions $D_{\tau\tau'}(\theta^*, \phi^*)$ describe the angular dependence of the decay $\mathrm{W} \to \mathrm{f\,\bar{f}'}$ and are normalised as

$$\int_{-1}^{+1} \int_{-\pi}^{+\pi} D_{\tau\tau'}(\theta^*, \phi^*) \mathrm{d}\cos\theta^* \mathrm{d}\phi^* = \frac{8\pi}{3}\delta_{\tau\tau'}. \tag{7.1}$$

They are universal and independent of the W production process. The differential cross-section for the process $\mathrm{e^+e^-} \to \mathrm{W^+W^-} \to \mathrm{f_1\bar{f}_2f_3\bar{f}_4}$ can be written as the product of helicity amplitudes $\mathcal{F}^{(\lambda)}_{\tau_-\tau_+}$ [4] for the production and D-functions for the decay of a W pair, summed over all possible helicity combinations

$$\begin{aligned} &\frac{\mathrm{d}^5\sigma(\mathrm{e^+e^-} \to \mathrm{W^+W^-} \to \mathrm{f_1\bar{f}_2f_3\bar{f}_4})}{\mathrm{d}\cos\theta_\mathrm{W}\mathrm{d}\cos\theta^*_{\mathrm{W^-}}\mathrm{d}\phi^*_{\mathrm{W^-}}\mathrm{d}\cos\theta^*_{\mathrm{W^+}}\mathrm{d}\phi^*_{\mathrm{W^+}}} = \\ &\quad \frac{\beta}{32\pi s}\left(\frac{3}{8\pi}\right)^2 Br(\mathrm{W} \to \mathrm{f_1\bar{f}_2}) Br(\mathrm{W} \to \mathrm{f_3\bar{f}_4}) \\ &\quad \times \sum_{\lambda,\tau_-,\tau_+,\tau'_-,\tau'_+} \mathcal{F}^{(\lambda)}_{\tau_-\tau_+}\left(\mathcal{F}^{(\lambda)}_{\tau'_-\tau'_+}\right)^* D_{\tau_-\tau'_-}(\theta^*_{\mathrm{W^-}}, \phi^*_{\mathrm{W^-}}) D_{\tau_+\tau'_+}(\pi - \theta^*_{\mathrm{W^+}}, \phi^*_{\mathrm{W^+}} + \pi) \end{aligned} \tag{7.2}$$

Integrating the W decay angles in equation (7.2) and using the normalisation (7.1) gives the cross-section for W-pair production:

$$\frac{\mathrm{d}\sigma(\mathrm{e^+e^-} \to \mathrm{W^+W^-})}{\mathrm{d}\cos\theta_\mathrm{W}} = \frac{\beta}{16\pi s}\sum_{\lambda,\tau_-,\tau_+}\left|\mathcal{F}^{(\lambda)}_{\tau_-\tau_+}\right|^2. \tag{7.3}$$

From the structure of the D-functions it follows, as expected, that only helicity amplitude products $\mathcal{F}_{\tau_-\tau_+}\mathcal{F}^*_{\tau'_-\tau'_+}$ contribute, where $\tau_- = \tau'_-$ and $\tau_+ = \tau'_+$.

The spin density matrix (SDM) elements [181] are normalised products of the helicity amplitudes and describe the polarisation of the W pair. The elements of the two-particle joint density matrix are defined by

$$\rho_{\tau_-\tau'_-\tau_+\tau'_+}(\cos\theta_\mathrm{W}) = \frac{\sum\limits_{\lambda} \mathcal{F}^{(\lambda)}_{\tau_-\tau_+}\left(\mathcal{F}^{(\lambda)}_{\tau'_-\tau'_+}\right)^*}{\sum\limits_{\lambda,\tau_+,\tau_-}\left|\mathcal{F}^{(\lambda)}_{\tau_-\tau_+}\right|^2}, \tag{7.4}$$

The SDM is hermitian which reduces the $9 \times 9 = 81$ complex elements including the normalisation

$$\sum_{\tau_+,\tau_-} \rho_{\tau_-\tau_-\tau_+\tau_+} = 1 \tag{7.5}$$

to $81 \cdot 2 - 9 - 36 \cdot 2 - 1 = 80$ independent real elements. 34 elements are CP conserving and 46 CP violating. The elements of the main diagonals are directly related to the polarisation of the W pair, as can be seen from equation (7.3). The differential cross-section in $\cos\theta_{\mathrm{W}}$ is given as

$$\begin{aligned}
\frac{\mathrm{d}\sigma^{TT}}{\mathrm{d}\cos\theta_{\mathrm{W}}} &= \frac{\mathrm{d}\sigma}{\mathrm{d}\cos\theta_{\mathrm{W}}}(\rho_{----} + \rho_{--++} + \rho_{++--} + \rho_{++++}) \\
\frac{\mathrm{d}\sigma^{LL}}{\mathrm{d}\cos\theta_{\mathrm{W}}} &= \frac{\mathrm{d}\sigma}{\mathrm{d}\cos\theta_{\mathrm{W}}}\rho_{0000} \\
\frac{\mathrm{d}\sigma^{LT}}{\mathrm{d}\cos\theta_{\mathrm{W}}} &= \frac{\mathrm{d}\sigma}{\mathrm{d}\cos\theta_{\mathrm{W}}}(\rho_{00++} + \rho_{00--}) \\
\frac{\mathrm{d}\sigma^{TL}}{\mathrm{d}\cos\theta_{\mathrm{W}}} &= \frac{\mathrm{d}\sigma}{\mathrm{d}\cos\theta_{\mathrm{W}}}(\rho_{++00} + \rho_{--00}),
\end{aligned} \tag{7.6}$$

where the label P^+P^- at the cross-section denotes the polarisation of the W^+ and W^- boson, respectively. The polarisation P can either be transversal (T) or longitudinal (L).

One-particle Spin Density Matrices

The number of elements can be reduced by considering only one-particle density matrices, one for each W boson. The one-particle SDM for one W boson is defined as the sum of the two-particle SDM over all helicity states of the other W

$$\begin{aligned}
\rho^{\mathrm{W}^-}_{\tau_-\tau'_-}(\cos\theta_{\mathrm{W}}) &= \sum_{\tau_+}\rho_{\tau_-\tau'_-\tau_+\tau_+} \\
\rho^{\mathrm{W}^+}_{\tau_+\tau'_+}(\cos\theta_{\mathrm{W}}) &= \sum_{\tau_-}\rho_{\tau_-\tau_-\tau_+\tau'_+}.
\end{aligned} \tag{7.7}$$

Using only one-particle spin density matrices neglects the spin correlations between the different W bosons. With the normalisation

$$\sum_{\tau}\rho^{\mathrm{W}^-}_{\tau\tau} = 1, \qquad \sum_{\tau}\rho^{\mathrm{W}^+}_{\tau\tau} = 1 \tag{7.8}$$

the number of independent real elements is reduced to $9\cdot 2 - 3 - 3\cdot 2 - 1 = 8$ for each W boson. The one-particle spin density matrix is hermitian and thus the diagonal elements $\rho^{\mathrm{W}^\pm}_{\tau\tau}$ are real. As for the case of the two-particle SDM they can be interpreted as the probability to produce a $\mathrm{W}^\pm$ boson with the helicity τ. The differential cross-section for producing longitudinal or transverse W bosons can be written as the product of the unpolarised cross-section and the sum of SDM elements:

$$\begin{aligned}
\frac{\mathrm{d}\sigma_L}{\mathrm{d}\cos\theta_{\mathrm{W}}} &= \frac{\mathrm{d}\sigma}{\mathrm{d}\cos\theta_{\mathrm{W}}}\rho_{00} \\
\frac{\mathrm{d}\sigma_T}{\mathrm{d}\cos\theta_{\mathrm{W}}} &= \frac{\mathrm{d}\sigma}{\mathrm{d}\cos\theta_{\mathrm{W}}}(\rho_{++} + \rho_{--})
\end{aligned} \tag{7.9}$$

The off-diagonal elements can be complex and describe interference effects between different helicity states. Figure 7.3 shows the real parts of the SDM elements for the Standard Model and an anomalous coupling of $\Delta g_1^{\mathrm{Z}} = 0.1$ at a centre-of-mass energy of 500 GeV. The diagonal elements show that the change in the W polarisation for this anomalous couplings very strong while not all off-diagonal elements show sensitivity at all.

In CP-conserving theories the imaginary part of the off-diagonal elements must vanish. This follows directly from the properties of the helicity amplitudes under CPT and CP transformations [182]. On the other hand the imaginary part of the off-diagonal elements are three CP-odd observables, which are very useful for investigating CP-odd anomalous couplings. Figure 7.4 shows the three imaginary parts of the off-diagonal elements for the two anomalous couplings $\tilde{\kappa}_Z = 1$ and $\tilde{\lambda}_Z = 1$ at Born-level and a centre-of-mass energy of 500 GeV. Not all three elements have the same sensitivity to each coupling but some elements show a high sensitivity to a particular coupling.

Spin Density Matrix Extraction

The SDM elements are extracted from data using projection operators [155]. The threefold differential cross-section can be expressed as the production cross-section multiplied by the sum of all SDM elements

$$\begin{aligned}\frac{\mathrm{d}^3\sigma(\mathrm{e^+e^-} \to \mathrm{W^+} + \mathrm{f\,\bar{f}'})}{\mathrm{d}\cos\theta_\mathrm{W}\,\mathrm{d}\cos\theta^*_{\mathrm{W^-}}\,\mathrm{d}\phi^*_{\mathrm{W^-}}} &= \frac{\mathrm{d}\sigma(\mathrm{e^+e^-} \to \mathrm{W^+W^-})}{\mathrm{d}\cos\theta_\mathrm{W}} \\ &\quad Br\frac{3}{8\pi}\sum_{\tau_-,\tau'_-} \rho^{\mathrm{W^-}}_{\tau_-\tau'_-}(\cos\theta_\mathrm{W}) D_{\tau_-\tau'_-}(\cos\theta^*,\phi^*),\end{aligned} \tag{7.10}$$

where Br is the branching ratio of the $\mathrm{W^+f\,\bar{f}'}$ channel. The D-functions are universal and independent of triple gauge boson couplings. This equation can be solved for the SDM elements by using appropriate projection operators $\Lambda_{\tau\tau'}$:

$$\begin{aligned}\Lambda^{\mathrm{W^+}}_{\pm\pm} &= \Lambda^{\mathrm{W^-}}_{\mp\mp} = \tfrac{1}{2}(5\cos^2\theta^* \mp 2\cos\theta^* - 1) \\ \Lambda^{\mathrm{W^+}}_{00} &= \Lambda^{\mathrm{W^-}}_{00} = 2 - 5\cos^2\theta^* \\ \Lambda^{\mathrm{W^+}}_{+-} &= \Lambda^{\mathrm{W^-}}_{-+} = 2\exp(2i\phi^*) \\ \left(\Lambda^{\mathrm{W^+}}_{\mp 0}\right)^* &= -\Lambda^{\mathrm{W^-}}_{\pm 0} = \tfrac{8}{3\pi\sqrt{2}}(1 \mp 4\cos\theta^*)\exp(\mp i\phi^*).\end{aligned} \tag{7.11}$$

The projection operators for the diagonal elements depend only on $\cos\theta^*$ while for the off-diagonal elements they depend on both decay angles $\cos\theta^*$ and ϕ^*. The matrix element of a certain bin k of $\cos\theta_\mathrm{W}$ can be obtained by

$$\rho^k_{\tau\tau'} = \frac{1}{N_k}\sum_{i=1}^{N_k}\Lambda_{\tau\tau'}(\theta^*_i,\phi^*_i) = \langle\Lambda_{\tau\tau'}(\theta^*_i,\phi^*_i)\rangle\,, \tag{7.12}$$

where N_k is the number of events in bin k and θ^*_i and ϕ^*_i are the decay angles of the i^{th} event. The SDM elements are the mean of the corresponding projection operator and hence the error of the SDM elements is given by

$$\sigma(\rho^k_{\tau\tau'}) = \sqrt{\frac{1}{N_k(N_k-1)}\sum_{i=1}^{N_k}\left(\Lambda_{\tau\tau'}(\theta^*_i,\phi^*_i) - \rho^k_{\tau\tau'}\right)^2}. \tag{7.13}$$

All nine SDM elements can only be extracted, if the decay angles $\cos\theta^*$ and ϕ^* for a W boson are fully and unambiguously reconstructed. This is no problem for W bosons decaying into leptons but for W bosons decaying into hadrons. Without flavour tags the decay angles

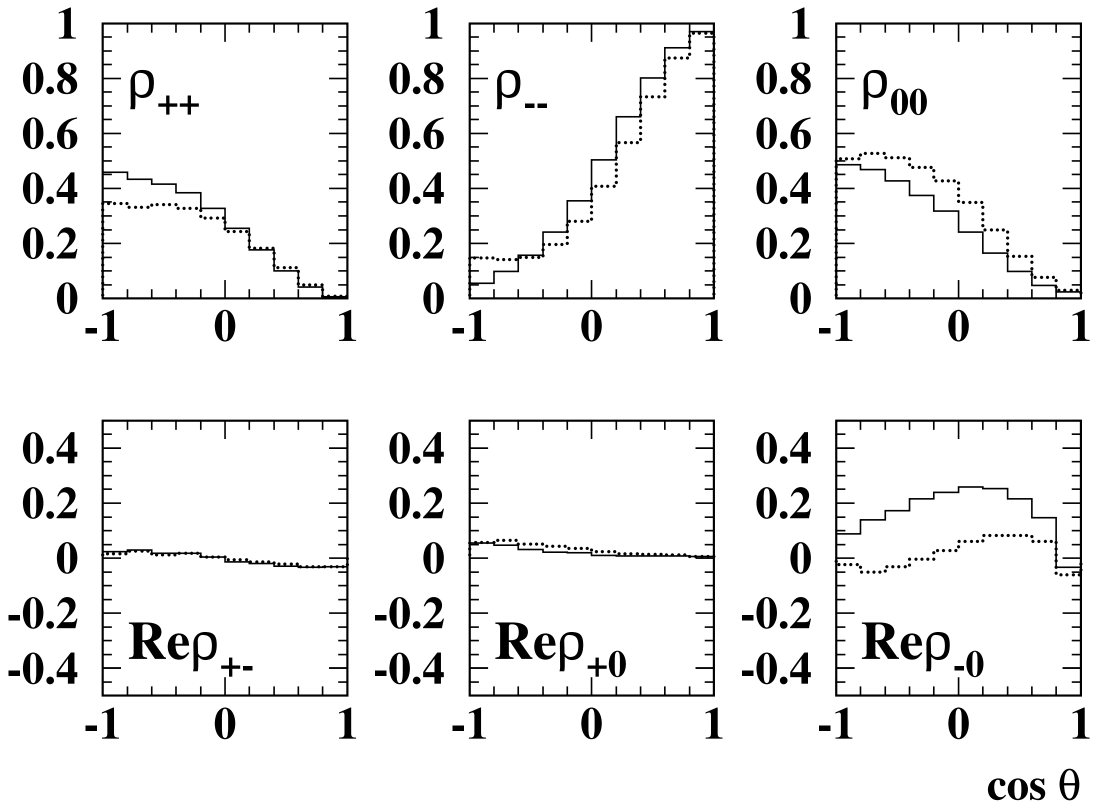

Figure 7.3: Real part of the SDM elements for the SM (solid line) and an anomalous coupling of $\Delta g_1^Z = 0.1$ (dashed line) at Born-level at 500 GeV. The imaginary parts are zero for these couplings.

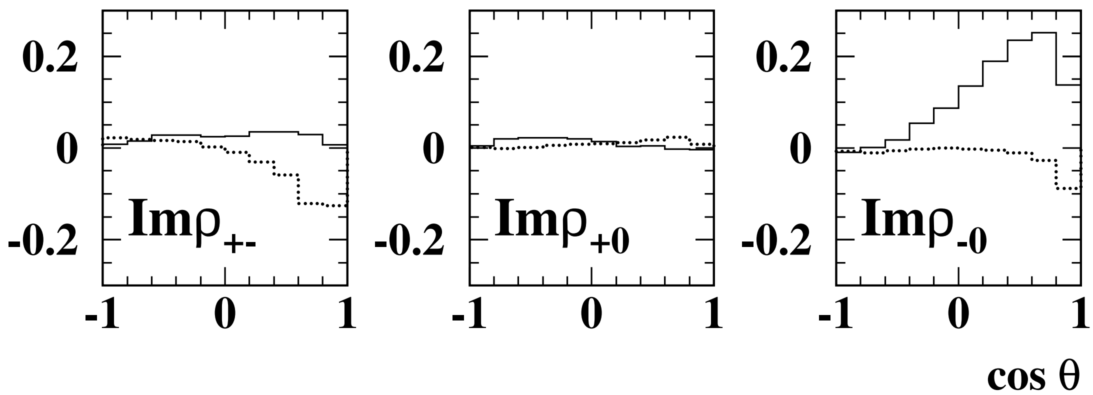

Figure 7.4: Imaginary parts of the off-diagonal SDM elements for the two anomalous couplings $\tilde{\kappa}_Z = 1$ (solid line) and $\tilde{\lambda}_Z = 1$ (dotted line) at Born-level at 500 GeV. For CP conserving couplings the imaginary parts must vanish.

are folded as shown in equation (3.7) and only five values can be extracted. Some SDM elements can be extracted unambiguously but some only as linear combinations of two. For example ρ_{00} can be extracted unambiguously because the projection operator depend only on $\cos^2\theta^*$ and the sign ambiguity in $\cos\theta^*$ does not matter. Similarly, the projection operator Λ_{+-} is invariant under a phase shift of π and ρ_{+-} can be extracted directly. The sum of ρ_{++} and ρ_{--} can be extracted because the linear terms in $\cos\theta^*$ chancel each other. Similar arguments for $\Lambda_{\pm 0}$ give $\mathrm{Re}(\rho_{+0}-\rho_{-0})$ and $\mathrm{Im}(\rho_{+0}+\rho_{-0})$.

7.5 Fit Method

For the extraction of the TGCs from the measured angles we use a χ^2-fit to the normalised $\cos\theta_\mathrm{W}$ distribution and the one-particle spin density matrix elements. The total cross-section is not used even though it is sensitive to TGCs. For this reason the normalised $\cos\theta_\mathrm{W}$ distribution is used in order to drop all cross-section information. The information from a cross-section measurement can easily be combined with the results from this study. The OPAL measurement of TGCs, as described in section 6.1, shows already that the total cross-section is good to exclude large anomalous couplings but its sensitivity is rather limited around the Standard Model im comparison with event shape type measurements. The reference distributions as a function of the anomalous TGCs are obtain by a reweighting technique. Each Monte Carlo event i is weighted by a weight

$$w_i = \frac{\mathrm{d}\sigma^{ano}}{\mathrm{d}\Omega} \bigg/ \frac{\mathrm{d}\sigma^{SM}}{\mathrm{d}\Omega}, \tag{7.14}$$

where $\mathrm{d}\Omega = \mathrm{d}\cos\theta_\mathrm{W}\mathrm{d}\cos\theta^*_{\mathrm{W}^-}\mathrm{d}\phi^*_{\mathrm{W}^-}\mathrm{d}\cos\theta^*_{\mathrm{W}^+}\mathrm{d}\phi^*_{\mathrm{W}^+}$. This is the ratio of the fivefold differential cross-section for the set of anomalous couplings under consideration to the SM differential cross-section. The weight is calculated from the Born level information and can be applied to either Born level or fully simulated distributions, hence including detector effects.

This fit method is simple and easy to use. Fits with more than one free variable are unproblematic. Also detector effects and selection efficiencies are included by reweighting angular distributions including detector simulation.

7.6 Unpolarised Beams

In the case of unpolarised beams we expect a luminosity of 500 fb^{-1} at a centre-of-mass energy of 500 GeV and 1000 fb^{-1}at 800 GeV in one or two years of running. For the extraction of the TGCs we use the normalised $\cos\theta_\mathrm{W}$ distribution and the SDM elements.

Table 7.5 shows the expected statistical error for the different couplings from a 1d-fit at 500 and 800 GeV at generator level. In a 1d-fit only one coupling is allowed to vary freely and all other are set to their Standard Model values. The fit results are arranged into three groups. The first group include the three C and P conserving couplings Δg_1^Z, $\Delta\kappa_\gamma$ and λ_γ with the $\mathsf{SU(2)}_L\times\mathsf{U(1)}_Y$ relations (3.7). In the second group the $\mathsf{SU(2)}_L\times\mathsf{U(1)}_Y$ relations are dropped and all five C and P conserving couplings are considered. The last group includes the four C or P violating couplings g_4^Z, g_5^Z, $\tilde{\kappa}_Z$ and $\tilde{\lambda}_Z$.

At 500 GeV the expected errors at generator level for Δg_1^Z, $\Delta\kappa_\gamma$ and λ_γ are $6-7\times10^{-4}$. Dropping the $\mathsf{SU(2)}_L\times\mathsf{U(1)}_Y$ relation increases the errors of $\Delta\kappa_\mathrm{Z}$, λ_γ and λ_Z a bit and of

Δg_1^Z by a factor of five while the error of $\Delta\kappa_\gamma$ decreases. The error of the C or P violating couplings ranges between 11×10^{-3} and 86×10^{-3}.

Further the fits were repeated at generator and detector level (with and without background inclusion) in order to learn more about the simulation of detector and background. A selection efficiency of 61.8% means an increase of the statistical error by 27% with respect to the results at generator level, assuming that the statistical error is proportional to the square root of the number of events. Comparing generator level with detector level without including background (see table 7.2) shows, that the statistical error increases on average only by 6%. This means that the data selection rejects mainly events with low sensitivity to TGCs. Naively, one would expect that the selection efficiency is higher for a TGC sensitive phase space region, but the differential efficiency distributions in $\cos\theta_{\mathrm{W}}$, $\cos\theta_1^*$ and $\cos\theta_2^*$ are almost flat. Further studies on the different decay channels show that the increase of around 6% is mainly due to the τ reconstruction. The difference between generator and detector level considering only electron or muon candidates is very small. This is due to the excellent resolution of all measured particles, especially electrons and muons. For τ candidates generator and detector level differ up to 20%. This is due to the non-optimal tau lepton reconstruction. The approximation of the τ direction by the direction of the visible τ decay products is very good, but the τ energy must be calculated from energy and momentum conservation. This calculated energy has a better resolution than the energy from the decay products but is still not optimal. This results in a degraded decay angle resolution compared to electron and muon candidates. The resolution could be improved for example by using a kinematic fit in the event reconstruction (see section 6.1).

Background is a more severe problem. The expected errors increase by around 24% with respect to generator level and the fraction of TGC fit results outside the expected errors is too high. However, the expected sensitive from this full simulation has the same order of magnitude as the sensitivity at generator level. The full simulation suffers from the following facts. The background is peak in the forward and backward region of $\cos\theta_{\mathrm{W}}$ (see figure 7.1). In the forward region the signal is dominant and the TGC sensitivity is low. However, the TGC sensitivity is high in the backward region and the signal rate is low. For the simulation of the background only two million events including detector simulation are generated for each single background. This results in scaling factors larger than one, e. g. for the two-fermion background the factor is around five. These scaling factor are included in the error

	$\Delta g_1^{\mathrm{Z}\,\mathrm{a}}$	$\Delta\kappa_\gamma{}^{\mathrm{a}}$	$\lambda_\gamma{}^{\mathrm{a}}$	Δg_1^Z	$\Delta\kappa_\gamma$	λ_γ	$\Delta\kappa_{\mathrm{Z}}$	λ_Z	g_4^Z	g_5^Z	$\tilde{\kappa}_Z$	$\tilde{\lambda}_Z$
500 GeV[b]	7.3	5.7	6.1	38.1	4.8	12.1	8.7	11.5	85.8	27.7	64.9	11.4
500 GeV[c]	7.8	5.7	6.8	47.5	4.8	13.9	9.0	12.8	82.4	28.7	64.4	11.9
500 GeV[d]	8.6	6.3	8.2	54.0	5.3	18.0	10.0	15.8	86.5	30.7	72.7	14.6

[a]With $\mathsf{SU(2)}_L \times \mathsf{U(1)}_Y$ relations.
[b]Generator level
[c]Detector level (without background)
[d]Detector level (with background)

Table 7.2: Expected sensitivity ($\times 10^{-4}$) for different couplings at a centre-of-mass energy of 500 GeV and a luminosity of 500 fb^{-1} without beam polarisation.

calculation and increases the statistical error significantly in the backward region. Finally, the tau lepton reconstruction is not optimal.

The reduction of the background is an important point for the measurement of triple gauge boson couplings at TESLA and more sophisticated method, as used at LEP(see section 6.1), have to be used. Nevertheless for all further TGC fits only the generator level is considered.

At 800 GeV we gain a factor up to two in sensitivity with respect to 500 GeV. The size of the data sample changes only slightly with energy because the decrease in the cross-section is compensated by a higher luminosity. However, the effects of anomalous couplings described by an effective theory are more pronounced at higher energies. We also see that we loose sensitivity by discarding the $\mathsf{SU(2)}_L \times \mathsf{U(1)}_Y$-relation (2.18). The sensitivity for the C or P violating couplings is almost an order of magnitude worse than the sensitivity for the standard couplings.

The high luminosity of TESLA gives us the opportunity to explore the correlation between the couplings with high precision in a multi dimensional fit. In tables 7.6 to 7.8 the expected sensitivity and correlation matrix are listed for different combinations of couplings at 500 and 800 GeV. For both energies the study shows roughly the same behaviour.

The behaviour of the three standard couplings (with $\mathsf{SU(2)}_L \times \mathsf{U(1)}_Y$ relation (2.18)) are shown in table 7.6. The correlation between Δg_1^{Z} and $\Delta\kappa_\gamma$ is almost 100% while the correlation between λ_γ and the other two couplings is small. This has great impact on the expected sensitivity in the 3d-fit. The sensitivity for λ_γ hardly changes while it decreases for $\Delta\kappa_\gamma$ and Δg_1^{Z} of around four to seven compared to the 1-d fit sensitivities.

The statistics and the sensitivity of this process is high enough to discard the $\mathsf{SU(2)}_L \times \mathsf{U(1)}_Y$-relation. Table 7.7 shows the expected sensitivity and correlation matrix for all five C and P conserving couplings. The simultaneous fit of five couplings seems feasible but the correlation between corresponding WWZ and WWγ couplings is very high. This is no surprise, because the structure of the corresponding couplings is the same for unpolarised beams. The high correlation between Δg_1^{Z} and $\Delta\kappa_\gamma$ in the three parameter fit is due to this high correlation. Equation (2.18) couples Δg_1^{Z} with the two couplings $\Delta\kappa_\gamma$ and $\Delta\kappa_{\mathrm{Z}}$. As before, the sensitivity increases drastically in the 5d-fit compared to the sensitivities in the 1d-fit due to the high correlations.

In table 7.8 the results for the four C or P violating couplings are listed. The couplings with different properties under C and P transformation are almost uncorrelated and the expected errors from the 4d-fit are the same as the errors from the 1d-fit, except for $\tilde{\kappa}_Z$ and $\tilde{\lambda}_Z$which are both C conserving and P violating. The correlation between them is around 50%.

Systematic Error Sources

First tests for the evaluation of possible systematic uncertainty sources have been carried out. We consider radiative corrections like initial state radiation (ISR) and beamstrahlung (BS) and the impact of uncertainties of other measurements, e. g. the W mass and the beam energy. Table 7.3 summarises the results of this study.

The effect of radiative corrections is investigated in a simple way. For ISR we compare the results of the standard fit with the results of a fit without ISR and assign the shift as the systematic error. For this we switch off the ISR correction in the data distributions and

	ISR (100%)	BS (100%)	M_{W}	E_{beam}	$\sigma_{\mathrm{sys}}{}^{\mathrm{a}}$	σ_{stat}
Δg_1^{Zb}	302.3	31.0	2.1	1.2	5.0	7.3
$\Delta\kappa_\gamma{}^{\mathrm{b}}$	829.1	18.0	1.7	1.1	8.7	5.7
$\lambda_\gamma{}^{\mathrm{b}}$	97.6	9.2	0.4	0.5	1.5	6.1
Δg_1^{Z}	651.6	315.0	14.7	5.3	35.8	38.1
$\Delta\kappa_\gamma$	1165.0	15.0	1.4	0.9	11.9	4.8
λ_γ	156.1	20.3	1.0	1.2	3.0	12.1
$\Delta\kappa_{\mathrm{Z}}$	382.9	28.6	2.5	1.5	5.6	8.7
λ_Z	79.4	10.4	0.5	0.8	1.6	11.5
g_4^Z	86.2	4.2	5.8	2.8	6.5	85.8
g_5^Z	602.4	160.4	15.6	3.5	23.4	27.7
$\tilde{\kappa}_Z$	2.9	39.7	8.7	1.4	9.7	64.9
$\tilde{\lambda}_Z$	16.3	2.9	2.9	0.6	3.0	11.4

(a) 500 GeV, no polarisation

	ISR (100%)	BS (100%)	M_{W}	E_{beam}	$\sigma_{\mathrm{sys}}{}^{\mathrm{a}}$	σ_{stat}
Δg_1^{Zb}	32.3	3.5	1.6	0.5	1.7	4.5
$\Delta\kappa_\gamma{}^{\mathrm{b}}$	116.1	3.7	1.1	0.3	1.7	3.1
$\lambda_\gamma{}^{\mathrm{b}}$	9.6	0.1	0.4	0.2	0.5	2.8
Δg_1^{Z}	7.7	2.5	11.2	3.4	11.7	39.0
$\Delta\kappa_\gamma$	177.8	3.7	0.9	0.3	2.0	2.6
λ_γ	8.3	0.2	0.9	0.2	0.9	5.2
$\Delta\kappa_{\mathrm{Z}}$	36.6	3.5	1.8	0.5	1.9	4.9
λ_Z	5.9	0.3	0.8	0.3	0.9	5.1
g_4^Z	0.2	2.1	2.8	1.2	3.1	41.8
g_5^Z	14.9	8.5	0.8	1.6	2.0	28.5
$\tilde{\kappa}_Z$	2.5	0.2	5.1	2.5	5.7	29.6
$\tilde{\lambda}_Z$	2.9	0.1	0.4	0.3	0.5	4.9

(b) 800 GeV, no polarisation

[a] Quadratic sum of all systematic errors, assuming 1% of ISR error and 10% of beamstrahlung error.
[b] With $\mathsf{SU(2)}_L \times \mathsf{U(1)}_Y$ relations.

Table 7.3: Estimated systematic error ($\times 10^{-4}$) for different systematic uncertainties.

leaving the reweighting distributions unchanged. This corresponds to a change of 100%. If this error should have only little impact on the total error of such a measurement an understanding of ISR in the order of 1% is needed under the assumption that the effect is linear. The same procedure is applied for beamstrahlung. As a rule of thumb the effects of beamstrahlung have to be understood up to 10% in order to have a systematic error of maximal the expected statistical error. Both requirements are realistic and can be achieved in the next few years. Also beamstrahlung can be studied from Bhabha scattering in the forward region [183] giving the opportunity to compare theoretical calculations with measurements.

Further systematic error sources are investigated. For estimating the effect of the W mass on this measurement M_{W} is changed by $\pm 50\,\mathrm{MeV}$ in the data distributions and the biggest shift between this measurement and the standard measurement is assigned as a systematic error. For the beam energy uncertainties, E_{beam} is changed by $10^{-4} \times E_{\mathrm{beam}}$ and the biggest shift between this and the standard measurement is assigned as a systematic error. Both sources of uncertainties are small compared to the statistical error and decrease a bit with an increase of the centre-of-mass energy.

The last column of table 7.3 summarises the systematic errors for the different couplings. All errors are added in quadrature and the above discussed goals for ISR (1%) and beamstrahlung (10%) are assumed. With this amount of understanding the measurement is not dominated by systematics.

7.7 Polarised Beams

Beam polarisation is a very interesting tool to control W-pair production. It gives the possibility to alter the production process for the needs of the measurement. Not only the cross-section can be increased or decreased but also the W production angle and the W polarisation are modified which results in a change of the four W decay angle distributions.

In W-pair production the total cross-section is calculated from the cross-section for left-handed electrons σ_L and right-handed electrons σ_R weighted by the polarisations for electrons $\mathcal{P}^-$ and positrons $\mathcal{P}^+$:

$$\sigma = \frac{1}{4}(1-\mathcal{P}^+)(1+\mathcal{P}^-)\sigma_R + \frac{1}{4}(1+\mathcal{P}^+)(1-\mathcal{P}^-)\sigma_L. \tag{7.15}$$

In lowest order σ_L includes the three CC03-diagrams while σ_R only the two s-channel diagrams as shown in figure 7.5. The ν-diagram vanishes because the charged current does not couple to right-handed electrons. The unpolarised cross-section is dominated by the contribution from σ_L. It is 160 times larger than σ_R at $500\,\mathrm{GeV}$ and 90 times larger at $800\,\mathrm{GeV}$. Some explicit numbers of the total cross-section are given in table 7.4 for the ideal case of 100% polarisation and the realistic case of 80% electron and 60% positron polarisation, which is used in this study.

The polarisation of electrons and positrons allows us to alter the mixing of both contributions with respect to the unpolarised case. For $\mathcal{P}^- = +1$ only σ_R contributes to the total cross-section, for $\mathcal{P}^- = -1$ only σ_L. This contribution is enhanced by a factor of $(1+\mathcal{P}^-)$ with respect to the contribution for the unpolarised case. In addition the use of polarised positrons enhances the total cross-section further by a factor of $(1+\mathcal{P}^+)$. This gives us the novel opportunity to switch off the irreducible background from the ν-diagram and study directly diagrams which involve TGCs. In addition, the weight of the Z exchange-diagram

energy	polarisation	RL	R	$-$	L	LR
500 GeV	$\mathcal{P}^- = \pm 1.0$, $\mathcal{P}^+ = \pm 1.0$	32.1	16.0	8.1	0.1	0.2
	$\mathcal{P}^- = \pm 0.8$, $\mathcal{P}^+ = \pm 0.6$	23.1	14.4	8.1	1.7	0.8
800 GeV	$\mathcal{P}^- = \pm 1.0$, $\mathcal{P}^+ = \pm 1.0$	18.1	9.0	4.6	0.1	0.2
	$\mathcal{P}^- = \pm 0.8$, $\mathcal{P}^+ = \pm 0.6$	12.0	8.1	4.6	1.0	0.5

Table 7.4: Total cross-section for different polarisation combinations at a centre-of-mass energies of 500 and 800 GeV. The polarisation combinations are described by R (right-handed) and L (left-handed). One letter denotes electron polarisation only, two letters electron and positron polarisation.

depends on the polarisation of the fermion, which couple to the Z boson while the contribution from the photon-diagram is independent of the polarisation. Therefore the use of two different beam polarisations gives us the opportunity to disentangle the contributions from WWZ- and WWγ-vertex.

For TESLA, the electron polarisation will be $\pm 80\%$. The positron polarisation is more difficult to achieve, but $\pm 60\%$ should be reachable (see section 4.3). In this case the ν-diagram cannot be switched off totally but the contribution can be suppressed or enhanced. For left polarised electrons the enhancement factor is still $(1 + \mathcal{P}^+)(1 - \mathcal{P}^-)$, which gives a factor of roughly 2.5 for electron and positron polarisation. It is different for right polarised electrons because σ_R is much smaller than σ_L and hence the total cross-section is dominated by σ_L. The suppression factor is roughly five for electron polarisation only. The positron polarisation decreases the total cross-section further by a factor of two in contrast to the above discussed increase of $1 + \mathcal{P}^+$.

Already in the Standard Model the differential distributions change when non-zero polarisation is used, which cannot be distinguished a priori from the effects of anomalous couplings. Thus it is very important to know the polarisation as precise as possible and to study the influence of a shift in the polarisation measurement.

For studies with polarised beams the $\cos\theta_{\mathrm{W}}$ distribution and the SDM elements are used as input variables to the fit. The total luminosity for a centre-of-mass energy is split up

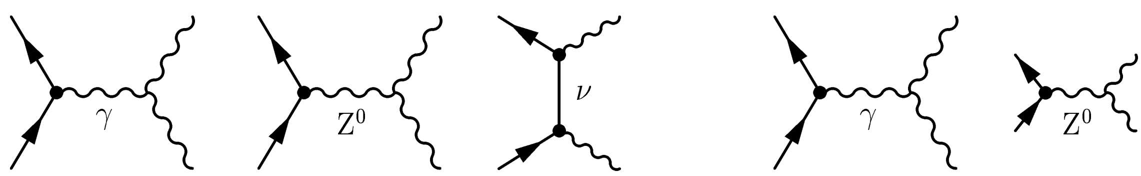

(a) left-handed electrons (b) right-handed electrons

Figure 7.5: Feynman diagrams for left-handed and right-handed electrons, which contribute to the production of W pairs.

equally on both polarisations, e. g. at an energy of 500 GeV 250 fb^{-1} on left-handed (L) and 250 fb^{-1} on right-handed (R) electrons with a polarisation of 80%. In the case of additional polarised positrons the absolute polarisation is 60% with the opposite polarisation with respect to the electron polarisation.

To get the maximal sensitivity for this measurement the data taken at both polarisation combinations are fitted at the same time. Only this ensures that we can disentangle the WWZ from the WWγ couplings.

Results

Table 7.5.b) and c) show the expected statistical error for electron and electron/positron polarisation at a centre-of-mass energy of 500 and 800 GeV for a 1d-fit. At 500 GeV the statistical error decreases by a factor of 1.5 – 2.5 using both electron and positron polarisation compared to no beam polarisation. The gain from switching from no polarisation to electron polarisation is roughly the same as switching from electron polarisation to electron and positron polarisation. At 800 GeV the behaviour is a bit different. The total gain of using both beams polarised instead of no polarisation is still the same but some couplings gain more from only electron polarisation than from electron and positron polarisation and vice versa. Still the expected errors at 800 GeV are smaller than at 500 GeV. This shows that the use of both beams at the highest achievable degree of polarisation will give the best measurement, but already a polarised electron beam helps very much.

For both polarisation cases, fits with more than one free parameter have been performed. The results are shown in table 7.6 to 7.8. In the case of the three C and P conserving couplings with relations (2.18), the use of polarised beams removes the high correlation between Δg_1^Z and $\Delta\kappa_\gamma$. At 500 GeV all three couplings are correlated moderately. At an energy of 800 GeV they are hardly correlated anymore. However, the main point of using polarised beams is to disentangle the five C and P conserving Z- and γ-couplings. For both beams polarised the correlation for example between $\Delta\kappa_\gamma$ and $\Delta\kappa_Z$ is around 20% at both considered energies and the correlation between λ_γ and λ_Z roughly 60% at 500 GeV and negligible at 800 GeV. Using only electron polarisation is already sufficient to reduce the correlation significantly. Results from the 5d-fit for four different C and P conserving coupling pairs for 500 and 800 GeV are shown in figure 7.6 and 7.7. The two dimensional projection of the error contours are plotted. At 500 GeV the correlation between the selected couplings can be seen but at 800 GeV the correlation are reduced much. For the four C or P violating couplings the use of polarised electrons or positrons is only needed to increase the sensitivity. The couplings are hardly correlated except $\tilde{\kappa}_Z$ and $\tilde{\lambda}_Z$ and the use of polarised beams does not help to decrease this correlation.

Polarisation Errors

As mentioned above it is very important to know the exact polarisation because deviation from the expected polarisation can fake contributions from anomalous couplings. The measurement of the polarisation will be performed by a polarimeter using either Compton scattering [101] or Møller scattering [102]. For both methods a relative error of $\Delta\mathcal{P}/\mathcal{P} = 0.5 - 1.0\%$ is reachable.

To estimate the systematic error in the TGC measurement from the uncertainty in the

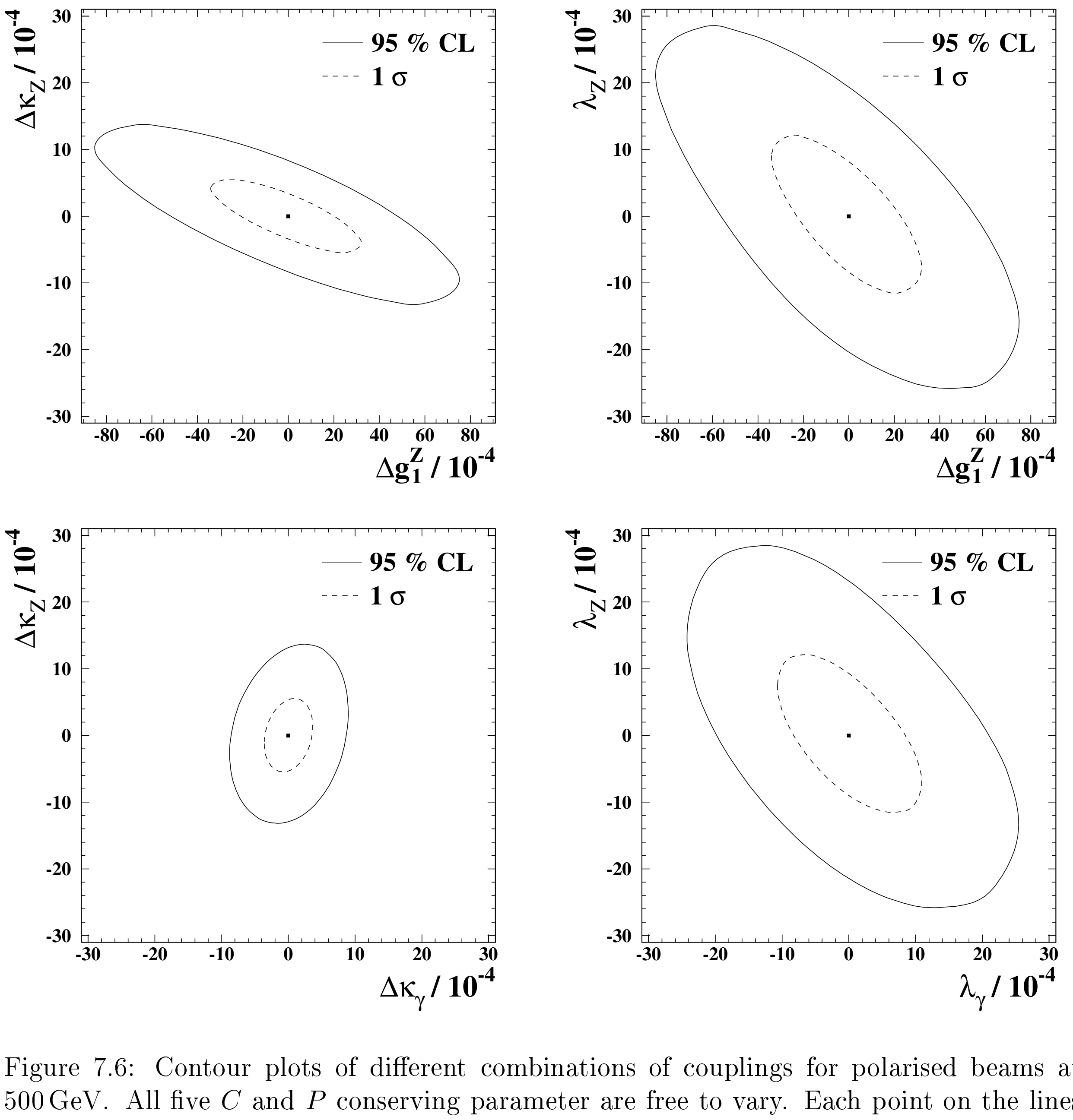

Figure 7.6: Contour plots of different combinations of couplings for polarised beams at 500 GeV. All five C and P conserving parameter are free to vary. Each point on the lines is a minimum with respect to the other 3 variables. The dashed line show the contour for $\Delta\chi^2 = 1.0$ and the solid line for $\Delta\chi^2 = 5.99$.

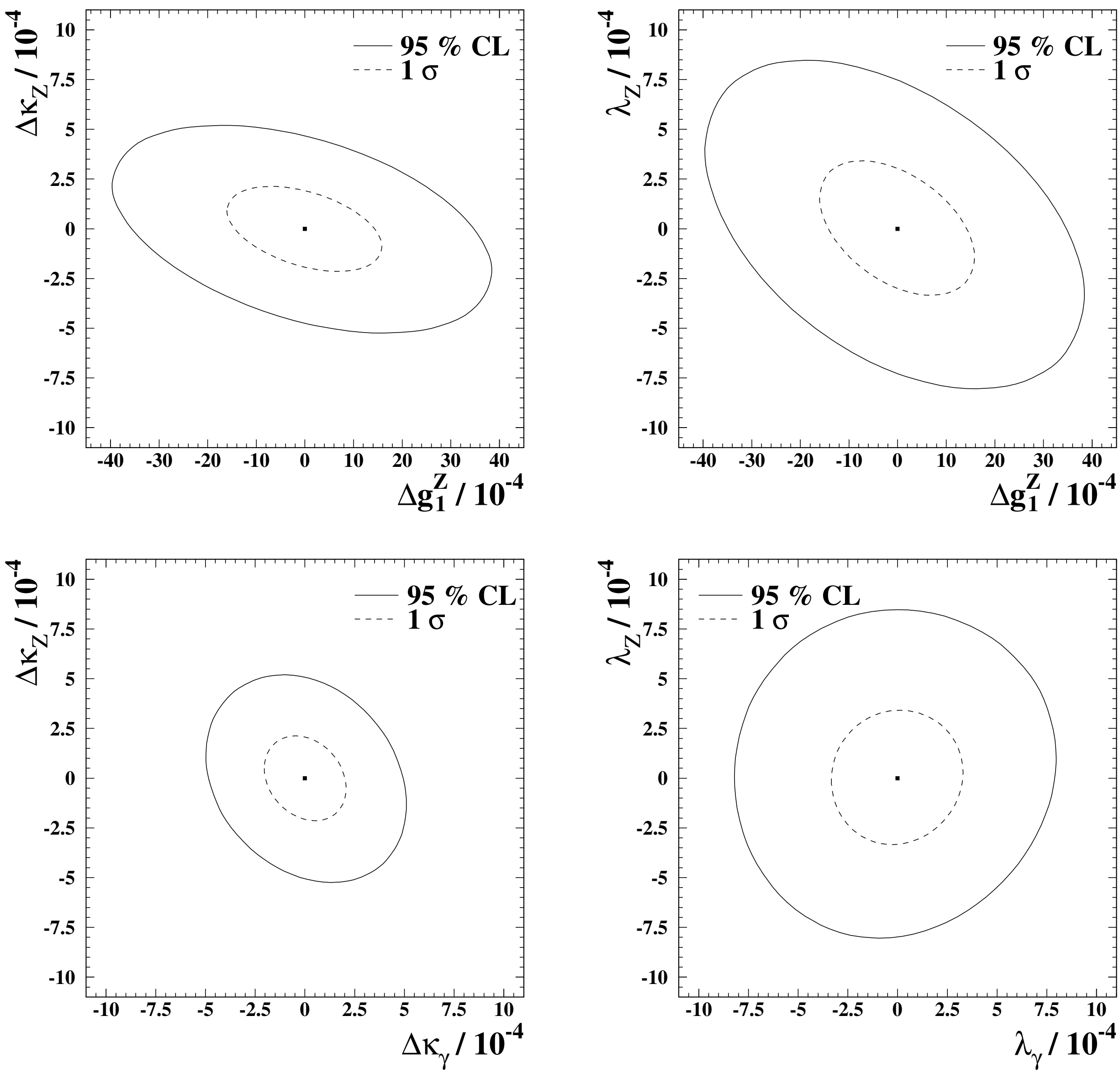

Figure 7.7: Contour plots of different combinations of couplings for polarised beams at 800 GeV. All five C and P conserving parameter are free to vary. Each point on the lines is a minimum with respect to the other 3 variables. The dashed line show the contour for $\Delta\chi^2 = 1.0$ and the solid line for $\Delta\chi^2 = 5.99$.

polarisation		Δg_1^{Z}[a]	$\Delta\kappa_\gamma$[a]	λ_γ[a]	Δg_1^Z	$\Delta\kappa_\gamma$	λ_γ	$\Delta\kappa_Z$	λ_Z	g_4^Z	g_5^Z	$\tilde{\kappa}_Z$	$\tilde{\lambda}_Z$
0.0	0.0	7.3	5.7	6.1	38.1	4.8	12.1	8.7	11.5	85.8	27.7	64.9	11.4
0.8	0.0	4.3	4.2	5.1	24.8	4.1	8.2	5.0	8.9	79.9	22.8	50.6	10.3
0.8	0.6	2.8	3.1	4.3	15.5	3.3	5.9	3.2	6.7	45.9	16.5	39.0	7.5

(a) 500 GeV

polarisation		Δg_1^{Z}[a]	$\Delta\kappa_\gamma$[a]	λ_γ[a]	Δg_1^Z	$\Delta\kappa_\gamma$	λ_γ	$\Delta\kappa_Z$	λ_Z	g_4^Z	g_5^Z	$\tilde{\kappa}_Z$	$\tilde{\lambda}_Z$
0.0	0.0	4.5	3.1	2.8	39.0	2.6	5.2	4.9	5.1	41.8	28.5	29.6	4.9
0.8	0.0	2.7	2.3	3.1	21.9	2.2	5.0	2.9	4.7	31.8	24.3	24.1	4.4
0.8	0.6	1.8	1.9	2.6	12.6	1.9	3.3	1.9	3.0	18.3	14.4	14.3	3.0

(b) 800 GeV

[a]With $\mathsf{SU(2)}_L \times \mathsf{U(1)}_Y$ relations.

Table 7.5: Expected sensitivity ($\times 10^{-4}$) for different couplings at a centre-of-mass energy of 500 and 800 GeV and a luminosity of 500 and 1000 fb^{-1}, respectively. All number are at generator-level. In the case of polarised beams the luminosity is split up equally on both combinations.

	$1d$	$3d$	Δg_1^Z	$\Delta\kappa_\gamma$	λ_γ
Δg_1^Z	7.3	34.0	1.000	−0.968	−0.253
$\Delta\kappa_\gamma$	5.7	22.9		1.000	0.173
λ_γ	6.1	6.6			1.000

(a) 500 GeV, no polarisation

	$1d$	$3d$	Δg_1^Z	$\Delta\kappa_\gamma$	λ_γ
Δg_1^Z	4.5	34.2	1.000	−0.987	−0.223
$\Delta\kappa_\gamma$	3.1	18.4		1.000	0.198
λ_γ	2.9	3.0			1.000

(b) 800 GeV, no polarisation

	$1d$	$3d$	Δg_1^Z	$\Delta\kappa_\gamma$	λ_γ
Δg_1^Z	4.3	4.3	1.000	0.043	−0.282
$\Delta\kappa_\gamma$	4.2	4.6		1.000	−0.215
λ_γ	5.1	5.5			1.000

(c) 500 GeV, e^- polarisation (R+L)

	$1d$	$3d$	Δg_1^Z	$\Delta\kappa_\gamma$	λ_γ
Δg_1^Z	2.7	2.4	1.000	−0.082	−0.101
$\Delta\kappa_\gamma$	2.3	2.4		1.000	−0.061
λ_γ	3.1	2.9			1.000

(d) 800 GeV, e^- polarisation (R+L)

	$1d$	$3d$	Δg_1^Z	$\Delta\kappa_\gamma$	λ_γ
Δg_1^Z	2.8	3.1	1.000	0.403	−0.383
$\Delta\kappa_\gamma$	3.1	3.5		1.000	−0.299
λ_γ	4.3	4.6			1.000

(e) 500 GeV, e^+e^- polarisation (RL+LR)

	$1d$	$3d$	Δg_1^Z	$\Delta\kappa_\gamma$	λ_γ
Δg_1^Z	1.8	1.7	1.000	−0.020	−0.095
$\Delta\kappa_\gamma$	1.9	2.0		1.000	−0.047
λ_γ	2.6	2.4			1.000

(f) 800 GeV, e^+e^- polarisation (RL+LR)

Table 7.6: Expected sensitivity ($\times 10^{-4}$) at generator-level and correlation matrix for an one and three parameter fit. The $\mathrm{SU}(2)_L \times \mathrm{U}(1)_Y$ relation is used in the fit.

	$1d$	$5d$	Δg_1^Z	$\Delta\kappa_\gamma$	λ_γ	$\Delta\kappa_Z$	λ_Z
Δg_1^Z	38.1	76.6	1.000	0.496	−0.097	−0.609	−0.189
$\Delta\kappa_\gamma$	4.8	33.4		1.000	−0.072	−0.981	−0.073
λ_γ	12.1	25.7			1.000	0.043	−0.818
$\Delta\kappa_Z$	8.7	85.7				1.000	0.112
λ_Z	11.5	22.8					1.000

(a) 500 GeV, no polarisation

	$1d$	$5d$	Δg_1^Z	$\Delta\kappa_\gamma$	λ_γ	$\Delta\kappa_Z$	λ_Z
Δg_1^Z	39.0	53.7	1.000	−0.048	−0.189	−0.018	−0.021
$\Delta\kappa_\gamma$	2.6	38.8		1.000	0.311	−0.995	−0.245
λ_γ	5.2	9.6			1.000	−0.304	−0.781
$\Delta\kappa_Z$	4.9	50.5				1.000	0.245
λ_Z	5.1	9.0					1.000

(b) 800 GeV, no polarisation

	$1d$	$5d$	Δg_1^Z	$\Delta\kappa_\gamma$	λ_γ	$\Delta\kappa_Z$	λ_Z
Δg_1^Z	24.8	45.2	1.000	0.006	0.263	−0.781	−0.544
$\Delta\kappa_\gamma$	4.1	4.7		1.000	−0.316	−0.185	0.100
λ_γ	8.2	11.7			1.000	−0.139	−0.536
$\Delta\kappa_Z$	5.0	8.4				1.000	0.280
λ_Z	8.9	12.2					1.000

(c) 500 GeV, e^- polarisation (R+L)

	$1d$	$5d$	Δg_1^Z	$\Delta\kappa_\gamma$	λ_γ	$\Delta\kappa_Z$	λ_Z
Δg_1^Z	21.9	26.6	1.000	−0.068	0.235	−0.523	−0.445
$\Delta\kappa_\gamma$	2.2	2.4		1.000	−0.044	−0.245	−0.016
λ_γ	5.0	4.8			1.000	−0.162	−0.229
$\Delta\kappa_Z$	2.9	3.2				1.000	0.208
λ_Z	4.7	4.9					1.000

(d) 800 GeV, e^- polarisation (R+L)

	$1d$	$5d$	Δg_1^Z	$\Delta\kappa_\gamma$	λ_γ	$\Delta\kappa_Z$	λ_Z
Δg_1^Z	15.5	30.0	1.000	−0.212	0.525	−0.784	−0.722
$\Delta\kappa_\gamma$	3.3	3.6		1.000	−0.362	0.232	0.151
λ_γ	5.9	11.0			1.000	−0.404	−0.649
$\Delta\kappa_Z$	3.2	5.5				1.000	0.434
λ_Z	6.7	12.0					1.000

(e) 500 GeV, e^+e^- polarisation (RL+LR)

	$1d$	$5d$	Δg_1^Z	$\Delta\kappa_\gamma$	λ_γ	$\Delta\kappa_Z$	λ_Z
Δg_1^Z	12.6	15.9	1.000	−0.109	0.235	−0.432	−0.449
$\Delta\kappa_\gamma$	1.9	2.1		1.000	−0.020	−0.237	−0.021
λ_γ	3.3	3.3			1.000	−0.173	0.059
$\Delta\kappa_Z$	2.0	2.1				1.000	0.187
λ_Z	3.0	3.3					1.000

(f) 800 GeV, e^+e^- polarisation (RL+LR)

Table 7.7: Expected sensitivity ($\times 10^{-4}$) at generator-level and correlation matrix for an one and five parameter fit.

	$1d$	$4d$	g_4^Z	g_5^Z	$\tilde{\kappa}_Z$	$\tilde{\lambda}_Z$
g_4^Z	85.8	88.4	1.000	-0.026	0.276	-0.048
g_5^Z	27.7	27.7		1.000	-0.002	0.013
$\tilde{\kappa}_Z$	64.9	75.0			1.000	0.445
$\tilde{\lambda}_Z$	11.4	13.1				1.000

(a) 500 GeV, no polarisation

	$1d$	$4d$	g_4^Z	g_5^Z	$\tilde{\kappa}_Z$	$\tilde{\lambda}_Z$
g_4^Z	41.8	41.4	1.000	0.013	0.140	-0.024
g_5^Z	28.5	28.4		1.000	-0.035	0.016
$\tilde{\kappa}_Z$	29.6	35.1			1.000	0.531
$\tilde{\lambda}_Z$	4.9	5.9				1.000

(b) 800 GeV, no polarisation

	$1d$	$4d$	g_4^Z	g_5^Z	$\tilde{\kappa}_Z$	$\tilde{\lambda}_Z$
g_4^Z	79.9	71.1	1.000	0.013	-0.362	-0.219
g_5^Z	22.8	23.5		1.000	0.200	0.089
$\tilde{\kappa}_Z$	50.6	59.9			1.000	0.517
$\tilde{\lambda}_Z$	10.3	10.7				1.000

(c) 500 GeV, e^- polarisation (R+L)

	$1d$	$4d$	g_4^Z	g_5^Z	$\tilde{\kappa}_Z$	$\tilde{\lambda}_Z$
g_4^Z	31.8	32.2	1.000	0.017	0.030	-0.028
g_5^Z	24.3	23.9		1.000	-0.031	-0.013
$\tilde{\kappa}_Z$	24.1	29.8			1.000	0.613
$\tilde{\lambda}_Z$	4.4	5.5				1.000

(d) 800 GeV, e^- polarisation (R+L)

	$1d$	$4d$	g_4^Z	g_5^Z	$\tilde{\kappa}_Z$	$\tilde{\lambda}_Z$
g_4^Z	42.7	45.9	1.000	-0.102	-0.410	-0.362
g_5^Z	16.5	16.7		1.000	-0.108	-0.045
$\tilde{\kappa}_Z$	39.0	40.7			1.000	0.662
$\tilde{\lambda}_Z$	7.5	10.1				1.000

(e) 500 GeV, e^+e^- polarisation (RL+LR)

	$1d$	$4d$	g_4^Z	g_5^Z	$\tilde{\kappa}_Z$	$\tilde{\lambda}_Z$
g_4^Z	18.3	18.6	1.000	-0.007	-0.053	-0.038
g_5^Z	14.4	14.4		1.000	-0.014	-0.009
$\tilde{\kappa}_Z$	14.3	18.2			1.000	0.618
$\tilde{\lambda}_Z$	3.0	3.8				1.000

(f) 800 GeV, e^+e^- polarisation (RL+LR)

Table 7.8: Expected sensitivity ($\times 10^{-4}$) at generator-level and correlation matrix for an one and four parameter fit.

	$\mathcal{P}^-$	σ_{stat}	$\mathcal{P}^-/\mathcal{P}^+$	σ_{stat}
Δg_1^{Za}	36.3	4.3	14.8	2.8
$\Delta\kappa_\gamma{}^{\text{a}}$	15.5	4.2	21.9	3.1
$\lambda_\gamma{}^{\text{a}}$	10.5	5.1	24.3	4.3
Δg_1^{Z}	134.2	24.8	74.5	15.5
$\Delta\kappa_\gamma$	21.8	4.1	18.7	3.3
λ_γ	21.4	8.2	34.8	5.9
$\Delta\kappa_{\text{Z}}$	44.2	5.0	16.9	3.2
λ_Z	9.1	8.9	39.4	6.7
g_4^Z	680.6	79.9	92.7	45.9
g_5^Z	242.3	22.8	163.8	16.5
$\tilde{\kappa}_Z$	50.9	50.6	169.1	39.0
$\tilde{\lambda}_Z$	64.1	10.3	23.2	7.5

(a) 500 GeV

	$\mathcal{P}^-$	σ_{stat}	$\mathcal{P}^-/\mathcal{P}^+$	σ_{stat}
Δg_1^{Za}	5.2	2.7	9.0	1.8
$\Delta\kappa_\gamma{}^{\text{a}}$	10.1	2.3	17.0	1.9
$\lambda_\gamma{}^{\text{a}}$	1.9	3.1	0.4	2.6
Δg_1^{Z}	30.6	21.9	32.6	12.6
$\Delta\kappa_\gamma$	8.1	2.2	13.0	1.9
λ_γ	5.6	5.0	2.7	3.3
$\Delta\kappa_{\text{Z}}$	5.4	2.9	9.5	1.9
λ_Z	1.9	4.7	1.8	3.0
g_4^Z	32.5	31.8	15.7	18.3
g_5^Z	7.5	31.8	5.2	14.4
$\tilde{\kappa}_Z$	20.1	24.1	6.7	14.3
$\tilde{\lambda}_Z$	1.3	4.4	0.9	3.0

(b) 800 GeV

[a]With $\mathsf{SU(2)}_L \times \mathsf{U(1)}_Y$ relations.

Table 7.9: Estimated systematic errors ($\times 10^{-4}$) from uncertainties in the polarisation measurement compared with the expected statistical error.

polarisation measurement, the polarisation is changed by $\Delta P = \pm 1\%$ in the data samples leaving the reweighting samples unchanged. From all possible combinations of changing the polarisation, the largest shift is used as an estimate of this systematic error.

Table 7.9 shows the systematic errors for a centre-of-mass energy of 500 and 800 GeV for both polarisation options. At 500 GeV all measurements are dominated by this polarisation error. This error is 5 – 10 times greater than the expected statistical error. At the higher centre-of-mass energy the behaviour is more mixed. Some couplings are almost not affected by the polarisation error while others are. This is more pronounced in the case of electron and positron polarisation. From this observations a polarisation error of $\Delta P = 0.1 - 0.2\%$ is needed for a TGC measurement, which is not dominated by this polarisation error. This translates into a relative errors for electron polarisation $\Delta\mathcal{P}^-/\mathcal{P}^- = 0.1 - 0.2\%$ and positron polarisation $\Delta\mathcal{P}^+/\mathcal{P}^+ = 0.2 - 0.3\%$.

If such a high precision polarisation measurement with a polarimeter is not possible, other ways must be considered to measure the polarisation. In the next section a method is presented for the simultaneous measurement of the beam polarisation and the anomalous couplings from the observed W-pair events.

Blondel Scheme

The polarisation can be measured from cross-section asymmetries. Such a scheme was first proposed by A. Blondel for the case of LEP [103]. K. Mönig proposed to use such a scheme at linear collider energies to improve the accuracy of the polarisation measurement for various physical analysis [184]. The idea is to measure the polarisation simultaneously with the anomalous couplings. The relevant variables for the polarisation measurement are the cross-sections at the different helicity combinations of the beams. There are two combinations in the case of electron polarisation and four in the case of electron and positron polarisation. In the latter case the combinations where the beams have the same helicity, i. e. LL and RR, are needed, because otherwise there are not enough variables to constrain the measurement.

For pure s-channel processes the cross-section for the different polarisation states can be written as

$$\sigma = \sigma_u \left[1 - \mathcal{P}^- \mathcal{P}^+ + (\mathcal{P}^+ - \mathcal{P}^-) A_{LR}\right], \tag{7.16}$$

where σ_u is the unpolarised cross-section and A_{LR} the left-right asymmetry of the cross-section. The structure of the cross-section (7.16) is not limited to s-channel processes. In the case of W-pair production, where a t-channel ν-exchange diagram contribute in addition to s-channel diagrams, the cross-section for the different polarisation states is given by equation (7.15). Defining the unpolarised cross-section as $\sigma_u = \sigma_L + \sigma_R$ and the left-right asymmetry as $A_{LR} = \frac{\sigma_L - \sigma_R}{\sigma_L + \sigma_R}$ leads to the same formula (7.16). This is due to the V-A structure of the charged current, which allows the ν-exchange only between left-handed electrons and right handed positron and vice versa.

With four different polarisation combinations (LL, LR, RL, RR) four cross-sections can be measured to extract the unpolarised cross-section, the left-right asymmetry and both polarisations, under the assumption that the polarisation for left-handed and right-handed beams is the same. From these four cross-sections the polarisation can be obtained:

$$|P_{e^\pm}| = \sqrt{\frac{(\sigma_{LR} + \sigma_{RL} - \sigma_{LL} - \sigma_{RR})(\pm\sigma_{LR} \mp \sigma_{RL} + \sigma_{LL} - \sigma_{RR})}{(\sigma_{LR} + \sigma_{RL} + \sigma_{LL} + \sigma_{RR})(\pm\sigma_{LR} \mp \sigma_{RL} - \sigma_{LL} + \sigma_{RR})}}. \tag{7.17}$$

For the simultaneous measurement of polarisation and anomalous couplings the total cross-section is very important. Upto this point in this study only normalised differential distributions are used, which are not very sensitive to the polarisation, especially for left-handed electrons. The total cross-sections of the different helicity combinations help to improve this significantly, as expected.

The total cross-section σ_{rew} as a function of anomalous couplings for different polarisation schemes is calculated by

$$\sigma_{rew} = \frac{\sigma_{gen}}{N_{gen}} \sum_i w_i, \tag{7.18}$$

where w_i is the weight for i^{th} event as a function of anomalous couplings. σ_{gen} is the cross-section and N_{gen} the number of events of the Monte Carlo sample, which is reweighted. This approximates the true cross-section very well. Crucial is the assumption of the cross-section error. The statistical error is much smaller than the expected error from the luminosity measurement (0.25%) and from theoretical uncertainties (0.5%). $\Delta\sigma/\sigma = 1\%$ is a conservative estimate for the total cross-section error considering the uncertainties above. A very optimistic assumption is $\Delta\sigma/\sigma = 0.25\%$, which could be possible in the future.

For an electron polarisation of $\mathcal{P}^- = 80\%$ at 800 GeV one anomalous coupling and the electron polarisation are measured. The expected polarisation error varies from $\Delta\mathcal{P}^- = 0.2\%$ to 0.05% for an assumed cross-section error of $\Delta\sigma/\sigma = 1.0\%$ to 0.25%. The correlation between polarisation and TGCs measurement is maximal 50% and the sensitivity to the couplings decreases. For an additional positron polarisation of $\mathcal{P}^+ = 60\%$ the expected error for electron polarisation stays the same and the error of the positron polarisation varies from $\Delta\mathcal{P}^+ = 0.31\%$ to 0.08% for an assumed cross-section error of $\Delta\sigma/\sigma = 1.0\%$ to 0.25%. The correlation between polarisation and TGCs measurement is also maximal 50%.

For the simultaneous measurement of TGCs and polarisation the total cross-section for the different helicity states of the beams is used as an input for the fit in addition to the normalised $\cos\theta_{\mathrm{W}}$ distribution and the SDM elements. The polarisation has been fitted simultaneously with the anomalous couplings and a free normalisation at a centre-of-mass energy of 800 GeV for only electron polarisation and electron and positron polarisation. In both cases the polarisations can be measured very accurately and the correlation between polarisation and TGC measurement is maximal 30%. This means that the sensitivity to the couplings decreases only slightly.

In the Blondel scheme various assumptions about the polarisation stability are made, which might not be fulfilled at run time. The polarisation is assumed to be the same for left and right polarised beams and stable in time. No deviations from these assumptions have been studied yet. A more detailed study is needed to see if this method really helps to control the systematic errors from polarisation uncertainties.

7.8 Strong Electroweak Symmetry Breaking

In section 2.3 strong electroweak symmetry breaking (EWSB), parametrised by the so-called α parameters, was motivated and the connection between the standard TGC and α parameters was introduced. With the help of equation (2.23), $\alpha_{1,2,3}$ can be expressed in terms of Δg_1^{Z}, κ_γ and κ_Z and the α parameters can be easily extracted with the already introduced techniques. However, the transformation (2.23) is singular and the three anomalous TGCs satisfy

$$(\Delta g_1^{\mathrm{Z}} - \Delta\kappa_{\mathrm{Z}}) \cdot \cos^2\theta_w = \Delta\kappa_\gamma \cdot \sin^2\theta_w. \tag{7.19}$$

Therefore only two dimensions of the α parameter space can be explored directly in the W-pair production. The blind direction

$$(\alpha_1,\ \alpha_2,\ \alpha_3)_{\mathrm{blind}} \propto (\cos^2\theta_w - \sin^2\theta_w,\ \cos^2\theta_w,\ -\sin^2\theta_w) \tag{7.20}$$

in the parameter space cannot be constrained from the three TGCs alone, but additional measurements of α_1 can be used to solve this problem. For convenience we fit α_2 and α_3 and take the SM value $\alpha_1 = 0$.

The results of a two dimensional fit of α_2 and α_3 with $\alpha_1 = 0$ are listed in table 7.10 for both energies and different combinations of beam polarisation. In the case of unpolarised beams α_2 and α_3 are strongly correlated, but fortunately this can already be suppressed with electron polarisation. Using additional positron polarisation suppresses the correlations even further. The results can be combined with the parameters of the blind direction (7.20) to obtain the allowed region in the three dimensional parameters space. Figure 7.8 shows the two-dimensional error projections of one sigma ($\Delta\chi^2 = 1.0$) and 68% C.L. ($\Delta\chi^2 = 2.3$) for both beams polarised at $\sqrt{s} = 800$ GeV.

Additional independent measurements can be used to constrain the parameters further. Good candidates are the S, T and U [185] or ϵ_1, ϵ_2 and ϵ_3 [186] parameters. Both parameter

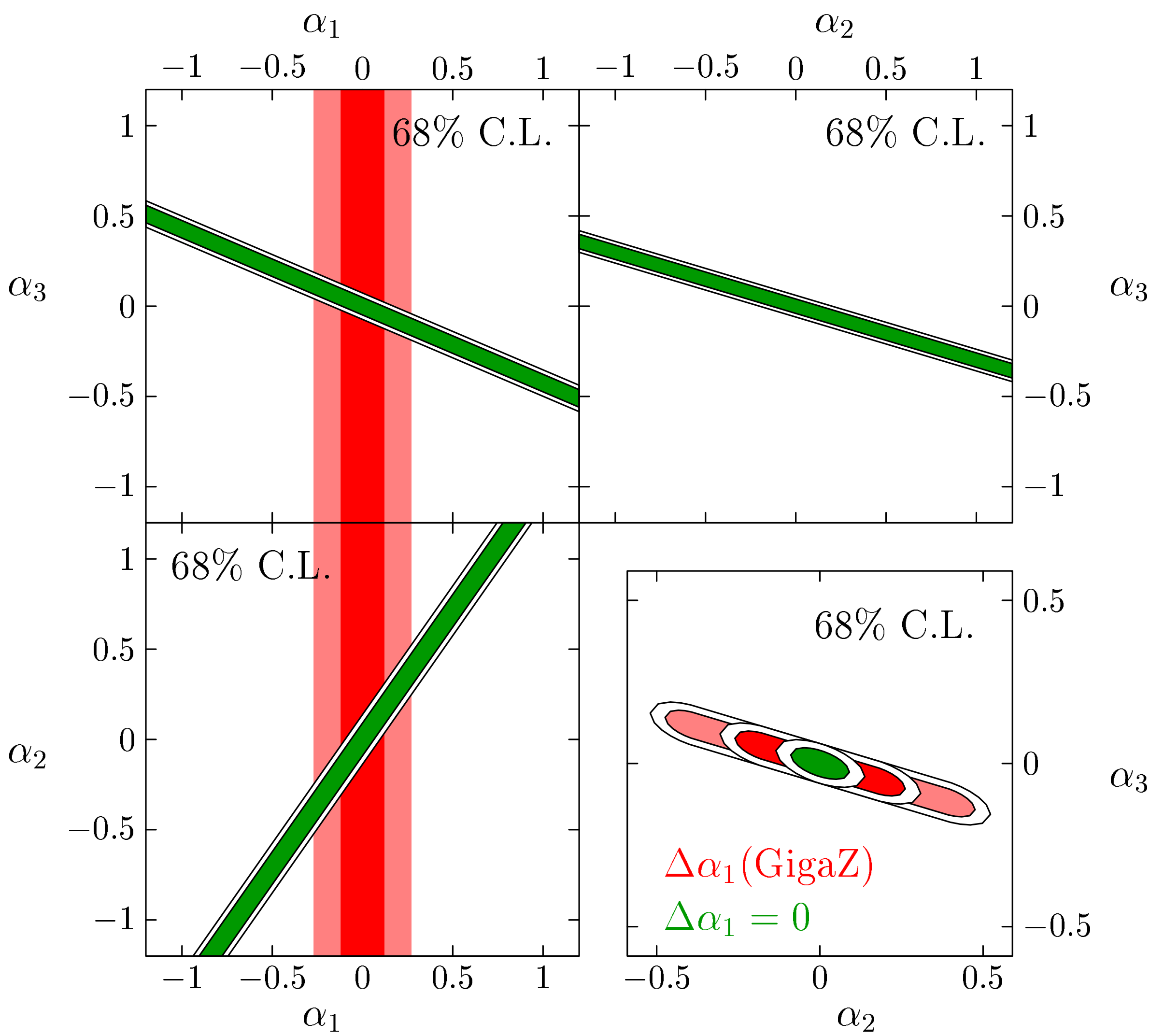

Figure 7.8: Sensitivity for the strong EWSB parameters $\alpha_{1,2,3}$ at $\sqrt{s} = 800\,\mathrm{GeV}$ and a beam polarisation of $\mathcal{P}^- = \pm 80\%$ and $\mathcal{P}^+ = \mp 60\%$. The inner shaded diagonals correspond to $\Delta\chi^2 = 1$, while the outer diagonals correspond to 68% C.L. in two dimensions. The dark and light vertical bands correspond to 68% C.L. limits on α_1 from fitting ϵ_3 at GigaZ with and without the constraint $\epsilon_2 = \epsilon_2(SM)$. The blowup in the lower right corner shows the allowed region in (α_2, α_3) for α_1 fixed and constrained at GigaZ, respectively.

polarisation	$\mathcal{P}^- = \mathcal{P}^+ = 0$		$\mathcal{P}^- = 80\,\%,\ \mathcal{P}^+ = 0$		$\mathcal{P}^- = 80\,\%,\ \mathcal{P}^+ = 60\,\%$	
energy[GeV]	500	800	500	800	500	800
$\Delta\alpha_2$	1.771	2.078	0.329	0.127	0.123	0.090
$\Delta\alpha_3$	0.935	1.004	0.143	0.071	0.083	0.048
$\mathrm{cor}(\alpha_2,\alpha_3)$	−0.993	−0.998	−0.755	−0.682	−0.343	−0.547
Λ_2^* [TeV]	2.3	2.1	5.4	8.7	8.8	10.3
Λ_3^* [TeV]	3.2	3.1	8.2	11.6	10.7	14.1

Table 7.10: Estimated statistical errors ($\Delta\chi^2 = 1.0$) for the strong EWSB parameters α_2 and α_3, assuming $\alpha_1 = 0$. Both parameters are fitted at the same time.

sets parametrise the so-called oblique electroweak corrections, which are radiative corrections to the vacuum-polarization amplitudes. These parameter can be extracted from measurements of precision observables, as the Z mass and its width and various asymmetries, which are measured at LEP 1/SLC. New physics beyond the Standard Model can contribute to the oblique corrections via loop effects. The S parameter of the oblique electroweak corrections is related to α_1 as $\Delta S = -\alpha_1/(2\pi)$ and measurements at LEP 1/SLC give $\Delta\alpha_1 = 0.69$ at 68% C.L., which is also included in figure 7.8. The constraint on S (or ϵ_3) can be improved by more than a factor of two at GigaZ. This observation motivates the blowup of the (α_2, α_3)-plane in the lower right corner of figure 7.8, where the blind direction is removed by the expected limits on α_1 from the measurement of ϵ_3 at GigaZ. The dark and light areas correspond to fits with and without the constraint $\epsilon_2 = \epsilon_2(SM)$. Also the ideal case of $\alpha_1 = 0$ is included.

These sensitivities can be interpreted using equation (2.22) as limits on scales of new physics Λ_i^* described by the corresponding operator in the effective Lagrangian (2.21). See table 7.10 for explicit numbers. In the case of no polarisation only energies around the symmetry breaking scale of 3 TeV can be probed. However, with the use of polarised beams energies well above the symmetry breaking scale of 3 TeV can be probed. The best limits are 10.3 TeV for Λ_2^* and 14.1 TeV for Λ_3^* at an energy of 800 GeV and both beams polarised. The resulting conservative limits from the blowup of the (α_2, α_3)-plane (figure 7.8) $\Delta\alpha_2 = 0.5$ and $\Delta\alpha_3 = 0.2$, i. e. $\Lambda_2^* = 4.4$ TeV and $\Lambda_3^* = 6.9$ TeV, still probe the EWSB parameters at their natural size of ≈ 3 TeV.

7.9 Comparision with Other Studies

In the last chapter only W-pair production is used to estimate the expected precision of the measurement of triple gauge boson couplings at TESLA. As at LEP, single-W [187] and single-γ [187] production can also be utilised to measure triple gauge boson couplings, but W-pair production is the most sensitive channel.

The use of a laser to produce high energy photons by backscattering of the beam electrons allows two interesting colliding options for TESLA: eγ and $\gamma\gamma$ collisions. At both options triple gauge boson couplings involving only the WWγ vertex can be studied. In the eγ mode single-W production (e$\gamma \to \nu_e$W) is much more sensitive than in e^+e^- collisions because the photon is much more energetic. In principle, the photon coupling to W^+ and W^- can be tested by using either an electron or a positron beam. In the $\gamma\gamma$ mode W-pair production is studied for the measurement of triple gauge boson couplings. The cross-section rises steeply at the threshold region and reaches a plateau of around 80 pb very fast. In this mode it is an order of magnitude bigger than in the e^+e^- mode, but the expected luminosity is only around 120 fb^{-1} per year because of the photon production process. The expected sensitivity for κ_γ and λ_γ of these two studies [188] and from W-pair production in the e^+e^- mode [178] are shown in figure 7.9 [189]. Comparing these three TESLA studies at a centre-of-mass energy of 500 GeV shows that the e^+e^- mode is the best option to measure triple gauge boson couplings. It must be noted however, that in the case of λ_γ the $e\gamma$ mode has a slightly higher precision as the e^+e^- mode. For comparison, the errors from measurements at LEP and Tevatron are also shown. The increase in sensitivity in performing such a measurement at a high luminosity linear collider is around two orders of magnitude compared to existing measurements.

The next new collider is the LHC at CERN with the experiments ATLAS and CMS, where collisions of protons at a centre-of-mass energy of 14 TeV are studied. As in the case of $p\bar{p}$ collisions at the Tevatron (see section 6.3), di-boson production can be used to measure triple gauge boson couplings at the LHC. The expected 95% C.L. limits from ATLAS [190] on the C and P conserving triple gauge boson couplings obtained from one-parameter fits to binned distributions of observables are listed in table 7.11. Only leptonic W and Z decay modes are considered. For comparison, the ideal case with maximal sensitivity using an unbinned fit to the complete 6 (8) dimensional phase-space distribution of $W\gamma$ (WZ) production at generator level is also shown. Such a method relies on the complete reconstruction of the event including the knowledge of the initial partonic configuration an will not be applicable to data.

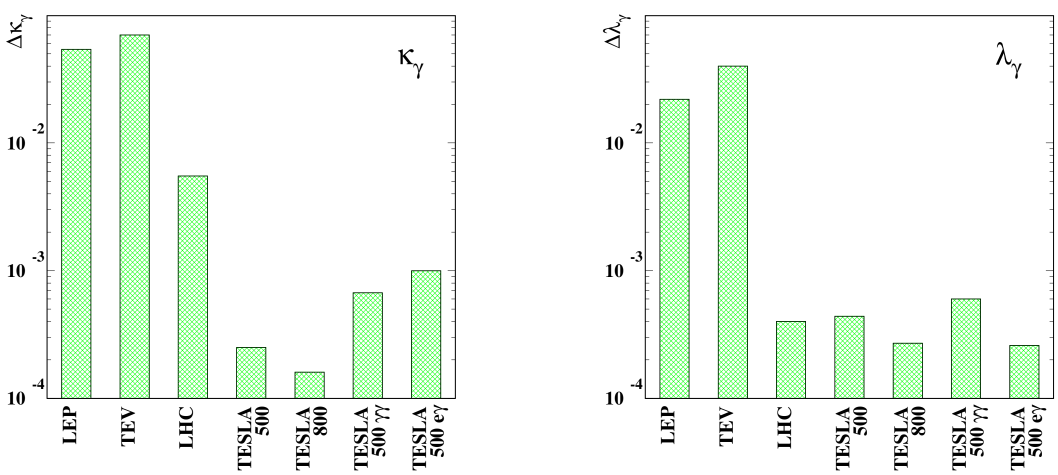

Figure 7.9: Comparison of $\Delta\kappa_\gamma$ and $\Delta\lambda$ at different machines. For LHC and TESLA three years of running are assumed (LHC: 300 fb^{-1}, TESLA$\sqrt{s} = 500$ GeV: 900 fb^{-1}, TESLA$\sqrt{s} = 800$ GeV: 1500 fb^{-1}).

Coupling	95% C.L. ($M_{W\gamma}$, $\lvert\eta^*\rvert$)	95% C.L. (p_t^γ, θ^*)	95% C.L. Ideal Case
g_1^Z	0.0078	0.0089	0.0053
κ_γ	0.035	0.046	0.028
κ_Z	0.069	0.100	0.058
λ_γ	0.0025	0.0027	0.0023
λ_Z	0.0058	0.0071	0.0055

Table 7.11: The expected 95% C.L. limits from one-parameter fits for C and P conserving couplings, assuming an integrated luminosity of $30\,\text{fb}^{-1}$. The limits are presented for two different sets of observables and the ideal case.

The one-parameter limits shown in table 7.11 represent the best possible precision in the search for anomalous triple gauge boson couplings. In the case of non-standard couplings, a general multi-parameter fit is the only way to establish the nature of the non-standard contribution. For the WWγ couplings the correlation between κ_γ and λ_γ is small and the two parameter limits are close to the limits in table 7.11. In contrast the correlation between g_1^Z and κ_Z is quite large ($\sim$ 50%) worsening the general three parameter limits with about 25%.

The expected precision for the couplings κ_γ and λ_γ at the LHC is compared to the other studies at TESLA and the measurements at LEP and Tevatron in figure 7.9. The numbers are adjusted to 68% C.L. limits, 3 years of high luminosity running ($100\,\text{fb}^{-1}$ per year) and two experiments. The sensitivity to $\Delta\kappa_\gamma$ is more than one order of magnitude better at TESLA than at the LHC. For λ the sensitivity is almost the same for the LHC and TESLA at $\sqrt{s} = 500\,\text{GeV}$. With a centre-of-mass of 800 GeV the expected error on λ at TESLA is 40% lower than at the LHC. If anomalous couplings are realised in nature due to some physics beyond the Standard Model, TESLA is the machine to perform precision measurements of these effects. Multi-parameter measurements with low correlations between different couplings are possible due to longitudinal polarised beams.

Chapter 8

Summary and Conclusions

The Standard Model of elementary particles is very successful in describing the fundamental particles and their interactions. The $\mathsf{SU(2)}_L \times \mathsf{U(1)}_Y$ gauge structure of the electroweak part of the Standard Model lead to certain self-couplings of gauge bosons. This are the couplings between a W pair and either a photon or a Z boson. The properties and the coupling strength of these vertices are fixed in the Standard Model. Extensions of the Standard Model may alter these predictions, and therefore deviations from the SM values are a clear signal for physics beyond the Standard Model.

In the first part of this thesis, a measurement of charged current triple gauge boson couplings is presented using the hadronic decay channel of W-pair production recorded with the OPAL detector at centre-of-mass energies of 183 to 209 GeV. The reconstruction of W-pairs out of four identical jets is not trivial, and efficient methods for jet pairing and charge estimation are used. However, the jet pairing and charge assignment efficiency depends strongly on the jet pairing likelihood output. An overall jet pairing efficiency of 80% is reached and the probability for the correct W-charge assignment is 77%.

The Method of Optimal Observables is used to calculate sensitive observables. In order to reflect the strong variation of the jet pairing and charge assignment efficiency as a function of the jet pairing likelihood, the events are divided into quality classes using the likelihood output. A study showed that the use of four classes give the highest precision on the measurement of triple gauge boson couplings.

Various sources of systematic errors are studied and the uncertainty in the modelling of the fragmentation and hadronisation of quarks is found to be the largest systematic error. A χ^2 fit with one free parameter to the optimal observables gives

$$\Delta\kappa_\gamma = 0.17^{+0.72}_{-0.28}, \quad \Delta g_1^{\mathrm{Z}} = 0.09^{+0.11}_{-0.10}, \quad \lambda = 0.01^{+0.33}_{-0.14} \tag{8.1}$$

for the three C and P conserving couplings and

$$g_5^Z \quad = \quad -0.37^{+0.24}_{-0.26} \tag{8.2}$$

for the C and P violating but CP conserving coupling g_5^Z. The errors include the statistical and systematic uncertainties. Performing a three-parameter fit to the three C and P conserving couplings give

$$\Delta\kappa_\gamma = +0.02^{+0.72}_{-0.24}, \quad \Delta g_1^{\mathrm{Z}} = +0.14^{+0.12}_{-0.20}, \quad \lambda = -0.09^{+0.17}_{-0.12} \tag{8.3}$$

with correlation coefficients of -0.58, -0.60 and -0.08 between ($\Delta\kappa_\gamma$, Δg_1^Z), ($\Delta\kappa_\gamma$, λ) and (Δg_1^Z, λ), respectively. The errors correspond to $\Delta\chi^2 = 1$.

The precision of the hadronic final state ranges between the semileptonic final state, as the golden channel with a sensitivity of 2 – 3 higher compared to the hadronic final state, and the leptonic final state. The combination of the measurements using W-pair, single-W and single-γ production from all four LEP experiments decrease the errors further by a factor of 1.5 – 2, depending on the considered coupling.

In the second part of this thesis, the potential of measuring charged current triple gauge boson couplings at a high luminosity linear collider as TESLA is studied. The study utilises semileptonic final states in W-pair production as the final state with a high branching ratio and the best reconstruction possibility. Using the Method of Spin Density Matrix to calculate sensitive observables gives an expected sensitivity of $\sim 3{-}4\times10^{-4}$ for the C and P conserving couplings $\Delta\kappa_\gamma$, Δg_1^Z and λ_γ. The sensitivity for the other couplings is up to a factor 10 lower, depending on the considered coupling. A few sources of systematic errors are considered, as beamstrahlung and the beam energy measurement, but the measurement is not dominated by them.

A unique feature of TESLA compared to former e^+e^- colliders is the longitudinal polarisation of both electron and positron beam. An electron polarisation of 80% is feasible and a positron polarisation of 60% may be possible. Different combinations of electron and positron polarisation can be used to decrease or enhance the triple gauge boson coupling contribution from the s-channel diagrams compared to the t-channel ν exchange in W-pair production. This increases the expected precision on anomalous couplings by a factor of 1.5 – 2. However, the main advantage is that data taken at two opposite beam polarisations allows to disentangle WWγ and WWZ couplings, which is not possible in the unpolarised case.

Unfortunately, a change in polarisation can fake the contributions from anomalous couplings and a precise polarisation measurement is needed. The systematic error from the uncertainties of a polarisation measurement dominates any measurement of triple gauge boson couplings. The study shows, that a precise measurement of triple gauge boson couplings and beam polarisation at the same time is possible using a scheme where data is taken with all possible combinations of beam polarisation.

This study showed that triple gauge boson couplings can be studied with a high precision at TESLA. This precision exceeds event the expected precision at the LHC. For example the sensitivity to $\Delta\kappa_\gamma$ is more than one order of magnitude better at TESLA than at the LHC. For λ the sensitivity is the same for the LHC and TESLA at a centre-of-massenergy of 500 GeV, while at 800 GeV the sensitivity increases by 40%. TESLA is the ideal collider to perform multi-parameter measurements of triple gauge boson couplings in order to explore the structure of new physics, if deviations from the Standard Model are seen.

Danksagung

An dieser Stelle möchte ich mich nach altem Brauch bei all denjenigen bedanken, die in irgendeiner Weise mich in den letzten drei Jahren unterstützt und so zum Gelingen dieser Arbeit beigetragen haben.

Vielen Dank!

Mein besonderer Dank gilt Herrn Professor Rolf-Dieter Heuer für das interessante Thema und die gute Unterstützung. Die Teilnahme an Meetings, Sommerschulen und Konferenzen war immer wieder sehr lehrreich und motivierend. Vielen Dank auch an die Professoren Robert Klanner, Peter Schleper und Götz Heinzelmann für die Erstellung von Gutachten bzw. der Durchführung der Disputation.

Weiter danke ich meinen vielen Betreuer. Explizit möchte ich Ties Behnke, Klaus Desch und Felix Sefkow aus der Gruppe FLC in Hamburg nennen, Klaus Mönig, Wolfgang Kilian und Thorsten Ohl aus der DESY/ECFA Studie und Gideon Bella, Dave Charlton und Helge Voss aus der OPAL Kollaboration. Ohne Helge wären meine wissenschaftlichen Schritte nicht so groß gewesen.

Die Arbeit am DESY in der Gruppe FLC hat mir sehr viel Spaß gemacht, auch wenn es ab und zu nicht einfach war. Ich möchte mich bei allen Mitgliedern für die gute Atmosphäre bedanken. Bei Petra, Kristian, Carsten, Markus, Nils, Marius und Andreas auch für die sehr gute Atmosphäre außerhalb der Arbeit. Vielen Dank auch an Sören und meine Theoriekollegen, die mir immer wieder etwas Nachhilfe gaben und so die Kluft zwischen Experiment und Theorie immer wieder aufs Neue geebnet haben. Vergessen möchte ich auch nicht Ramona, die mir oft geholfen hat.

Zum Schluß bedanke ich mich ganz herzlich bei meiner Familie und Andrea, die unermüdlich wissen wollte, was die W-Bosonen so machen und was für einen Sinn das hat.

Bibliography

[1] S. Weinberg, *A Model of Leptons*, Phys. Rev. Lett. **19**(1967) 1264.

S. L. Glashow, *Partial Symmetries of Weak Interactions*, Nucl. Phys. **22**(1961) 579.

A. Salam, *Weak and Electromagnetic Interactions* (1968) 367, originally printed in *Svartholm: Elementary Particle Theory, Proceedings Of The Nobel Symposium Held 1968 At Lerum, Sweden*.

[2] The LEP Collaborations ALEPH, DELPHI, L3, OPAL, and the LEP GC Working Group, *A Combination of Preliminary Elektroweak Measurements and Constraints on the Standard Model* (2003), LEP-EWWG/2003-02.

[3] K. J. F. Gaemers and G. J. Gounaris, *Polarization Amplitudes for* $e^+e^- \to W^+W^-$ *and* $e^+e^- \to ZZ$, Zeit. Phys. **C1**(1979) 259.

[4] K. Hagiwara, R. D. Peccei, D. Zeppenfeld, and K. Hikasa, *Probing the Weak Boson Sector in* $e^+e^- \to W^+W^-$, Nucl. Phys. **B282**(1987) 253.

[5] H. Aronson, Phys. Rev. **186**(1969) 1434.

[6] B. C. Regan, E. D. Commins, C. J. Schmidt, and D. DeMille, *New Limit on the Electron Electric Dipole Moment*, Phys. Rev. Lett. **88**(2002) 071805.

K. F. Smith *et al.*, *A Search for the Electric Dipole Moment of the Neutron*, Phys. Lett. **B234**(1990) 191.

P. G. Harris *et al.*, *New Experimental Limit on the Electric Dipole Moment of the Neutron*, Phys. Rev. Lett. **82**(1999) 904.

S. K. Lamoreaux and R. Golub, *Comment on 'New Experimental Limit on the Electric Dipole Moment of the Neutron'*, Phys. Rev. **D61**(2000) 051301.

M. V. Romalis, W. C. Griffith, and E. N. Fortson, *A new Limit on the Permanent Electric Dipole Moment of Hg- 199*, Phys. Rev. Lett. **86**(2001) 2505.

[7] W. J. Marciano and A. Queijeiro, *Bound on the* W *Boson Electric Dipole Moment*, Phys. Rev. **D33**(1986) 3449.

F. Boudjema, K. Hagiwara, C. Hamzaoui, and K. Numata, *Anomalous Moments of Quarks and Leptons from Nonstandard* $WW\gamma$ *Couplings*, Phys. Rev. **D43**(1991) 2223.

[8] M. J. G. Veltman, *Second Threshold in Weak Interactions*, Acta Phys. Polon. **B8**(1977) 475.

P. Sikivie, L. Susskind, M. B. Voloshin, and V. I. Zakharov, *Isospin Breaking in Technicolor Models*, Nucl. Phys. **B173**(1980) 189.

[9] T. Appelquist and C. Bernard, *Strongly Interacting Higgs Bosons*, Phys. Rev. **D22**(1980) 200.

A. C. Longhitano, *Heavy Higgs Bosons in the Weinberg-Salam Model*, Phys. Rev. **D22**(1980) 1166.

A. C. Longhitano, *Low-Energy Impact of a Heavy Higgs Boson Sector*, Nucl. Phys. **B188**(1981) 118.

T. Appelquist and G.-H. Wu, *The Electroweak Chiral Lagrangian and CP Violating Effects in Technicolor Theories*, Phys. Rev. **D51**(1995) 240.

[10] S. Weinberg, *Phenomenological Lagrangians*, Physica **A96**(1979) 327.

A. Manohar and H. Georgi, *Chiral Quarks and the Nonrelativistic Quark Model*, Nucl. Phys. **B234**(1984) 189.

H. Georgi and L. Randall, *Flavor Conserving CP Violation in Invisible Axion Models*, Nucl. Phys. **B276**(1986) 241.

[11] E. N. Argyres, G. Katsilieris, A. B. Lahanas, C. G. Papadopoulos, and V. C. Spanos, *One Loop Corrections to Three Vector Boson Vertices in the Standard Model*, Nucl. Phys. **B391**(1993) 23.

[12] E. N. Argyres, A. B. Lahanas, C. G. Papadopoulos, and V. C. Spanos, *Trilinear Gauge Boson Couplings in the MSSM*, Phys. Lett. **B383**(1996) 63.

[13] C. P. Burgess and A. Pilaftsis, *Anomalous Vector Boson Couplings in Majorana Neutrino Models*, Phys. Lett. **B333**(1994) 427.

[14] E. Asakawa, M. Marui, N. Oshimo, T. Saito, and A. Sugamoto, *CP-odd* WWZ *Couplings Induced by Vector-like Quarks*, Eur. Phys. J. **C10**(1999) 327.

[15] A. Arhrib, J. L. Kneur, and G. Moultaka, *Radiative Contributions to TGC in the MSSM* (1996), [hep-ph/9603268].

A. Arhrib, J. L. Kneur, and G. Moultaka, *MSSM Radiative Contributions to the* $\mathrm{WW}\gamma$ *and* WWZ *Form Factors*, Phys. Lett. **B376**(1996) 127.

M. Kitahara, M. Marui, N. Oshimo, T. Saito, and A. Sugamoto, *CP-odd Anomalous* W *Boson Couplings from Supersymmetry*, Eur. Phys. J. **C4**(1998) 661.

[16] A. Miyamoto, *Experimental Aspects of Gauge Boson Studies at Next Linear* $\mathrm{e^+e^-}$ *Colliders*, in *Physics and Experiments with Linear* $\mathrm{e^+e^-}$ *Colliders*, edited by F. A. Harris, S. L. Olsen, S. Pakvasa, and X. Tata, volume 1 (1993) 141–165.

[17] ALEPH Collaboration, R. Barate *et al.*, *Measurement of the* W *Mass in* $\mathrm{e^+e^-}$ *Collisions at Production Threshold*, Phys. Lett. **B401**(1997) 347.

ALEPH Collaboration, R. Barate *et al.*, *Measurement of the* W *Pair Cross Section in* $\mathrm{e^+e^-}$ *Collisions at 172 GeV*, Phys. Lett. **B415**(1997) 435.

ALEPH Collaboration, R. Barate *et al.*, *Measurement of* W *Pair Production in* e^+e^- *Collisions at 183 GeV*, Phys. Lett. **B453**(1999) 107.

ALEPH Collaboration, R. Barate *et al.*, *Measurement of* W *Pair Production in* e^+e^- *Collisions at 189 GeV*, Phys. Lett. **B484**(2000) 205.

[18] DELPHI Collaboration, P. Abreu *et al.*, *Measurement and Interpretation of the* W *Pair Cross-Section in* e^+e^- *Interactions at 161 GeV*, Phys. Lett. **B397**(1997) 158.

DELPHI Collaboration, P. Abreu *et al.*, *Measurement of the* W *Pair Cross-Section and of the* W *Mass in* e^+e^- *Interactions at 172 GeV*, Eur. Phys. J. **C2**(1998) 581.

DELPHI Collaboration, P. Abreu *et al.*, W *Pair Production Cross-Section and* W *Branching Fractions in* e^+e^- *Interactions at 183 GeV*, Phys. Lett. **B456**(1999) 310.

DELPHI Collaboration, P. Abreu *et al.*, W *Pair Production Cross-Section and* W *Branching Fractions in* e^+e^- *Interactions at 189 GeV*, Phys. Lett. **B479**(2000) 89.

[19] L3 Collaboration, M. Acciarri *et al.*, *Pair-Production of* W *Bosons in* e^+e^- *Interactions at* $\sqrt{s} = 161$ *GeV*, Phys. Lett. **B398**(1997) 223.

L3 Collaboration, M. Acciarri *et al.*, *Measurement of* W *Pair Cross Sections in* e^+e^- *Interactions at* $\sqrt{s} = 172$ *GeV and* W *Decay Branching Fractions*, Phys. Lett. **B407**(1997) 419.

L3 Collaboration, M. Acciarri *et al.*, *Measurement of* W *Pair Cross Sections in* e^+e^- *Interactions at* $\sqrt{s} = 183$ *GeV and* W *Decay Branching Fractions*, Phys. Lett. **B436**(1998) 437.

L3 Collaboration, M. Acciarri *et al.*, *Measurement of the* W *Pair Production Cross Section and* W *Decay Branching Fractions in* e^+e^- *Interactions at* $\sqrt{s} = 189$ *GeV*, Phys. Lett. **B496**(2000) 19.

[20] OPAL Collaboration, K. Ackerstaff *et al.*, *Measurement of the Mass of the* W *Boson in* e^+e^- *Collisions at* $\sqrt{s} = 161$ *GeV*, Phys. Lett. **B389**(1996) 416.

OPAL Collaboration, K. Ackerstaff *et al.*, *Measurement of the* W *Boson Mass and* W^+W^- *Production and Decay Properties in* e^+e^- *Collisions at* $\sqrt{s} = 172$ *GeV*, Eur. Phys. J. **C1**(1998) 395.

[21] OPAL Collaboration, G. Abbiendi *et al.*, W^+W^- *Production and Triple Gauge Boson Couplings at LEP Energies up to 183 GeV*, Eur. Phys. J. **C8**(1999) 191.

[22] OPAL Collaboration, G. Abbiendi *et al.*, W^+W^- *Production Cross Section and* W *Branching Fractions in* e^+e^- *Collisions at 189 GeV*, Phys. Lett. **B493**(2000) 249.

[23] S. Jadach, W. Płaczek, M. Skrzypek, B. F. L. Ward, and Z. Wąs, *Final-State Radiative Effects for the Exact* $\mathcal{O}(\alpha)$ *YFS Exponentiated (Un)Stable* W^+W^- *Production at and beyond LEP2 Energies*, Phys. Rev. **D61**(2000) 113010.

S. Jadach, W. Płaczek, M. Skrzypek, B. F. L. Ward, and Z. Wąs, *The Monte Carlo Event Generator YFSWW3 Version 1.16 for W Pair Production and Decay at LEP2/LC Energies*, Comput. Phys. Commun. **140**(2001) 432.

[24] M. Skrzypek, S. Jadach, W. Płaczek, and Z. Wąs, *Monte Carlo Program KORALW-1.02 for W Pair Production at LEP2/NLC Energies with Yennie-Frautschi-Suura Exponentiation*, Comput. Phys. Commun. **94**(1996) 216.

M. Skrzypek, S. Jadach, M. Martinez, W. Płaczek, and Z. Wąs, *Initial State QED Corrections to W Pair Production at LEP2/NLC: Monte Carlo Versus Semianalytical Approach*, Phys. Lett. **B372**(1996) 289.

S. Jadach, W. Płaczek, M. Skrzypek, B. F. L. Ward, and Z. Wąs, *Monte Carlo Program KoralW 1.42 for all Four-Fermion Final States in* $\mathrm{e^+e^-}$ *Collisions*, Comput. Phys. Commun. **119**(1999) 272.

[25] S. Jadach, W. Płaczek, M. Skrzypek, B. F. L. Ward, and Z. Wąs, *The Monte Carlo Program KoralW Version 1.51 and the Concurrent Monte Carlo KoralW&YFSWW3 with all Background Graphs and First Order Corrections to W Pair Production*, Comput. Phys. Commun. **140**(2001) 475.

[26] A. Denner, S. Dittmaier, M. Roth, and D. Wackeroth, *Predictions for all Processes* $\mathrm{e^+e^-} \to 4fermions + \gamma$, Nucl. Phys. **B560**(1999) 33.

[27] A. Denner, S. Dittmaier, M. Roth, and D. Wackeroth, *Electroweak Radiative Corrections to* $\mathrm{e^+e^-} \to \mathrm{W^+W^-} \to$ *4fermions in Double-Pole Approximation: The RACOONWW Approach*, Nucl. Phys. **B587**(2000) 67.

A. Denner, S. Dittmaier, M. Roth, and D. Wackeroth, *Probing Anomalous Quartic Gauge-Boson Couplings via* $\mathrm{e^+e^-} \to 4fermions + \gamma$, Eur. Phys. J. **C20**(2001) 201.

A. Denner, S. Dittmaier, M. Roth, and D. Wackeroth, *Off-Shell W Pair Production: Universal Versus Non-Universal Corrections*, in *Proceedings of the 5th International Symposium on Radiative Corrections - RADCOR 2000: Applications of Quantum Field Theory to Phenomenology*, edited by H. E. Haber, Carmel, California (2001) .

A. Denner, S. Dittmaier, M. Roth, and D. Wackeroth, *RACOONWW 1.3: A Monte Carlo Program for Four-Fermion Production at* $\mathrm{e^+e^-}$ *Colliders*, submitted to Comp. Phys. Comm. (2002), [hep-ph/0209330].

[28] A. Denner, S. Dittmaier, M. Roth, and D. Wackeroth, $\mathcal{O}(\alpha)$ *Corrections to* $\mathrm{e^+e^-} \to \mathrm{W^+W^-} \to$ *4fermions (+*γ*): First Numerical Results from RACOONWW*, Phys. Lett. **B475**(2000) 127.

A. Denner, S. Dittmaier, M. Roth, and D. Wackeroth, *W Pair Production at Future* $\mathrm{e^+e^-}$ *Colliders: Precise Predictions from RACOONWW*, Eur. Phys. J. direct **C2**(2000) 4.

[29] OPAL Collaboration, G. Abbiendi *et al.*, *Measurement of the* $\mathrm{W^+W^-}\gamma$ *Cross-Section and First Direct Limits on Anomalous Electroweak Quartic Gauge Couplings*, Phys. Lett. **B471**(1999) 293.

OPAL Collaboration, G. Abbiendi *et al.*, *A Study of* $\mathrm{W^+W^-}\gamma$ *Events at LEP*, accepted by Phys. Letts. **B**(2003), [hep-ex/0309013].

[30] L3 Collaboration, P. Achard *et al.*, *Study of the* $\mathrm{W^+W^-}\gamma$ *Process and Limits on Anomalous Quartic Gauge Boson Couplings at LEP*, Phys. Lett. **B527**(2002) 29.

[31] DELPHI Collaboration, J. Abdallah *et al.*, *Measurement of the* $e^+e^- \to WW\gamma$ *Cross-Section and Limits on Anomalous Quartic Gauge Couplings with DELPHI*, Eur. Phys. J. **C31**(2003) 139.

[32] ALEPH Collaboration, R. Barate *et al.*, *Measurement of the* $e^+e^- \to ZZ$ *Production Cross Section at Centre-of-Mass Energies of 183 GeV and 189 GeV*, Phys. Lett. **B469**(1999) 287.

[33] DELPHI Collaboration, P. Abreu *et al.*, *Measurement of the* ZZ *Cross-Section in* e^+e^- *Interactions at 183 GeV - 189 GeV*, Phys. Lett. **B497**(2001) 199.

DELPHI Collaboration, J. Abdallah *et al.*, ZZ *Production in* e^+e^- *Interactions at* $\sqrt{s} = 183$ *GeV - 209 GeV*, submitted to Eur. Phys. J. **C**(2003), [hep-ex/0307050].

[34] L3 Collaboration, M. Acciarri *et al.*, *Study of Neutral-Current Four-Fermion and ZZ Production in* e^+e^- *Collisions at* $\sqrt{s} = 183$ *GeV*, Phys. Lett. **B450**(1999) 281.

L3 Collaboration, M. Acciarri *et al.*, *Study of Z Boson Pair Production in* e^+e^- *Collisions at LEP at* $\sqrt{s} = 189$ *GeV*, Phys. Lett. **B465**(1999) 363.

L3 Collaboration, M. Acciarri *et al.*, *Study of Z Boson Pair Production in* e^+e^- *interactions at* $\sqrt{s} = 192$ *GeV to 202 GeV*, Phys. Lett. **B497**(2001) 23.

L3 Collaboration, P. Achard *et al.*, Z *Boson Pair-Production at LEP*, submitted to Phys. Lett. **B**(2003), [hep-ex/0308013].

[35] OPAL Collaboration, G. Abbiendi *et al.*, Z *Boson Pair Production in* e^+e^- *Collisions at* $\sqrt{s}$ *= 183 GeV and 189 GeV*, Phys. Lett. **B476**(2000) 256.

OPAL Collaboration, G. Abbiendi *et al.*, *Study of* Z *Pair Production and Anomalous Couplings in* e^+e^- *Collisions at* $\sqrt{s}$ *between 190 GeV and 209 GeV*, accepted by Eur. Phys. J. **C**(2003).

[36] ALEPH Collaboration, R. Barate *et al.*, *A Study of Single* W *Production in* e^+e^- *Collisions at* $\sqrt{s}$ *= 161 GeV to 183 GeV*, Phys. Lett. **B462**(1999) 389.

[37] ALEPH Collaboration, A. Heister *et al.*, *Measurement of Triple Gauge Boson Couplings at LEP Energies up to 189 GeV*, Eur. Phys. J. **C21**(2001) 423.

DELPHI Collaboration, P. Abreu *et al.*, *Measurement of Trilinear Gauge Couplings in* e^+e^- *Collisions at 161 GeV and 172 GeV*, Phys. Lett. **B423**(1998) 194.

DELPHI Collaboration, P. Abreu *et al.*, *Measurements of the Trilinear Gauge Boson Couplings* WWV *(*$V = \gamma$, Z*) in* e^+e^- *Collisions at 183 GeV*, Phys. Lett. **B459**(1999) 382.

DELPHI Collaboration, P. Abreu *et al.*, *Measurement of Trilinear Gauge Boson Couplings* WWV, *(*$V =$ Z, γ*) in* e^+e^- *Collisions at 189 GeV*, Phys. Lett. **B502**(2001) 9.

[38] L3 Collaboration, M. Acciarri *et al.*, *Production of Single* W *Bosons at LEP*, Phys. Lett. **B403**(1997) 168.

L3 Collaboration, M. Acciarri *et al.*, *Production of Single* W *Bosons in* e^+e^- *Interactions at 130 GeV* $\leq \sqrt{s} \leq$ *183 GeV and Limits on Anomalous* $WW\gamma$ *Couplings*, Phys. Lett. **B436**(1998) 417.

L3 Collaboration, M. Acciarri *et al.*, *Production of Single* W *Bosons at* $\sqrt{s}$ *= 189 GeV and Measurement of* $WW\gamma$ *Gauge Couplings*, Phys. Lett. **B487**(2000) 229.

L3 Collaboration, P. Achard *et al.*, *Production of Single* W *Bosons at LEP and Measurement of* $WW\gamma$ *Gauge Coupling Parameters*, Phys. Lett. **B547**(2002) 151.

[39] DELPHI Collaboration, P. Abreu *et al.*, *Single Intermediate Vector Boson Production in* e^+e^- *Collisions at* $\sqrt{s} = 183$ *GeV and 189 GeV*, Phys. Lett. **B515**(2001) 238.

L3 Collaboration, P. Achard *et al.*, *Study of the* $e^+e^- \to Ze^+e^-$ *Process at LEP*, Phys. Lett. **B561**(2003) 73.

OPAL Collaboration, G. Abbiendi *et al.*, *First Measurement of Z/*γ^* *Production in Compton Scattering of Quasi-Real Photons*, Phys. Lett. **B438**(1998) 391.

OPAL Collaboration, G. Abbiendi *et al.*, *Measurement of Z/*γ^* *Production in Compton Scattering of Quasi-Real Photons*, Eur. Phys. J. **C24**(2002) 1.

[40] F. Boudjema *et al.*, *Standard Model Processes at LEP2*, in Altarelli *et al.* [191] (1996) 207–248, CERN-96-01.

[41] R. Nisius, *The Photon Structure from Deep Inelastic Electron Photon Scattering*, Phys. Rept. **332**(2000) 165.

[42] W. Beenakker *et al.*, WW *Cross-Sections and Distributions*, in Altarelli *et al.* [191] (1996) 79–139, CERN-96-01.

[43] A. Vicini, $\mathcal{O}(\alpha)$ *1-Loop Radiative Corrections to* $e^+e^- \to 4f$, Acta Phys. Polon. **B29**(1998) 2847.

[44] E. A. Kuraev and V. S. Fadin, *On Radiative Corrections to* e^+e^- *Single Photon Annihilation at High-Energy*, Sov. J. Nucl. Phys. **41**(1985) 466.

G. Altarelli and G. Martinelli, *Radiative Corrections to the* Z^0 *Line Shape at LEP*, in *Physics at LEP*, edited by J. R. Ellis and R. Peccei, volume 1 of *Cern Yellow Reports* (1986) 47–57, CERN-86-02.

[45] F. A. Berends, W. L. van Neerven, and G. J. H. Burgers, *Higher Order Radiative Corrections at LEP Energies*, Nucl. Phys. **B297**(1988) 429.

O. Nicrosini and L. Trentadue, *Soft Photons and Second Order Radiative Corrections to* $e^+e^- \to Z^0$, Phys. Lett. **B196**(1987) 551.

O. Nicrosini and L. Trentadue, *Second Order Electromagnetic Radiative Corrections to* $e^+e^- \to \gamma^*, Z^0 \to \mu^+\mu^-$, Z. Phys. **C39**(1988) 479.

[46] D. R. Yennie, S. C. Frautschi, and H. Suura, *The Infrared Divergence Phenomena and High-Energy Processes*, Ann. Phys. **13**(1961) 379.

[47] A. Aeppli and D. Wyler, *Hard Bremsstrahlung Processes at LEP2*, Phys. Lett. **B262**(1991) 125.

[48] J. Fujimoto *et al.*, *Non-Resonant Diagrams in Radiative Four-Fermion Processes*, Nucl. Phys. Proc. Suppl. **37B**(1994) 169.

[49] F. Caravaglios and M. Moretti, e^+e^- *into 4 fermions* + γ *with ALPHA*, Z. Phys. **C74**(1997) 291.

[50] F. Jegerlehner and K. Kołodziej, *The Hard Bremsstrahlung Correction to* $e^+e^- \to 4f$ *with Finite Fermion Masses: Results for* $e^+e^- \to u\bar{d}\mu\overline{\nu}_\mu$, Eur. Phys. J. **C12**(2000) 77.

F. Jegerlehner and K. Kołodziej, *Fermion Mass Effects in* $e^+e^- \to 4f$ *and* $e^+e^- \to 4f\gamma$ *with Cuts*, Eur. Phys. J. **C20**(2001) 227.

F. Jegerlehner and K. Kołodziej, *Results for all Reactions* $e^+e^- \to 4f$, $4f\gamma$ *with Nonzero Fermion Masses*, Eur. Phys. J. **C23**(2002) 463.

[51] V. S. Fadin, V. A. Khoze, and A. D. Martin, *On* W^+W^- *Production Near Threshold*, Phys. Lett. **B311**(1993) 311.

V. S. Fadin, V. A. Khoze, A. D. Martin, and A. Chapovsky, *Coulomb Effects in* W^+W^- *Production*, Phys. Rev. **D52**(1995) 1377.

[52] D. Y. Bardin, W. Beenakker, and A. Denner, *The Coulomb Singularity in Off-Shell W Pair Production*, Phys. Lett. **B317**(1993) 213.

A. P. Chapovsky and V. A. Khoze, *Screened-Coulomb Ansatz for the Non-Factorizable Radiative Corrections to the Off-Shell* W^+W^- *Production*, Eur. Phys. J. **C9**(1999) 449.

[53] V. S. Fadin, V. A. Khoze, A. D. Martin, and W. J. Stirling, *Higher Order Coulomb Corrections to the Threshold* $e^+e^- \to W^+W^-$ *Cross-Section*, Phys. Lett. **B363**(1995) 112.

[54] R. G. Stuart, *Gauge Invariance, Analyticity and Physical Observables at the* Z^0 *Resonance*, Phys. Lett. **B262**(1991) 113.

H. G. J. Veltman, *Mass and Width of Unstable Gauge Bosons*, Z. Phys. **C62**(1994) 35.

A. Aeppli, F. Cuypers, and G. J. van Oldenborgh, $\mathcal{O}(\Gamma)$ *Corrections to W Pair Production in* e^+e^- *and* $\gamma\gamma$ *Collisions*, Phys. Lett. **B314**(1993) 413.

[55] A. Aeppli, G. J. van Oldenborgh, and D. Wyler, *Unstable Particles in One Loop Calculations*, Nucl. Phys. **B428**(1994) 126.

[56] M. Böhm *et al.*, *Electroweak Radiative Corrections to* $e^+e^- \to W^+W^-$, Nucl. Phys. **B304**(1988) 463.

J. Fleischer, F. Jegerlehner, and M. Zralek, *Radiative Corrections to Helicity Amplitudes for W Pair Production in* e^+e^- *Annihilation*, Z. Phys. **C42**(1989) 409.

[57] D. Y. Bardin, S. Riemann, and T. Riemann, *Electroweak One Loop Corrections to the Decay of the Charged Vector Boson*, Z. Phys. **C32**(1986) 121.

F. Jegerlehner, *Vector Boson Parameters: Scheme Dependence and Theoretical Uncertainties*, Z. Phys. **C32**(1986) 425.

[58] W. Beenakker, A. P. Chapovsky, and F. A. Berends, *Non-Factorizable Corrections to W Pair Production*, Phys. Lett. **B411**(1997) 203.

W. Beenakker, A. P. Chapovsky, and F. A. Berends, *Non-Factorizable Corrections to W-Pair Production: Methods and Analytic Results*, Nucl. Phys. **B508**(1997) 17.

[59] A. Denner, S. Dittmaier, and M. Roth, *Non-Factorizable Photonic Corrections to* $\mathrm{e^+e^-} \to \mathrm{W^+W^-} \to$ *4fermions*, Nucl. Phys. **B519**(1998) 39.

[60] W. Beenakker, A. Denner, S. Dittmaier, and R. Mertig, *On Shell W Pair Production in the TeV Range*, Phys. Lett. **B317**(1993) 622.

W. Beenakker, A. Denner, S. Dittmaier, R. Mertig, and T. Sack, *High-Energy Approximation for On-Shell W Pair Production*, Nucl. Phys. **B410**(1993) 245.

[61] M. Melles, *Electroweak Radiative Corrections in High Energy Processes*, Phys. Rept. **375**(2003) 219.

[62] G. Gustafson, *Dual Description of a Confined Color Field*, Phys. Lett. **B175**(1986) 453.

G. Gustafson and U. Pettersson, *Dipole Formulation of QCD Cascades*, Nucl. Phys. **B306**(1988) 746.

B. Andersson, G. Gustafson, L. Lönnblad, and U. Pettersson, *Coherence Effects in Deep Inelastic Scattering*, Z. Phys. **C43**(1989) 625.

B. Andersson, G. Gustafson, and L. Lönnblad, *Gluon Splitting in the Color Dipole Cascades*, Nucl. Phys. **B339**(1990) 393.

[63] A. Krzywicki and B. Petersson, *Breakdown of Hadronic Scaling or Evidence for Clustering?*, Phys. Rev. **D6**(1973) 924.

J. Finkelstein and R. D. Peccei, *Bootstrap Model of Inclusive Reactions*, Phys. Rev. **D6**(1972) 2606.

F. Niedermayer, *Dynamical Connections between Quark Fragmentation Functions*, Nucl. Phys. **B79**(1974) 355.

A. Casher, J. B. Kogut, and L. Susskind, *Vacuum Polarization and the Absence of Free Quarks*, Phys. Rev. **D10**(1974) 732.

[64] T. D. Gottschalk, *A Simple Phenomenological Model for Hadron Production from Low Mass Clusters*, Nucl. Phys. **B239**(1984) 325.

T. D. Gottschalk, *An Improved Description of Hadronization in the QCD Cluster Model for* $\mathrm{e^+e^-}$ *Annihilation*, Nucl. Phys. **B239**(1984) 349.

B. R. Webber, *A QCD Model for Jet Fragmentation Including Soft Gluon Interference*, Nucl. Phys. **B238**(1984) 492.

[65] X. Artru and G. Mennessier, *String Model and Multiproduction*, Nucl. Phys. **B70**(1974) 93.

[66] B. Andersson, G. Gustafson, G. Ingelman, and T. Sjöstrand, *Parton Fragmentation and String Dynamics*, Phys. Rept. **97**(1983) 31.

[67] T. Sjöstrand, *High-Energy Physics Event Generation with PYTHIA 5.7 and JETSET 7.4*, Comput. Phys. Commun. **82**(1994) 74.

[68] G. Marchesini *et al.*, *HERWIG: A Monte Carlo Event Generator for Simulating Hadron Emission Reactions with Interfering Gluons. Version 5.1 - April 1991*, Comput. Phys. Commun. **67**(1992) 465.

G. Corcella *et al.*, *HERWIG 6: An Event Generator for Hadron Emission Reactions with Interfering Gluons (Including Supersymmetric Processes)*, JHEP **01**(2001) 010.

[69] L. Lönnblad, *ARIADNE Version 4: A Program for Simulation of QCD Cascades Implementing the Color Dipole Model*, Comput. Phys. Commun. **71**(1992) 15.

[70] M. Bengtsson and T. Sjöstrand, *Coherent Parton Showers Versus Matrix Elements: Implications of PETRA - PEP Data*, Phys. Lett. **B185**(1987) 435.

M. Bengtsson and T. Sjöstrand, *A Comparative Study of Coherent and Noncoherent Parton Shower Evolution*, Nucl. Phys. **B289**(1987) 810.

[71] D. Y. Bardin *et al.*, *Event Generators for WW Physics*, in *Physics at LEP2*, edited by G. Altarelli, T. Sjöstrand, and F. Zwirner, volume 2 of *Cern Yellow Reports* (1997) 3–101, CERN-96-01.

[72] M. W. Grünewald *et al.*, *Four-Fermion Production in Electron Positron Collisions*, in *Report of the Working Groups on Precision Calculations for LEP2 Physics*, edited by S. Jadach, G. Passarino, and R. Pittau, Cern Yellow Reports (2000) 1–135, CERN-2000-009.

[73] E. Barberio and Z. Wąs, *PHOTOS: A Universal Monte Carlo for QED Radiative Corrections. Version 2.0*, Comput. Phys. Commun. **79**(1994) 291.

[74] J. Fujimoto *et al.*, *grc4f v1.1: A Four-fermion Event Generator for* $\mathrm{e}^+\mathrm{e}^-$ *Collisions*, Comput. Phys. Commun. **100**(1997) 128.

[75] F. A. Berends, R. Pittau, and R. Kleiss, *Excalibur: A Monte Carlo Program to Evaluate all Four Fermion Processes at LEP200 and Beyond*, Comput. Phys. Commun. **85**(1995) 437.

F. A. Berends and A. I. van Sighem, *Anomalous Four Fermion Processes in Electron - Positron Collisions*, Nucl. Phys. **B454**(1995) 467.

[76] H. Anlauf, P. Manakos, T. Ohl, and H. D. Dahmen, *WOPPER, Version 1.5: A Monte Carlo Event Generator for* $\mathrm{e}^+\mathrm{e}^- \to \mathrm{W}^+\mathrm{W}^- \to 4f(n)\gamma$ *at LEP2 and Beyond* (1996), [hep-ph/9605457].

[77] T. Ohl, *CIRCE Version 1.0: Beam Spectra for Simulating Linear Collider Physics*, Comput. Phys. Commun. **101**(1997) 269.

[78] T. Sjöstrand *et al.*, *High-Energy-Physics Event Generation with PYTHIA 6.1*, Comput. Phys. Commun. **135**(2001) 238.

[79] W. Kilian, *WHIZARD 1.0: A Generic Monte-Carlo Integration and Event Generation Package for Multi-Particle Processes. Manual*, LC-TOOL-2001-039.

[80] T. Stelzer and W. F. Long, *Automatic Generation of Tree Level Helicity Amplitudes*, Comput. Phys. Commun. **81**(1994) 357.

[81] A. Pukhov *et al.*, *CompHEP: A Package for Evaluation of Feynman Diagrams and Integration over Multi-particle Phase Space. User's Manual for Version 33* (1999), [hep-ph/9908288].

[82] M. Moretti, T. Ohl, and J. Reuter, *O'Mega: An Optimizing Matrix Element Generator* (2001), [hep-ph/0102195].

[83] R. Assmann, M. Lamont, and S. Myers, *A Brief History of the LEP Collider*, Nucl. Phys. Proc. Suppl. **109B**(2002) 17.

[84] L. Arnaudon *et al.*, *Accurate Determination of the LEP Beam Energy by Resonant Depolarization*, Z. Phys. **C66**(1995) 45.

R. Assmann *et al.*, *Calibration of Centre-of-Mass Energies at LEP1 for Precise Measurements of* Z *Properties*, Eur. Phys. J. **C6**(1999) 187.

[85] A. A. Sokolov and I. M. Ternov, *On Polarization and Spin Effects in the Theory of Synchrotron Radiation*, Phys. Dokl. **8**(1964) 1203.

[86] LEP Energy Working Group, A. Blondel, *et al.*, *Evaluation of the LEP Centre-of-Mass Energy above the* W *Pair Production Threshold*, Eur. Phys. J. **C11**(1999) 573.

LEP Energy Working Group, *Evaluation of the LEP Centre-of-Mass Energy for Data Taken in 1998* (1998).

LEP Energy Working Group, *Evaluation of the LEP Centre-of-Mass Energy for Data Taken in 1999* (2000).

LEP Energy Working Group, *Evaluation of the LEP Centre-of-Mass Energy for Data Taken in 2000* (2001).

[87] C. Menot *et al.*, *The LEP Spectrometer*, prepared for 9th LEP Performance Workshop, Chamonix, France, 26-29 Jan 1999.

[88] *TESLA Technical Design Report* (2001), [DESY-01-011].

[89] American Linear Collider Working Group, T. Abe, *et al.*, *Linear Collider Physics Resource Book for Snowmass 2001*, Snowmass, Colorado (2001).

[90] American Linear Collider Working Group, T. Abe, *et al.*, *Introduction*, in *Linear Collider Physics Resource Book for Snowmass 2001* [89] (2001) .

American Linear Collider Working Group, T. Abe, *et al.*, *Higgs and Supersymmetry Studies*, in *Linear Collider Physics Resource Book for Snowmass 2001* [89] (2001) .

American Linear Collider Working Group, T. Abe, *et al.*, *Studies of Exotic and Standard Model Physics*, in *Linear Collider Physics Resource Book for Snowmass 2001* [89] (2001) .

American Linear Collider Working Group, T. Abe, *et al.*, *Theoretical, Accelerator, and Experimental Options*, in *Linear Collider Physics Resource Book for Snowmass 2001* [89] (2001) .

[91] ACFA Linear Collider Working Group, K. Abe, *et al.*, *Particle Physics Experiments at JLC* (2001).

[92] R. Brinkmann *et al.*, editors, *The Accelerator*, Part II of [88].

[93] K. Yokoya and P. Chen, *Beam-beam Phenomena in Linear Colliders*, Tsukuba KEK - KEK-Prepr.-91-002.

[94] S. Schreiber, *Performance Status of the RF-gun based Injector of the TESLA Test Facility Linac*, prepared for 7th European Particle Accelerator Conference (EPAC 2000), Vienna, Austria, 26-30 Jun 2000.

[95] R. Alley *et al.*, *The Stanford Linear Accelerator Polarized Electron Source*, Nucl. Instrum. Meth. **A365**(1995) 1.

[96] J. E. Clendenin, *Polarized Electron Sources*, talk given at 16th IEEE Particle Accelerator Conference (PAC 95) and International Conference on High Energy Accelerators, Dallas, Texas, 1-5 May 1995.

[97] K. Flöttmann and F. Stephan, *RF Photoinjectors as a Sources for Electron Bunches of Extremely Short Length and Small Emittance – Proposal to the BMBF*, [http://desyntwww.desy.de/pitz].

[98] K. Flöttmann, *Investigations Toward the Development of Polarized and Unpolarized High Intensity Positron Sources for Linear Colliders*, DESY-93-161.

[99] G. Alexander *et al.*, *Undulator-Based Production of Polarized Positrons – A Proposal for the 50 GeV Beam in the FFTB* (2003), [SLAC-PROPOSAL-E-166(bis)].

[100] SLD Collaboration, M. Woods, *The Scanning Compton Polarimeter for the SLD Experiment* (1996), [hep-ex/9611005].

[101] V. Gharibyan, N. Meyners, and P. Schuler, *The TESLA Compton Polarimeter* (2001), LC-DET-2001-047.

[102] G. Alexander and I. Cohen, *Møller Scattering Polarimetry for High Energy* $\mathrm{e^+e^-}$ *Linear Colliders*, Nucl. Instrum. Meth. **A486**(2002) 552.

[103] A. Blondel, *A Scheme to Measure the Polarization Asymmetry at the* Z *Pole in LEP*, Phys. Lett. **B202**(1988) 145.

[104] J. Kent *et al.*, *Precision Measurements of the SLC Beam Energy* (1989), presented at IEEE Particle Accelerator Conf., Chicago, Ill., Mar 20-23, 1989.

[105] P. Galumian, C. Joseph, J. P. Perroud, M. T. Tran, and M. Werlen, *A Method for Precise Calibration of Electron Beam Energy*, Nucl. Instrum. Meth. **A327**(1993) 269.

C. Cecchi, J. H. Field, and T. Kawamoto, *Beam Energy Measurement at LEP2 Using Møller Scattering*, Nucl. Instrum. Meth. **A385**(1997) 445.

[106] OPAL Collaboration, K. Ahmet *et al.*, *The OPAL Detector at LEP*, Nucl. Instrum. Meth. **A305**(1991) 275.

[107] R. Brun, R. Hagelberg, M. Hansroul, and J. C. Lassalle, *GEANT: Simulation Program for Particle Physics Experiments. User Guide and Reference Manual*, CERN-DD-78-2-REV.

[108] J. Allison *et al.*, *The Detector Simulation Program for the OPAL Experiment at LEP*, Nucl. Instrum. Meth. **A317**(1992) 47.

[109] P. P. Allport *et al.*, *The OPAL Silicon Microvertex Detector*, Nucl. Instrum. Meth. **A324**(1993) 34.

P. P. Allport *et al.*, *The OPAL Silicon Strip Microvertex Detector with Two Coordinate Readout*, Nucl. Instrum. Meth. **A346**(1994) 476.

S. Anderson *et al.*, *The Extended OPAL Silicon Strip Microvertex Detector*, Nucl. Instrum. Meth. **A403**(1998) 326.

[110] R. D. Heuer and A. Wagner, *The OPAL Jet Chamber*, Nucl. Instrum. Meth. **A265**(1988) 11.

O. Biebel *et al.*, *Performance of the OPAL Jet Chamber*, Nucl. Instrum. Meth. **A323**(1992) 169.

[111] M. Hauschild *et al.*, *Particle Identification with the OPAL Jet Chamber*, Nucl. Instrum. Meth. **A314**(1992) 74.

[112] G. Aguillion *et al.*, *Thin Scintillating Tiles with High Light Yield for the OPAL Endcaps*, Nucl. Instrum. Meth. **A417**(1998) 266.

[113] OPAL Collaboration, G. Abbiendi *et al.*, *Precision Luminosity for* Z^0 *Lineshape Measurements with a Silicon-Tungsten Calorimeter*, Eur. Phys. J. **C14**(2000) 373.

[114] T. Behnke, S. Bertolucci, R. D. Heuer, and R. Settles, editors, *A Detector for TESLA*, Part IV of [88].

[115] C. J. S. Damerell, *A CCD-based Vertex Detector for TESLA* (2001), LC-DET-2001-023.

[116] M. Winter *et al.*, *A CMOS based VTC Detector* (2001), LC-DET-2001-017.

[117] P. Fischer, *et al.*, *A DEPFET based Pixel Vertex Detector for the Detector at TESLA* (2002), LC-DET-2002-004.

[118] M. Battaglia *et al.*, *A Pixel Vertex Tracker for the TESLA Detector* (2001), LC-DET-2001-042.

[119] J. Hauschildt, *Studies on a Silicon Intermediate Tracker for the TESLA Detector* (2001), LC-DET-2001-036.

[120] R. Settles *et al.*, *A TPC for a Future Linear Collider* (2002), LC-DET-2002-008.

[121] T. Behnke *et al.*, *Performance Study of the Proposed TESLA Detector Using a Realistic Track Reconstruction Package* (2001), LC-DET-2001-029.

[122] F. Badaud *et al.*, *Si-W Calorimeter Performances* (2001), LC-DET-2001-058.

[123] A. C. Benvenuti *et al.*, *Overview of an Electromagnetic Calorimeter for a Linear Collider based on the Shashlik Technique with Longitudinal Segmentation* (2001), LC-DET-2001-027.

[124] P. Hassler *et al.*, *The Hadronic Tile Calorimeter for the TESLA Detector, Design, Construction and Installation.* (2001), LC-DET-2001-049.

[125] CMS Collaboration, G. Acquistapace *et al.*, *CMS, the Magnet Project: Technical Design Report* (1997), CERN-LHCC-97-10.

[126] R. Santonico and R. Cardarelli, *Development of Resistive Plate Counters*, Nucl. Instrum. Meth. **187**(1981) 377.

[127] H. M. Araujo, A. Stahl, and D. J. Miller, *A Lead Tungstate Detector with Integrated Light Readout for the TESLA Luminosity Calorimeter* (2001), LC-DET-2001-080.

[128] T. Behnke *et al.*, *BRAHMS: A Monte Carlo for a Detector at a 500/800 GeV Linear Collider* (2001), LC-PHSM-2001-005.

[129] M. Pohl and H. J. Schreiber, *SIMDET - Version 3: A Parametric Monte Carlo for a TESLA Detector* (1999), [DESY-99-030].

M. Pohl and H. J. Schreiber, *SIMDET - Version 4: A Parametric Monte Carlo for a TESLA Detector* (2002), [DESY-02-061].

[130] S. Jadach, B. F. L. Ward, and Z. Wąs, *Coherent Exclusive Exponentiation CEEX: The Case of the Resonant* $\mathrm{e^+e^-}$ *Collision*, Phys. Lett. **B449**(1999) 97.

[131] S. Jadach, B. F. L. Ward, and Z. Wąs, *The Precision Monte Carlo Event Generator KK for Two- Fermion Final States in* $\mathrm{e^+e^-}$ *Collisions*, Comput. Phys. Commun. **130**(2000) 260.

[132] S. Jadach, B. F. L. Ward, and Z. Wąs, *The Monte Carlo Program KORALZ, Version 4.0, for the Lepton or Quark Pair Production at LEP / SLC Energies*, Comput. Phys. Commun. **79**(1994) 503.

[133] S. Jadach, W. Płaczek, and B. F. L. Ward, *BHWIDE 1.00: O(alpha) YFS Exponentiated Monte Carlo for Bhabha scattering at Wide Angles for LEP1/SLC and LEP2*, Phys. Lett. **B390**(1997) 298.

[134] J. A. M. Vermaseren, *Two Photon Processes at Very High-Energies*, Nucl. Phys. **B229**(1983) 347.

[135] F. A. Berends, P. H. Daverveldt, and R. Kleiss, *Monte Carlo Simulation of Two Photon Processes. 1. Radiative Corrections to Multiperipheral* $\mathrm{e^+e^-}\mu^+\mu^-$ *Production*, Comput. Phys. Commun. **40**(1986) 271.

[136] OPAL Collaboration, G. Alexander *et al.*, *Measurement of the* Z^0 *Line Shape Parameters and the Electroweak Couplings of Charged Leptons*, Z. Phys. **C52**(1991) 175.

[137] N. Brown and W. J. Stirling, *Jet Cross-sections at Leading Double Logarithm in e^+e^- Annihilation*, Phys. Lett. **B252**(1990) 657.

S. Catani, Y. L. Dokshitzer, M. Olsson, G. Turnock, and B. R. Webber, *New Clustering Algorithm for Multi-jet Cross-sections in e^+e^- Annihilation*, Phys. Lett. **B269**(1991) 432.

S. Bethke, Z. Kunszt, D. E. Soper, and W. J. Stirling, *New Jet Cluster Algorithms: Next-to-Leading Order QCD and Hadronization Corrections*, Nucl. Phys. **B370**(1992) 310.

S. Bethke, Z. Kunszt, D. E. Soper, and W. J. Stirling, *Erratum: Jet Cluster Algorithms in e^+e^- Annihilation* (1998), [hep-ph/9803267].

N. Brown and W. J. Stirling, *Finding Jets and Summing Soft Gluons: A New Algorithm*, Z. Phys. **C53**(1992) 629.

[138] OPAL Collaboration, K. Ackerstaff *et al.*, *Search for Chargino and Neutralino Production at $\sqrt{s}$ = 170 GeV and 172 GeV at LEP*, Eur. Phys. J. **C2**(1998) 213.

[139] E. Torrence, $W^+W^- \rightarrow$ *qqqq Event Selection at 189 GeV* (2000), OPAL Technical Note TN650.

[140] E. Torrence *et al.*, *WW115 Manual* (2002).

[141] S. Catani and M. H. Seymour, *The Dipole Formalism for the Calculation of QCD Jet Cross Sections at Next-to-Leading Order*, Phys. Lett. **B378**(1996) 287.

[142] R. K. Ellis, D. A. Ross, and A. E. Terrano, *The Perturbative Calculation of Jet Structure in e^+e^- Annihilation*, Nucl. Phys. **B178**(1981) 421.

[143] O. Nachtmann and A. Reiter, *A Test for the Gluon Selfcoupling in the Reactions* $e^+e^- \rightarrow$ *Four Jets and* $Z^0 \rightarrow$ *Four Jets*, Z. Phys. **C16**(1982) 45.

M. Bengtsson, *Finding the Three Gluon Vertex from Four Jet Events in* e^+e^- *Annihilation*, Z. Phys. **C42**(1989) 75.

[144] D. Karlen, *Using Projections and Correlations to Approximate Probability Distributions*, Computers in Physics **12**(1998) 380.

[145] D. R. Ward and C. P. Ward, *WWFIX - Fixups for the W Mass Analysis* (2002), OPAL Technical Note TN715.

[146] OPAL Collaboration, R. Akers *et al.*, *Measurement of the Time Dependence of* $B^0_d \longleftrightarrow \overline{B}^0_d$ *Mixing using a Jet Charge Technique*, Phys. Lett. **B327**(1994) 411.

[147] OPAL Collaboration, K. Ackerstaff *et al.*, *Measurements of the b Quark Forward-Backward Asymmetry around the* Z^0 *Peak using Jet Charge and Vertex Charge*, Z. Phys. **C75**(1997) 385.

[148] I. Trigger and S. Dobschütz, *A Likelihood Jet Paring Method and a Jetcharge Technique for Reconstruction and Determining the* W*-charges in* $W^+W^- \rightarrow q\overline{q}q'\overline{q}'$ *Events* (1997), OPAL Technical Note TN476.

[149] D. Karlen and E. Torrence, *PC105 Manual* (2001).

[150] D. Atwood and A. Soni, *Analysis for Magnetic Moment and Electric Dipole Moment Form-Factors of the Top Quark via* $e^+e^- \to t\bar{t}$, Phys. Rev. **D45**(1992) 2405.

M. Davier, L. Duflot, F. Le Diberder, and A. Rouge, *The Optimal Method for the Measurement of Tau Polarization*, Phys. Lett. **B306**(1993) 411.

[151] M. Diehl and O. Nachtmann, *Optimal Observables for the Measurement of Three Gauge Boson Couplings in* $e^+e^- \to W^+W^-$, Z. Phys. **C62**(1994) 397.

M. Diehl and O. Nachtmann, *Anomalous Three Gauge Boson Couplings in* $e^+e^- \to W^+W^-$ *and "Optimal" Strategies for their Measurement*, Eur. Phys. J. **C1**(1998) 177.

[152] H. Cramér, *Mathemetical Methods of Statistics*, Princeton University Press, New Jersey (1958).

[153] G. K. Fanourakis, D. Fassouliotis, and S. E. Tzamarias, *A Method to Include Detector Effects in Estimators Sensitive to the Trilinear Gauge Couplings*, Nucl. Instrum. Meth. **A412**(1998) 465.

G. K. Fanourakis, D. Fassouliotis, and S. E. Tzamarias, *Accurate Estimation of the Trilinear Gauge Couplings using Optimal Observables Including Detector Effects*, Nucl. Instrum. Meth. **A414**(1998) 399.

[154] H. Voss, *Messung der Drei-Eichboson-Kopplungen in* $W^+W^- \to q\bar{q}\ell\bar{\nu}_\ell$ *Ereignissen mit optimalen Observablen bei OPAL*, PhD thesis, University of Bonn, Germany (2000), [http://hvoss.home.cern.ch/hvoss] (in german).

[155] G. Gounaris, J. Layssac, G. Moultaka, and F. M. Renard, *Analytic Expressions of Cross-sections, Asymmetries and* W *Density Matrices for* $e^+e^- \to W^+W^-$ *with General Three Boson Couplings*, Int. J. Mod. Phys. **A8**(1993) 3285.

[156] CDF Collaboration, T. Affolder *et al.*, *Measurement of the* W *Boson Mass with the Collider Detector at Fermilab*, Phys. Rev. **D64**(2001) 052001.

[157] D0 Collaboration, B. Abbott *et al.*, *A Measurement of the* W *Boson Mass using Electrons at Large Rapidities*, Phys. Rev. Lett. **84**(2000) 222.

[158] CDF and D0 Collaboration, A. Kotwal, *Combination of CDF and D0 Results on W Boson Mass and Width* (2002), FERMILAB-FN-0716.

[159] OPAL Collaboration, G. Alexander *et al.*, *A Comparison of b and (u d s) quark jets to gluon jets*, Z. Phys. **C69**(1996) 543.

[160] OPAL Collaboration, P. D. Acton *et al.*, *A Study of Differences between Quark and Gluon Jets using Vertex Tagging of Quark Jets*, Z. Phys. **C58**(1993) 387.

[161] OPAL Collaboration, G. Abbiendi *et al.*, *Tests of Models of Color Reconnection and a Search for Glueballs using Gluon Jets with a Rapidity Gap*, submitted to Eur. Phys. J. **C**(2003), [hep-ex/0306021].

[162] ALEPH Collaboration, R. Barate *et al.*, *Studies of Quantum Chromodynamics with the ALEPH Detector*, Phys. Rept. **294**(1998) 1, the Lund a parameter APRJ(41) is adjusted to 0.52 to obtain a better agreement of charged multiplicity in Z events.

[163] OPAL Collaboration, G. Abbiendi *et al.*, *Measurement of Charged Current Triple Gauge Boson Couplings using* W *Pairs at LEP*, accepted by Eur. Phys. J. **C**(2003), [hep-ex/0308067].

[164] OPAL Collaboration, G. Abbiendi *et al.*, *Measurement of Triple Gauge Boson Couplings from* $\mathrm{W}^+\mathrm{W}^-$ *Production at LEP Energies up to 189 GeV*, Eur. Phys. J. **C19**(2001) 1.

[165] ALEPH Collaboration, R. Barate *et al.*, *Measurement of Triple Gauge-Boson Couplings at 172 GeV*, Phys. Lett. **B422**(1998) 369.

L3 Collaboration, M. Acciarri *et al.*, *Measurements of Mass, Width and Gauge Couplings of the* W *Boson at LEP*, Phys. Lett. **B413**(1997) 176.

[166] L3 Collaboration, M. Acciarri *et al.*, *Measurement of Triple-Gauge-Boson Couplings of the* W *Boson at LEP*, Phys. Lett. **B467**(1999) 171.

[167] ALEPH Collaboration, R. Barate *et al.*, *Measurement of Triple Gauge* $\mathrm{WW}\gamma$ *Couplings at LEP2 Using Photonic Events*, Phys. Lett. **B445**(1998) 239.

[168] J. Alcaraz, *A proposal for the Combination of TGC Measurements*, L3 Note 2718.

[169] D0 Collaboration, S. Abachi *et al.*, *Measurement of the* $\mathrm{WW}\gamma$ *Gauge Boson Couplings in* $p\bar{p}$ *Collisions at* $\sqrt{s} = 1.8$ *TeV*, Phys. Rev. Lett. **75**(1995) 1034.

D0 Collaboration, S. Abachi *et al.*, *Limits on Anomalous* $\mathrm{WW}\gamma$ *Couplings from* $p\bar{p} \rightarrow \mathrm{W}\gamma + \mathrm{X}$ *Events at* $\sqrt{s} = 1.8$ *TeV*, Phys. Rev. Lett. **78**(1997) 3634.

[170] CDF Collaboration, F. Abe *et al.*, *Measurement of* $\mathrm{W} - \gamma$ *Couplings with CDF in* $p\bar{p}$ *Collisions at* $\sqrt{s} = 1.8$ *TeV*, Phys. Rev. Lett. **74**(1995) 1936.

[171] D0 Collaboration, S. Abachi *et al.*, *Search for* W *Boson Pair Production in* $p\bar{p}$ *Collisions at* $\sqrt{s} = 1.8$ *TeV*, Phys. Rev. Lett. **75**(1995) 1023.

D0 Collaboration, B. Abbott *et al.*, *Limits on* $\mathrm{WW}\gamma$ *and* WWZ *Couplings from* W *Boson Pair Production*, Phys. Rev. **D58**(1998) 051101.

[172] CDF Collaboration, F. Abe *et al.*, *Observation of* $\mathrm{W}^+\mathrm{W}^-$ *Production in* $p\bar{p}$ *Collisions at* $\sqrt{s} = 1.8$ *TeV*, Phys. Rev. Lett. **78**(1997) 4536.

[173] D0 Collaboration, B. Abbott *et al.*, *Studies of* WW *and* WZ *Production and Limits on Anomalous* $\mathrm{WW}\gamma$ *and* WWZ *Couplings*, Phys. Rev. **D60**(1999) 072002.

[174] D0 Collaboration, S. Abachi *et al.*, *Search for Anomalous* WW *and* WZ *Production in* $p\bar{p}$ *Collisions at* $\sqrt{s} = 1.8$ *TeV*, Phys. Rev. Lett. **77**(1996) 3303.

D0 Collaboration, B. Abbott *et al.*, *Limits on* WWZ *and* $\mathrm{WW}\gamma$ *Couplings from* $p\bar{p} \rightarrow \mathrm{e}\overline{\nu}_{\mathrm{e}}\mathrm{jjX}$ *Events at* $\sqrt{s} = 1.8$ *TeV*, Phys. Rev. Lett. **79**(1997) 1441.

D0 Collaboration, B. Abbott *et al.*, *Limits on Anomalous* $\mathrm{WW}\gamma$ *and* WWZ *Couplings from* $\mathrm{WW/WZ} \rightarrow \mathrm{e}\overline{\nu}_{\mathrm{e}}\mathrm{jj}$ *Production*, Phys. Rev. **D62**(2000) 052005.

[175] CDF Collaboration, F. Abe *et al.*, *Limits on* WWZ *and* WWγ *Couplings from* WW *and* WZ *Production in* $p\bar{p}$ *Collisions at* $\sqrt{s} = 1.8$ *TeV*, Phys. Rev. Lett. **75**(1995) 1017.

[176] U. Baur *et al.*, *Report of the working group on photon and weak boson production* (2000), published in *Batavia 1999, QCD and weak boson physics in Run II* 115-164.

[177] ECFA/DESY LC Physics Working Group, J. A. Aguilar-Saavedra, *et al.*, *Physics at an* e^+e^- *Linear Collider* (2001), Part III of [88].

[178] W. Menges, *A Study of Charged Current Triple Gauge Couplings at TESLA*, in Behnke *et al.* [192] (2001) 1635–1669, [LC-PHSM-2001-022].

[179] D. Choudhury, J. Kalinowski, and A. Kulesza, *CP-Violating Anomalous* WWγ *Couplings in* e^+e^- *Collisions*, Phys. Lett. **B457**(1999) 193.

[180] W. Menges, *Measurement of the Trilinear Gauge Boson Couplings with the OPAL Detector at LEP*, Diploma thesis, University of Hamburg, Germany (2000), [DESY-THESIS-2000-025] (in german).

[181] M. Bilenkii, J. L. Kneur, F. M. Renard, and D. Schildknecht, *Trilinear Couplings among the Electroweak Vector Bosons and their Determination at LEP200*, Nucl. Phys. **B409**(1993) 22.

[182] G. Gounaris, D. Schildknecht, and F. M. Renard, *Genuine Tests of CP Invariance in* $e^+e^- \to W^+W^-$, Phys. Lett. **B263**(1991) 291.

[183] K. Mönig, *Measurement of the Differential Luminosity using Bhabha Events in the Forward-Tracking Region at TESLA*, in Behnke *et al.* [192] (2001) [LC-PHSM-2000-060].

[184] K. Mönig, *The Use of Positron Polarization for Precision Measurements*, in Behnke *et al.* [192] (2001) [LC-PHSM-2000-059].

[185] M. E. Peskin and T. Takeuchi, *A New Constraint on a Strongly Interacting Higgs Sector*, Phys. Rev. Lett. **65**(1990) 964.

M. E. Peskin and T. Takeuchi, *Estimation of Oblique Electroweak Corrections*, Phys. Rev. **D46**(1992) 381.

[186] G. Altarelli, R. Barbieri, and F. Caravaglios, *Nonstandard Analysis of Electroweak Precision Data*, Nucl. Phys. **B405**(1993) 3.

G. Altarelli, R. Barbieri, and F. Caravaglios, *The Epsilon Variables for Electroweak Precision Tests: A Reappraisal*, Phys. Lett. **B349**(1995) 145.

[187] V. V. Braguta, A. A. Likhoded, and A. E. Chalov, *Anomalous Three-Boson Coupling Constants in the Single Production of* W *Bosons at a Future* e^+e^- *Linear Collider*, Phys. Atom. Nucl. **64**(2001) 1643.

[188] K. Mönig and J. Sekaric, *A Study of Charged Current Triple Gauge Couplings at an* eγ*-Collider* (2003), [LC-PHSM-2003-072].

I. Bozovic-Jelisavcic, K. Monig, and J. Sekaric, *Measurement of Trilinear Gauge Couplings at a* $\gamma\gamma$ *and* eγ *Collider* (2002), [hep-ph/0210308].

[189] K. Mönig, *Electroweak Gauge Theories and Alternative Theories at a Future Linear* e^+e^- *Collider* (2003), [hep-ph/0309021].

[190] The ATLAS Collaboration, *ATLAS Detector and Physics Performance. Technical Design Report, volume 2* (1999), [CERN-LHCC-99-15].

[191] G. Altarelli, T. Sjöstrand, and F. Zwirner, editors, *Physics at LEP2*, volume 1 of *Cern Yellow Reports* (1996), CERN-96-01.

[192] T. Behnke *et al.*, editors, *Physics and Experimentation at a Linear Electron-Positron Collider*, volume 3 (2001), contribution to the 2nd ECFA/DESY Study, 1998-2001.

[193] J. R. Ellis, M. K. Gaillard, and G. G. Ross, *Search for Gluons in* e^+e^- *Annihilation*, Nucl. Phys. **B111**(1976) 253.

[194] V. N. Gribov and L. N. Lipatov, *Deep Inelastic ep Scattering in Perturbation Theory*, Yad. Fiz. **15**(1972) 781.

[195] V. N. Gribov and L. N. Lipatov, e^+e^- *Pair Annihilation and Deep Inelastic ep Scattering in Perturbation Theory*, Yad. Fiz. **15**(1972) 1218.

[196] Y. L. Dokshitzer, *Calculation of the Structure Functions for Deep Inelastic Scattering and* e^+e^- *Annihilation by Perturbation Theory in Quantum Chromodynamics. (in Russian)*, Sov. Phys. JETP **46**(1977) 641.

[197] G. Altarelli and G. Parisi, *Asymptotic Freedom in Parton Language*, Nucl. Phys. **B126**(1977) 298.

[198] A. H. Mueller, *On the Multiplicity of Hadrons in QCD Jets*, Phys. Lett. **B104**(1981) 161.

[199] A. Bassetto, M. Ciafaloni, and G. Marchesini, *Jet Structure and Infrared Sensitive Quantities in Perturbative QCD*, Phys. Rept. **100**(1983) 201.

[200] R. D. Field and R. P. Feynman, *A Parametrization of the Properties of Quark Jets*, Nucl. Phys. **B136**(1978) 1.

[201] B. Andersson, G. Gustafson, and T. Sjöstrand, *A Model for Baryon Production in Quark and Gluon Jets*, Nucl. Phys. **B197**(1982) 45.

[202] T. Meyer, *A Monte Carlo Model to Produce Baryons in* e^+e^- *Annihilation*, Zeit. Phys. **C12**(1982) 77.

[203] B. Andersson, G. Gustafson, and T. Sjöstrand, *Baryon Production in Jet Fragmentation and Upsilon Decay*, Phys. Scripta **32**(1985) 574.

[204] ALEPH Collaboration, D. Decamp *et al.*, *A Study of Bose-Einstein Correlations in* e^+e^- *Annihilation at 91 GeV*, Z. Phys. **C54**(1992) 75.

[205] DELPHI Collaboration, P. Abreu *et al.*, *Bose-Einstein Correlations in the Hadronic Decays of the* Z^0, Phys. Lett. **B286**(1992) 201.

[206] OPAL Collaboration, G. Abbiendi *et al.*, *Transverse and Longitudinal Bose-Einstein Correlations in Hadronic* Z^0 *Decays*, Eur. Phys. J. **C16**(2000) 423.

[207] L3 Collaboration, P. Achard *et al.*, *Bose-Einstein Correlations of Neutral and Charged Pions in Hadronic Z Decays*, Phys. Lett. **B524**(2002) 55.

[208] OPAL Collaboration, G. Abbiendi *et al.*, *Bose-Einstein Correlations of* π^0 *Pairs from Hadronic* Z^0 *Decays*, Phys. Lett. **B559**(2003) 131.

[209] ALEPH Collaboration, D. Buskulic *et al.*, *Production of* K^0 *and Lambda in Hadronic Z Decays*, Z. Phys. **C64**(1994) 361.

[210] DELPHI Collaboration, P. Abreu *et al.*, *Interference of Neutral Kaons in the Hadronic Decays of the* Z^0, Phys. Lett. **B323**(1994) 242.

[211] OPAL Collaboration, R. Akers *et al.*, *The Production of Neutral Kaons in* Z^0 *Decays and their Bose-Einstein Correlations*, Z. Phys. **C67**(1995) 389.

[212] DELPHI Collaboration, P. Abreu *et al.*, *Kaon Interference in the Hadronic Decays of the* Z^0, Phys. Lett. **B379**(1996) 330.

[213] OPAL Collaboration, G. Abbiendi *et al.*, *Bose-Einstein Correlations in* $K^\pm K^\pm$ *Pairs from* Z^0 *Decays into two Hadronic Jets*, Eur. Phys. J. **C21**(2001) 23.

[214] ALEPH Collaboration, R. Barate *et al.*, *Bose-Einstein Correlations in W-Pair Decays*, Phys. Lett. **B478**(2000) 50.

[215] DELPHI Collaboration, P. Abreu *et al.*, *Measurement of Correlations between Pions from Different* W*'s in* $e^+e^- \to W^+W^-$ *Events*, Phys. Lett. **B401**(1997) 181.

[216] L3 Collaboration, P. Achard *et al.*, *Measurement of Bose-Einstein Correlations in* $e^+e^- \to W^+W^-$ *Events at LEP*, Phys. Lett. **B547**(2002) 139.

[217] OPAL Collaboration, G. Abbiendi *et al.*, *Bose-Einstein Correlations in* $e^+e^- \to W^+W^-$ *at 172 and 183 GeV*, Eur. Phys. J. **C8**(1999) 559.

[218] L. Lönnblad and T. Sjöstrand, *Modelling Bose-Einstein Correlations at LEP 2*, Eur. Phys. J. **C2**(1998) 165.

[219] T. Sjöstrand and V. A. Khoze, *On Color Rearrangement in Hadronic* W^+W^- *Events*, Z. Phys. **C62**(1994) 281.

[220] T. Sjöstrand and V. A. Khoze, *Does the W Mass Reconstruction Survive QCD Effects?*, Phys. Rev. Lett. **72**(1994) 28.

[221] The OPAL Collaboration, *Colour Reconnection Studies in* $e^+e^- \to W^+W^-$ *at* $\sqrt{s} = 189 - 208$ *GeV using Particle Flow* (2000), OPAL Physics Note PN506.

[222] V. A. Khoze and T. Sjöstrand, *Soft-particle Spectra as a Probe of Interconnection Effects in Hadronic* W^+W^- *Events*, Eur. Phys. J. **C6**(1999) 271.

Appendix A

Fragmentation and Hadronisation

In this appendix the fragmentation and hadronisation process is discussed with emphasis on more technical details. In the case of two bosons production the question is raised if both bosons fragment independently or not. Two possible source of final state interaction, both leading to non-independent hadronisation, are considered: Bose-Einstein Correlation (BEC) and Colour Reconnection (CR).

A.1 Fragmentation

The radiation of high energy gluons from quarks can in principle be calculated to an arbitrary order using perturbative QCD. The lowest order cross-section for $\mathrm{e^+e^-} \to \mathrm{q\overline{q}g}$ for quarks with negligible mass $m_\mathrm{q} \ll Q = \sqrt{s}$ is [193]

$$\frac{\mathrm{d}\sigma}{\mathrm{d}x_1\mathrm{d}x_2} = \sigma_0 \frac{\alpha_s}{2\pi}\frac{4}{3}\frac{x_1^2 + x_2^2}{(1-x_1)(1-x_2)}, \tag{A.1}$$

where σ_0 is the lowest order cross-section for $\mathrm{e^+e^-} \to \mathrm{q\overline{q}}$, α_s the QCD coupling constant and x_1 and x_2 the scaled momenta, $x_i = 2E_i/Q$, of the two quarks. This formula diverges for either $x_i \to 1 (i = 1, 2)$ and for gluons of zero energy. These divergences cancel in the full calculation due to corresponding divergences in the lowest order vertex and propagator corrections.

The three-parton matrix element $\mathrm{M_{q\overline{q}g}}$ has also been calculated up to two-loop level and first order matrix elements are available for final states up to five partons, but calculations of higher order or with more partons in the final state are very complex. Implementations of these matrix elements in Monte Carlo generators exist, but their ability to describe hadronic $\mathrm{e^+e^-}$ events at high energy is limited because of the limited number of partons and the limited precision due to low order α_s calculations.

A more suitable approach of this issue is the *parton shower method.* A shower is a sequence of consecutive branchings of a mother parton a into two daughter partons b and c. Each daughter is free to branch again, and therefore a tree-like structure is build up. In addition to quarks and gluons photons are also treated as partons in this section and they can take part in the showering process. Looking at triple vertices in QED and QCD, the following five branchings involving quarks, gluons and photons are of interest: $\mathrm{q} \to \mathrm{qg}$, $\mathrm{q} \to \mathrm{q}\gamma$, $\mathrm{g} \to \mathrm{gg}$, $\mathrm{g} \to \mathrm{qq}$ and $\gamma \to \mathrm{q\overline{q}}$. Here, the last one is suppressed compared with the third and forth once and can be neglected.

The kinematics of each branching is given in terms of two variables, Q^2 and z, where the particular choice of these variables differ in various implementations. Q^2 has dimension of squared mass and is related to the mass or the transverse momentum of the branching, whereas z gives the sharing of the mother energy and momentum between the two daughters, with parton b taking a fraction z and parton c a fraction $(1-z)$.

The probability for a parton to branch is related to the splitting functions, which are a crucial building block of the parton evolution equations called DGLAP [194] or Altarelli-Paris equations [197]. It is convenient to introduce $t = \ln(Q^2/\Lambda^2)$, where Λ is the QCD scale. In terms of the two variables t and z, the differential probability $\mathrm{d}\mathcal{P}$ for parton a to branch is

$$\mathrm{d}\mathcal{P}_a = \sum_{b,c} \frac{\alpha}{2\pi} P_{a\to bc}(z)\,\mathrm{d}t\,\mathrm{d}z. \tag{A.2}$$

We sum over all allowed branchings and α is either α_{em} for QED branchings or α_s for QCD ones. The splitting kernels $P_{a\to bc}$, describing the splitting of a parton a into two partons b and c, are

$$\begin{aligned}
P_{\mathrm{q}\to\mathrm{qg}} &= \frac{4}{3}\frac{1+z^2}{1-z}, \\
P_{\mathrm{q}\to\mathrm{q}\gamma} &= e_{\mathrm{q}}^2\frac{1+z^2}{1-z}, \\
P_{\mathrm{g}\to\mathrm{gg}} &= 3\,\frac{(1-z(1-z))^2}{z(1-z)}, \\
P_{\mathrm{g}\to\mathrm{qq}} &= \frac{3}{2}\,(z^2+(1-z)^2),
\end{aligned} \tag{A.3}$$

where e_{q}^2 is the squared electric charge for quarks. The variable t plays the role of a kind of time for the shower evolution. In the evolution of the shower, t is constrained to be gradually decreasing from the hard scattering scale into a soft regime and a cutoff must be introduced to stop the process at some point.

Parton shower Monte Carlo models are based on the probability that a given parton branches during a step in $\mathrm{d}t$, decreasing t, using equation (A.2). The probability for branching at a certain t must be evaluated within the allowed phase space and is randomly chosen. Afterwards the exact branching and the kinematics must be fixed. This procedure is repeated until the cutoff is reached. Usually a kind of effective parton masses is used and the cutoff is chosen to be of the order of 1 GeV.

Parton shower models are very successful in modelling the distributions of daughter partons, which are comparably soft and almost collinear to the mother parton, but their results for additional high energy partons with large transverse momentum (leading to three or more distinct jets) is not optimal. To give a better description of these properties an additional weight is included at the first branching, which is derived from matrix element calculations for three partons. Hence the parton shower is matched to the matrix element calculations. In addition to the mass ordering from the branching algorithm, an angle ordering is applied. The opening angle of subsequent branchings must be smaller than the previous one. This ordering suppresses certain regions in the phase space as suggested by calculations of soft gluon interference effects [198].

An alternative approach is the *colour dipole model* [62], where the initial $\mathrm{q\overline{q}}$ pair is treated as a colour dipole, which can radiate off gluons. For the second gluon radiation the three partons $\mathrm{qg\bar{q}}$ are split into two dipoles, namely qg and $\mathrm{g\bar{q}}$. For further gluon radiation this procedure is repeated.

For gluon emission the following three colour dipoles must be considered: $\mathrm{q\overline{q}}$, qg (or $\mathrm{\bar{q}g}$) and gg. The cross-sections are given by

$$\begin{aligned}
\frac{\mathrm{d}\sigma_{\mathrm{q\overline{q}}}}{\mathrm{d}x_{\mathrm{q}}\mathrm{d}x_{\bar{\mathrm{q}}}} &= \sigma_0 \frac{2\alpha_s}{3\pi} \frac{x_{\mathrm{q}}^2 + x_{\bar{\mathrm{q}}}^2}{(1-x_{\mathrm{q}})(1-x_{\bar{\mathrm{q}}})} \\
\frac{\mathrm{d}\sigma_{\mathrm{qg}}}{\mathrm{d}x_{\mathrm{q}}\mathrm{d}x_{\mathrm{g}}} &= \sigma_0 \frac{3\alpha_s}{4\pi} \frac{x_{\mathrm{q}}^2 + x_{\mathrm{g}}^2}{(1-x_{\mathrm{q}})(1-x_{\mathrm{g}})} \\
\frac{\mathrm{d}\sigma_{\mathrm{gg'}}}{\mathrm{d}x_{\mathrm{g}}\mathrm{d}x_{\mathrm{g'}}} &= \sigma_0 \frac{2\alpha_s}{3\pi} \frac{x_{\mathrm{g}}^2 + x_{\mathrm{g'}}^2}{(1-x_{\mathrm{g}})(1-x_{\mathrm{g'}})},
\end{aligned} \tag{A.4}$$

where x_i are the scaled momenta $x_i = 2E_i/Q_d$ in the final state and Q_d the dipole's invariant mass. For the scale of the running coupling α_s $p_\perp^2$ is chosen. The cross-section of photon emission from the $\mathrm{q\overline{q}}$ dipole is given in analogy to the gluon case as

$$\frac{\mathrm{d}\sigma_{\mathrm{q\overline{q}}}}{\mathrm{d}x_{\mathrm{q}}\mathrm{d}x_{\bar{\mathrm{q}}}} = \sigma_0 \frac{\alpha_{em}}{2\pi} e_q^2 \frac{x_{\mathrm{q}}^2 + x_{\bar{\mathrm{q}}}^2}{(1-x_{\mathrm{q}})(1-x_{\bar{\mathrm{q}}})}. \tag{A.5}$$

The emission of photons is treated in the right way if only additional gluons are radiated. If a $\mathrm{q\overline{q}}$ pair is produced, as described later, the dipole picture for photon radiation is not valid any more and photon radiation have to be treated as quadrupole radiation or screening effects have to be included. Fortunately, the cross-section for further photon radiation is small after a $\mathrm{q\overline{q}}$ pair creation, hence switching photon radiation off is also a possible solution. The process of splitting gluons into a $\mathrm{q\overline{q}}$ pair cannot simply be introduced into the dipole picture. Looking at the diagrams for $\mathrm{e^+e^-} \to \mathrm{q\overline{q}q'\bar{q}'}$ in the limit of small $p_\perp^2$ and small invariant mass of the $\mathrm{q'\bar{q}'}$ pair, it can be factorised into a $\mathrm{e^+e^-} \to \mathrm{qg\bar{q}} \to \mathrm{q\overline{q}q'\bar{q}'}$. The first part is already handled by equation (A.4) and the second part can be described by splitting a gluon into a $\mathrm{q\overline{q}}$ pair:

$$\frac{\mathrm{d}\sigma_{\mathrm{qg\to qq'\bar{q}'}}}{\mathrm{d}x_{\mathrm{q'}}\mathrm{d}x_{\bar{\mathrm{q}}'}} = \frac{3\alpha_s}{8\pi} \frac{(1-x_{\mathrm{q'}})^2 + (1-x_{\bar{\mathrm{q}}'})^2}{1-x_{\mathrm{q}}}. \tag{A.6}$$

All cross-sections reproduce the splitting kernels (A.3) in the limit of low $p_\perp$.

The $p_\perp^2$ scale is also used for the ordering of the emissions. This ordering means that an emission at a scale $p_{\perp,1}^2$ is performed before an emission at a lower scale $p_{\perp,2}^2 < p_{\perp,1}^2$ and it must be respected in the process of choosing randomly the emissions.

One controversial point in this discussion is the inclusion of photon radiation in the parton shower. The structure of the splitting kernels for gluon or photon radiation of a quark is the same and only weighted by a colour factor or the electric charge. Both processes are competing if a splitting of a quark occurs. As discussed in the previous section, gauge invariance dictates, that final state and initial state photon radiation can not be treated independently and should be included in the hard scattering process. This would either treat the photon radiation twice or spoil the rate of gluon radiation in the parton shower.

It is not really clear how this problem can be solved. It is more a matter of taste either to include final state photon radiation into the hard scattering process and switch it off in the parton shower or do it vice versa. The OPAL collaboration chose the second option, because it makes more sense from the point of the fragmentation and hadronisation tuning to include the final state photons in the fragmentation process. Furthermore in most Monte Carlo generators the calculation of initial state radiation is separated from the final state photon radiation.

A.2 Hadronisation

For the hadronisation process there are mainly three different approaches: The independent hadronisation, the cluster hadronisation and the string hadronisation.

The *independent hadronisation* [63] is the simplest and oldest one but has a couple of disadvantages and is not used anymore. Nevertheless the model is quite good to introduce the main ideas of hadronisation.

An iterative procedure is applied for each parton from the fragmentation process. In each step a $q\overline{q}$ pair is created and one of the new (anti-)quarks is combined with the isolated parton to form a hadron. The left over parton is the start parton for the next iteration. Since this method does not work for gluons, these are usually split into a $q\overline{q}$ pair before hadronisation. During each step a fraction

$$z = \frac{E_{\mathrm{hadron}} + p_{z,\mathrm{hadron}}}{E_{\mathrm{parton}} + p_{z,\mathrm{parton}}} \tag{A.7}$$

of the light cone momentum of the isolated parton is assigned to the formed hadron. The remaining momentum fraction $(1 - z)$ is left over for further iterations. The process is stopped, if not enough fraction is left over to form new hadrons. The actual fraction z assigned to the hadron is described by a probability function $f(z)$, which is unfortunately called fragmentation function. The functional form of this function can be derived from first principles but the explicit choice is not fixed [200].

This approach has some shortcomings: There is no adequate termination of the iteration. If insufficient energy is left over to form another hadron, the remaining isolated parton is usually discarded. This means that energy, momentum, charge, colour and flavour are not strictly conserved and must be fixed afterwards. Jet correlations, as observed in data, are by construction not implemented in this scheme. There are more properties of independent hadronisation which have been clearly excluded by e^+e^- data.

One goal of the *cluster hadronisation* [64] is to fix some shortcomings of the independent hadronisation: The non-conservation of energy, momentum, charge, colour and flavour. This is done by combining the partons from the fragmentation process into massive, colourless clusters, which then undergo hadronisation. This idea is guided by the fact that the partons created in the fragmentation process tend to form colour-neutral sets of partons with similar momentum and small spatial separation. These sets have invariant masses of the order of the cutoff scale of the fragmentation process, which does not depend on the energy scale of the hard scattering process. Therefore, it seems reasonable to treat these sets, or clusters, in analogy to hadronic resonances with averaged properties, i. e. isotropic decay, predominantly two-body, and other decay properties from first principles.

Clusters are constructed from a quark, an anti-quark and an arbitrary number of gluons. Practically the gluons are split into $q\overline{q}$ pairs before cluster formation, and clusters are formed from quarks only. Each cluster decays into two hadrons, where the one flavour of each resulting hadron is determined from the intrinsic cluster (anti-)flavour and the other flavour is created by an additional $q\overline{q}$ pair. Very massive and very light clusters have to be treated in a special way. Very massive clusters are split into two sub clusters and very light ones are directly transformed into one hadron.

Comparisons of earlier versions of this cluster model with data showed, that the assumptions of isotropic decay leads to a momentum spectrum of hadrons with a heavy quark that is much too soft. A large fraction of heavy hadrons is emitted against the cluster flight direction if isotropy is assumed, hence softening the spectrum. Therefore, in newer implementations of the cluster fragmentation, the original flight direction of the parton from the fragmentation process can be enforced.

The *string hadronisation* [65] is the last and very popular class of hadronisation models. The picture of a rubber string is used for the colour flux tube connecting two quarks. While the two quarks move further apart, their movement is slowed down and energy is transfered into the colour field. If enough energy is transfered, the string breaks and the colour flux tube is interrupted by a virtual $q\overline{q}$ pair coming from the vacuum along the string. The treatment of hard gluons seems more natural in this approach than in the others: They are simply incorporated in the strings connecting two nearby quarks and appear as kinks in the string. This complicates the dynamics, but does not lead to fundamentally different effects, and is therefore neglected in the following discussion.

In the naive approach, the force between two coloured sources, which are separated by a large distance, is assumed constant because of the self-interaction of gluons from the colour flux tube. Hence the energy density, or string tension, κ, is constant along the string. As the quarks fly apart and the string is stretched, the energy stored in the string increases according to $E(d) \propto \kappa d$, where d is the distance of quark and anti-quark, the string length. If a virtual $q\overline{q}$ pair with the same colour as the endpoint quarks of the string fluctuates out of the vacuum along the string, the colour field is locally compensated and the string breaks into two pieces. This procedure happens repeatedly until the remaining energy of the individual string segments is not sufficient to transform another virtual $q\overline{q}$ pair into a real one. Then the connected $q\overline{q}$ pairs are transformed into hadrons by examining their flavour and fixing the momentum and spin state. As in the other models the probability distribution $f(z)$ of momentum fraction assigned to hadrons can be chosen arbitrarily.

In the Lund string model [66], however, the probability to split the string is not assumed to be constant as in other string models. The string is broken exactly where it is necessary to form on-shell hadrons. Since all string breaks are causally disconnected, they can be treated in arbitrary order. The Lund scheme starts from the outer ends of the string and moves inside until the invariant mass of the remaining string drops below a cutoff. The remainder is then split into two on-shell hadrons like in a cluster decay.

Strictly speaking, all hadronisation models discussed above are only able to describe the production of mesons and not the production of baryons, which needs the combination of three quarks. For the creation of baryons, two different schemes exist. In the more general approach, a certain amount of di-quark anti-di-quark pairs are created in the same manor as quark anti-quark pairs in the hadronisation process [201]. These can then be combined with an additional quark from a $q\overline{q}$ pair to form a baryon as described above. The other approach is called popcorn model [203]. In this model, colour fluctuations are possible in the string colour field resulting in the creation of virtual quark anti-quark pairs with different colours than of the quarks at the end points of the string. If in addition a second virtual quark anti-quark pair with a third colour is created or pops up in such a colour fluctuation, it is possible to build two colourless baryons. The density and the size of the colour fluctuations will determine the properties of the baryon anti-baryon production process and must be partly tuned on measurements.

A.3 Monte Carlo Implementation

There are mainly three programs with different implementations of the fragmentation or hadronisation process discussed above, namely JETSET [67], HERWIG [68] and ARIADNE [69]. Partons involved in the branching of a parton a into the two partons b and c are described by their energy E, momentum p and mass m. In the Lund fragmentation model [70], as implemented in JETSET, the two variables $Q^2 = m_a$ and $z = E_b/E_a$ in the centre-of-mass frame of the hard scattering process are used as kinematic variables. The parton shower is followed by the Lund string hadronisation. HERWIG also uses a parton shower approach with branchings described by splitting kernels like JETSET, but it uses the parton energy fraction z and an angular variable ξ as kinematic variables. $\xi_{bc} = (p_b p_c)/(E_b E_c)$, which is approximately $\frac{1}{2}\theta_{bc}^2$ for massless partons at small angles. The cluster model is used for the hadronisation. One important aspect is, that the JETSET implementation of the parton shower is explicitly Lorentz covariant at all stages of the branching in contrast to the HERWIG implementation. ARIADNE is an implementation of the colour dipole model for the parton shower and the hadronisation is usually done using the Lund string model within the JETSET framework. The relevant energy scale in the parton shower is given by $Q^2 = p_\perp^2 \sim z(1-z)m_a^2$, where $p_\perp$ is a kind of transversal momentum.

A.4 Bose-Einstein Correlation

Most of the particles produced in hadronic events are pions and kaons obeying Bose-Einstein statistics. It is therefore expected, that the production of identical particles at small momentum separation is enhanced, relative to what uncorrelated production would have lead to. For the exact theoretical description the amplitudes for the particle production must be symmetrised, which then should give the Bose-Einstein enhancement. Unfortunately no amplitudes exist for nonidentical particles, because particle production is in the non-perturbative regime of QCD. Thus theoretical descriptions of BEC are based on phenomenological models only.

Nevertheless BEC leads to an enhancement of the production of identical bosons close in phase space which can be searched for. First reported for pairs of charged pions produced in hadron-hadron collisions, BEC has been studied for two and more identical bosons in various types of collisions, and particularly in e^+e^- annihilation in hadronic Z decays by all LEP collaborations. For example, BEC has been observed for charged and neutral pion pairs [204, 207], $K_S^0K_S^0$ [209] and also for $K^\pm K^\pm$ [212]. Hadronic W^+W^- decays in e^+e^- annihilation have also been used to study BEC [214]. With the possibility of producing W pairs at LEP 2 the question was raised, if BEC can take place between identical bosons coming from different W bosons, but the theoretical discussion is not yet settled. Intra-W BEC is observed using charged pion pairs, but the measurements of full BEC, namely intra-W and inter-W BEC, are not significant enough to hint in any direction. Hopefully, the combination of measurements from all four LEP collaborations with the full integrated luminosity will favour one scenario.

Even though the measurements confirm BEC for identical particle pairs coming from one boson, BEC is not implemented in the standard Monte Carlo generators used for the fragmentation and hadronisation process. In PYTHIA, BEC effects are implemented via the PYBOEI [218] model. Here, the particle momenta are adjusted after the fragmentation in order to reproduce a phenomenological form,

$$R_2(Q) \sim 1 + \lambda \exp(-r^2 Q^2), \tag{A.8}$$

with Q the four-momentum difference between a pair of identical bosons, r representing the BEC source radius and λ the BEC strength in the so-called static incoherent picture. R_2 is the ratio of the two-particle densities ρ_2 to the product of the two single-particle densities ρ_1. Local energy-momentum conservation is achieved by also adjusting pairs of unlike-sign particles. Various implementations of the model can be tested, among them the extreme options of full (intra-W plus inter-W) BEC and intra-W BEC only.

A.5 Colour Reconnection

The decay products of the two W decays have a significant space-time overlap as the separation of their decay vertices at LEP 2 energies is small compared to characteristic hadronic distance scales of about 1 fm. In the fully hadronic W^+W^- channel this may lead to new types of final state interactions. The interactions with colour exchange between decay products of the two W bosons are called colour reconnection. A modification of the colour flow in this way could have a significant influence on the reconstruction of W bosons and their properties. With the current understanding of non-perturbative QCD, such interference can be estimated only in the context of specific models. In the following we consider only models proposed by Sjöstrand and Khoze.

The Sjöstrand-Khoze (SK) models [219] are based upon the Lund string model of colour confinement, in which a string is created that spans between the decay product partons associated with each W. These strings expand from the respective decay vertices and subsequently fragment to hadrons. Before this fragmentation occurs, at most one reconnection is allowed between sections of the two strings.

The main scenarios considered here are called type I (SK-I) and type II (SK-II) in analogy to the two types of superconducting vortices which could correspond to colour strings. In the SK-I scenario, the two colour flux tubes have a lateral extent comparable to hadronic dimensions. The probability for reconnection to occur is given by $P^r = 1 - \exp(-Vk_I)$, where V is the integrated space-time volume over which the two flux tubes cross and k_I is a free strength parameter. The space-time volume depends on the momenta of primary quarks and is reduced with increasing energy. Hence the reconnection probability is not constant over energy for a fixed strength parameter k_I. For $k_I = 100$ the reconnection probability is almost 100%. Current measurements favour a strength parameter of $k_I = 0.95$ [221], which is close to the widely used value of 0.9, giving a reconnection probability of 30–40% at LEP 2 energies. In the SK-II scenario, the strings have infinitesimal small radii and a unit reconnection probability upon their first crossing. The variant SK-II' requires, that a reconnection is allowed only, if it leads to a reduction of the string length. Both scenarios SK-II and SK-II' have no free parameters and predict the probability of reconnection, which is between 15% and 20%.

As pointed out in reference [222] the only necessary tuning of these models is to ensure that the Jetset hadronisation model gives a good description of the Z data. Therefore the same parameters for the Jetset hadronisation model were used as for the non-reconnected $e^+e^- \to W^+W^-$ events. The parton shower cut-off parameter, Q_0, to which the predictions of the SK-I model in particular are sensitive, is set to 1.9 GeV in the standard OPAL tune of the Jetset hadronisation model.

Appendix B

Additional Material for the OPAL Analysis

For the signal all four-fermion final states have been considered. The samples have been split up into TGC-dependent four-fermion final states generated by KandY and TGC-independent four-fermion final states generated by KoralW. For the process $Z/\gamma \to q\overline{q}$ the KK2f Monte Carlo generator is used. The explicit run numbers are listed in table B.1.

For systematic studies the four-fermion samples from KandY and KoralW are exchanged for samples from Excalibur and `grc4f` as listed in table B.1.

Table B.4 lists the used Monte Carlo samples with triple gauge boson couplings different from the Standard Model.

The contribution from various sources of systematic uncertainties for the measurement of the four triple gauge boson couplings $\Delta\kappa_\gamma$, Δg_1^Z, λ and g_5^Z are given in tables B.5 to B.8 for each centre-of-mass energy separately.

Energy	183	189	192	196	200	202	205	207
KANDY 4f	11801	11802	11803	11804	11805	11806	11807	11808
KORALW 4f	10304	11372	9920	9921	9922	9923	11404	11414
KK2F qq	5184	5188	5195	5196	5119	5199	5183	5193
		5189						5186
KORALW WW	7323	8626	8700	11099	9210	9809	-	10108
EXCALIBUR 4f	11786	11810	9484	9486	9488	9850	-	10351
								10714
EXCALIBUR 4f	11787	11813	9585	9487	9590	9851	-	10352
								10715
`grc4f`eeee	7052	7862	9095	9192	9315	9806	11215	10072
`grc4f`eemm	7053	7863	9275	9278	9316	9807	11216	10073
`grc4f`eett	7054	7864	9276	9279	9317	9808	11217	10074
`grc4f`eeqq	7055	7865	9277	9280	9318	9713	11218	10075

Table B.1: Used Monte Carlo runs for the simulation of signal and Standard Model processes.

BEC model	188.6 GeV	199.5 GeV	206.0 GeV
no BEC	11513	11523	11533
intra BEC	11512	11522	11532
full BEC	11511	11521	11531

Table B.2: Used Monte Carlo runs and three different Bose-Einstein models.

	188.6 GeV		199.5 GeV		206.0 GeV	
CR model	run	P^r	run	P^r	run	P^r
no CR	11711	0.0%	11721	0.0%	11731	0.0%
SK-I ($k_I = 100$)	11712	98.3%	11722	97.2%	11732	96.2%
SK-I ($k_I = 0.9$)	11711/2	38.8%	11721/2	34.3%	11731/2	31.9%
SK-II	11713	19.9%	11723	16.4%	11733	14.8%
SK-II'	11714	17.9%	11724	14.7%	11734	13.3%

Table B.3: Used Monte Carlo run numbers and reconnection probabilities for various colour reconnection models.

coupling	183	189		192	196	200	202	205	207
$\Delta\kappa_\gamma = +1.0$	11788	8105	11814	10012	9746	9761	10018	-	10528
$\Delta\kappa_\gamma = +0.5$	-	8252	-	-	9747	9762	-	-	10716
$\Delta\kappa_\gamma = -0.5$	-	8253	-	-	9748	9763	-	-	10717
$\Delta\kappa_\gamma = -1.0$	11789	8106	11815	10013	9749	9764	10019	-	10529
$\Delta g_1^Z = +1.0$	11792	8107	11818	10016	9754	9769	10022	-	10532
$\Delta g_1^Z = +0.5$	-	8256	-	-	9755	9770	-	-	10720
$\Delta g_1^Z = -0.5$	-	8257	-	-	9756	9771	-	-	10721
$\Delta g_1^Z = -1.0$	11793	8108	11819	10017	9757	9772	10023	-	10533
$\lambda = +1.0$	11790	8109	11816	10014	9750	9765	10020	-	10530
$\lambda = +0.5$	-	8260	-	-	9751	9766	-	-	10718
$\lambda = -0.5$	-	8261	-	-	9752	9767	-	-	10719
$\lambda = -1.0$	11791	8110	11817	10015	9753	9768	10021	-	10531
$g_5^Z = +1.0$	11794	10741	11820	10743	10745	10702	10747	-	10749
$g_5^Z = -1.0$	11795	10742	11823	10744	10746	10703	10748	-	10750

Table B.4: Used Monte Carlo samples with anomalous couplings at the different centre-of-mass energies.

Source	183	189	192	196	200	202	205	207
$\mathcal{O}(\alpha)$ correction	0.023	0.021	0.017	0.032	0.035	0.045	0.041	0.044
ISR	0.027	0.029	0.023	0.027	0.025	0.021	0.025	0.029
TGC matrix element	0.013	0.013	0.014	0.015	0.013	0.014	0.015	0.014
Detector simulation	0.042	0.105	0.016	0.019	0.008	0.008	0.011	0.012
Background	0.095	0.086	0.071	0.113	0.028	0.134	0.040	0.062
$\sqrt{s}$	0.002	0.003	0.002	0.002	0.002	0.001	0.001	0.002
M_W	0.046	0.033	0.029	0.029	0.034	0.011	0.017	0.010
Fragmentation	0.142	0.157	0.150	0.143	0.134	0.125	0.116	0.108
Bose-Einstein correlations	0.192	0.127	0.100	0.001	0.001	0.000	0.123	0.118
Colour reconnection	0.045	0.029	0.022	0.002	0.002	0.001	0.026	0.025
Total	0.253	0.250	0.201	0.191	0.148	0.191	0.184	0.182

Table B.5: The estimate of the systematic uncertainties for $\Delta\kappa_\gamma$ for all energies separately.

Source	183	189	192	196	200	202	205	207
$\mathcal{O}(\alpha)$ correction	0.006	0.007	0.006	0.010	0.013	0.018	0.017	0.018
ISR	0.011	0.011	0.009	0.011	0.010	0.009	0.010	0.013
TGC matrix element	0.004	0.005	0.005	0.006	0.005	0.006	0.006	0.006
Detector simulation	0.010	0.050	0.006	0.005	0.003	0.001	0.003	0.003
Background	0.026	0.034	0.032	0.039	0.014	0.023	0.021	0.021
$\sqrt{s}$	0.001	0.001	0.001	0.001	0.001	0.001	0.001	0.001
M_{W}	0.012	0.011	0.010	0.010	0.016	0.004	0.009	0.006
Fragmentation	0.058	0.052	0.052	0.049	0.045	0.044	0.040	0.036
Bose-Einstein correlations	0.055	0.044	0.039	0.003	0.002	0.002	0.038	0.038
Colour reconnection	0.019	0.015	0.013	0.008	0.007	0.007	0.016	0.016
Total	0.088	0.094	0.075	0.066	0.053	0.054	0.065	0.063

Table B.6: The estimate of the systematic uncertainties for Δg_1^{Z} for all energies separately.

Source	183	189	192	196	200	202	205	207
$\mathcal{O}(\alpha)$ correction	0.006	0.005	0.006	0.010	0.017	0.018	0.014	0.018
ISR	0.017	0.018	0.016	0.017	0.016	0.014	0.015	0.017
TGC matrix element	0.003	0.004	0.004	0.004	0.004	0.004	0.004	0.005
Detector simulation	0.007	0.112	0.009	0.004	0.005	0.003	0.005	0.003
Background	0.046	0.073	0.065	0.082	0.061	0.054	0.053	0.044
$\sqrt{s}$	0.001	0.001	0.001	0.001	0.001	0.001	0.001	0.001
M_{W}	0.014	0.018	0.017	0.014	0.016	0.001	0.017	0.014
Fragmentation	0.093	0.088	0.091	0.088	0.086	0.081	0.079	0.073
Bose-Einstein correlations	0.071	0.056	0.049	0.061	0.056	0.043	0.008	0.008
Colour reconnection	0.048	0.037	0.033	0.034	0.039	0.027	0.026	0.025
Total	0.137	0.175	0.129	0.141	0.126	0.112	0.103	0.093

Table B.7: The estimate of the systematic uncertainties for λ for all energies separately.

Source	183	189	192	196	200	202	205	207
$\mathcal{O}(\alpha)$ correction	0.026	0.037	0.040	0.036	0.048	0.058	0.066	0.045
ISR	0.005	0.009	0.009	0.006	0.011	0.010	0.016	0.011
TGC matrix element	0.014	0.013	0.014	0.012	0.013	0.014	0.014	0.013
Detector simulation	0.018	0.023	0.020	0.017	0.016	0.013	0.017	0.008
Background	0.082	0.032	0.046	0.033	0.025	0.038	0.046	0.016
$\sqrt{s}$	0.003	0.003	0.003	0.003	0.003	0.003	0.003	0.004
M_{W}	0.074	0.052	0.039	0.043	0.020	0.009	0.052	0.017
Fragmentation	0.182	0.171	0.149	0.151	0.146	0.141	0.138	0.141
Bose-Einstein correlations	0.044	0.030	0.025	0.005	0.003	0.003	0.055	0.050
Colour reconnection	0.039	0.027	0.023	0.001	0.000	0.000	0.020	0.018
Total	0.224	0.192	0.171	0.166	0.159	0.159	0.180	0.160

Table B.8: The estimate of the systematic uncertainties for g_5^Z for all energies separately.

Appendix C

Additional Figures for the OPAL Analysis

In chapter 5 a few figures are shown, where the data combined for the centre-of-mass energies from 183–209 GeV is plotted. In this appendix these figures are shown for each energy separately. In figure C.1 to C.8 the jet pairing likelihood output and the absolute value of the jet charge difference for the pairing combination with the highest likelihood output are shown. In figure C.9 to C.16 the W production angle and the W decay angles $\cos\theta^*_{jet}$ and ϕ^*_{jet} are shown. The nine optimal observables for the C and P conserving couplings $\Delta\kappa_\gamma$, Δg_1^Z and λ are shown in figure C.17 to C.24 and the two optimal observables for g_5^Z are shown in figure C.25 to C.32.

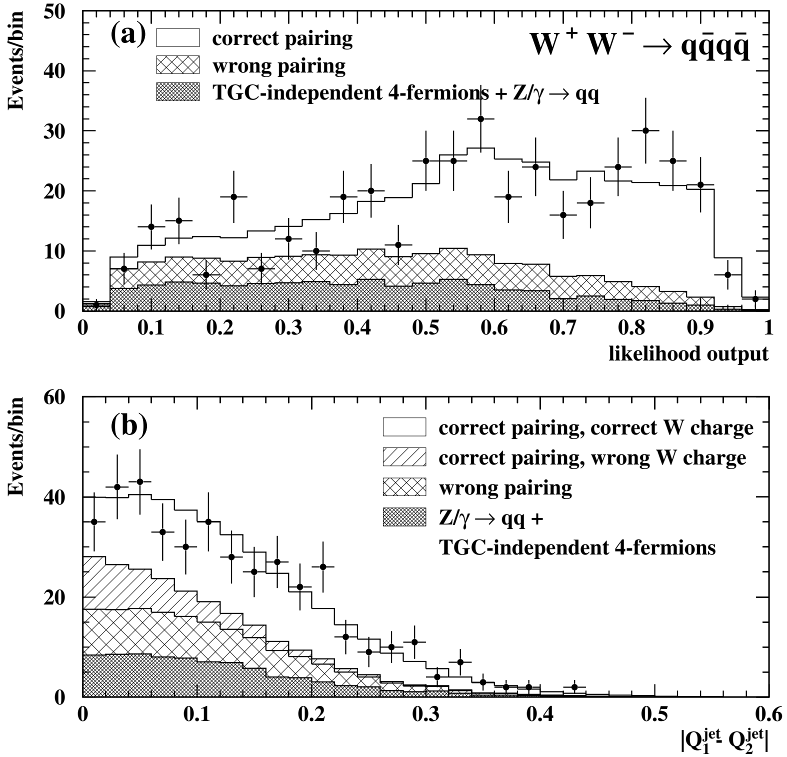

Figure C.1: The 183 GeV data. The description is given in the caption of figure 5.5.

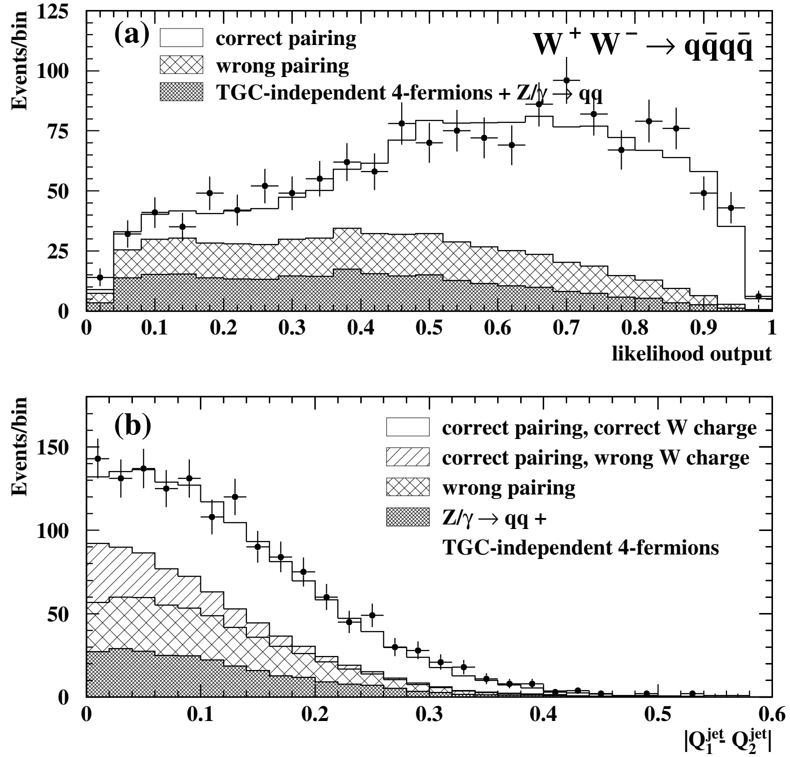

Figure C.2: The 189 GeV data. The description is given in the caption of figure 5.5.

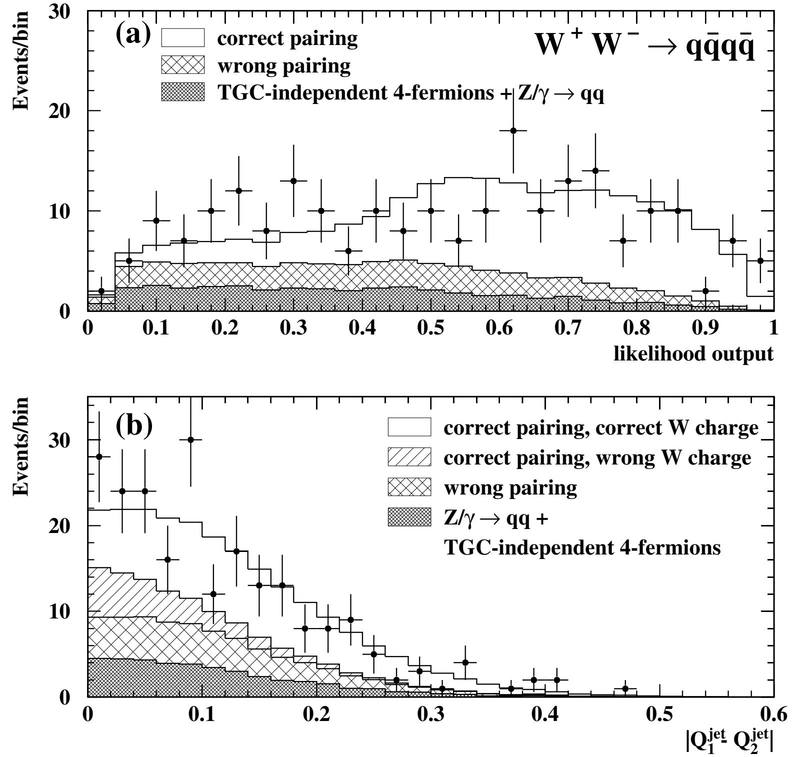

Figure C.3: The 192 GeV data. The description is given in the caption of figure 5.5.

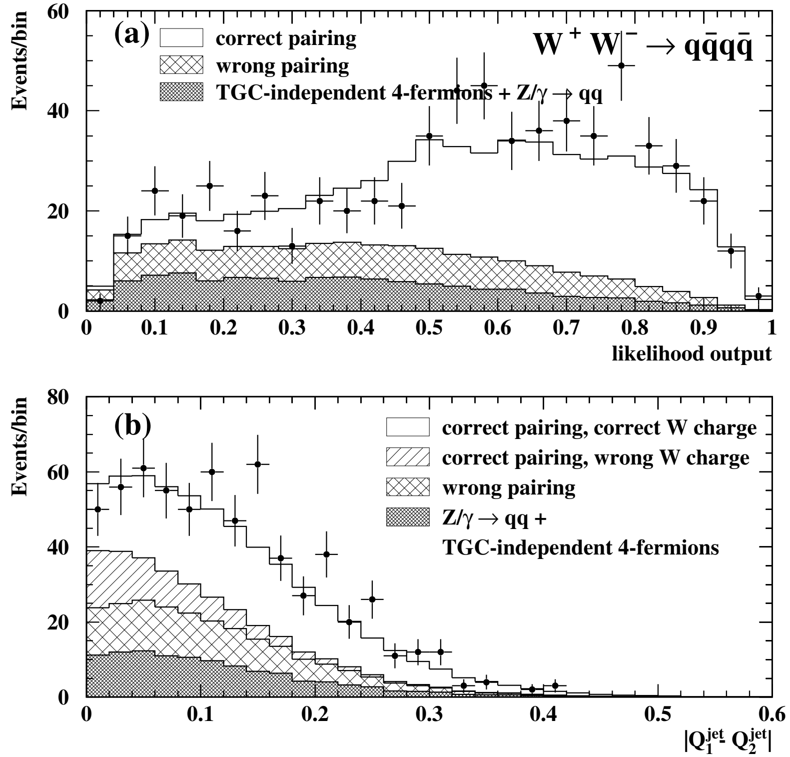

Figure C.4: The 196 GeV data. The description is given in the caption of figure 5.5.

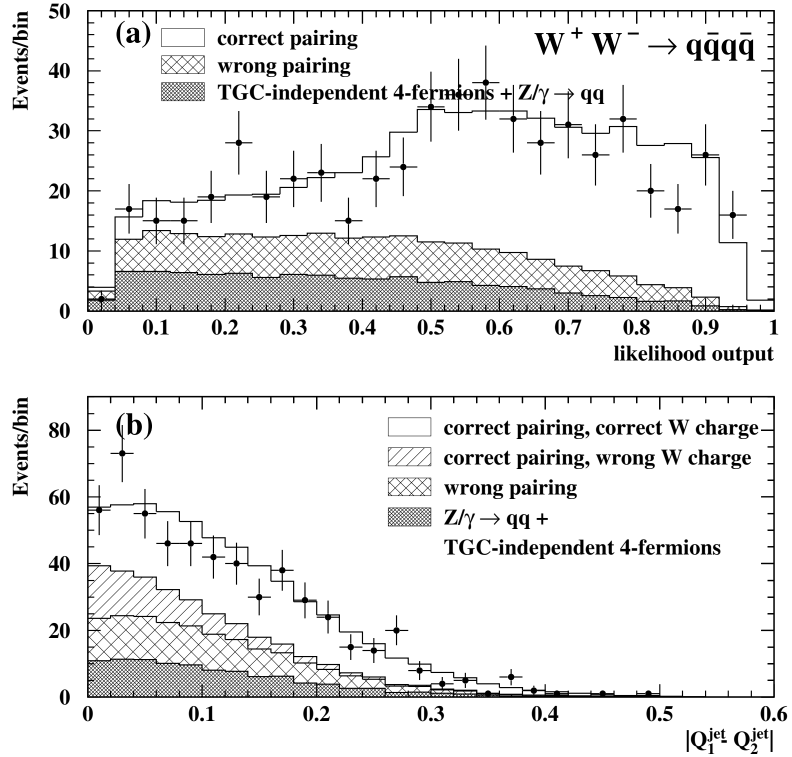

Figure C.5: The 200 GeV data. The description is given in the caption of figure 5.5.

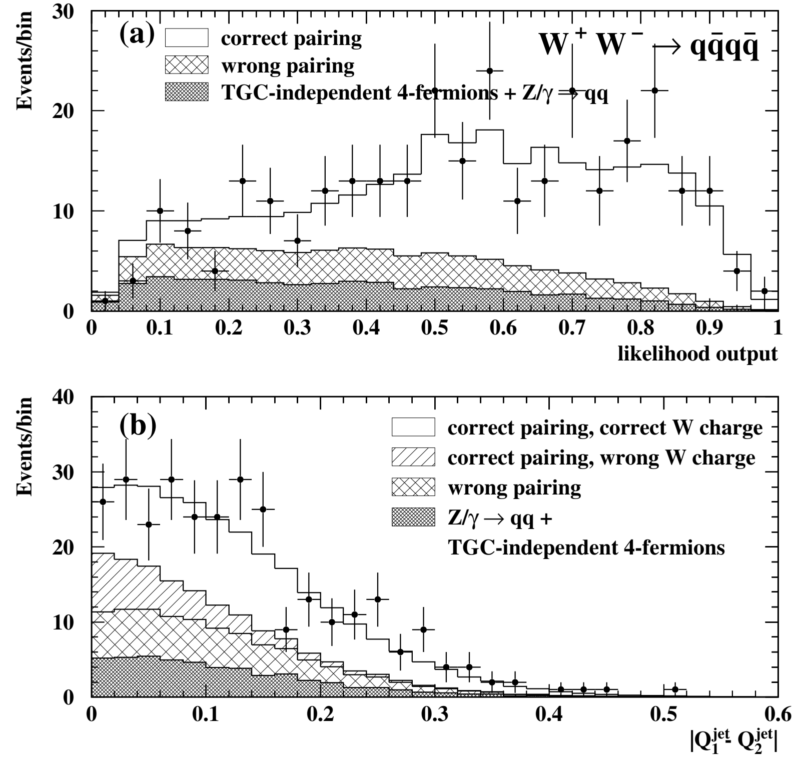

Figure C.6: The 202 GeV data. The description is given in the caption of figure 5.5.

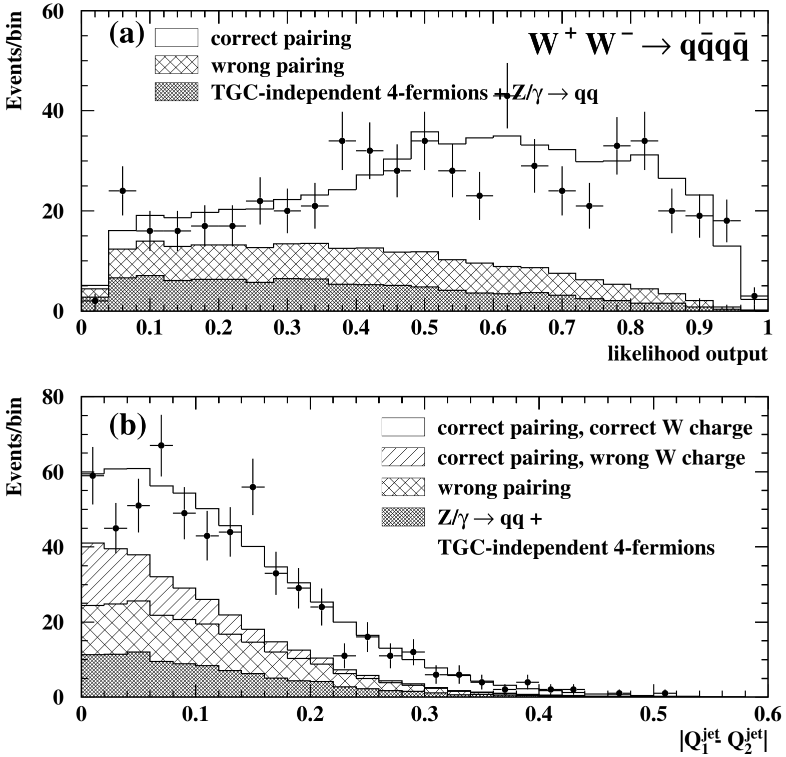

Figure C.7: The 205 GeV data. The description is given in the caption of figure 5.5.

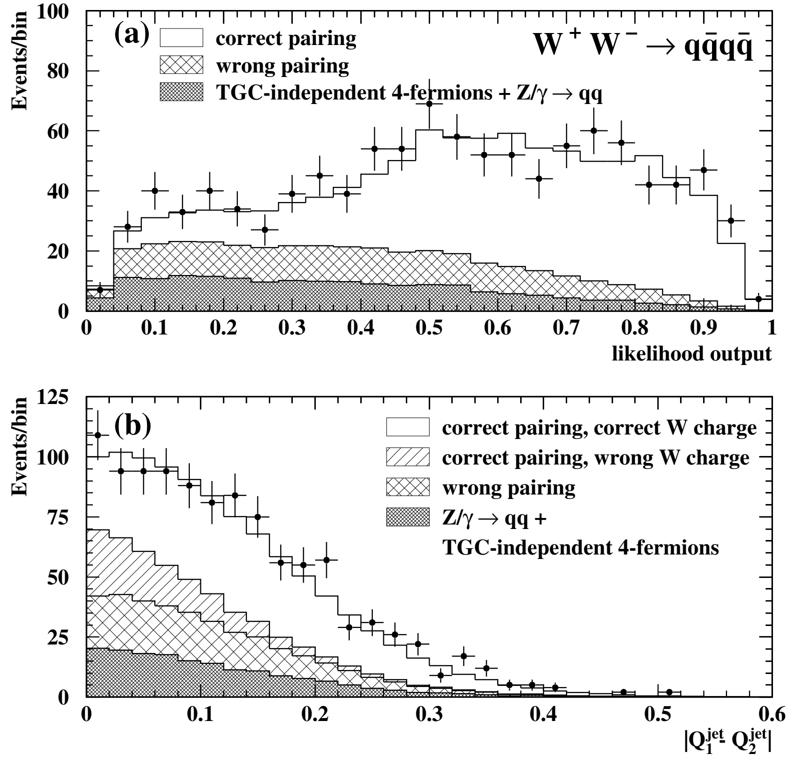

Figure C.8: The 207 GeV data. The description is given in the caption of figure 5.5.

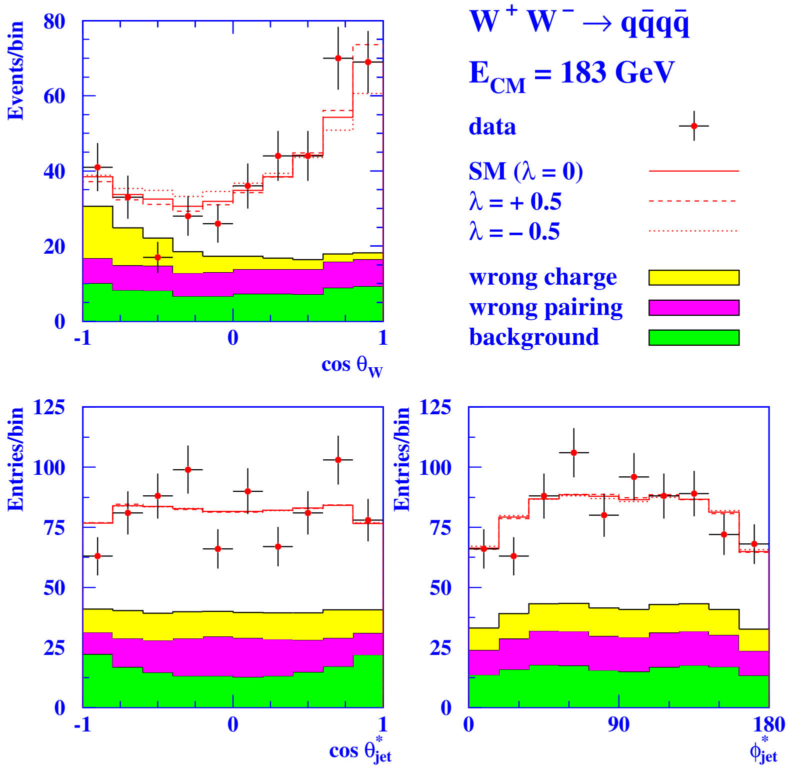

Figure C.9: The 183 GeV data. The description is given in the caption of figure 5.7.

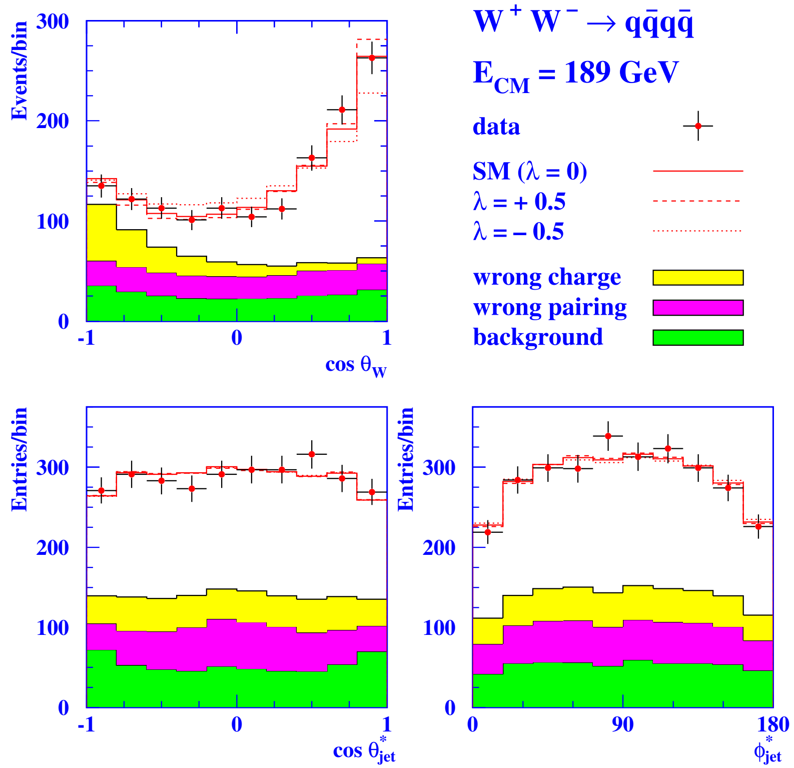

Figure C.10: The 189 GeV data. The description is given in the caption of figure 5.7.

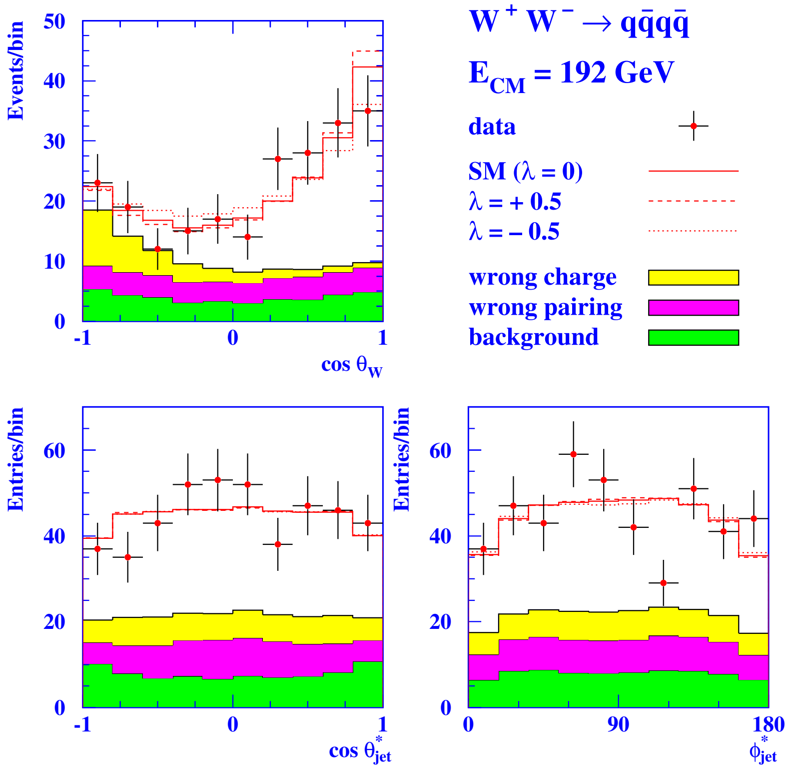

Figure C.11: The 192 GeV data. The description is given in the caption of figure 5.7.

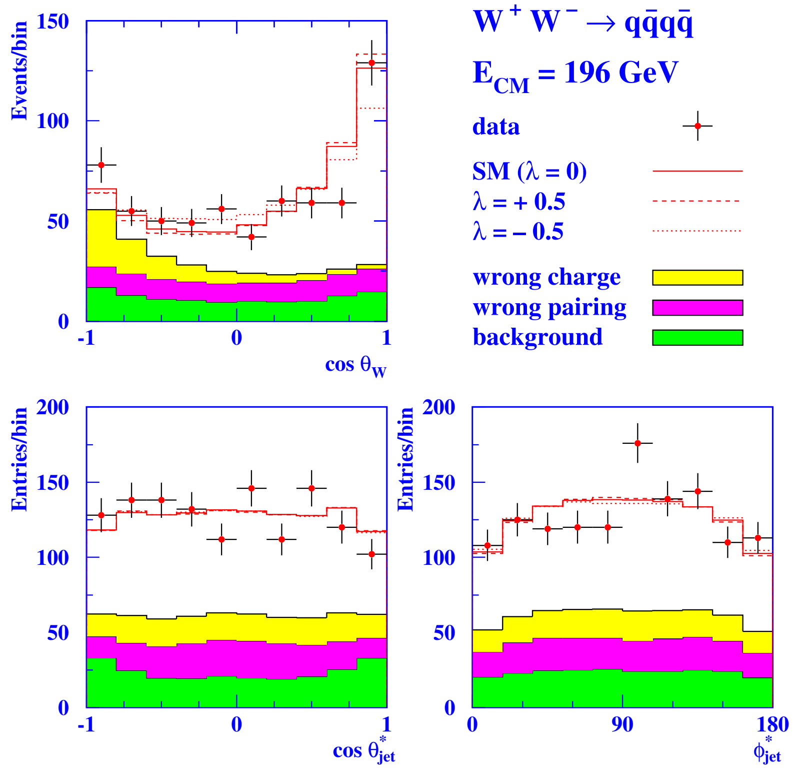

Figure C.12: The 196 GeV data. The description is given in the caption of figure 5.7.

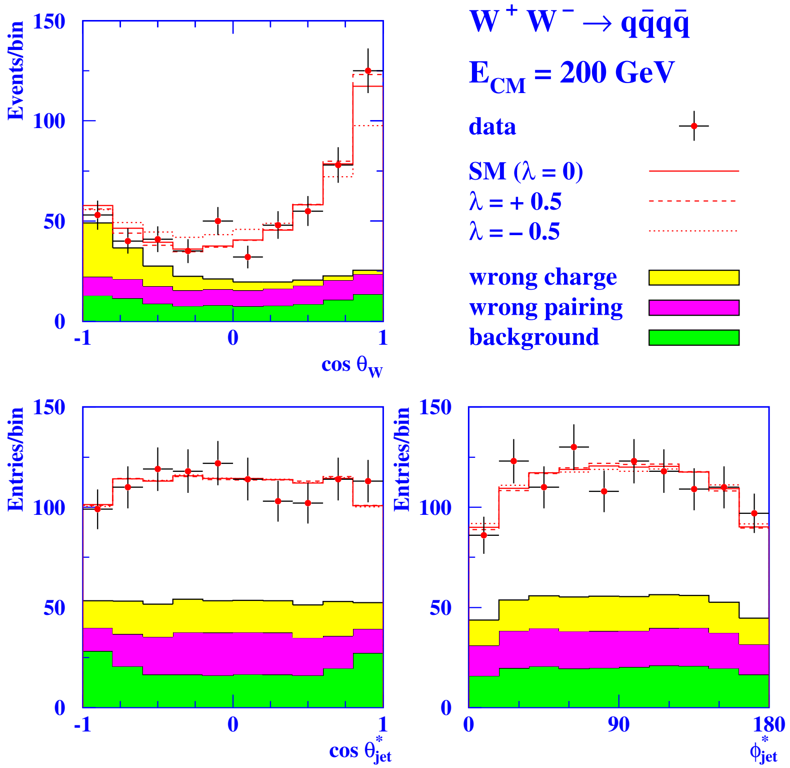

Figure C.13: The 200 GeV data. The description is given in the caption of figure 5.7.

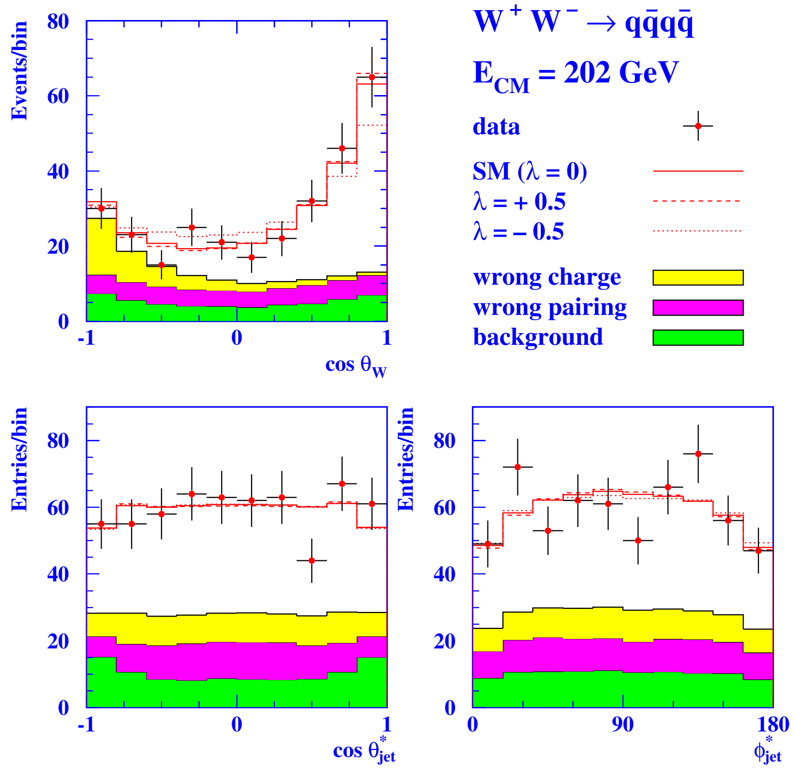

Figure C.14: The 202 GeV data. The description is given in the caption of figure 5.7.

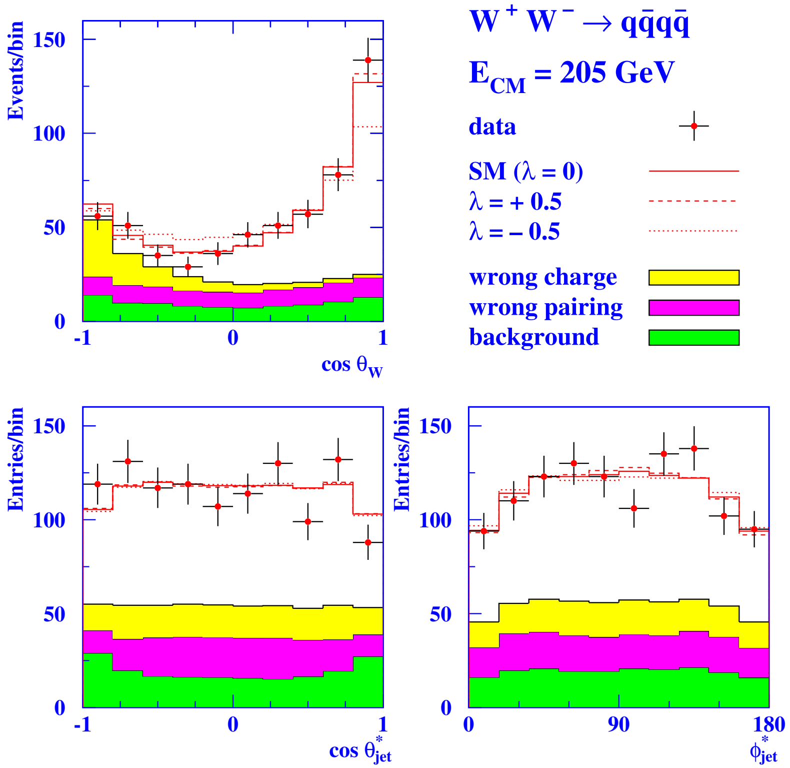

Figure C.15: The 205 GeV data. The description is given in the caption of figure 5.7.

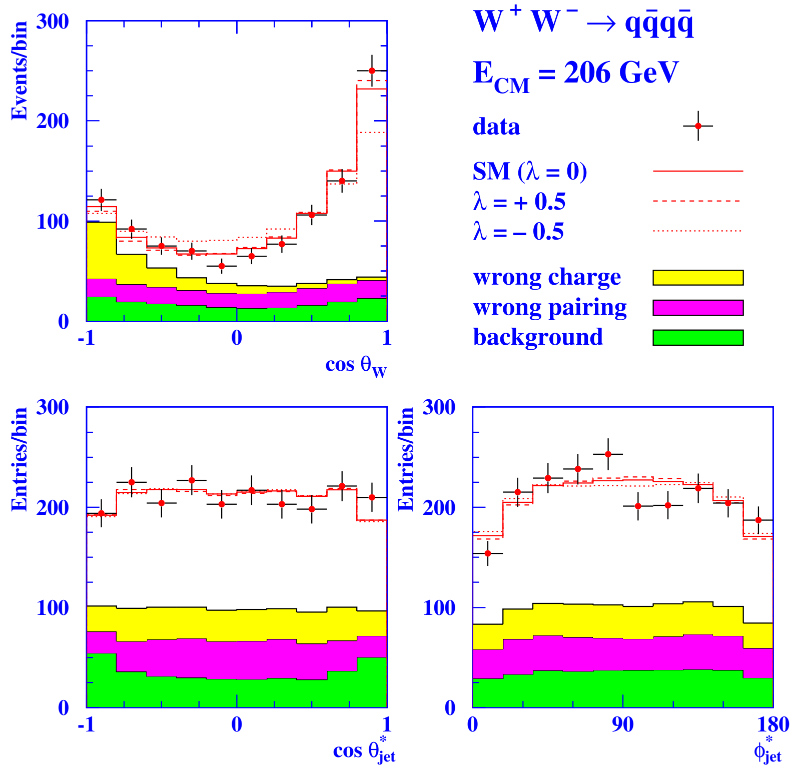

Figure C.16: The 207 GeV data. The description is given in the caption of figure 5.7.

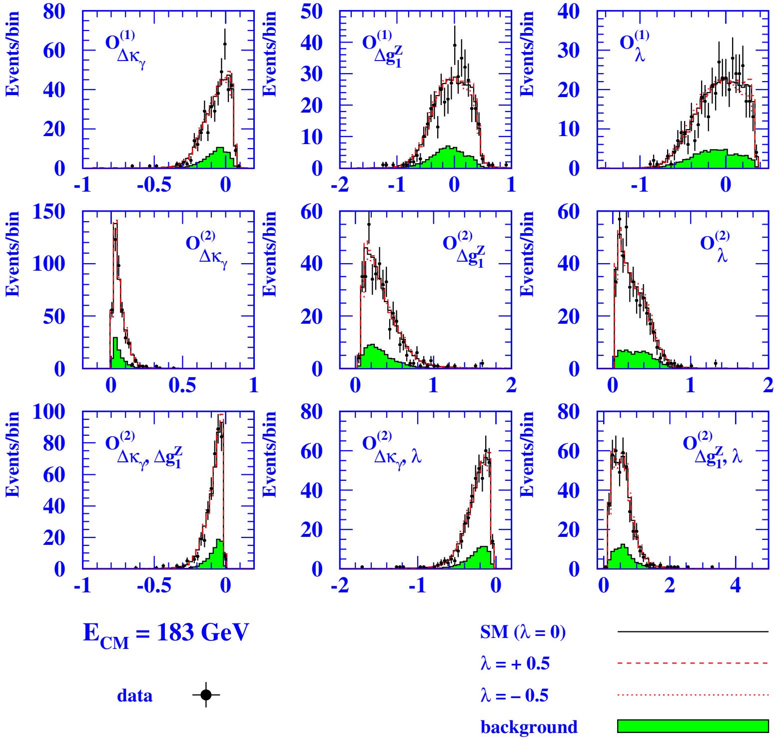

Figure C.17: The 183 GeV data. The description is given in the caption of figure 5.10.

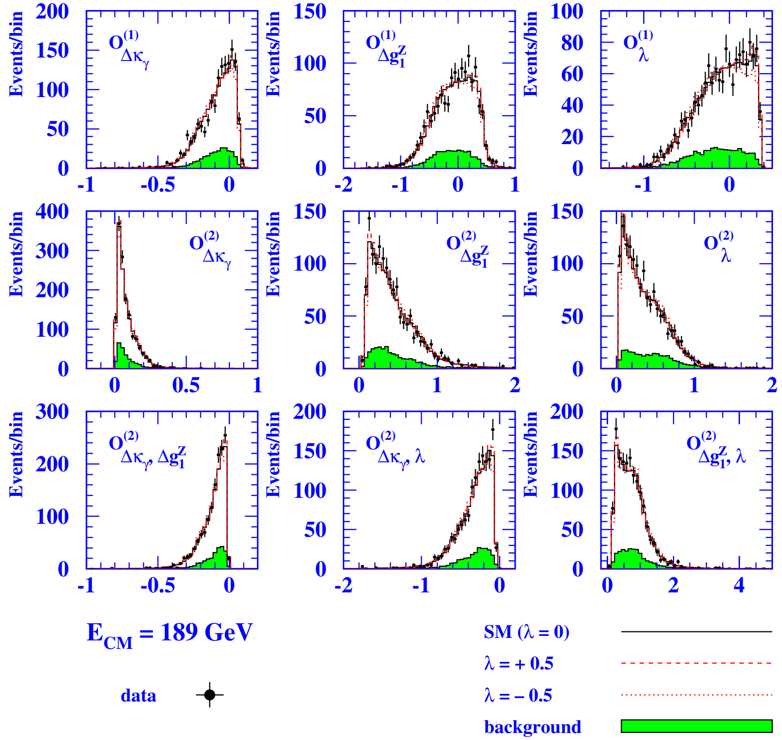

Figure C.18: The 189 GeV data. The description is given in the caption of figure 5.10.

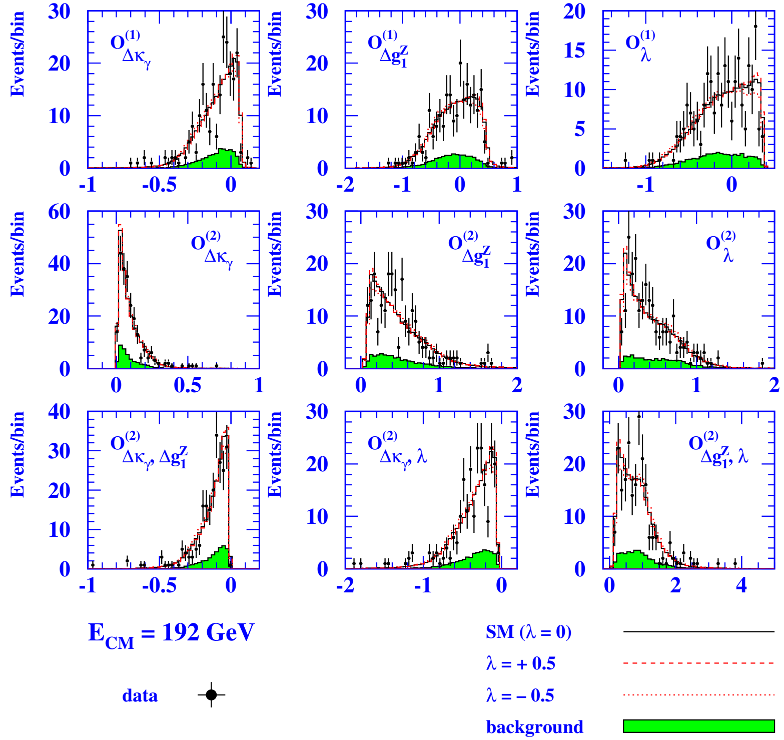

Figure C.19: The 192 GeV data. The description is given in the caption of figure 5.10.

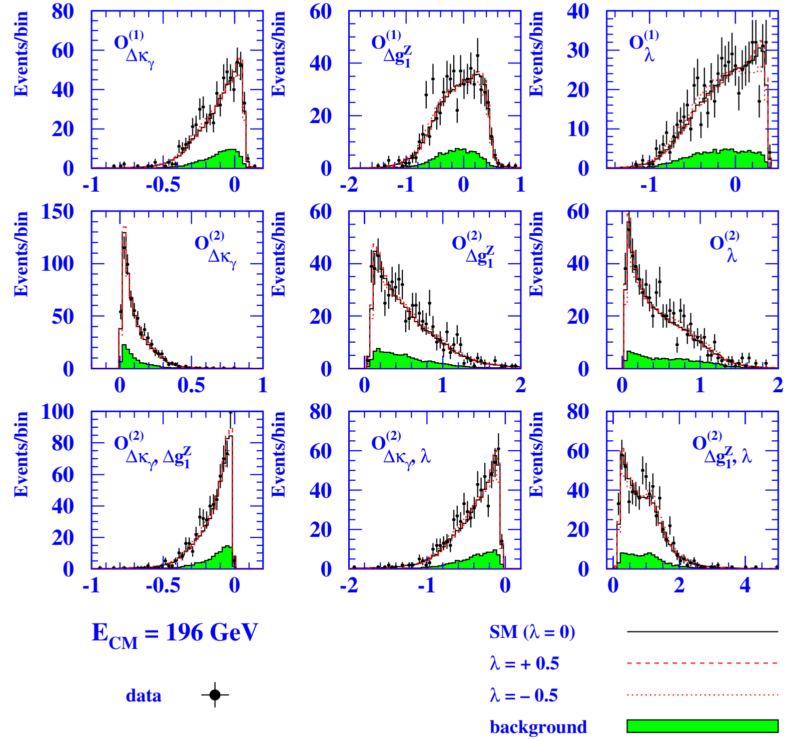

Figure C.20: The 196 GeV data. The description is given in the caption of figure 5.10.

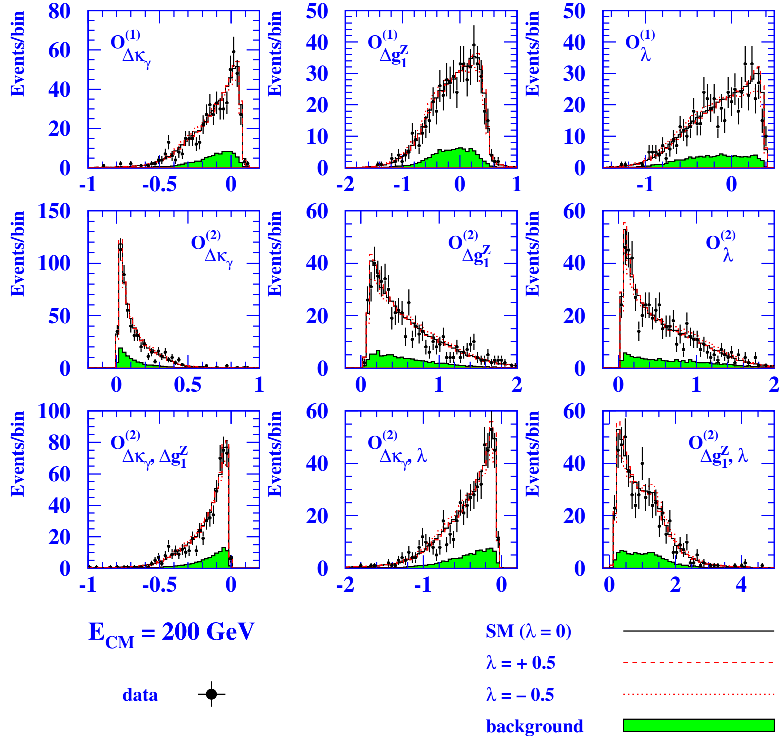

Figure C.21: The 200 GeV data. The description is given in the caption of figure 5.10.

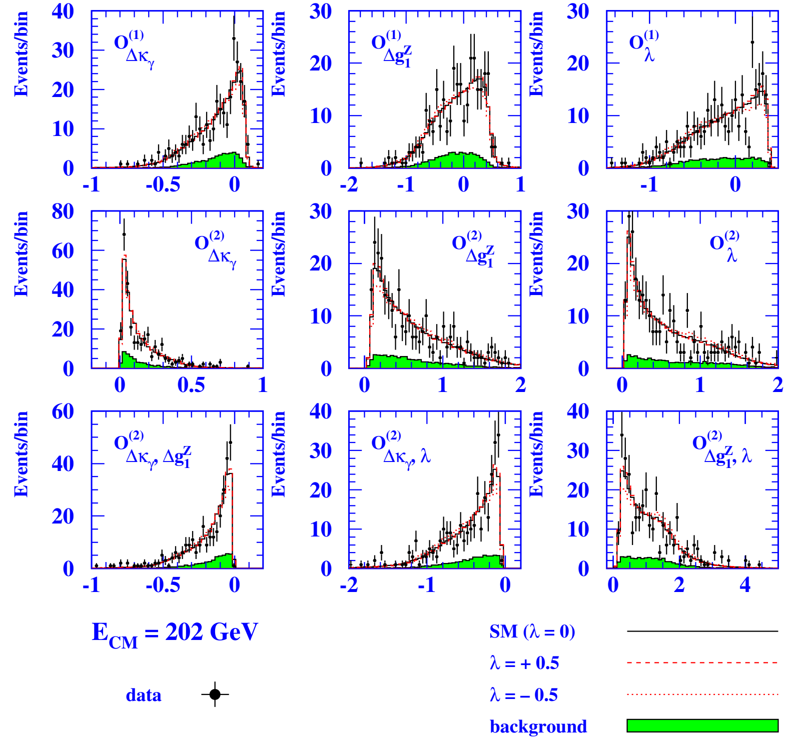

Figure C.22: The 202 GeV data. The description is given in the caption of figure 5.10.

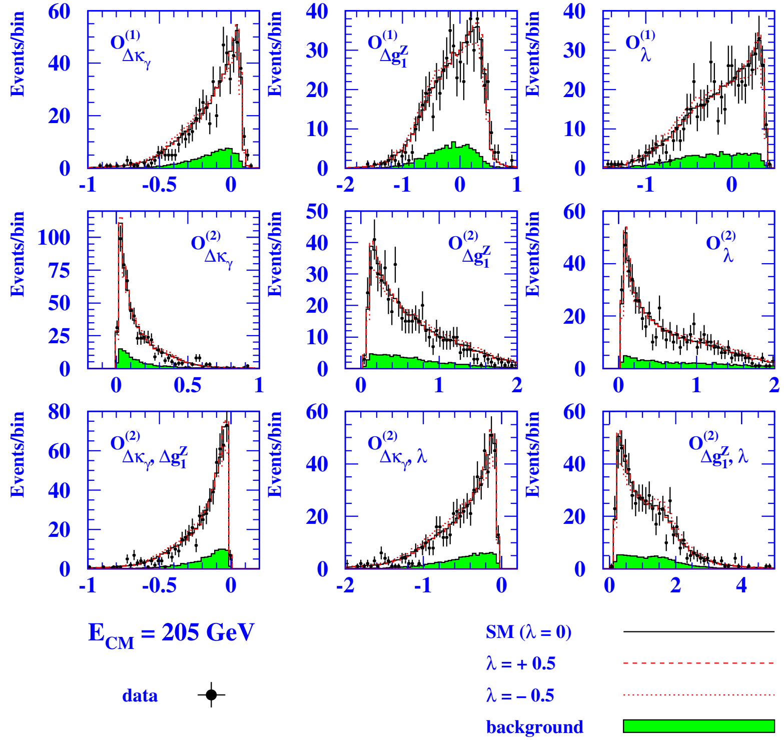

Figure C.23: The 205 GeV data. The description is given in the caption of figure 5.10.

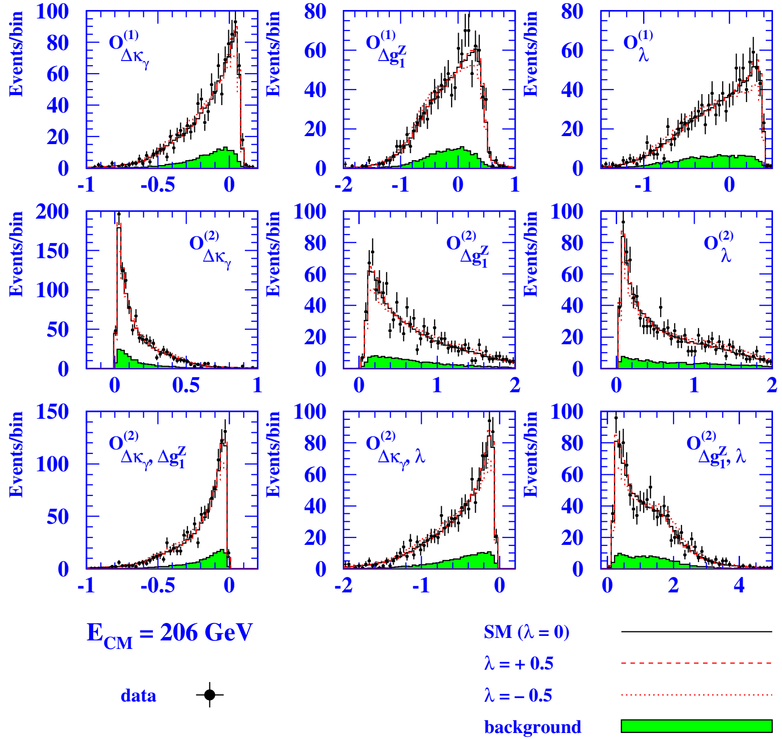

Figure C.24: The 207 GeV data. The description is given in the caption of figure 5.10.

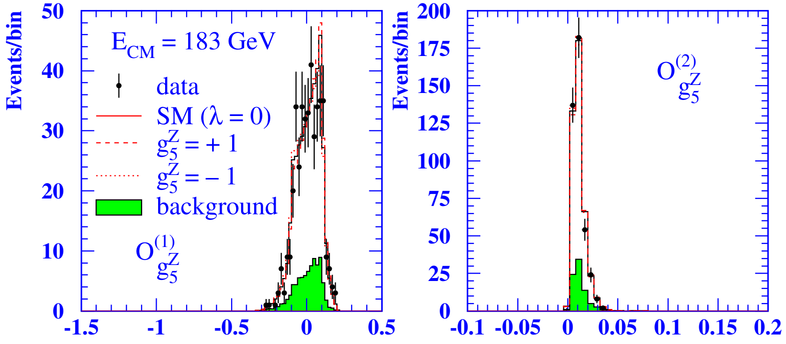

Figure C.25: The 183 GeV data. The description is given in the caption of figure 5.11.

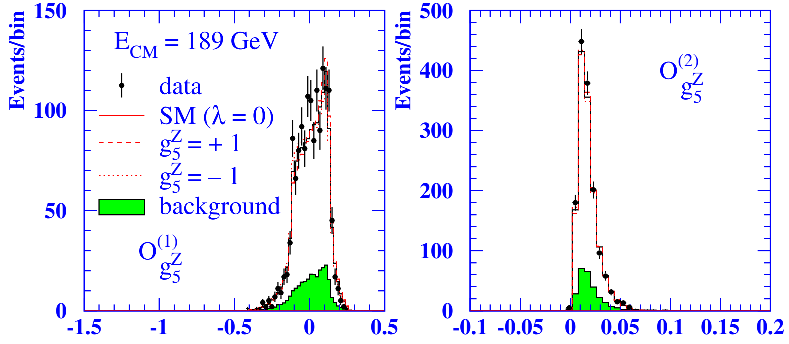

Figure C.26: The 189 GeV data. The description is given in the caption of figure 5.11.

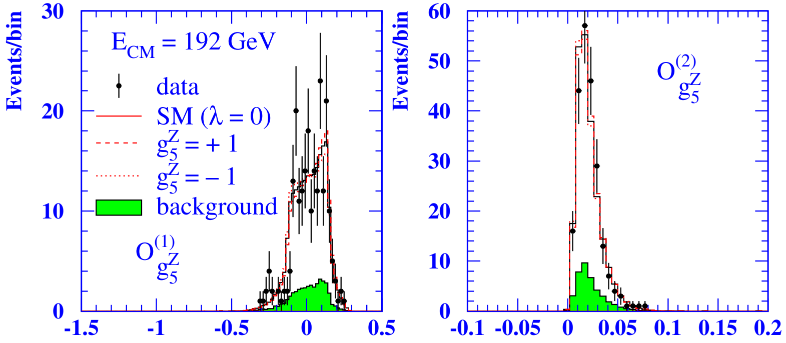

Figure C.27: The 192 GeV data. The description is given in the caption of figure 5.11.

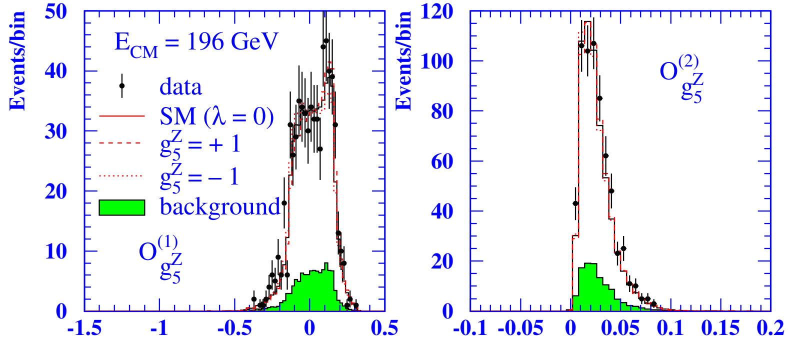

Figure C.28: The 196 GeV data. The description is given in the caption of figure 5.11.

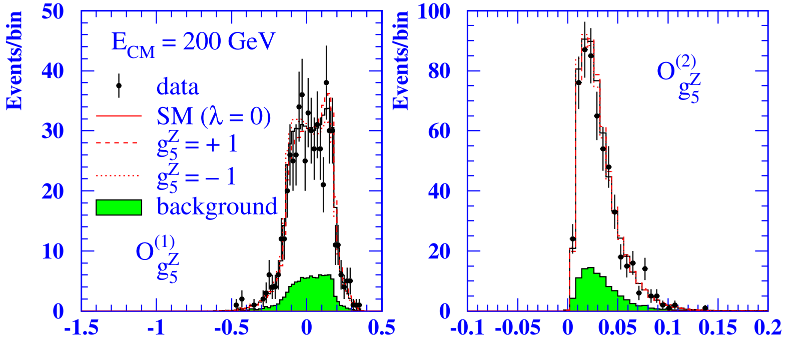

Figure C.29: The 200 GeV data. The description is given in the caption of figure 5.11.

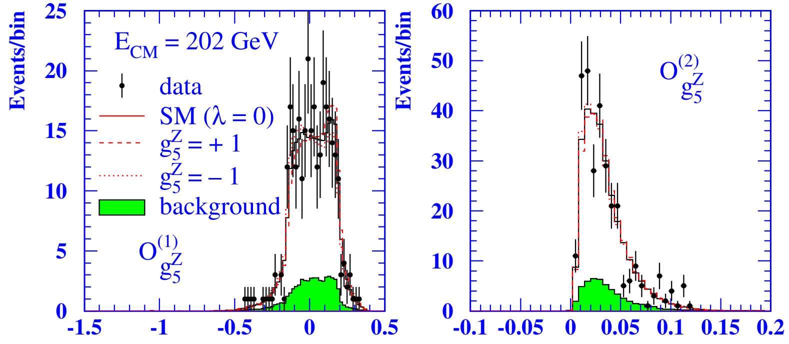

Figure C.30: The 202 GeV data. The description is given in the caption of figure 5.11.

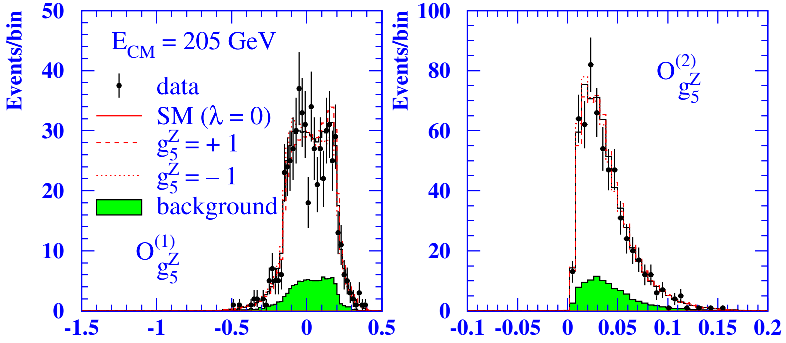

Figure C.31: The 205 GeV data. The description is given in the caption of figure 5.11.

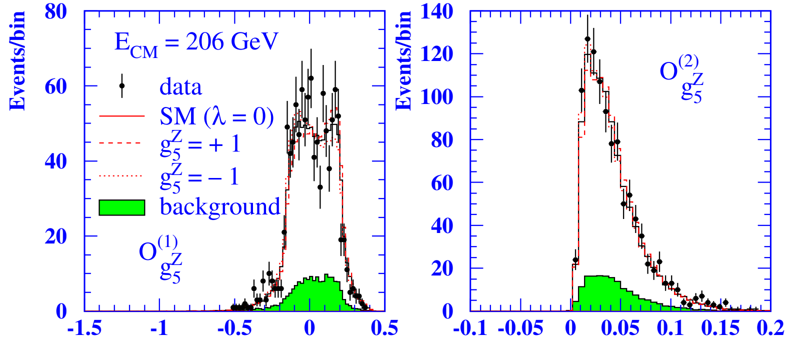

Figure C.32: The 207 GeV data. The description is given in the caption of figure 5.11.